Fast-Neutron Multiplicity Counting Techniques for Nuclear Safeguards Applications

by

Tony H. Shin

A dissertation submitted in partial fulfillment
of the requirements for the degree of
Doctor of Philosophy
(Nuclear Engineering and Radiological Sciences)
in The University of Michigan
2019

Doctoral Committee:

        Professor Sara A. Pozzi, Chair
        Doctor David L. Chichester
        Professor Igor Jovanovic
        Professor Alfred O. Hero III

Tony H. Shin
ORCID ID: 0000-0003-2697-9790
thshin@umich.edu

For my family and friends.

ACKNOWLEDGEMENTS

First and foremost, I thank my loving family. This dissertation would not have been possible without the help of my advisors, mentors, and colleagues. I thank my advisor Sara Pozzi for her support throughout my years at University of Michigan; none of this work would have been possible otherwise. I also thank David Chichester for his advising and hosting of multiple experiments integral to this work. There are numerous past and present members of my research group that have been a large part of my work, and I am grateful to have worked with them all. In particular, I thank Shaun Clarke, Angela Di Fulvio, and Matthew Marcath for their advising and mentoring. Thanks to Cameron Miller; he and I frequently discussed research ideas and findings. Michael Hua and Caiser Bravo also have my thanks for their assistance in research. Special thanks to Cameron Miller, William Steinberger, and Michael Hua for reviewing this work.

TABLE OF CONTENTS

LIST OF FIGURES

LIST OF TABLES

LIST OF APPENDICES

Appendix

LIST OF ABBREVIATIONS

CFD Constant Fraction Discrimination

DA Destructive analysis

DCFD Digital constant fraction discrimination

DPP-PSD Digital Pulse Processing for Pulse Shape Discrimination

DU Depleted Uranium

ENMC Epithermal Neutron Multiplicity Counter

FNMC Fast-Neutron Multiplicity Counting

FOM Figure of merit

FWHM Full-width at half maximum

HEU Highly enriched uranium

IAEA International Atomic Energy Agency

if induced fission

INL Idaho National Laboratory

LEU Low enriched Uranium

MCA Materials Control & Accountability

MCNP Monte Carlo N-particle

MSR Multiplicity Shift Register

MPPost MCNPX-PoliMi Post-Proecessing Detector Algorithm

NDA Nondestructive Assay

NMC Neutron Multiplicity Counting

NNWS Non-Nuclear weapon state

NPT Treaty on the Nonproliferation of Nuclear Weapons

NWS Nuclear-weapon state

PGF Probability Generating Function

PHA Pulse Height Analysis

PIA Pulse Integral Analysis

PID Pulse integral distribution

PKE Point Kinetics Equation

PMT Photomultiplier tube

PSD Pulse-shape Discrimination

PWR Pressurized Water Reactor

RTI Randomly triggered inspection

sf spontaneous fission

SNM Special Nuclear Material

STI Signal-triggered inspection

TCA Time Correlation Analysis

TIA Time Interval Analysis

TOF Time-of-flight

UNCL Uranium Neutron Collar

ZPPR Zero Power Physics Reactor

ABSTRACT

Nuclear safeguards inspections are performed in accessible facilities of Nonnuclear Weapon States by international inspectorates such as the International Atomic Energy Agency. The objective of the safeguards inspections is to detect diversion of significant quantities of fissile material, defined as 8 kg plutonium and 25 kg of highly enriched uranium. The fidelity of detecting clandestine diversion of fissile material depends on the speed, precision, and accuracy of characterizing pertinent physical properties. Special nuclear materials emit multiplets of correlated neutrons that exhibit characteristic signatures. Traditional neutron multiplicity counting is a well-established method that uses an array of capture-based neutron detectors embedded in polyethylene to measure the emitted time-correlated neutrons. However, traditional systems are only sensitive to the emitted neutron multiplicity distribution as the polyethylene thermalizes the emitted neutrons and modulates the initial angular and energy information.

Organic scintillators are scatter-based detectors that directly detect the emitted fast neutrons and therefore measured quantities are closely related to the emitted neutron properties. The time-correlated response of an array of organic scintillators can be used to measure portions of the emitted neutron multiplicity, energy, and angular distribution simultaneously, offering a unique capability unavailable to capture-based systems. The absence of polyethylene allows time-correlation analysis to be implemented on much shorter time scales, which improves measurement precision benefiting the speed and precision of detecting mass diversions.

This dissertation summarizes the feasibility and improvements of a fast-neutron multiplicity counting system for nondestructive assay of special nuclear material. Experimental results of passive (Pu-bearing material) and active (U-bearing material) nondestructive assay are presented, demonstrating the system capability for estimating fissile mass and detecting fissile mass diversions. New point kinetics equations for analytic estimation of the fissile mass were derived to account for the inherent phenomena of neutron cross-talk, where a single neutron enters and registers counts in multiple detectors adversely increasing the observed multiplicity counts. The newly derived equations are verified with experimental results showing improved accuracy of estimating fissile mass when accounting for the spurious cross-talk counts. This work also summarizes experiments performed to characterize angular and energy-angle correlations of special nuclear material in relevant configurations to investigate additional capabilities unavailable to traditional systems. Experimental results are presented for the first time that relate the observed neutron-neutron angular and energy-angle correlations as a function of fissile material physical properties (i.e., leakage multiplication, α-ratio).

CHAPTER I

Introduction

1.1 Motivation for Nuclear Safeguards

The world was introduced to the immense potential of nuclear technology ever since the discovery of the nuclear fission process [1, 2]. After the discovery of the neutron in 1932 by James Chadwick, the concept of self-sustaining nuclear chain reactions was conceived by Leo Szilard and Enrico Fermi, eventually leading to the historic successful nuclear reactor test at the Chicago Pile-1 in 1942; this would be the first major technical achievement towards the creation of the atomic bomb [3].

The knowledge that nuclear technology could be leveraged for both peaceful and destructive use was known quite early on, as evident by the so-called "Einstein-Roosevelt" letter written on August 2nd, 1939 [4]. The letter projects many of the impending difficulties that may arise from the rapid development of nuclear technology. Of particular interest is the concern for the potential of creating the atomic bomb. After detailing the recently conceived idea of self-sustaining nuclear chain reactions, the letter states [4]:

> *"This new phenomenon would also lead to the construction of bombs, and it is conceivable - though much less certain - that extremely powerful bombs of a new type thus be constructed."*

The letter also expresses his warning on Germany's clandestine nuclear research urging addi-

tional funding for his own work; this would eventually lead to the funding of the Manhattan Project. After the Second World War, the United States and the Soviet Union would continue to further their nuclear weapons capabilities, where the hydrogen bomb was developed in the early 1950s. However, a different perspective on nuclear technology came about with President Eisenhower's 1953 "Atoms for Peace" address on the peaceful uses of nuclear energy [5]. The Atoms for Peace initiative aimed to establish an international agency where states with nuclear materials would contributed uranium and other fissionable materials in hope to develop peaceful uses. The initiative provided the global infrastructure for future international safeguards agreements to be implemented, primarily due to the emphasis on the storage, accountancy, and inspection of the nuclear material [6].

The Treaty on Nuclear Nonproliferation of Nuclear Weapons (NPT) was signed in 1968 and is the foundation for international safeguards in today's world [7]. The primary objective of the NPT is to prevent the spread of nuclear weapons and associated weapons technology. Specifically, the NPT defines nuclear-weapon states (NWS) and non-nuclear weapon states (NNWS) as countries that had or had not built and tested a nuclear device prior to 1967. Under the NPT agreement, the NWS pledge to not spread, influence, or assist any NNWS in the acquisition of a nuclear weapon, while the NNWS pledge to not pursue any technology, materials, or assistance from NWS to acquire a nuclear weapon [7]. The NNWS also pledge to accept IAEA safeguards inspections to ensure that all nuclear activities serve only peaceful uses [7].

The objective of the IAEA safeguards inspections in NNWS is to detect the diversion of significant quantities of plutonium (8 kg) and highly enriched uranium (HEU) (25 kg), which is the approximate quantity required to develop a nuclear weapon [8]. The IAEA safeguards inspections encompass various scopes including containment and surveillance, physical security, and materials control and accountability (MCA). MCA focuses on tracking the amount of all special nuclear material (SNM) (i.e., all fissile materials) in an accessible NNWS facility [8, 9]. MCA can be implemented primarily with two fields of analysis techniques: nonde-

structive assay (NDA) and destructive assay (DA). DA techniques are intrusive methods that require the destruction of the tested sample of SNM for chemical analysis; although these techniques provide the most accurate characterization, the analysis is limited by the homogeneity of the SNM and the relatively long analysis time. NDA techniques are nonintrusive methods that measure characteristic signatures without direct contact with the SNM. Most NDA techniques are based on detecting the radiation emitted from the SNM from spontaneous or induced fission reactions to infer the amount of fissile mass, and to ultimately implement a declaration-verification protocol between the inspector and the NNWS.

There exists limitations of implementing international safeguards inspections, mainly concerned with the sensitivity, accuracy, and speed of declaring that fissile mass has indeed been diverted [6, 8]. That is, the detection system used for NDA could fail to detect fissile mass diversions if very small amounts of SNM are being diverted throughout a long time period [6]. Furthermore, the timely detection of diversion scenarios with high confidence is essential to minimize operational costs and maximize the number of inspected items [8].

1.2 Thesis Overview and Contributions

In this dissertation, I use a fast-neutron multiplicity counting (FNMC) system consisting of an array of scatter-based organic scintillators to simultaneously measure portions of the emitted neutron multiplicity, energy, and angular distributions to be used for NDA of SNM. Organic scintillators can detect the emitted fast neutrons without the need for moderation. The absence of intervening moderating material between the SNM and the detectors enables additional information to be retained that is typically unavailable to the traditional ^{3}He capture-based systems. Specifically, an FNMC system is sensitive to portions of the emitted neutron multiplicity, energy, and angular distribution from the SNM. Furthermore, FNMC systems operate on timescales that are orders of magnitude shorter than capture-based NMC systems, which in turn, provides improvements in the measurement precision for fixed acquisition times. This dissertation leverages the energy, angular, and multiplicity information

3

available to FNMC systems to measure correlated fission signatures to characterizes SNM, while also demonstrating the improvement in the sensitivity, speed, and accuracy in the FNMC system compared to traditional capture-based neutron multiplicity counting (NMC) systems. The following is a brief description of each chapter in this dissertation:

Chapter II: I describe the nuclear fission process and the associated particles emitted from fission events. I also summarize the characteristic distributions of prompt fission and nonfission neutrons, and relate them to the physical fissile material properties of interest for NDA. Lastly, I provide an overview of the previous theoretical work based on the point kinetics approximation, and how it relates to the fissile material properties.

Chapter III: I briefly discuss the detection mechanisms for organic scintillators, and provide a detailed characterization of the organic scintillator used for the FNMC system. I show how the experimentally-informed parameters from the characterization measurements can be used to simulate high-fidelity Monte Carlo simulations of detector response. I also discuss the inherent neutron cross-talk effect, and the expected influence to the overall observed counts

Chapter IV: I present the data analysis techniques for extracting the neutron multiplicity count rates using two different methods: time series analysis and event-by-event extraction. The first method is used in traditional NMC systems, but the much shorter time scales offer benefits when using an FNMC system. The second method is unique to FNMC systems, and is used to extract neutron-neutron angular and energy-angle correlations. I discuss the effects of neutron cross-talk for time series analysis, and present newly derived point kinetics equations with neutron cross-talk corrections.

Chapter V: I analyzed measured data from an experimental campaign at Idaho National Laboratory to demonstrate the FNMC capability to perform passive NDA on

Pu-metal assemblies for estimating fissile mass using a one-parameter, two-parameter, and three-parameter approach.

Chapter VI: I performed active NDA measurements using two AmLi interrogation sources on fuel-bundle like uranium oxide pin assemblies to characterize the sensitivity of the FNMC system to detect mass diversions. I also extend the study in simulations, and directly compare the performance of FNMC system to the currently-deployed capture-based Uranium Neutron Collar UNCL system.

Chapter VII: I analyze the data from the passive plutonium measurements at Idaho National Laboratory to extract event-by-event neutron-neutron angular and energy-angle correlations as a function of the leakage multiplication. I measured neutron-neutron angular and energy-angle correlations and demonstrate that they are dependent on the leakage multiplication of the measured Pu-metal assembly. The dependence of neutron-neutron angular and energy-angle correlations on leakage multiplication has not been measured prior to my work.

Chapter VIII: I performed a dedicated FNMC experiment at Los Alamos National Laboratory to characterize the observed neutron-neutron angular and energy-angle correlations as a function of the α-ratio, which is one of the physical properties of interest. I present the dependence of these correlations on the α-ratio, a result that has not been measured prior to my work.

Chapter IX: I summarize the findings of each chapter, and present possible pathways for future work.

CHAPTER II

Fissile Material: Correlated Signatures and Physical Properties

This chapter provides an overview of nuclear fission and the characteristic neutron signatures that arise from fission events in the context of nuclear safeguards applications. The nuclear fission process is discussed in Section 2.1, establishing the expected time scale of the fission process and associated particles. The characteristic distributions of prompt fission neutrons are detailed in Sections 2.2 including the expected multiplicity, energy, and angular distribution. Section 2.3 is a brief discussion on the characteristics of nonfission neutrons. Section 2.4 provides definitions for the fissile material physical properties of interest in nuclear safeguards applications in relation to the neutrons emitted from spontaneous fission (sf), induced fission (if), and nonfission reactions. Section 2.5 provides a detailed overview of the fundamental principles of the point kinetics equations along with a discussion on the underlying assumptions and limitations. Portions of this chapter were adapted from my technical note titled "A Note on the Nomenclature in Neutron Multiplicity Mathematics" published in Nuclear Science and Engineering [10].

2.1 Nuclear Fission Process

When certain heavy nuclides undergo fission, each fission event produces several neutron-rich unstable fission fragments. These fission fragments will emit multiplicities of neutrons (order of 10^{-18} 10^{-15} seconds) and gamma rays (order of 10^{-14} 10^{-10} seconds) following the initial split to disperse the energy created in the process to reach a stable state; these emitted particles are known as prompt neutrons and prompt gamma rays [11]. However, even after the emission of these prompt particles, the fission fragments may still be unstable and will undergo radioactive decay (order of $> 10^{-3}$ seconds), which also emit neutrons and gamma rays; these emitted particles are known as delayed neutrons and delayed gamma rays as they are emitted much later in time [11]. Both prompt and delayed neutrons can initiate subsequent fission events; these self-propagating fissions are known as fission chains and are the essence of any self-sustaining fission system. The fissile material of interest in typical safeguards applications exhibit relatively short fission chains, where detection systems are designed to measure correlated neutrons on a time scale much shorter than the average delayed neutron period. Therefore, measurements made by the detection system are primarily representative of the prompt neutron behavior [12]. This chapter will focus on prompt fission neutron emissions from spontaneous and induced fissions.

2.2 Prompt Fission Neutron Emissions and Characteristics

Prompt fission neutrons can originate from either spontaneous fission (*sf*) or induced fission (*if*) reactions. Neutrons emitted from *sf* reactions are typically dominated by the *sf* reactions of the even isotopes of the sample (e.g., ^{240}Pu, ^{238}Pu, ^{242}Pu), and are the initiators of the subsequent fission chains. The *if* reactions are most prevalent in the odd isotopes of the sample (e.g., ^{239}Pu), and are responsible for the self-sustaining nature of the fission chains in reactors and weapons alike. The observation of the *sf* neutrons can provide insight about the total *sf* rate within the sample, which is closely related to the effective fissile mass.

The observation of the *if* neutrons (can be thought of as the excess neutrons observed from just the *sf* neutrons) provide information about the multiplicative properties of the sample. A third source of neutrons from nonfission reactions may also induce fission, and is discussed in detail in Section 2.3.

2.2.1 Multiplicity Distribution

The multiplicity of neutrons that are emitted in a single fission event is described by the neutron multiplicity distribution, and is specific to each unique isotope and type of fission. Neutron multiplicity distributions are unique to fission reactions; it is rare to see multiplicities of neutrons greater than two for nonfission reactions. The neutrons emitted in a given fission event are correlated in both number and time, where detection systems are designed to measure these correlated fission neutrons within some allocated time window. Figures 2.1 and 2.2 show the ^{240}Pu *sf* and ^{239}Pu *if* neutron multiplicity distributions [13].
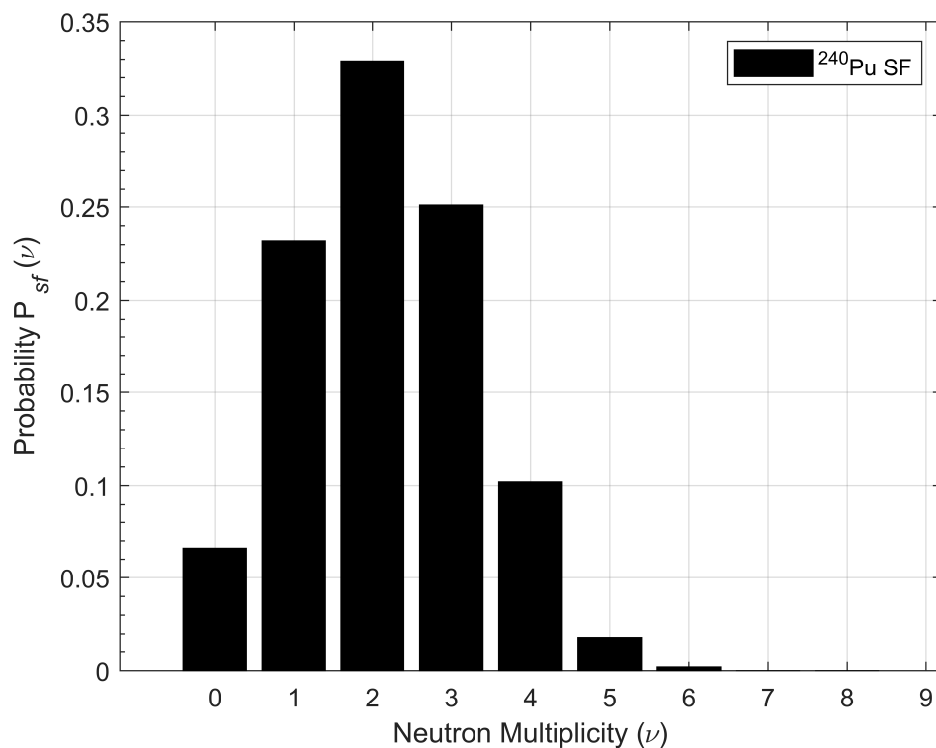
Figure 2.1: Neutron multiplicity distribution for ^{240}Pu *sf* reactions
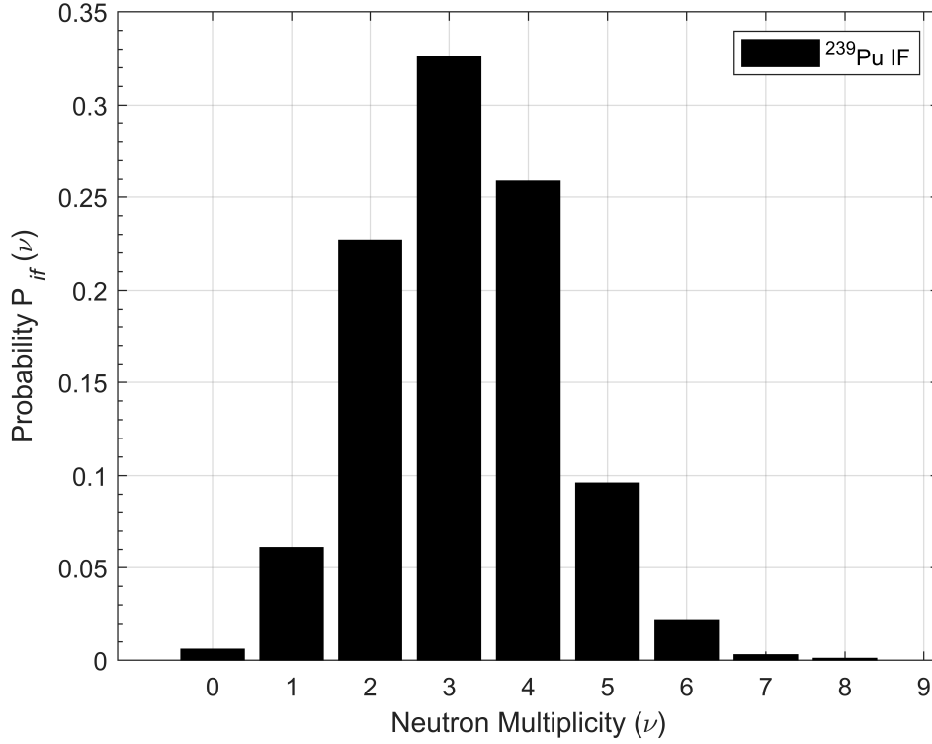
Figure 2.2: Neutron multiplicity distribution for ^{239}Pu *if* reactions with 2 MeV incident neutron energy

The effective number of neutron combinations that can be grouped together from a single fission event is quantified using reduced factorial moments of the neutron multiplicity distribution [14, 15]. For safeguards applications, the first-, second-, and third-order reduced factorial moments of the *sf* and *if* neutron multiplicity distribution are calculated using

$$\nu_{sf,m} = \sum_{\nu=m}^{\infty} \binom{\nu}{m} P_{sf}(\nu), \tag{2.1}$$

and

$$\nu_{if,m} = \sum_{\nu=m}^{\infty} \binom{\nu}{m} P_{if}(\nu), \tag{2.2}$$

respectively, where m denotes the order of the moments, and ν denotes the number of emitted neutrons [15–17]. These factorial moments are considered to be fundamental nuclear data previously determined through independent measurements [14–17]. Table 2.1 shows the first-

, second-, and third-order reduced factorial moments for the ^{240}Pu sf and ^{239}Pu if multiplicity distributions [13].

Table 2.1: First-, second-, and third-order reduced factorial moments of the ^{240}Pu sf and ^{239}Pu if neutron multiplicity distribution

^{240}Pu	$\nu_{sf,1}$	$\nu_{sf,2}$	$\nu_{sf,3}$
	2.156	3.825	5.336
^{239}Pu	$\nu_{if,1}$	$\nu_{if,2}$	$\nu_{if,3}$
	3.163	8.240	17.321

2.2.2 Energy Distribution

The neutron energy distribution for the emitted fission neutrons ranges from below thermal (0.025 eV) to fast (10 MeV) energies, where the typical mean energy of fission neutrons is approximately 2 MeV. The full neutron energy distribution can be approximated by the Watt spectrum, which has the form [13, 18]

$$f(E) = C exp\left(\frac{-E}{a}\right) sinh\left(\sqrt{bE}\right),\tag{2.3}$$

where C is the normalization factor and a and b are constants that are specific to the fissioning isotope. The relationship between the number and energy of emitted neutrons is still considered to be an open area of research; however, this work assumes that the energy of the emitted neutrons is independent of the multiplicity [19, 20]. Figure 2.3 shows the neutron energy distribution for neutrons emitted from ^{240}Pu sf and ^{239}Pu if reactions (1 MeV incident neutron energy) [18].

2.2.3 Angular Distribution

Since the prompt fission neutrons are emitted from the fully accelerated fission fragments, an anisotropic distribution of neutron-neutron coincidences can be observed in the fission-fragment frame of reference. The anisotropic distribution of prompt fission neutrons in single-
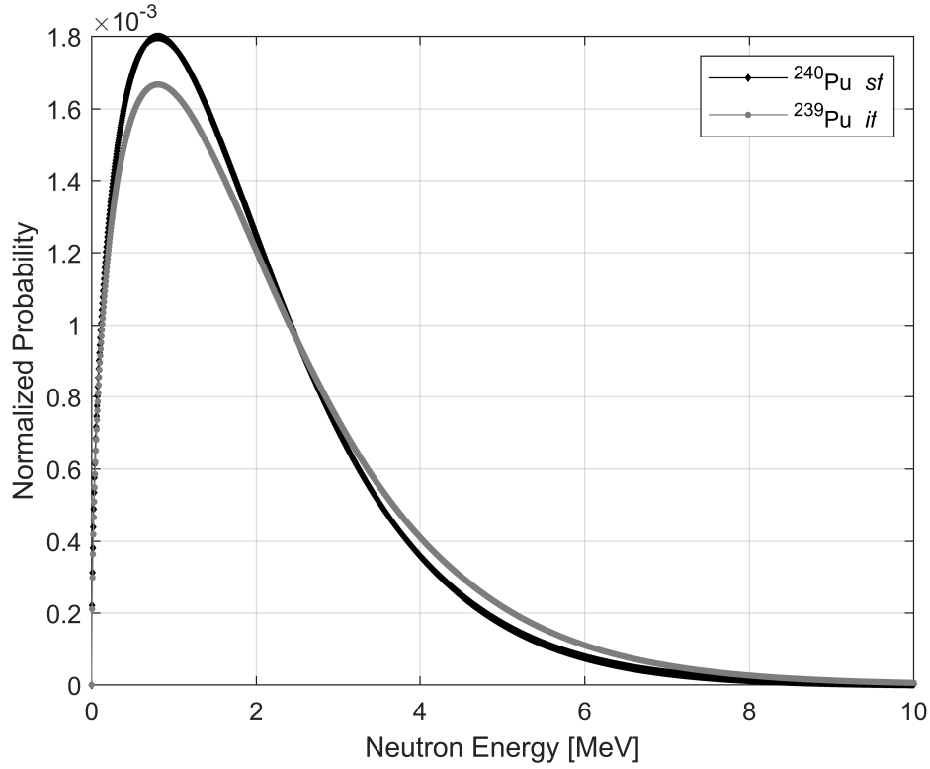
Figure 2.3: Neutron energy distribution for ^{240}Pu *sf* and ^{239}Pu *if* (1 MeV incident neutron energy) reactions.

fission events has been studied extensively [21–27], and is attributed to the kinematic boost in energy and momentum the fission neutron receives depending on whether the direction of the emitted neutron relative to the direction of the fragments. We expect to see higher rates of neutron coincidences at smaller (0°) and larger (180°) angles, and a minimum at 90° corresponding to the momentum boost along the fission fragment direction [21–27]. One way to quantify the anisotropy is by taking the ratio of the coincidences observed at 180° to those at 90°, where a value of one indicates a purely isotropic source. In addition to the directional bias of these emitted neutrons, there exists a positive correlation between the energy of the emitted neutrons and the magnitude of the directional bias [26, 27]. Again, this positive correlation is attributed to the fission kinematics, where neutrons emitted along the fragment direction also receive a boost in energy. The correlation between the neutron anisotropy and energy is one of the primary observable signatures that is investigated in this

thesis, hereafter referred to as energy-angle correlations.

2.3 Nonfission Neutron Emissions and Characteristics

There exist other sources of neutrons in SNM that may originate from nonfission reactions. The nonfission reactions that emit neutrons in typical SNM for safeguards applications arise from (α,n) reactions on low-z impurities [13, 17], where a single neutron is emitted per reaction. These singly emitted neutrons share no correlation in time, angle, energy, or multiplicity with their fission neutron counterparts since they are emitted from a fundamentally different nuclear process. In other words, the (α,n) neutron multiplicity distribution is simply a uniform distribution about $\nu = 1$, they have an appreciably different energy spectrum due to the Q-value nature of the (α,n) reaction . Furthermore, the (α,n) neutrons are emitted purely isotropically. The ability to distinguish between fission and (α,n) neutrons is significant for accurate characterization of SNM physical properties. Table 2.2 shows the neutron energy and expected yield for (α,n) reactions on various low-z impurities [13].

Table 2.2: Neutron yield and average neutron energy for (α,n) reactions on various impurities [13].

Impurity (natural isotopic composition)	Neutron yield per 10^6 5.2 MeV a-particles (Pu average)	Average neutron energy for 5.2 MeV a-particles [MeV]
O	0.059 $\pm$ 0.002	1.9
Si	0.076 $\pm$ 0.003	1.2
Al	0.41 $\pm$ 0.01	1.0
Mg	0.89 $\pm$ 0.02	2.7

2.4 Fissile Material Physical Properties

The fissile material physical properties that are pertinent to SNM samples are inferred by measuring the emitted neutron multiplicities [13, 17]. The three physical properties of

interest for characterizing SNM include the sample fissile mass, multiplication, and α-ratio. This section first describe the possible pathways for neutrons to be created or eliminated during their lifetime in an SNM sample, and the definitions of the physical properties and how they relate to the neutron creation/elimination mechanisms immediately follow.

Therefore, the observable neutrons emitted from an SNM sample include contributions from *sf*, *if*, and (α,n) neutrons. We introduce three physical properties that are directly related to each of the three different contributions; the physical properties are the sample fissile mass, leakage multiplication, and the α-ratio.

2.4.1 Fissile Mass

The fissile mass of the sample is closely related to the rate of detected spontaneous fission neutrons, and is typically estimated as the parametric quantity [13, 17]

$$^{240}Pu_{eff} = 2.52^{238}Pu + {}^{240}Pu + 1.68^{242}Pu, \tag{2.4}$$

where $^{240}Pu_{eff}$ is the ^{240}Pu effective mass, and represents the mass of pure ^{240}Pu that would yield the same number of neutron multiplicity counts (specifically doubles) as that obtained from the combination of all the even isotopes within the sample (assuming no surplus of neutrons emitted from induced fissions). The $^{240}Pu_{eff}$ calculated in Eq. (2.4) is derived from scaling the specific *sf* neutron yield, and is shown in Table 2.3 [13, 17]. Once the

Table 2.3: *sf* yield for the even isotopes of plutonium [13, 17].

	^{238}Pu	^{240}Pu	^{242}Pu
sf Yield [n/s-g]	2.59 x 10^3	1.02 x 10^3	1.72 x 10^3

$^{240}Pu_{eff}$ is estimated from the neutron multiplicity measurements, a secondary measurement is conducted to obtain the isotopic composition of the sample (e.g., high-resolution gamma-ray spectroscopy, mass spectroscopy, etc.) [13]. Given the $^{240}Pu_{eff}$, the total plutonium

mass of the sample is estimated using [13, 17]

$$^{\text{Total}}Pu = \frac{^{240}Pu_{eff}}{(2.52f_{238} + f_{240} + 1.68f_{242})}, \tag{2.5}$$

where f_{238}, f_{240}, and f_{242} are the isotopic fractions of the respective plutonium isotopes. Therefore, neutron multiplicity measurements infer the amount of total fissile material, where subsequent isotopic measurements can provide details on the amount of each specific isotope of plutonium. Since the $^{240}Pu_{eff}$ is based only on sf neutrons, we introduce the effective spontaneous fission rate of ^{240}Pu within the sample, Q_{sf}, where the $^{240}Pu_{eff}$ is calculated with

$$^{240}Pu_{eff} = \frac{Q_{sf}}{Q_{sf_{240}}}, \tag{2.6}$$

where $Q_{sf_{240}}$ is the specific activity of ^{240}Pu sf reactions in units of fissions/(s-g).

2.4.2 Multiplication

In most practical settings the SNM sample typically has varying amounts of ^{239}Pu, which in turn will cause or produce induced fissions from the initiating sf neutrons. The concept of neutron multiplication in fission systems was first introduced by Serber et al. [28], and is a quantity that describes the efficiency of inducing fission chains. The total neutron multiplication, M_T, refers to the cumulative number of neutrons produced within the system from induced fission chains given a single initiating neutron, and is mathematically expressed as

$$M_T = \frac{1}{1 - p_{if}\nu_{if,1}}, \tag{2.7}$$

where p_{if} is the induced fission probability, and $\nu_{if,1}$ is the mean number of neutrons emitted from an induced fission event (i.e., first-order reduced factorial moment of the ^{239}Pu if neutron multiplicity distribution) [28]. Equation (2.7) is the ratio of the excess neutrons that were created in the current generation divided by the number of neutrons in the previous generation. Not all the neutrons in the previous generation will induce fissions, rather,

14

a majority of neutrons will escape or "leak" out of the SNM sample volume without any interactions. We introduce the concept of the sample leakage multiplication, M_L, which is defined as

$$M_L = \frac{1 - p_{if}}{1 - p_{if}\nu_{if,1}},\tag{2.8}$$

and reflects the total number of multiplied neutrons that have escaped the sample [28]. From Eqs. (2.7) and (2.8), it is clear to see that M_L will always be less than or equal to M_T.

2.4.3 α-ratio

The α-ratio is defined as the ratio of neutrons emitted from sf reactions [13, 15, 17], N_{sf} to those emitted from (α,n) reactions, N_α, and has the form

$$\alpha\text{-ratio} = \frac{N_\alpha}{N_{sf}}.\tag{2.9}$$

For plutonium metal samples, where there is no low-z impurity, the α-ratio is equal to zero. For plutonium samples in the form of oxides and fluorides, the α-ratio is nonzero, and can be calculated using the (α,n) reaction yields [13].

2.5 Point Kinetics Equations

The point kinetics equations (PKE) presented in this section describe the time and number behavior of the neutron population in a sample of SNM. The derivation of the PKE involves a fundamental understanding of the possible pathways for the production and loss of neutrons within a sample of SNM for any neutron. The possible pathways for neutron production within an SNM sample with an internal initiating neutron source consist of (i.e., no external interrogation source) [15, 17, 29]:

1. Neutrons produced from sf reactions, where multiplicities of neutrons are emitted as described by Figure 2.1

2. Neutrons produced from *if* reactions, where multiplicities of neutrons are emitted as described by Figure 2.2. Both *sf* and (α,n) neutrons can induce fissions.

3. Neutrons produced from (α,n) reactions, where a single neutron is emitted per reaction.

Similarly, there exist pathways for neutron loss within a sample of SNM and consist of [15, 17, 29]:

1. Neutrons lost from inducing fissions. Both *sf* and (α,n) neutrons can be lost from inducing fissions.

2. Neutrons lost from parasitic nonfission capture reactions

Of all the neutrons that were produced, only those neutrons that escape or leak the sample volume are readily available for detection. It is assumed that neutrons that do not not undergo any loss pathways escape the volume.

2.5.1 Time-Dependent Neutron Population

The point kinetics approximation can be seen as the simplification of the well known Boltzman's neutron transport equation, where a purely time-dependent description of the neutron number behavior is obtained by integrating over the entire space and energy domains. This integration is quite useful in that the underlying relationship between the detected neutron multiplicity rates and the physical SNM properties are only a function of the time-dependent detected neutron number distribution [11, 12, 30–35]. Consider a point-like sample of SNM with one neutron energy group (space- and energy-independent). The point kinetics equation describing the change in the neutron population, $dn(t)$, can be described by the balance equation of neutron production and loss terms, and is given by

$$\frac{dn(t)}{dt} = V n(t) \left(\nu_{if,1} \Sigma_f - \Sigma_c - D B^2 \right),$$ (2.10)

where V is the average neutron velocity, DB^2 is the product of the diffusion coefficient and the geometric buckling terms (related to the leakage of neutrons), and Σ_f and Σc are the macroscopic fission and nonfission capture reaction cross-sections, respectively [33, 35, 36]. In Eq. (2.10), the neutron production term is described by the neutrons produced from *if* reactions, $Vn(t)\nu_{if,1}\Sigma_f$, while the loss term is described by the nonfission captures, $Vn(t)\Sigma_c$, and the leakage, $Vn(t)DB^2$, of neutrons. Equation (2.10) can be rewritten with the average time behavior of the production and loss components by defining the mean time to leakage and capture as

$$\tau_L = \frac{1}{VDB^2}, \tag{2.11}$$

and

$$\tau_c = \frac{1}{V\Sigma_c}, \tag{2.12}$$

which describes the average time for a neutron to escape through leakage and nonfission captures. The mean time to fission (i.e., the mean generation time), τ_f, has the form

$$\tau_f = \frac{1}{V\Sigma_f}, \tag{2.13}$$

and describes the average time for a neutron to be lost through an *if* reaction. Using Eqs. (2.11), (2.12), and (2.13), the probability of a neutron being removed from the system is described by the mean neutron lifetime, τ_0, as the sum of all competing events, and is given by

$$1 = \frac{\tau_0}{\tau_f} + \frac{\tau_0}{\tau_c} + \frac{\tau_0}{\tau_L} = p_{if} + p_c + p_L, \tag{2.14}$$

where p_{if}, p_c, and p_L are the *if*, nonfission capture, and leakage probability of a neutron, respectively. Using the probabilities defined in Eq. (2.14), the neutron balance equation in

17

Eq. (2.10) following an instantaneous injection of initiating neutrons can be rewritten as

$$
\begin{aligned}
\frac{dn(t)}{dt} &= -\frac{n(t)}{\tau_0} + \frac{n(t)}{\tau_f}\nu_{if,1} \\
&= -\frac{n(t)}{\tau_0} + \frac{n(t)p_{if}\nu_{if,1}}{\tau_0} \\
&= n(t)\frac{(k_p - 1)}{\tau_0},
\end{aligned}
\tag{2.15}
$$

where

$$
k_p = \frac{\nu_{if,1} - \Sigma f}{\Sigma_f + \Sigma_c + DB^2} = \frac{\nu_{if,1}\tau_0}{\tau_f} = \nu_{if,1}p_{if}
\tag{2.16}
$$

is the prompt neutron multiplication factor given by the ratio of the production and loss terms [35]. Equation (2.15) is typically written as

$$
\frac{dn(t)}{dt} = \alpha n(t), \quad \alpha = \frac{1 - k_p}{\tau_0},
\tag{2.17}
$$

where α is defined as the prompt neutron decay constant [12, 30, 32]. Solving Eq. (2.17) given $n_0 = 1$ initial neutrons at $t = 0$ describes the probable number of neutrons at some later time, t, and has the form

$$
n(t) = n_0 e^{-\alpha t}.
\tag{2.18}
$$

It is useful to relate Eq. (2.18) to the definition of the total multiplication, M_T, and is derived by first noting that the probable number of if, dQ_{if}, produced in dt about time t for n_0 initiating neutrons is given by

$$
dQ_{if} = n_0 e^{-\alpha t}\frac{dt}{\tau_f},
\tag{2.19}
$$

The number of neutrons resulting from the fissions produced in dt is

$$
dn = \nu_{if,1} \cdot dQ_{if} = \nu_{if,1}n_0 e^{-\alpha t}\frac{dt}{\tau_f} \quad .
\tag{2.20}
$$

The total number of neutrons, including those produced in subsequent *if* reactions due to $n_0 = 1$ initiating neutrons emitted at $t = 0$ is given by

$$
\begin{aligned}
n_0 + \int_0^\infty \nu_{if,1} n_0 e^{-\alpha t} \frac{dt}{\tau_f} &= 1 + \frac{\nu_{if,1}}{\tau_f} \left(\frac{1}{\alpha} \right) \\
&= 1 + \frac{\nu_{if,1}}{\tau_f} \left(\frac{\tau_0}{1 - k_p} \right) \\
&= 1 + \frac{k_p}{1 - k_p} \\
&= \frac{1}{1 - k_p} \\
&= M_T.
\end{aligned}
\tag{2.21}
$$

For SNM assemblies that are near-critical where M_T is relatively very high, the observed time-dependent neutron number behavior is primarily attributed to the internal fission kinematics of the assembly. In other words, a near-critical assembly is viewed to have a continuous self-modulated production of neutrons from *if* chains and therefore the production is dominated by prompt neutrons born from *if* reactions. Under these circumstances, it is possible to directly measure α [37]; measuring α is the underlying principle of reactor noise analysis techniques [12, 30–32, 34, 36, 38].

For typical nuclear safeguards applications, SNM assemblies are highly subcritical where M_T is typically much closer to one (i.e., relatively short fission chains). The observed time-dependent neutron number behavior is not dominated by the neutrons produced from *if* chain reactions, but rather the neutrons emitted from *sf* and (α,n) reactions also contribute significantly. Furthermore, the average neutron time behavior for all competing channels (i.e., α) for highly subcritical assemblies is typically dominated by detector and environmental effects, and thus a direct measurement of α is not possible [35]. Therefore, the observed average neutron time behavior in highly subcritical assemblies is indicative of systematic effects and a characterization of these effects can provides aggregate corrections in practical applications. To avoid confusion between the observed α for near-critical versus highly

subcritical SNM assemblies, we can introduce the following distinction:

$$
\begin{aligned}
\alpha &= \frac{k_p - 1}{\tau_0}, \quad k_p \approx 1 \\
\alpha &= \frac{1}{\lambda}, \quad k_p \approx 0
\end{aligned}
\tag{2.22}
$$

where λ is referred to as the system die-away constant, and describes the mean time to detection of all emitted neutrons.

2.5.2 Factorial Moments of the Total Emitted Neutron Distribution

In the case of highly subcritical SNM assemblies, a set of physical assumptions can be made to derive the (PKE) that relate the total emitted neutron multiplicity distribution to the physical properties of SNM. The assumptions governing the reliability of the PKE are as follows [15, 29]:

1. All neutrons from *if* are emitted simultaneously with the initiating *sf* or (α,n) neutron. This is commonly referred to as the superfission concept, and is valid for highly subcritical assemblies (much like the ones in typical safeguards applications).

2. The SNM of interest behaves as if it had a point-like geometry. Specifically, the neutron detection efficiency and the *if* probability is uniform throughout the SNM volume.

3. The neutron detection efficiency, the *if* probability, and the *if* neutron multiplicity are independent of the *sf* or (α,n) neutron energy.

4. Nonfission neutron capture reactions within the SNM are considered a negligible neutron loss mechanism. This assumption allows the total multiplication, M_T, to be inferred from the estimated leakage multiplication, M_L.

5. There is no correlation between the emitted neutron multiplicity and energy distributions.

20

6. The system die-away time can be described as a first-order exponential function with a system die-away constant, λ.

It is useful to establish the factorial moments of all the initiating events (i.e., *sf* and (α,n) reactions). These moments can then be related to the moments of the *if* events by considering the multiplication of neutrons [15, 29, 34, 39]. To derive the expressions for the factorial moments of the two initiating events, we first define the total rate of initiating events, Q_S, as

$$Q_S = Q_\alpha + Q_{sf}, \tag{2.23}$$

where Q_α and Q_{sf} denote the reaction rate of (α,n) and *sf* reactions, respectively. Equation (2.23) can be expressed as a joint probability distribution in terms of the two neutron emission rates using

$$P_{Q_S}(\nu) = \frac{Q_{sf}}{Q_S} P_{sf}(\nu) + \frac{Q_\alpha}{Q_S} \delta_{1,\nu}, \tag{2.24}$$

where $\delta_{1,\nu}$ is the kronecker delta function representing a single neutron emission per (α,n) reaction, and P_{sf} is the *sf* neutron multiplicity distribution given in Eq. (2.1) [29, 39]. The α-ratio from Eq. (2.9) is rewritten in terms of *sf* and (α,n) reaction rates, and has the form

$$\alpha\text{-ratio} \equiv \frac{Q_\alpha}{\nu_{sf,1} Q_{sf}}. \tag{2.25}$$

Substituting Eq. (2.25) into Eq. (2.23) gives the definition of the total initiating reaction rate in terms of $\nu_{sf,1}$ and α, which has the form

$$Q_S = Q_{sf}(1 + \alpha\nu_{sf,1}). \tag{2.26}$$

Similarly, the probability distribution of the emitted neutrons from the initiating events can be written as

$$P_{Q_S}(\nu) = \frac{\alpha\nu_{sf,1}\delta_{1,\nu} + P_{sf}(\nu)}{1 + \alpha\nu_{sf,1}}. \tag{2.27}$$

21

Using the probability distribution function in Eq. (2.27), the corresponding n^{th}-order factorial moments, $\nu_{Q_S,n}$, for the neutron emitted from the initiating events have the form

$$\nu_{Q_S,1} = \frac{\nu_{sf,1}\,(1+\alpha)}{(1+\alpha\nu_{sf,1})}, \quad n = 1 \quad \text{and}$$

$$\nu_{Q_S,n} = \frac{\nu_{sf,n}}{(1+\alpha\nu_{sf,n})}, \quad n \neq 1.$$

(2.28)

Lastly, the factorial moments of the initiating events can then be related to the nth-order factorial moments of the total emitted neutron distribution, $\nu_{Q_T,n}$, including the multiplied neutrons from if reactions. Using Eq. (2.28), the nth-order factorial moments of the total emitted neutron distribution have the form

$$\nu_{Q_T,1} = M_L \nu_{Q_S,1}$$
$$= \frac{M_L}{(1+\alpha\nu_{sf,1})\,\nu_{sf,1}\,(1+\alpha)},$$

(2.29)

$$\nu_{Q_T,2} = M_L^2 \left[\nu_{Q_S,2} + \left(\frac{M_L - 1}{\nu_{if,1} - 1} \right) \nu_{Q_S,1}\nu_{if,1} \right]$$
$$= \frac{M_L^2}{(1+\alpha\nu_{sf,1})} \left[\nu_{sf,2} + \left(\frac{M_L - 1}{\nu_{if,1} - 1} \right) \nu_{sf,1}\,(1+\alpha)\,\nu_{if,2} \right],$$

(2.30)

and

$$\nu_{Q_T,3} = M_L^3 \left[\nu_{Q_S,3} + \left(\frac{M_L - 1}{\nu_{if,1} - 1} \right) (3\nu_{Q_S,2}\nu_{if,2} + \nu_{Q_S,1}\nu_{if,3}) + 3 \left(\frac{M_L - 1}{\nu_{if,1} - 1} \right)^2 \nu_{Q_S,1}\nu_{if,2}^2 \right]$$
$$= \frac{M_L^3}{(1+\alpha\nu_{sf,1})} \left[\nu_{sf,3} + \left(\frac{M_L - 1}{\nu_{if,1} - 1} \right) (3\nu_{sf,2}\nu_{if,2} + \nu_{sf,1}\,(1+\alpha)\,\nu_{if,3}) \right.$$
$$\left. + 3 \left(\frac{M_L - 1}{\nu_{if,1} - 1} \right)^2 \nu_{sf,1}\,(1+\alpha)\,\nu_{if,2}^2 \right].$$

(2.31)

2.5.3 Relationship Between Factorial Moments and Fissile Material Physical Properties

Equations (2.29), (2.30), and (2.31) describe the factorial moments of the total emitted neutron distribution, Q_T, per initiating event. Recalling the relationship between the total initiating reaction rate in Eq. (2.26), the reduced factorial moments of Q_T (without redundant permutations) can be written in terms of the *sf* rate, Q_{sf} using

$$
\begin{aligned}
C_k &= Q_S \frac{\nu_{Q_T,k}}{k!} \\
&= Q_{sf} \left(1 + \alpha \nu_{sf,1}\right) \frac{\nu_{Q_T,k}}{k!},
\end{aligned}
\tag{2.32}
$$

where C_k is the kth-order reduced factorial moment of Q_T in terms of Q_{sf} and α [34, 39]. Therefore, the final expressions for the first-, second-, and third-order reduced factorial moments (i.e., singles, S, doubles, D, and triples, T) of Q_T is given by

$$
C_1 \equiv S = Q_{sf} M_L \nu_{sf,1} \left(1 + \alpha\right),
\tag{2.33}
$$

$$
C_2 \equiv D = \frac{Q_{sf} M_L^2}{2} \left[\nu_{sf,2} + \left(\frac{M_L - 1}{\nu_{if,1} - 1} \right) \nu_{sf,1} \left(1 + \alpha\right) \nu_{if,2} \right],
\tag{2.34}
$$

and

$$
\begin{aligned}
C_3 \equiv T = \frac{Q_{sf} M_L^3}{6} \Bigg[\nu_{sf,3} + \left(\frac{M_L - 1}{\nu_{if,1} - 1} \right) \left(3\nu_{sf,2}\nu_{if,2} + \nu_{sf,1} \left(1 + \alpha\right) \nu_{if,3} \right) \\
+ 3 \left(\frac{M_L - 1}{\nu_{if,1} - 1} \right)^2 \nu_{sf,1} \left(1 + \alpha\right) \nu_{if,2}^2 \Bigg],
\end{aligned}
\tag{2.35}
$$

and is given in terms of known quantities (i.e., $\nu_{sf,n}$, $\nu_{if,n}$), measurable quantities (i.e., S, D, and T), and three unknown quantities pertinent to the physical properties of SNM (i.e., Q_{sf}, M_L, and α). Relating the emitted S, D, and T to the actual observed S, D, and T involves considering effects from the detection system used (e.g., neutron detection efficiency, systematic timing corrections, etc.,) and allows for an analytic estimation of the

three physical properties.

CHAPTER III

Scatter-based Fast-Neutron Detectors: Organic Scintillators

This chapter provides a general overview of organic scintillators for fast-neutron detection and associated digital pulse processing techniques. The traditional capture-based ^{3}He detectors/systems that are currently deployed in accessible nuclear facilities under the IAEA safeguards agreement, require the emitted neutrons be thermalized (with intervening moderating material in front of the detectors) prior to being detected through a thermal neutron capture reaction [40]. The moderating material modulates the initial direction and energy of the emitted neutrons, and subsequently the arrival time of neutrons; this modulation effect necessitates time correlation analysis (TCA) using time gates on the order of 10^{-6} seconds [13, 17]. The use of organic scintillators is motivated by the ability to detect emitted fast neutrons without the need of intervening moderation material; this enables organic scintillators to retain portions of the initial direction and energy of the emitted neutrons [40, 41]. Additionally, TCA can be implemented using time gates on the order of 10^{-9} seconds, thereby improving measurement precision for fixed acquisition times [42, 43]. After testing a variety of different organic scintillators including EJ-309, EJ-299, small-molecule organic glass, and *trans*-stilbene, *trans*-stilbene was determined to be the optimal organic scintillator of choice for this work [44]. The detailed characterization presented in this chapter will be focused on the *trans*-stilbene detector. The characterization is focused on neutrons emitted below ap-

proximately 10 MeV associated with typical fission neutron emissions. Portions of the work in this chapter were adapted from my journal article titled "Measured neutron light-output response for *trans*-stilbene and small-molecule organic glass detectors" published in Nuclear Instruments and Methods in Physics Research Section A: Accelerators, Spectrometers, Detectors and Associated Equipment [45].

3.1 Organic Scintillators: *Trans*-stilbene

Using scintillators to detect ionizing radiation has been ubiquitous in the field of nuclear science for decades, and is one of the most established methods to date [40, 41]. Scintillators will emit luminescence (visible or ultraviolet) when ionizing radiation deposits energy through nuclear interactions; the collected luminescence is proportional to the energy deposited by the radiation. This work focuses on scintillators that are composed of organic molecules and have the ability to simultaneously detect fast neutrons and photons. Specifically, *trans*-stilbene scintillators are used; Table 3.1 shows the material composition of a *trans*-stilbene scintillator [46].

Table 3.1: Material properties of a *trans*-stilbene scintillator [46]

Light yield for 0.478 MeVee energy deposition [photons/MeVee]	Density [g/cm^3]	Hydrogen content [at. %]	Carbon content [at. %]
15,000	1.160	46.15	53.85

The scintillation light created in the *trans*-stilbene scintillator must be collected and converted to a usable voltage signal using a photosensor such as a photomultiplier tube (PMT) [40, 41]. Recent works have investigated alternative photosensors (e.g., silicon photomultipliers) for scintillation readout, which offer a drastic reduction in the form factor of the detector assembly and comparable performance to PMTs [47]. This work focuses on the use of PMT for scintillation readout of the *trans*-stilbene crystals. A PMT is coupled to the one open side of each *trans*-stilbene scintillator, where the remaining facets of the scintillator

were wrapped with polytetrafluoroethylene (PTFE) reflective tape to redirect the scintillation light towards the photocathode. A silicone coupling grease (EJ-550) is used between the scintillator and the PMT, where the index of refraction is optimized to be some value between the scintillator and the PMT photocathode to mitigate any small-angle deviations when entering the photocathode. The photocathode then converts the optical photons into photoelectrons, and are then focused and drifted through the vacuum to a series of dynodes. When the electron strikes a dynode, many more electrons can be liberated, where the number of liberated electrons is proportional to the amount of energy deposited by the initial electron; this mechanism provides a multiplication effect enabling an amplification of the electrical signal [40, 41]. The gain from this multiplication process for the PMT used in this work (9214B PMT from Electron Tube Enterprises) is on the order of 10^6 depending on the applied voltage bias. The multiplied current from the photoelectrons is then read out as a voltage signal, which can then be digitized by a waveform digitizer. Figure 3.1 shows an image of a bare 5.08 Ø cm x 5.08 cm *trans*-stilbene scintillator provided by Inrad Optics [46].
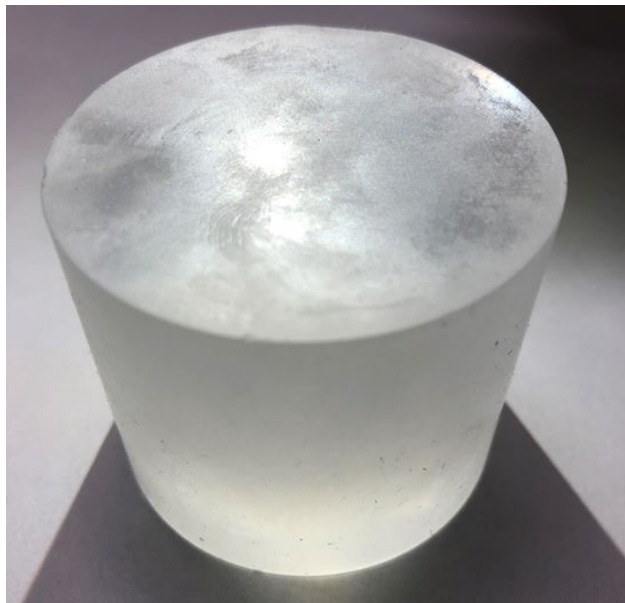
Figure 3.1: A bare 5.08 Ø cm x 5.08 cm *trans*-stilbene scintillator.

The *trans*-stilbene scintillators were encapsulated in a thin aluminum housing of 0.18

Figure 3.2: An aluminum encased 5.08 Ø cm x 5.08 cm *trans*-stilbene scintillator (left) and the 9214B PMT from Electron Tube Enterprises (right).

cm thickness with a fused silica optical window of 0.16 cm thickness. Figure 3.2 shows an image of the fully-encapsulated *trans*-stilbene scintillators along with the 9214B PMT from Electron Tube Enterprises). The fully-assembled *trans*-stilbene detectors were then housed in a plastic 3D-printed detector housing to provide additional structural integrity. Figure 3.3 shows an image of the fully-assembled *trans*-stilbene detector.

3.1.1 Neutron/Photon Interactions and Energy Deposition

The simultaneous sensitivity to fast neutrons and photons is a unique capability for organic scintillators, and leverages the different nuclear reactions that occur for the two different types of radiation. Fast neutrons primarily undergo elastic scattering on hydrogen and carbon nuclei, while photons interact primarily through Compton (incoherent) scattering

Figure 3.3: The fully-assembled *trans*-stilbene detector.

on electrons. Figure 3.4 and Figure 3.5 show the neutron and photon interaction cross section in *trans*-stilbene [48, 49].

For photons that undergo Compton scattering, only a portion of the initial photon energy, $h\nu$, can be deposited to the recoil electron and the partial energy transfer is described by [40]

$$h\nu' = \frac{h\nu}{1 + \frac{h\nu}{m_0 c^2}\left(1 - cos\theta\right)}, \tag{3.1}$$

where $h\nu'$ is the energy of the outgoing photon, $m_0 c^2$ is the electron rest mass energy (0.511 MeV), and θ is the angle of the outgoing photon relative to its initial direction. According to Eq. (3.1), the maximum energy transfer occurs when θ is 180° and describes the case of a backscatter event between the photon and the recoil electron. Using Eq. (3.1), the maximum energy transferred from a 0.662 MeV ^{137}Cs photon to a recoil electron would be 0.478 MeV. In practice, the location of the [137]Cs Compton Edge is used for calibrating the detectors to ensure detector response uniformity and additionally provides the conversion
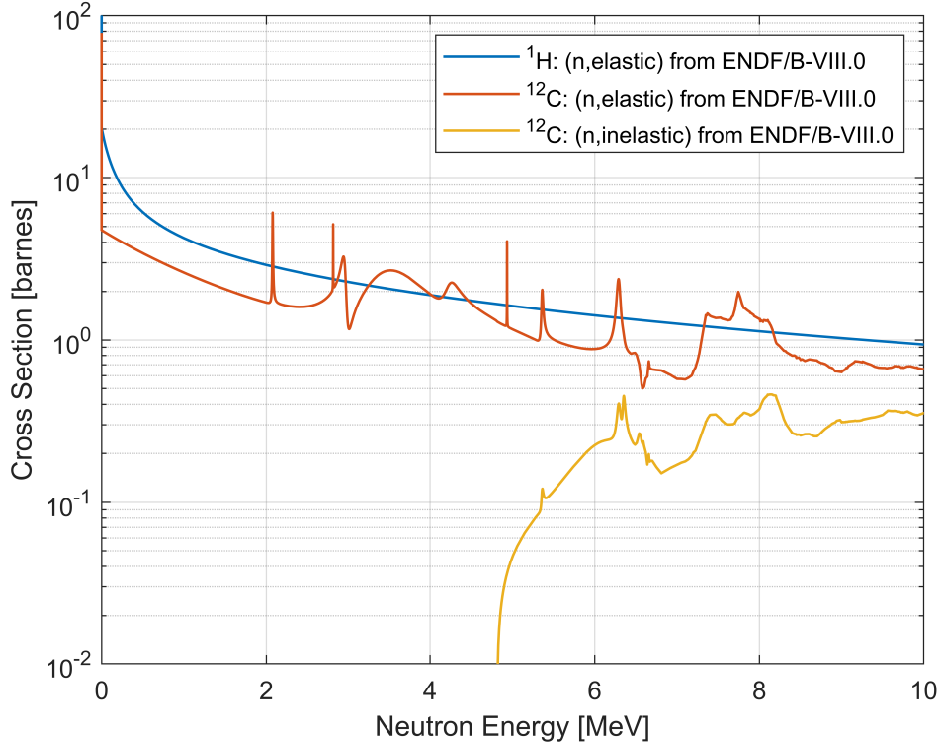
Figure 3.4: *Trans-* stilbene neutron interaction cross sections to neutrons of typical fission energies [48].

from the digitized voltage signal (in units of V or V-ns) to light output (in units of MeVee).

For neutrons that undergo elastic scattering on hydrogen or carbon nuclei, the energy deposited to the (assuming nonrelativistic energies), E_R, is given by [40]

$$E_R = \frac{4A}{(1+A)^2} \left(cos^2 \theta \right) E_n, \tag{3.2}$$

where A is the atomic mass of the recoil nucleus ($A = 1$ for hydrogen, $A = 12$ for carbon), and θ is the angle between the initial direction of the neutron and the recoil nucleus. According to Eq. (3.2), we see that a neutron can deposit all of its energy in a single scatter on hydrogen, while a maximum of approximately 28.4 % of the initial neutron energy can be deposited in a single scatter on carbon.

In summary, the nuclear interactions for photons are primarily dominated by Compton scattering events for typical fission energies, while the nuclear interactions for neutrons are
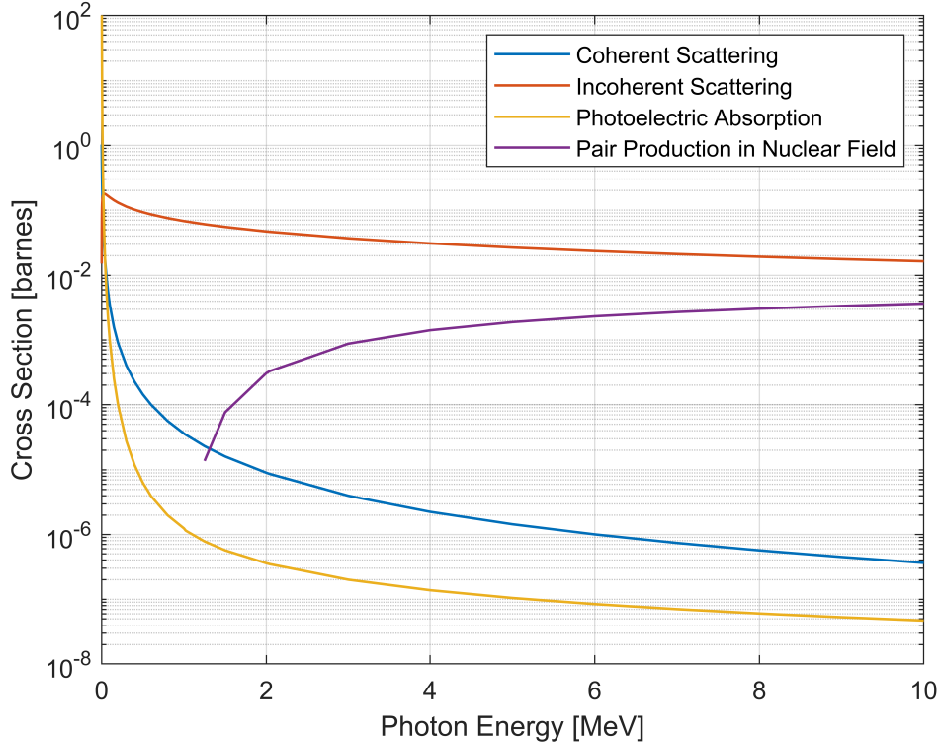
Figure 3.5: *Trans-* stilbene photon interaction cross sections to photons of typical fission energies [49].

composed primarily of elastic scatters on hydrogen and carbon nuclei. The recoil particles from photon and neutron interactions will then traverse and excite the molecular states in the *trans*-stilbene scintillator, subsequently creating luminescence. The photophysical properties of the luminescence created within the *trans*-stilbene scintillator are discussed in the next section.

3.1.2   Scintillation Light Production

In organic scintillators, the charged particles that ionize and excite these molecular states are the recoil particles from neutron and photon interactions. The amount and type of luminescence produced in the scintillator are primarily dependent on the linear stopping power of the recoil particle, dE_{dep}/dx, which dictates the density of ionized and excited molecules for some differential path length, dx [41]. For photons that undergo Compton

scattering on electrons, the amount of luminescence emitted is directly proportional to the energy deposited. This direct proportionality is attributed to the low electron stopping power in typical organic scintillators, which excites organic molecules that are relatively far apart from one another (i.e., spaced several molecular distances apart along the electron path) thus the interaction between them is considered to be negligible. Within these conditions, the emitted luminescence, L, is given by

$$L = SE_{dep},$$
(3.3)

or alternatively in its differential form

$$\frac{dL}{dx} = S\left(\frac{dE_{dep}}{dx}\right),$$
(3.4)

where dx is the differential path length of the recoil electron, dE_{dep}/dx is the differential energy deposited per path length of the recoil electron, and S is the absolute scintillation efficiency (i.e., number of optical photons created per energy deposition) [40, 41]. Noting that the amount of light produced, L, is directly proportional to the energy deposited by a photon on a recoil electron, we introduce the units of MeVee (i.e., MeV electron-equivalent) defined as the amount of light produced for photon depositing 1 MeV on a recoil electron. Of course, this is a linear one-to-one relationship for photon interactions, but it is an important distinction for neutron interactions, where L has a nonlinear relationship with the energy deposited by the neutron.

For neutron interactions that undergo elastic scattering on hydrogen and carbon nuclei, there exists a nonlinear relationship between the amount of light produced and the energy deposited by the neutron. This is attributed to the photophysical effects due to the much higher stopping power of the recoil hydrogen and carbon nuclei. Since the stopping power of the recoil hydrogen and carbon nuclei is much greater than that of recoil electrons, a higher population of molecular states are excited along a much shorter particle track and

thus the effects of ionization quenching (i.e., prompt quenching) is significant [40, 41]. A semi-empirical relationship for the amount of light produced, L, for a differential energy deposition, dE_{dep}/dx, has been proposed by Birks et al. [41], which considers the ionization quenching effect and has the form

$$\frac{dL}{dx} = \frac{S\left(\frac{dE_{dep}}{dx}\right)}{1 + kB\left(\frac{dE_{dep}}{dx}\right)}, \tag{3.5}$$

where S is the absolute scintillation efficiency, BdE_{dep}/dx is the specific density of the ionized and excited molecules along the recoil nuclei track (B is constant), and k is a the quenching parameter. Equation (3.5) reverts back to Eq. (3.4) in the case of small dE_{dep}/dx (i.e., recoil electrons). It is also important to note here that the amount of light produced from elastic scatters on carbon nuclei is much less than that produced from elastic scatters on hydrogen nuclei due to the much higher quenching effect (dE_{dep}/dx for carbon nuclei $>> dE_{dep}/dx$ for hydrogen nuclei). In practice, the majority of the detected neutron signals is primarily from neutrons elastically scattering on hydrogen nuclei.

Another important aspect of organic scintillators are the temporal characteristics of the scintillation light pulse from neutron and photon interactions. For typical organic scintillator materials, there are three types of luminescence that can occur corresponding to the π-electronic energy levels of organic molecules. The three types of luminescence are [41]:

1. Prompt Fluorescence, related to the de-excitation to ground state of the lowest singlet excited state and is emitted promptly (10^{-8} - 10^{-9}s decay time)

2. Phosphorescence, related to the de-excitation to ground state of the lowest triplet excited state and is emitted with longer decay times (10^{-4} or longer decay times)

3. Delayed Fluorescence, related to the de-excitation to ground state of the singlet excited and singlet ground state formed from a prior triplet-triplet annihilation and is emitted promptly immediately after the triplet-triplet annihilation (10^{-8} - 10^{-9}s decay time)

The proclivity for emitting the different types of luminescence is also directly related to the recoil particle stopping power. As mentioned previously, hydrogen and carbon nuclei exhibit a much higher specific density of ionized and excited molecules, which in turn enables a higher rate of triplet-triplet annihilation (i.e., delayed fluorescence) and singlet-state prompt quenching (i.e., prompt fluorescence), hence the quenching parameter in the semi-empirical relationship described in Eq. (3.5). Photon interactions on recoil electrons have much lower specific density of ionized and excited molecules, therefore scintillation pulses from photon interactions exhibit much less singlet-state prompt quenching and triplet-triplet annihilation (i.e., more prompt fluorescence and less phosphorescence and delayed fluorescence).

The ability to discriminate between detected neutron and photon signals is predicated on the temporal differences of the produced light. Figure 3.6 shows the expected light intensity for photons, neutrons, and alpha particles, which corresponds to recoil particles of increasing stopping power [40, 41].
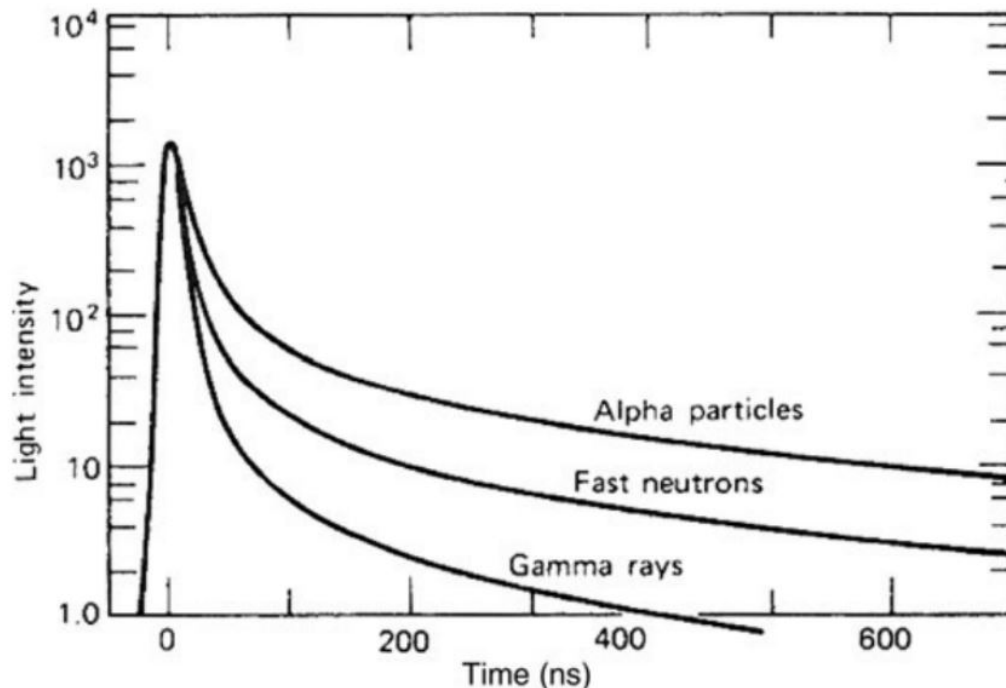
Figure 3.6: Light output intensity in arbitrary units as a function of time after a charged particle recoil in a *trans*-stilbene scintillator (normalized by height) [40, 41]

34

Figure 3.6 demonstrates that as the stopping power of the recoil particle increases, the amount of light in the latter region of the scintillation pulse increases. Pulse-shape discrimination (PSD) techniques are implemented to exploit the differences in shape of the detected scintillation pulse, and is detailed in Section 3.2.3.

3.2 Digital Pulse Processing and Detector Characterization

All PMT voltage signals from each *trans*-stilbene detector are passed through a waveform digitizer; the waveform digitizer chosen for this work was the CAEN V1730 waveform digitizer, which has a 14-bit resolution, 2-V dynamic range, 16 input channel, and a 500-MHz sampling rate (2-ns samples). The CAEN V1730 waveform digitizer is able to perform on-board calculations to extract useful information about the acquired digitized pulses; the CAEN Digital Pulse Processing for Pulse Shape Discrimination firmware (DPP-PSD) is used throughout this work [50]. There are three essential pieces of information required from every acquired waveform that include the time of detection, energy deposited by the incident particle, and the type of incident particle.

3.2.1 Pulse Timing and Time Resolution

The time of detection (i.e., pulse time stamp) for all waveforms is calculated using a digital constant fraction discrimination (DCFD) algorithm implemented directly on the digitizer board [50]. The DCFD algorithm can be seen as the digital counterpart to the traditional constant fraction discriminator for analog signals, where the time stamp is set to the time when the pulse reaches some fixed fraction of its maximum amplitude [50]. Figure 3.7 shows a schematic diagram of the DCFD algorithm implemented on the digitizer board.

The DCFD algorithm is implemented in the same manner as its analog predecessor, where the digitized input pulse is attenuated by a factor, f, equal to the desired fraction of the full amplitude where the time stamp is set [40, 50]. The input pulse is then inverted and delayed with delay time of d, where d is set equal to the time it takes the input pulse

35
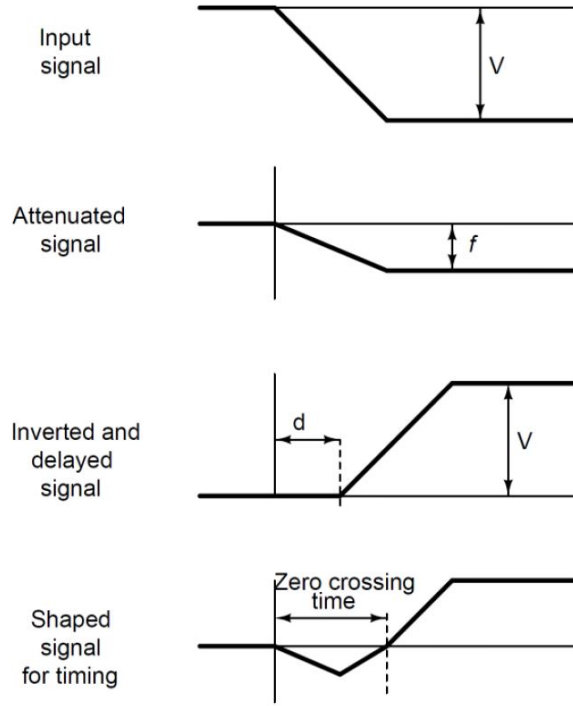
Figure 3.7: A schematic diagram of the DCFD algorithm implemented on the digitizer board [50].

to go from the constant fraction level to the full amplitude. The inverted and delayed signal is then summed with the initial input pulse to produce a bipolar waveform, where the time stamp is set at the zero crossing time of the summed pulse. The two samples immediately before and after the zero crossing time is linearly interpolated to extract time stamps with precision beyond the fixed digitizer sampling routine (i.e., fine time stamps). The values for the attenuation factor, f, and the delay time, d, were set to 75% and 6 ns, respectively, based on the average pulse shape.

Using the DCFD algorithm to extract time stamps, a time-gated coincidence measurement of a ^{22}Na source was conducted to characterize the time resolution between pairs of *trans*-stilbene detectors. The ^{22}Na is placed at the center of two *trans*-stilbene detectors to measure the 0.511 MeV annihilation photons that are emitted simultaneously and 180° from one another. Figure 3.8 show the image of the time-gate coincidence measurement.

The time differences between all successive coincident photon detections within a 10 ns
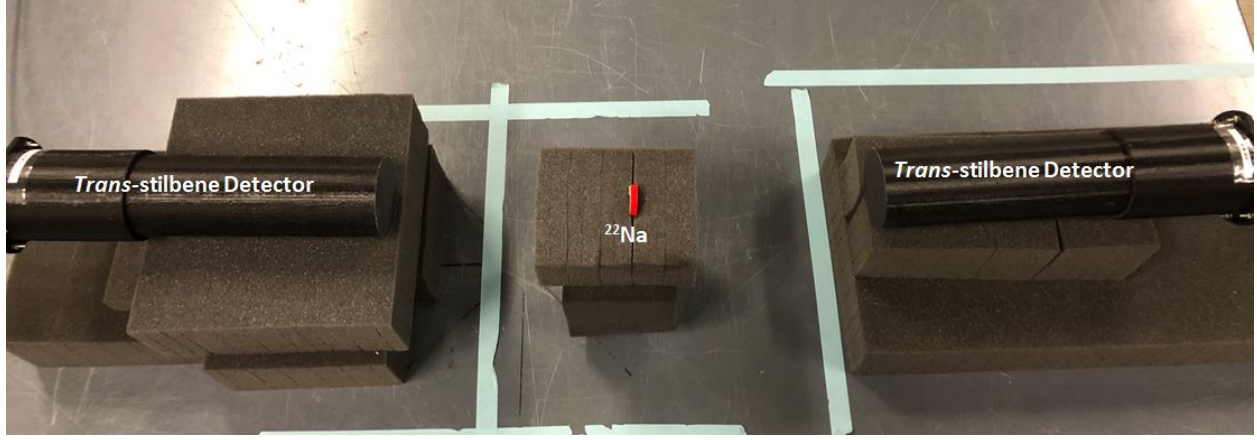
Figure 3.8: Experimental setup for time-gated coincidence measurement to characterize the time resolution between pairs of *trans*-stilbene detectors.

window are used to produce a histogram, and a Gaussian distribution is fit on the resulting data to estimate the full-width at half maximum (FWHM). The time resolution, quantified by the FWHM, was estimated to be approximately 1.34 ± 0.04 ns. Figure 3.9 shows the measured time resolution for a pair of *trans*-stilbene detectors.
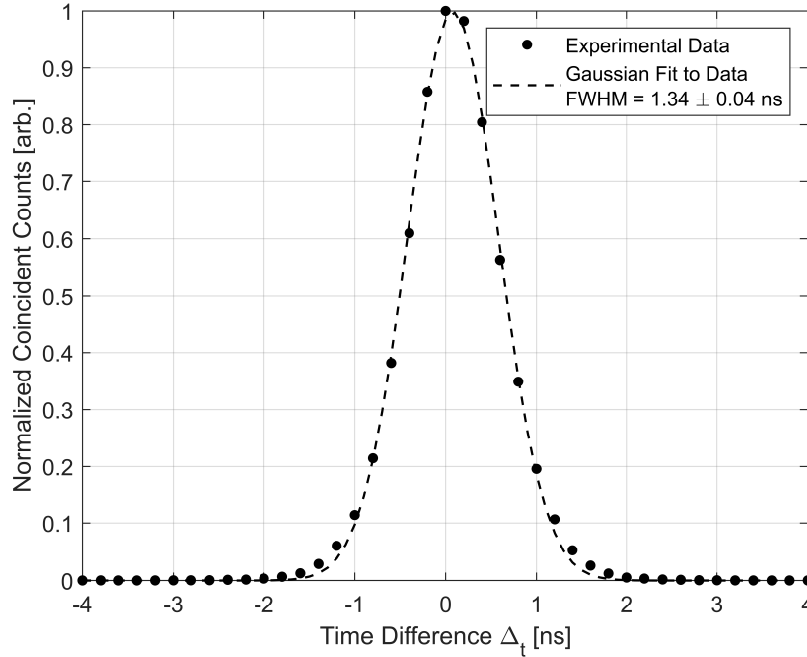
Figure 3.9: Measured time difference distribution for a pair of *trans*-stilbene detectors along with the Gaussian fit. The FWHM was estimated to be approximately 1.34 ± 0.04 ns for 0.511 MeV photons.

3.2.2   Energy Deposition and Light Output Response Functions

A detailed understanding of the energy deposited by the incident particles and the corresponding light output in the *trans*-stilbene detector is necessary for implementing low-energy light output detection thresholds and relating it back to its neutron-equivalent energy (assuming a full single-scatter energy deposition on hydrogen nuclei). There are two methods for extracting pulse information for inferring energy deposited in the detector that include pulse height analysis (PHA) and pulse integral analysis (PIA). As mentioned previously, the amount of light produced in a scintillation pulse is proportional to the energy deposited (linearly for photon energy deposition and nonlinearly for neutron energy deposition). Therefore, creating a histogram distribution using the pulse heights or integrals provides the measured detector light output distribution. However, the amount of light (and its corresponding light output response function) depends on which method is used for pulse analysis. That is, PHA yields a light output response function that is proportional to the maximum amount of luminescence created in the scintillation pulse, where as PIA provides a light output response function that is proportional to the total amount of luminescence created [51]. Furthermore, PIA provides better energy resolution in the light output distribution due to the increased statistics from integration [52]. This subtle yet important distinction is essential when inferring the neutron-equivalent energy from the measured light output, as well as for implementing the response functions in high fidelity Monte Carlo simulations. PIA is used for the *trans*-stilbene characterization shown in this chapter.

Recalling the cross sections for photon interactions in *trans*-stilbene, we expect to see only the Compton Edge from a ^{137}Cs measurement. The exact location of the Compton Edge on the measured PID must be characterized as it falls slightly passed the peak of the Compton Edge distribution due to detector resolution and multiple scattering effects [40]. Knowledge of the Compton Edge location (relative to the peak) is of particular important when calibrating an array of *trans*-stilbene detectors as it provides a fixed relative calibration point for all detectors. An energy-time gated backscatter coincidence measurement using a

trans-stilbene and an inorganic scintillator (NaI detector) was done to isolate the Compton Edge location for the 0.662 MeV ^{137}Cs photons. Figure 3.10 show an images of the experimental setup for the backscatter coincidence measurement.
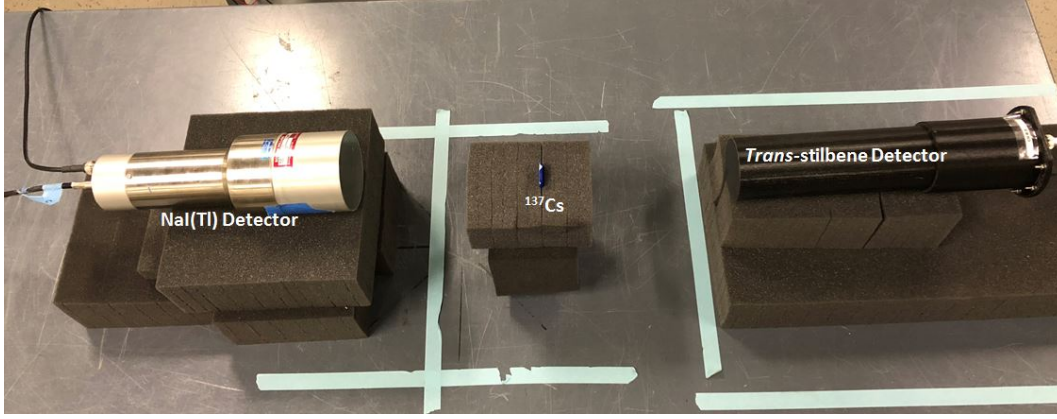
Figure 3.10: Experimental setup for the backscatter coincidence measurement to characterize the Compton Edge location and the energy resolution.

A ^{137}Cs source is placed between the *trans*-stilbene and NaI detector, and coincident counts within 100 ns are recorded. The goal is to measure the 0.662 MeV photons that have backscattered in the *trans*-stilbene detector (depositing 0.478 MeV) and then subsequently have deposited its remaining energy into the NaI detector (0.184 MeV photons). The full-energy deposition in the NaI detector provides the basis for an additional energy gating routine, where the PID for the *trans*-stilbene is extracted only for coincident counts that arrived within 100 ns *and* that have deposited 0.184 MeV in the NaI detector. Figure 3.11 shows an image of the measured pulse integral distribution (PID) for the *trans*-stilbene detector from a ^{137}Cs measurement, and the corresponding energy-time gated PID.

The energy-time gated data shown in Figure 3.11 was fit with a Gaussian distribution, where the FWHM quantifies the energy resolution of the *trans*-stilbene detector. The energy resolution for a light output of 0.478 MeVee was estimated to be 12.90 ± 0.24 %. Using the relative Compton Edge location characterized in Figure 3.11, the Compton Edges for 0.511 MeV and 1.274 MeV photons from ^{22}Na and 0.662 MeV photons from ^{137}Cs is plotted demonstrating the expected linear light output response functions to photon interactions.
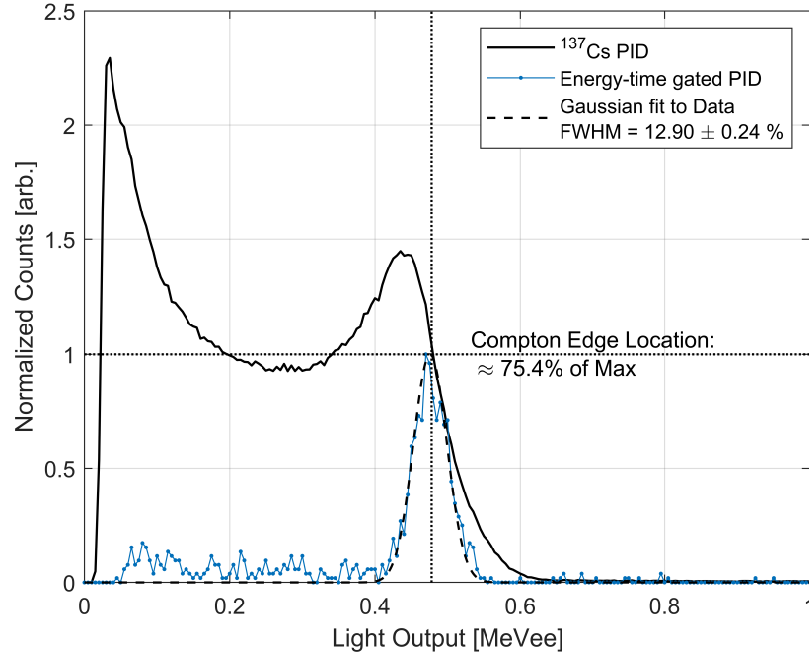
Figure 3.11: Measured *trans*-stilbene PID and energy-time gated PID for ^{137}Cs photons showing the isolated Compton Edge location. The Compton Edge location is estimated to be approximately 75 % of the maximum.

Figure 3.12 shows the measured *trans*-stilbene PID and the linear calibration response curve used to convert from digitizer samples to light output.
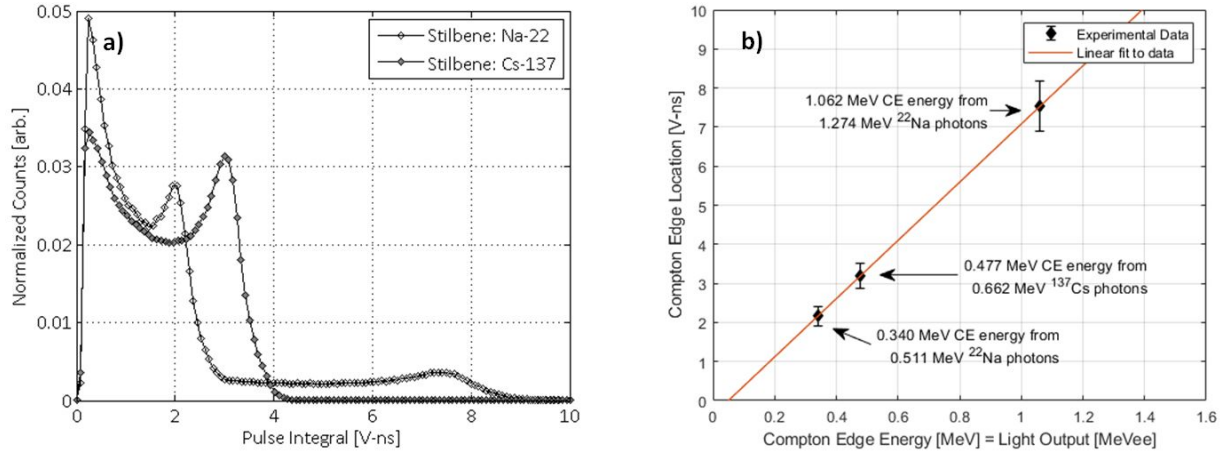
Figure 3.12: Measured *trans*-stilbene PID for a ^{137}Cs and ^{22}Na calibration measurement (a), and the linear calibration curve for converting digitizer samples to light output (b).

For neutron interactions, the nonlinear light output response can be characterized from

40

a neutron time-of-flight (TOF) experiment with a ^{252}Cf *sf* source. A neutron TOF experiment is a time-tagged coincidence measurement technique that aims to isolate the detector response to quasi-monoenergetic neutrons by extracting time-gated neutron PIDs. The ^{252}Cf source is placed directly in front of a trigger detector (2.54 cm Ø x 2.54 cm *trans*-stilbene detector), where the *trans*-stilbene detector that is to be characterized is placed at some known distance from the ^{252}Cf source. With a known flight distance, D, the incident neutron energy can be calculated using the relationship [41]

$$t_F = \frac{72.3 \cdot D}{\sqrt{E_n}}, \tag{3.6}$$

where t_F is the time of flight [ns], and E_n is the incident neutron energy in MeV. Time-gated PIDs can then be extracted from the *trans*-stilbene detector that correspond to the calculated incident neutron energy in Eq. (3.6). The minimum energy resolution of the time-gated PIDs is determined by the width of the time gate, T, through [41]

$$\frac{\Delta E_n}{E_n} = \frac{2 \cdot T}{t_F}. \tag{3.7}$$

Figure 3.13 shows an image of the experimental setup for neutron TOF at a distance of two meters to measure the nonlinear neutron light output of a *trans*-stilbene detector.

Since we only want to characterize the detector response for neutrons that have travelled directly from the ^{252}Cf source to the *trans*-stilbene detector, a polyethylene shadow bar was placed in front of the detector to measure the room return; this provides an aggregate subtraction to the measured time-gated PIDs, where the subtraction of the bare and the shadow bar cases gives the PIDs for unscattered neutrons. Figure 3.14 shows the resulting TOF distribution for the bare, shadow bar, and subtracted cases, and Figure 3.15 shows the subtraction done on the time-gated PIDs for 2.10 ± 0.17 MeV neutrons

The light output that corresponds to the maximum energy transfer of the neutron (i.e., full energy deposition from a single scatter on a recoil hydrogen nuclei) is determined as the
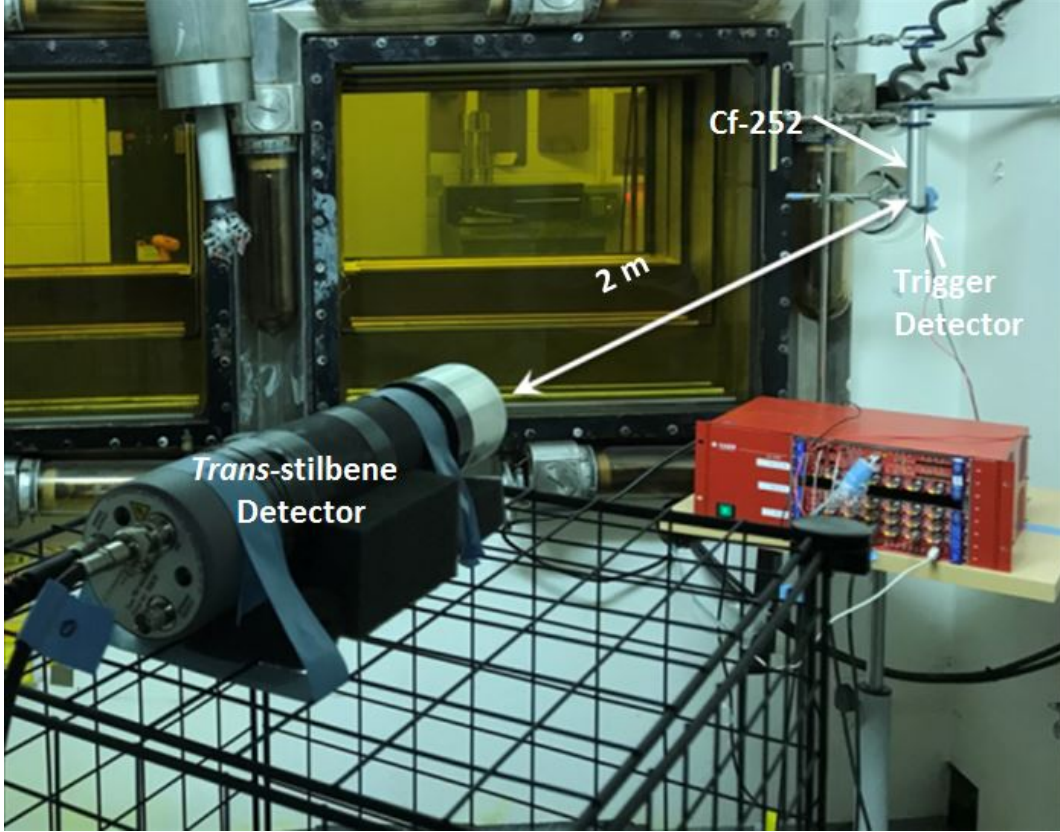
Figure 3.13: Experimental setup for the neutron TOF measurement at a distance of 2 meters to measure the nonlinear neutron light output response of a *trans*-stilbene detector.

maximum inflection point of the time-gated PID [53]. The time-gated PID is differentiated, where the mean of the right-most distribution yields the light output corresponding to the maximum energy transfer of the neutron. A Gaussian distribution is fit on the differentiated data to compute the mean and variance, where the variance provides an estimate of the uncertainty in the measured light output. Implementing this analysis for all time-gated PIDs provides discrete data points for the neutron light output response. Using the semi-empircal relationship between the nonlinear light output and the energy deposited by the neutrons shown in Eq. (3.5), we are then able to fit the measured data points to establish a neutron light output response function. A parameterized version of Eq. (3.5) is used to fit the data, and has the form [54]
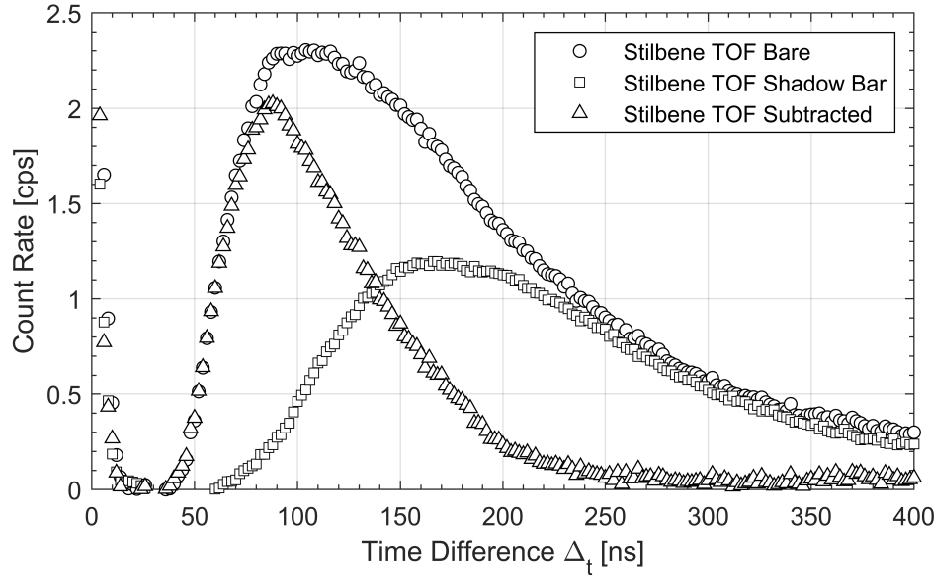
Figure 3.14: TOF distribution for the bare, shadow bar, and subtracted cases showing that scattered neutrons (i.e., shadow bar case) are detected later in time as they have previously scattered within the room.
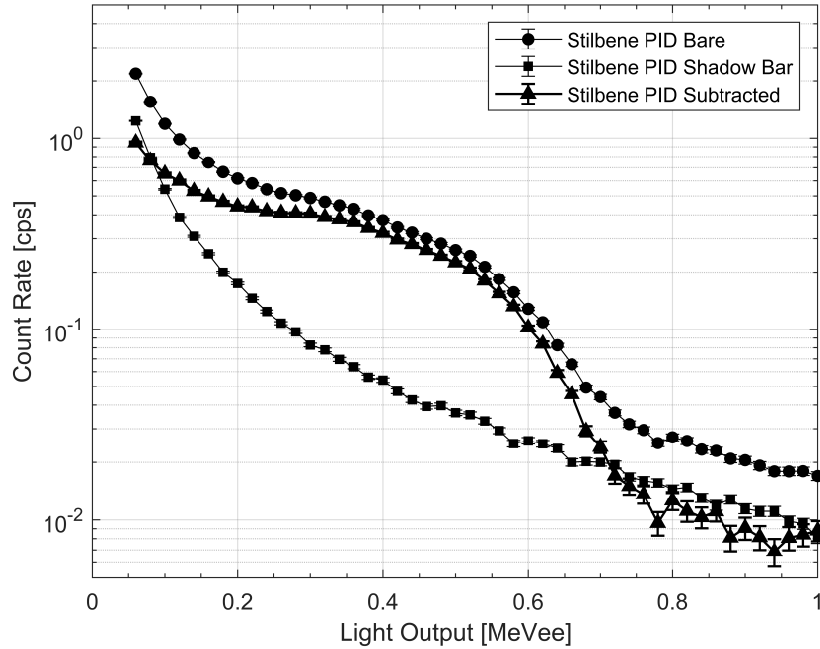
Figure 3.15: The time-gated PID for 2.10 ± 0.17 MeV neutrons for the bare, shadow bar, and subtracted cases.

$$L(E_{dep}) = \int \frac{a}{1 + b\left(\frac{dE}{dx}\right)} dE_{dep}, \tag{3.8}$$

where a, and b are fit parameters. Figure 3.16 shows the measured *trans*-stilbene neutron light output response to quasi-monoenergetic neutrons and the fitted semi-empirical light output response function. The parameters a and b were calculated to be 2.027 and 27.83, respectively.
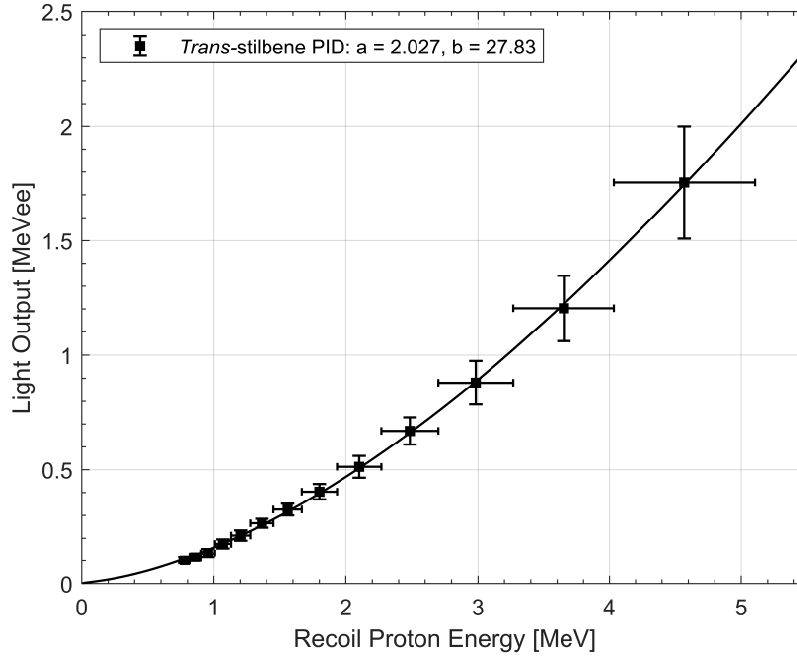
Figure 3.16: Measured neutron light output response to quasi-monoenergetic neutrons and the fitted semi-empirical light output response function. Parameters a and b were calculated to be 2.027 and 27.83, respectively.

Using the light output response function for photon interactions (Figure 3.12) and neutron interactions (Figure 3.16), the energy deposited by neutrons and photons can be inferred from the measured light output.

3.2.3 Pulse Integrals and Pulse-Shape Discrimination for Particle Identification

The ability to discriminate and identify neutron and photon interactions is practically the most important aspect for fast neutron detection using organic scintillators. We discussed

previously the characteristics of the luminescence created from recoil particles of low (i.e., electrons) and high (i.e., hydrogen nuclei) stopping powers (shown in Figure 3.3). Figure 3.17 shows template neutron and photon pulses (average waveforms for 1.00 ± 0.10 MeVee) from a *trans*-stilbene detector demonstrating neutron pulses exhibit a longer decay in the tail region compared to the photon pulses.
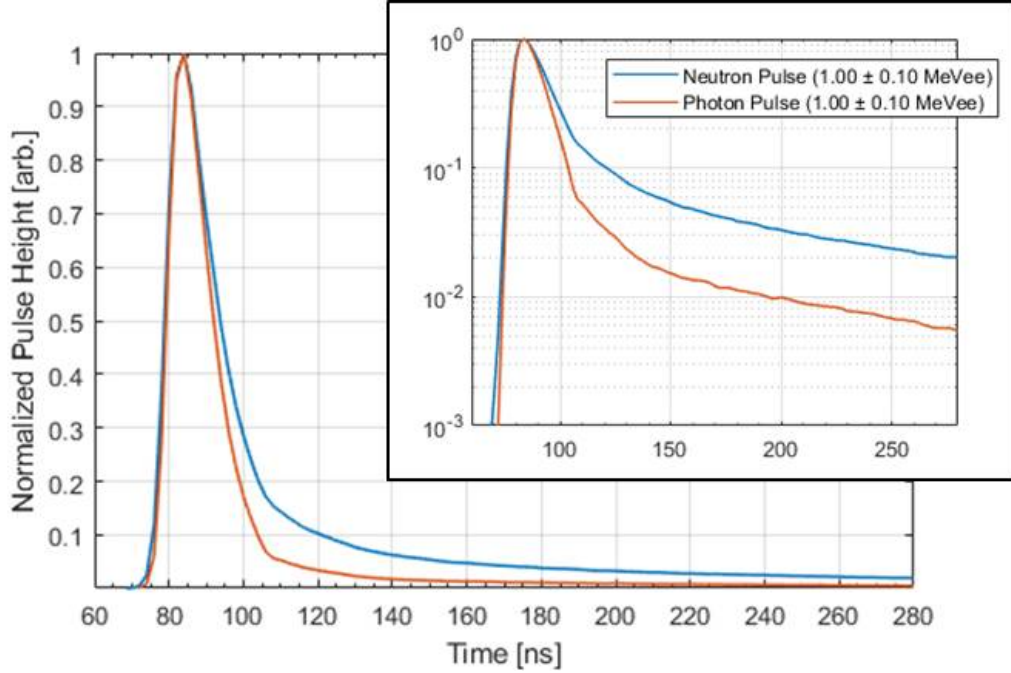
Figure 3.17: Template neutron and photon pulses (average waveforms for 1.00 ± 0.10 MeVee) demonstrating the difference in the tail-region of the measured pulse, where neutron pulses have a longer-lived decay compared to photon pulses. Particles were identified through timing from the neutron TOF measurement.

Pulse-shape discrimination (PSD) based on charge integration is implemented to exploit the characteristic difference observed in the tail-region of the measured pulses. Charge integration for PSD is a well established technique that compares the total integrated charge to that of the integrated charge in the tail-region of the pulse [41, 55, 56]. The ratio of the tail-integral to the total-integral, hereafter referred to as the tail-to-total integral, provides a discriminating parameter that separates neutron and photon pulses. Figure 3.18 shows the histogram distribution of the tail-to-total ratio that yields two normally-distributed data corresponding to the neutron and photon detections.
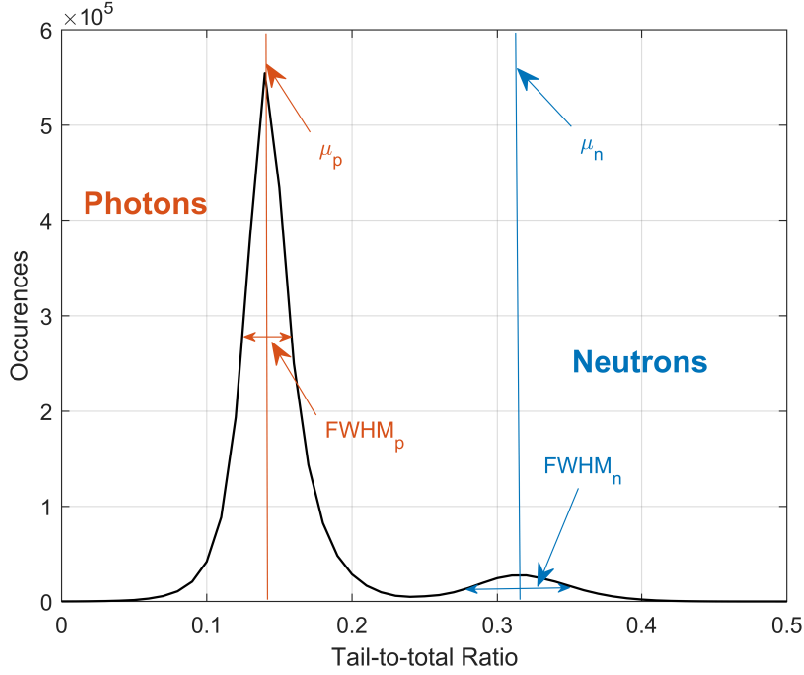
Figure 3.18: Histogram of the tail-to-total ratio showing the neutron and photon data distributions from detected ^{252}Cf neutrons and photons.

The canonical definition of the figure of merit (FOM) for the PSD performance is calculated as [55, 56]

$$FOM = \frac{|\mu_p - \mu_n|}{FWHM_p + FWHM_n},$$ (3.9)

where μ_n and μ_p is the mean of the neutron and photon distributions, and $FWHM_n$ and $FWHM_p$ are the FWHM if the neutron and photon distributions, respectively. The FOM provides a quantitative assessment of the PSD capability, and is used to optimize the total-integral range and the tail-integral start point. A tail-integral start point of 26 ns past the maximum of the pulse yields the highest FOM value. The total integral range should be set to the maximum allowable range based on the allocated record length (typically $\approx$ 200 ns). Figure 3.19 shows the measured tail-to-total ratio integrals as a function of the measured light output (total integral for PIA). The FOM can also be computed as a function of the measured light output, and is shown in Figure 3.20. In Figure 3.19, the PSD performance begins to degrade for pulses with lower light output; there is less prompt quenching for

46
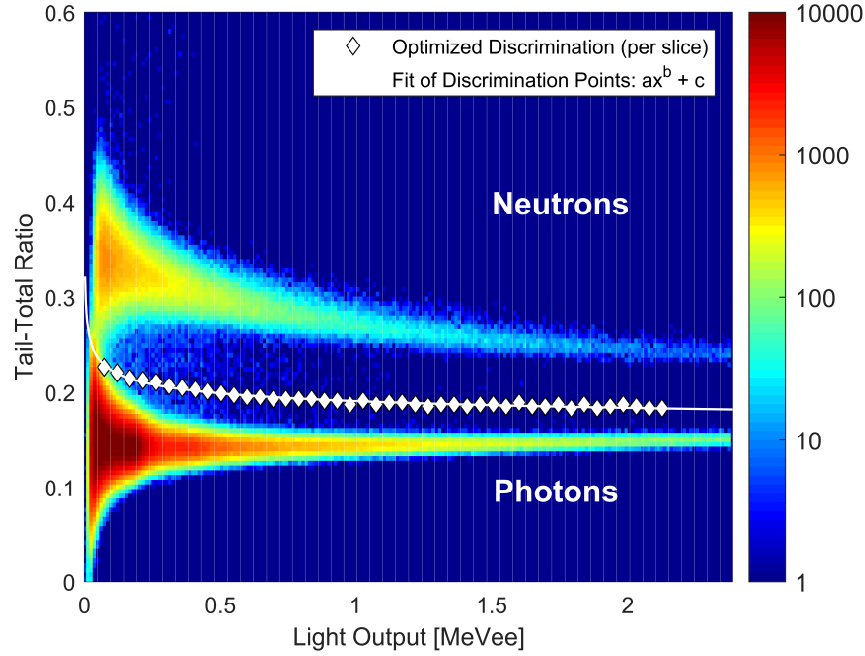
Figure 3.19: Measured tail-to-total ratio as a function of the light output from detected ^{252}Cf neutrons and photons. The white discrimination line is used to discriminate neutron and photon detections.

interactions that had lower light emissions from the *trans*-stilbene scintillator and thus the difference in the tail-region is less pronounced. Rather than using a linear discrimination line with a qualitative visual optimization to separate neutron and photon events, a PSD algorithm proposed by J.K. Polack et al. [57] is implemented that computes optimized discrimination values that are energy-dependent. The algorithm offers an automated and systematic optimization that is less prone to human error compared to a visual optimization. The algorithm also provides diagnostic metrics (i.e., FOM, misclassification rate, etc.) as a function of the measured light output. The measured tail-to-total ratio data is binned by measured light output, and the optimization of the discrimination value is determined for each of "slice" of data. The white markers in Figure 3.19 is the optimized values from the PSD algorithm for each slice of data, where these values are then fit with a power function to yield the discrimination curve. Appendix B shows the source code for the PSD algorithm used in this work.
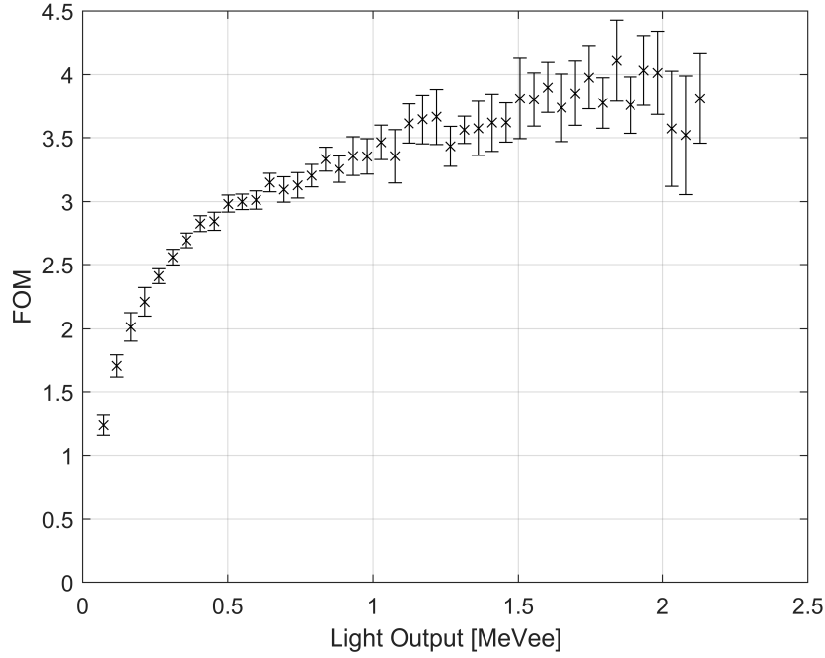
Figure 3.20: PSD FOM as a function of the measured light output. Error bars represent the combined uncertainty from counting statistics and the uncertainty in the Gaussian fit parameters. The uncertainty is typically dominated by the counting statistics, in particular at higher measured light outputs.

3.3 Detector Response Simulations in MCNPX-PoliMi with MP-Post

MCNPX-PoliMi is a code that utilizes the MCNPX-V2.7 particle transport code package, and has the ability to simulate emission of fission particles on an event-by-event basis for emulating detector response [18, 58]. A detailed MCNP simulation model of the *trans*-stilbene detector was established to simulate the neutron interactions (energy deposited by incident particles) that occur within the detector active volume. Figure 3.21 shows the detailed MCNP detector model for the *trans*-stilbene detector assembly. Using the recorded energy depositions from the MCNPX-PoliMi output, the MCNPX-PoliMi post-processing (MPPost) detector response code is used to convert the energy depositions to the detector light output including appropriate broadening terms [59]. The measured characteristics of the *trans*-stilbene detector including the energy resolution, time resolution, and neutron light

48
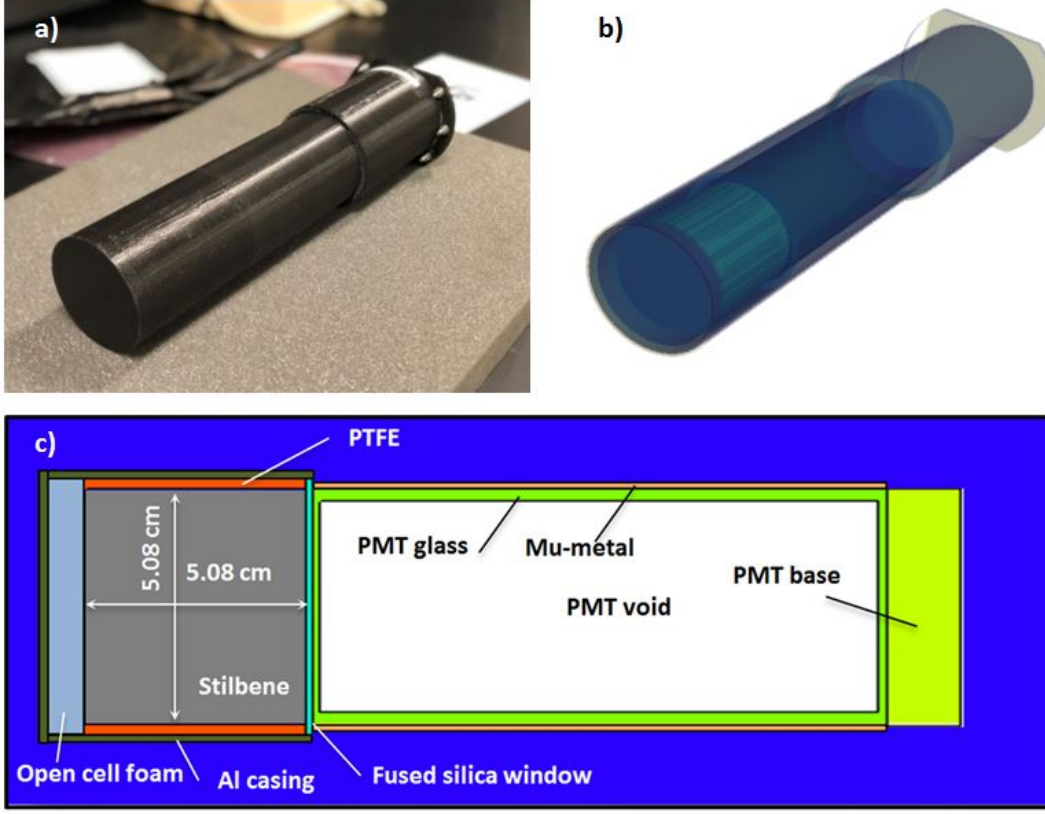
Figure 3.21: Image of the *trans*-stilbene detector assembly (a), a 3D rendering of the MCNP detector geometry (b), and the detailed components of the MCNP model including the PMT (c).

output response function is inputted directly into MPPost to provide high fidelity detector response simulations. A semi-empirical energy resolution function is used that has the form

$$\frac{\Delta L}{L} = \sqrt{\alpha^2 + \frac{\beta^2}{L} + \frac{\gamma^2}{L^2}}, \tag{3.10}$$

where L is the measured light output, ΔL is the resolution at FWHM, and α, β, and γ are semi-empirical fitting parameters [60]. The fitting parameters were estimated by minimizing the χ^2 between the simulated and measured PID; the parameter values were estimated to be 0.078, 0.017, and 0.028 for α, β, and γ, respectively. The resulting resolution function was then independently verified with the measured results from the backscatter experiment. Figure 3.22 shows the measured and simulated *trans*-stilbene response to 0.662 MeV ^{137}Cs photons.
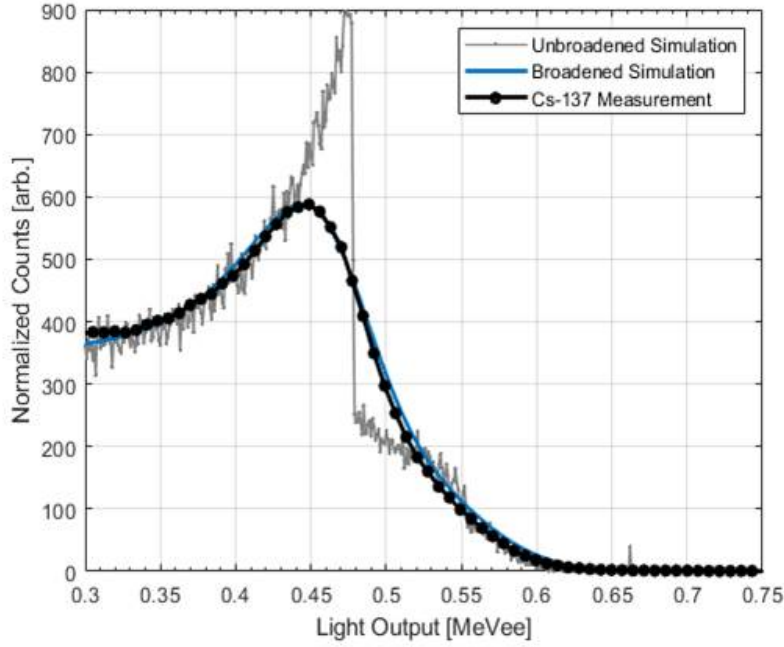
Figure 3.22: Measured and simulated *trans*-stilbene response to ^{137}Cs photons, with and without broadening. The resolution function yields a resolution of 12.70 % for 0.478 MeVee energy deposition, whereas the backscatter experiment resulted in a resolution of 12.90 $\pm$ 0.24 %.

A Gaussian broadening function informed by the experimental results in Section 3.2.1 is implemented for broadening the time response in simulations. Figure 3.23 shows the measured and simulated coincident time-difference distribution for a pair of *trans*-stilbene detectors from ^{252}Cf photons.

Lastly, the measured nonlinear neutron light output response function is implemented, where the light output corresponding to the energy deposition from each individual scatter event in the detector is calculated using Eq. (7.2). Figure 3.26 shows an absolute comparison of the measured and simulated PIDs for ^{252}Cf neutrons, and Figure 3.25 shows the absolute fractional difference showing excellent agreement.
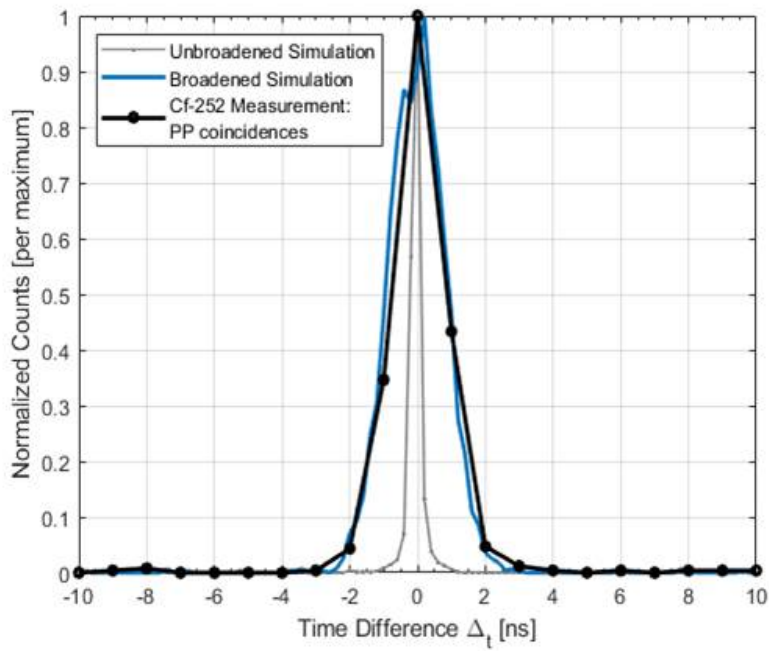
Figure 3.23: Measured and simulated coincident time-difference distribution for a pair of *trans*-stilbene detectors to ^{252}Cf photons, with and without broadening.
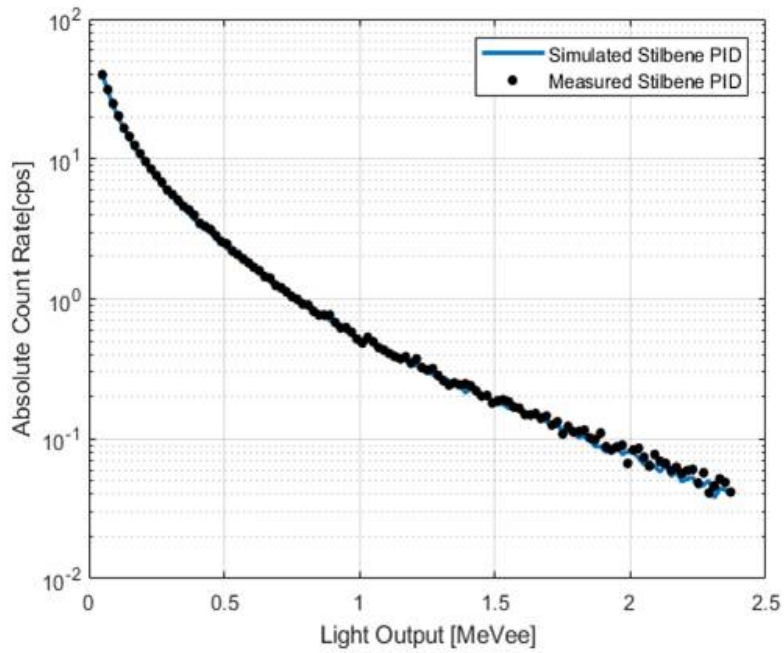
Figure 3.24: Measured and simulated neutron PID for 0.060 MeVee detection threshold (approx. 0.60 MeV neutron-equivalent)
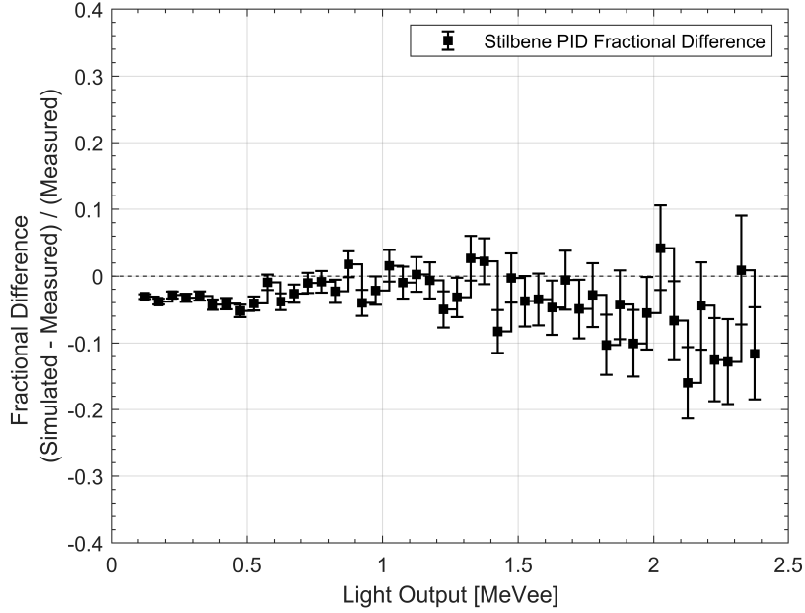
Figure 3.25: The fractional difference between simulated and measured PID for 0.060 MeVee detection threshold (approx. 0.60 MeV neutron-equivalent). The fractional difference between the integrated measured and simulated counts was calculated to be 2.41 ± 0.15 %.

3.4 Neutron Cross-Talk Events

An inherent phenomena that occurs when using an array of organic scintillators is neutron cross-talk, where a single neutron may deposit energy in multiple detectors causing a spurious increase in the total observed counts [61, 62]. Neutron cross-talk effects is primarily dependent on the system geometry (i.e., relative proximity between detectors), applied detection threshold, and the energy spectrum of the emitted neutrons. An experiment was performed with two 7.62 Ø cm x 7.62 cm EJ-309 liquid organic scintillators (*trans*-stilbene detectors were unavailable at the time of the experiment) and a ^{252}Cf *sf* source to isolate neutron cross-talk events to characterize its influence as a function of the detection threshold and the angle between the two detectors. The detectors were incrementally moved by 10°; the angle between detectors for all measured configurations ranged from 10° - 90°.Figure 3.26 shows the experimental setup. Figure 3.27 shows the measured cross-talk influence (cross-talk coincidences per total observed coincidences) as a function of the angle between the
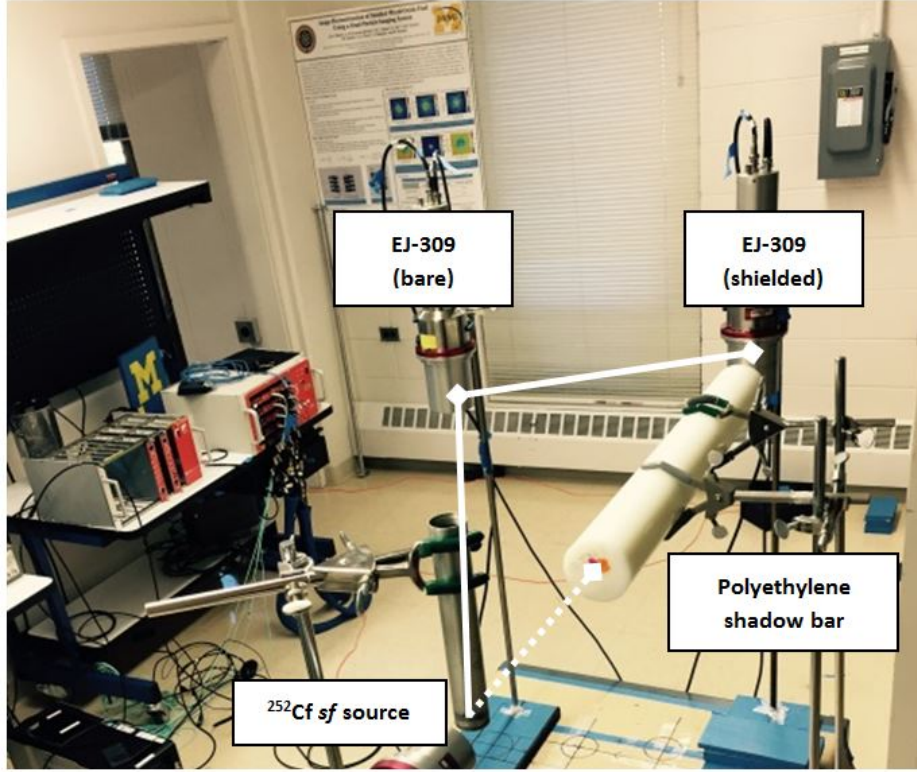
Figure 3.26: Experimental setup for measuring neutron cross-talk counts that have scattered from the bare EJ-309 detector into the shielded EJ-309 detector. The ^{252}Cf source was placed equidistant from both detectors at a distance of 1 meter. The angle between detectors for all configurations ranged from 10° - 90°

detectors and the detection threshold. Figure 3.27 demonstrates that the cross-talk influence decreases as the detection threshold is increased. Additionally, the cross-talk influence is greater when detectors are in close proximity, and scales linearly with the relative solid angle between detector pairs (i.e., $1/r^2$, where r is the distance between detectors). Although the results shown in Figure 3.27 is specific to the geometry and EJ-309 detectors used in the experiment, the observed trend in the neutron cross-talk influence is expected to hold when using an array of organic scintillators of any type. In general, detector pairs that are closer in proximity will have greater cross-talk influence on one another, and raising the detection threshold will suppress the cross-talk influence.
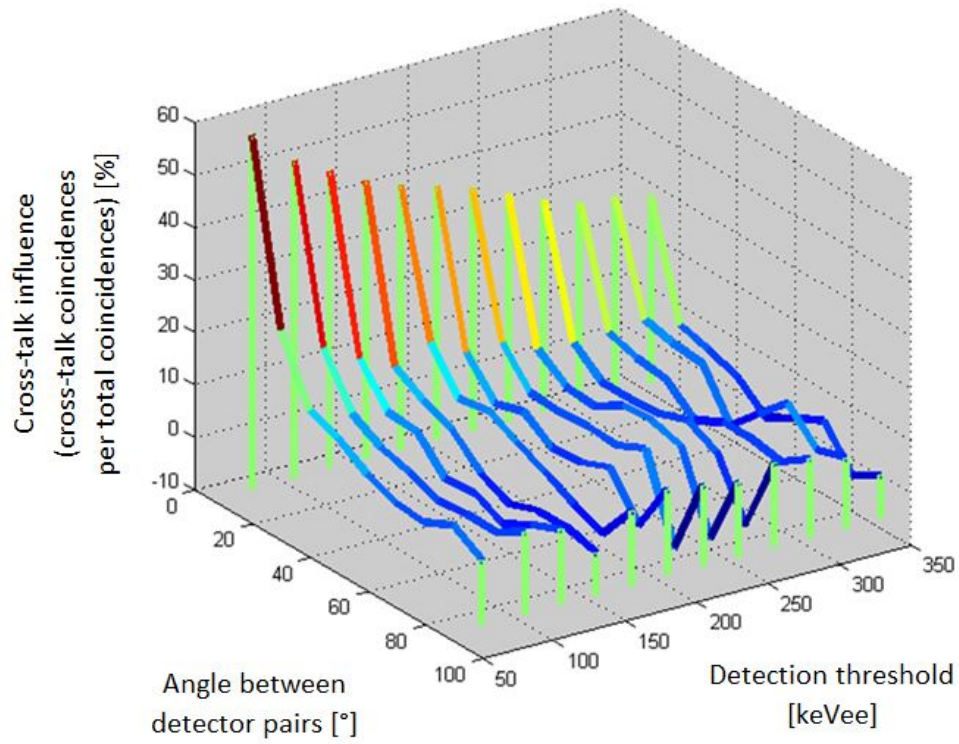
Figure 3.27: The measured cross-talk influence as a function of the detection threshold and the angle between EJ-309 detectors for ^{252}Cf *sf* neutrons.

CHAPTER IV

Fast-Neutron Multiplicity Counting Techniques

This chapter summarizes the theory and practical implementation of neutron multiplicity counting specifically for an FNMC system that utilizes an array of scatter-based organic scintillators for fast-neutron detection. The FNMC system is able to extract neutron multiplicity counts using two fundamentally different methods. One method is based on the well established procedure (for capture-based systems) that involves time-interval and time-correlation analyses on a time series of neutron detections to perform factorial moment counting from the detected neutron number distribution. The second method is unique to FNMC systems, where there is no intervening moderating material and thus the timing information of the emitted neutrons is unmodulated prior to detection. Access to this type of information is possible due to the fast response times of organic scintillators, which allow for extraction of neutron-neutron correlations on an event-by-event basis. Portions of this chapter were adapted from my technical note titled "A Note on the Nomenclature in Neutron Multiplicity Mathematics" published in Nuclear Science and Engineering [10] and from my journal article titled "Neutron Multiplicity Counting Moments for Fissile Mass Estimation in Scatter-based Neutron Detection Systems" published in Nuclear Science and Engineering [63].

4.1 Neutron Pulse Train Time Series Analysis for Neutron Multiplicity Counts

Neutron multiplicity counting (NMC) is a generalized extension of the traditional gross neutron counting and coincidence neutron counting techniques [13, 17]. NMC simply refers to the fact that we can measure and use higher-order moments of the detected multiplicity distribution. That is, traditional gross neutron counting uses the gross count rate, which is the first-order moment of the detected multiplicity distribution (i.e., singles count rate, S). Coincidence neutron counting uses the information from the second-order moment (i.e., doubles count rate, D) since two-neutron events can discriminate fission neutrons from (α,n) neutrons. Neutron multiplicity counting introduces the third-order moment (i.e., triples count rate, T) as another measurable quantity, and allows for an analytic estimate of all three fissile material physical properties introduced in Section 2.2 without any a priori calibration measurements [13, 16, 17, 29, 34, 39].

Typical neutron multiplicity counting systems have an array of neutron-sensitive radiation detectors where the time of each detected neutron is passed through a data acquisition system for analysis. FNMC systems specifically use organic scintillators that do not require intervening moderating material, thus the timing information of the emitted neutrons is minimally unperturbed prior to detection. The resulting series of detection times is referred to as the neutron pulse train, and is used to extract the neutron multiplicity count rates. Figure 4.1 shows an example of a neutron pulse train from an FNMC system. The neutron pulse train in Figure 4.1 shows neutron detections from *sf*, *if*, and (α,n) reactions, where correlated signals (i.e., *sf* and *if* neutrons) appear in groups where as the uncorrelated signals appear independent of subsequent detections, which is ideal for extracting neutron multiplicity counts.

The extraction of the multiplicity counts from a neutron pulse train requires an analysis of the correlations that exist in both the time and number of the detected neutrons [13, 17].

Figure 4.1: Visualization of the detected neutron time series in an FNMC system, referred to as the neutron pulse train. The neutron pulse train includes the correlated signals from fission neutrons and uncorrelated signals from nonfission neutrons.

The analysis of the timing behavior of the detected neutrons is referred to as time interval analysis (TIA), where correlations in the time-difference distribution of detected neutrons within a time gate is characterized [35]. The analysis of the number of detected neutrons is referred to as time correlation analysis (TCA), where correlations in the number distribution of detected neutrons within the same time gate is characterized [35]. In practical settings, the information from TIA offers aggregate correction factors to account for any systematic effects (e.g., neutron slowing-down time, system predelay, etc.) and also provides insight for optimal system parameters (e.g., time gate width, long delay, etc.) [64]. The information from TCA gives the measured neutron multiplicity count rates [35, 65].

4.1.1 Time Interval Analysis of The Neutron Pulse Train: Rossi-α Distributions

TIA on a neutron pulse train involves looking at the average behavior of the time differences between any and all neutron signals. The two most common methods for neutron TIA is the Feynman-Y and the Rossi-α techniques, and their implementation was originally proposed to study the prompt fission neutron behavior of near-critical assemblies; however, TIA can also provide system parameters when measuring materials that are far from critical [12, 30–32, 36]. This work implements a Rossi-α type I triggering analysis that uses overlapping time gates, which in turn provides improved precision compared to nonoverlapping time gates (i.e., Feynman-Y). Thethe time difference between the trigger signal and all subsequent signals within a time window, Δ, is used to produce a histogram with fine binning

[32, 38]. The time window is then shifted to the next signal and the process is repeated for all signals. Let us consider a simplified neutron pulse train absent of any neutron cross-talk effects. Figure 4.2 is a visualization of TIA with type I triggering for characterizing the average time difference behavior [32, 38].
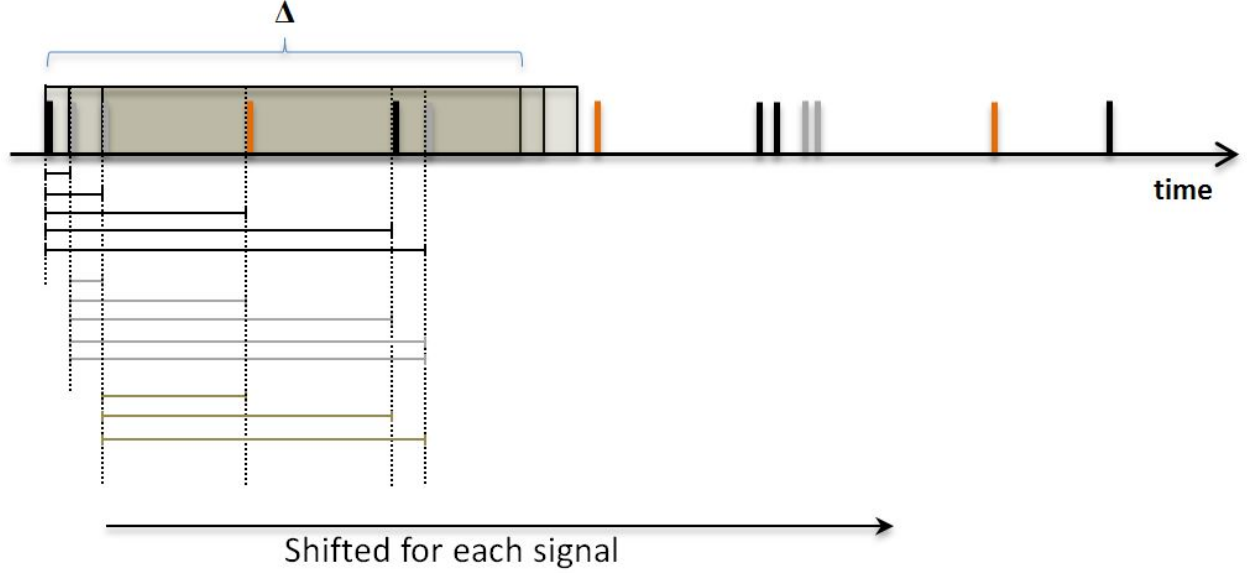
Figure 4.2: TIA on the neutron pulse train using type I triggering.

The resulting histogram of the time differences produces unique regions of interest that pertain to the magnitude of correlation observed in the neutron pulse train. Figure 4.3 is a heuristic representation of the time difference histogram, commonly referred to as the Rossi-α distribution.

Figure 4.3 shows two regions that correspond to the uncorrelated counts, represented by a uniform flat region, and the correlated counts, represented by a nonuniform region as t approaches 0 [13, 17]. That is, correlated signals are detected within shorter time differences, while uncorrelated signals are detected uniformly independent of the time differences. Assuming the nonuniform region behaves as a first-order exponential, the distribution in Figure 4.3 can be described by

$$P(t)\Delta = A\Delta + Re^{-\lambda t}\Delta, \tag{4.1}$$

58
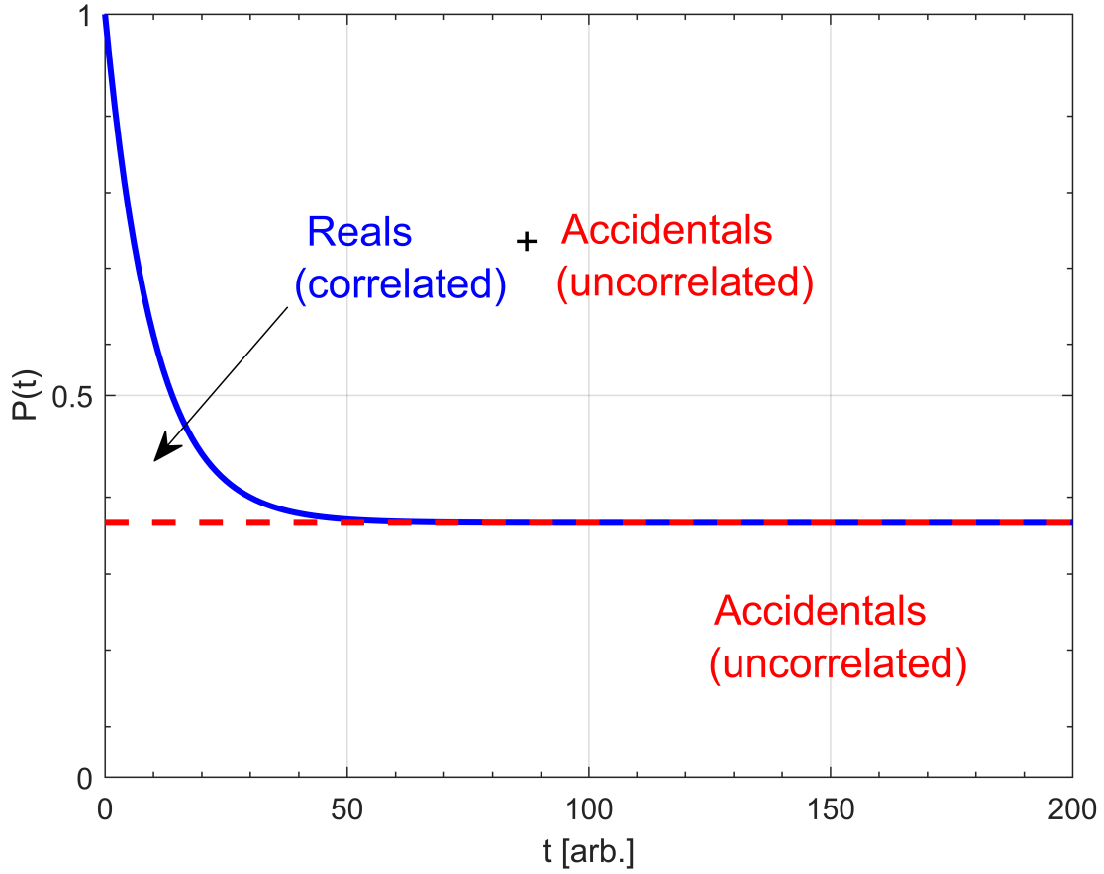
Figure 4.3: Typical shape of the Rossi-α distribution showing a uniform flat region of uncorrelated accidental counts and an exponential region at shorter time difference representing correlated counts.

where $P(t)\Delta$ is probability of detecting a neutron within Δ at time t given a detection at $t = 0$, $A\Delta$ is the uniform region due to uncorrelated counts, and $Re^{-\lambda t}\Delta$ is the exponential region with a decay constant of λ. The decay constant, λ, is referred to as the system die-away time, and describes the mean detection time of correlated neutrons given a detection at $t = 0$. The value of λ is a system-specific parameter dependent on the system geometry and type of detectors used; this parameter can be experimentally characterized with a ^{252}Cf or a small non-multiplying plutonium source [13, 17, 64].

Using TIA on the neutron pulse train, we obtain two important timing characteristics of the system that are used for TCA to extract the neutron multiplicity count rates. Firstly, the

system die-away time is used to separate the correlated and uncorrelated neutron number distribution where corrections for redundant counting are implemented, [66]. Secondly, the Rossi-α distribution in Figure 4.3 provides insight for the optimal time gate widths for extracting correlated counts [13, 17, 35, 64, 65].

4.1.2 Time Correlation Analysis on Neutron Pulse Train: Time-Gate Generation Methods

There are various methods of generating the time gate windows in a time series of detected neutron pulses; the three most commonly used methods are randomly triggered inspection (RTI) , signal-triggered inspection (STI), and a simultaneous combination of RTI and STI, hereafter referred to as the multiplicity shift register (MSR) [16, 66]. S. Croft et al. have shown the underlying differences of the different methods for generating time gates [35, 65], and M. Prasad et al. have derived the associated uncertainties pertaining to the different methods [67]; the expressions for the uncertainties can be found in Appendix A. The RTI technique uses a series of randomly triggered time gates (i.e., constant window gating) independent of any signal, whereas STI opens time gates for each detected signal. Suppose we have a neutron pulse train (much like the one shown in Figure 4.1) that is to be analyzed through either STI or RTI an inspection time gate width, T_G. Figures 4.4 and 4.5 show a visualization of RTI and STI gate generation methods.
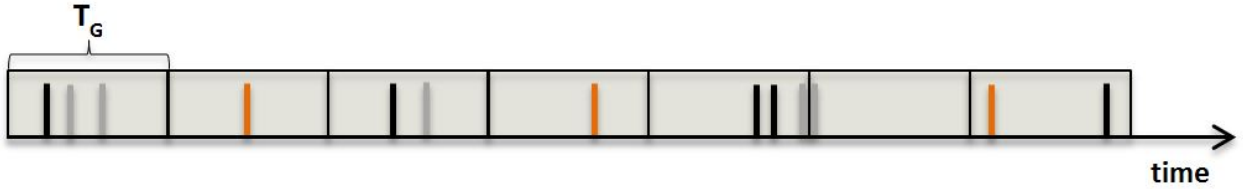
Figure 4.4: Visualization of the time gate generation for RTI analysis, with time gate widths of T_G.

A histogram of the number of detected signals within all time gates is extracted and normalized by the total number of generated gates. The number distribution from RTI and
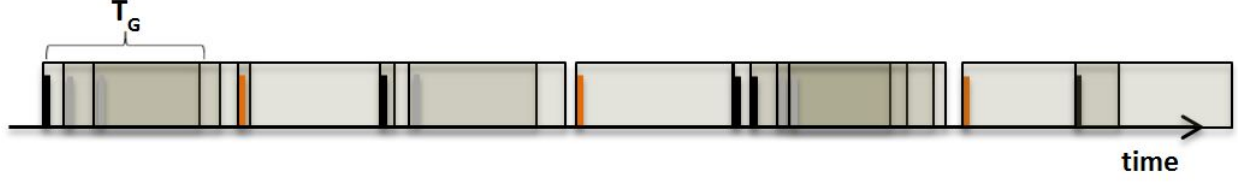
Figure 4.5: Visualization of the time gate generation for STI analysis, with time gate widths of T_G.

STI analyses are given by $B_x(T_G)$ and $N_x(T_G)$, where $B_x(T_G)$ is the number of events with x signals inside K total RTI intervals, and $N_x(T_G)$ is the number of events with x signals inside N_T STI intervals for a total measurement time of T_M [16, 35, 66]. Both number distributions can be expressed as frequencies by normalizing by the number of inspection intervals using

$$b_x(T_G) = \frac{B_x(T_G)}{K}, \tag{4.2}$$

and

$$n_x(T_G) = \frac{N_x(T_G)}{N_T}, \tag{4.3}$$

where $b_x(T_G)$ and $n_x(T_G)$ are the normalized number distributions using RTI and STI analyses. The first-, second-, and third-order reduced factorial moments are then calculated from $b_x(T_G)$ and $n_x(T_G)$ as

$$m_{b(\mu)} = \sum_{x=\mu}^{\infty} \binom{x}{\mu} b_x(T_G), \tag{4.4}$$

and

$$m_{n(\mu)} = \sum_{x=\mu}^{\infty} \binom{x}{\mu} n_x(T_G), \tag{4.5}$$

where $m_{b(\mu)}$ and $m_{n(\mu)}$ represent the μth reduced factorial moments for the RTI and STI number distributions [16].

4.1.3 Extraction of Detected Neutron Multiplicity Counts

The neutron multiplicity count rates can be extracted using just the RTI reduced factorial moments, or a combination of the RTI and STI reduced factorial moments [16, 35, 66]. If only the RTI moments are used, then the neutron multiplicity count rates are calculated as

$$S = \frac{m_{b(1)}}{T_G w_1}, \tag{4.6}$$

$$D = \frac{1}{T_G w_2} \left[m_{b(2)} - \frac{1}{2} m_{b(1)}^2 \right], \tag{4.7}$$

and

$$T = \frac{1}{T_G w_3} \left[m_{b(3)} - m_{b(2)} m_{b(1)} + \frac{1}{3} m_{b(1)}^3 \right], \tag{4.8}$$

where S, D, and T, are the neutron singles, doubles, and triples count rates, and w_μ is the gate utilization factor for RTI gates having the form

$$w_\mu = \sum_{j=0}^{\mu-1} \binom{\mu - 1}{J} (-1)^j \left(\frac{1 - e^{-jT_G\lambda}}{jT_G\lambda} \right), w_1 = 1. \tag{4.9}$$

The RTI gate utilization factor provides an aggregate correction to S, D, and T to account for the unfolding of the correlated counts given that the time gate triggers are random; the gate utilization factor is based on the Feynman-Y counting approach for reactivity measurements [31, 64].

The S, D, and T count rates can also be extracted with a combination of the RTI and STI moments, where two independent analyses using both gate generation techniques are used [16, 35, 66]. Since the STI method involves overlapping time gates, the number of time gates that are generated will typically be greater than the number of time gates generated using RTI method. In other words, the STI method samples the neutron pulse train at a greater frequency compared to RTI method ($K << N_T$). Therefore, the relative standard deviation of the extract multiplicity count rates will be less when using a combination of

RTI and STI moments relative to just using RTI moments. The S, D, and T neutron count rates are calculated as

$$S = \frac{N_T}{T_M} m_{n(0)} = \frac{N_T}{T_M}, \tag{4.10}$$

$$D = \frac{N_T}{T_M f} \left[m_{n(1)} - m_{b(1)} \right], \tag{4.11}$$

and

$$T = \frac{N_T}{T_M f^2} \left[m_{n(2)} - m_{b(2)} - m_{b(1)} \left(m_{n(1)} - m_{b(1)} \right) \right], \tag{4.12}$$

where T_M is the total measurement time, and f is the STI gate utilization factor. The value of f applies similar aggregate corrections to w_μ, and accounts for triggers caused by accidental signals. f has the form [13, 16, 17, 35, 66]

$$f = \left(e^{-T_{PD}\lambda} \left(1 - e^{-T_G\lambda} \right) \right), \tag{4.13}$$

where T_{PD} is the system predelay between the trigger signal and the start of the time gate window.

The multiplicity shift register (MSR) method of gate generation is a form of autocorrelation analysis, where the detections in two signal-triggered time gates of equal widths separated by a fixed long delay are used [16, 35, 66]. Using the MSR method to extract the multiplicity count rates is similar to the mixed RTI-STI method, but considers the special case when $(K = N_T)$. Figure 4.6 shows a visualization of the MSR gate generation method.

The fundamental principle behind the MSR method lies in the simultaneous sampling of the two time gates, where the (R+A) window provides an observation for correlated and uncorrelated counts, and the (A) window provides an observation of uncorrelated counts (relative to the trigger signal). The fixed long delay is set such that there exists no correlations between the trigger signal (start of the (R+A) gate) and the signals observed in the (A) gate. Since $(K = N_T)$, this method can be seen as exactly analogous to the mixed RTI-STI method, but effectively involves an oversampling of the RTI moments providing more
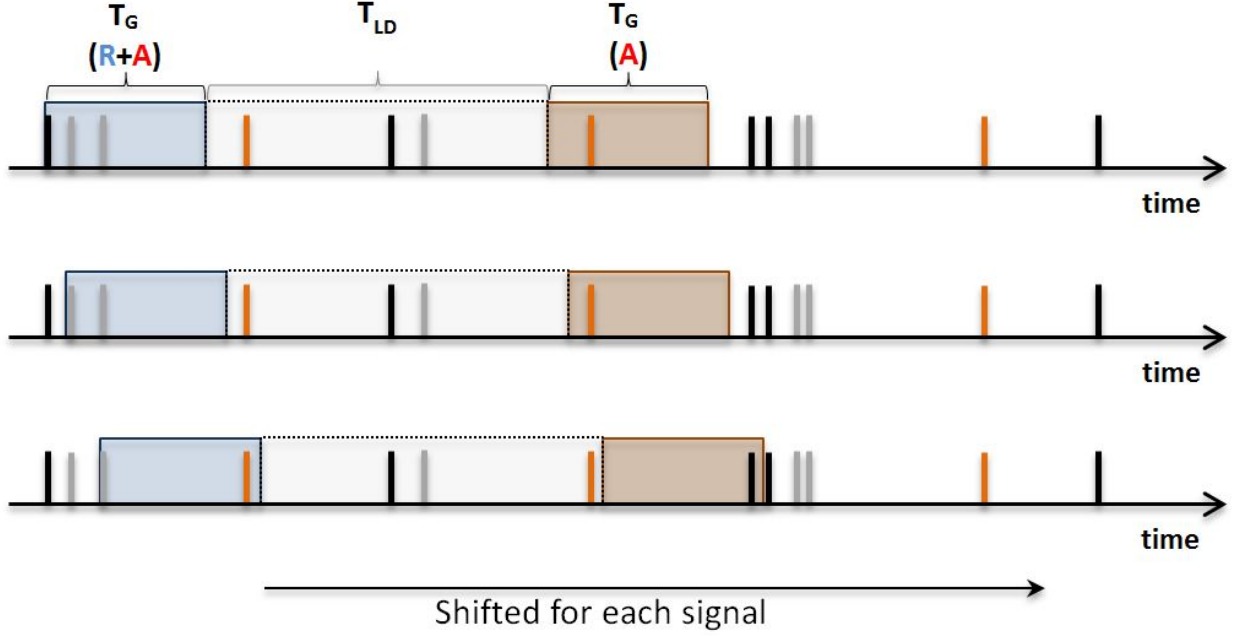
Figure 4.6: Visualization of the time gate generation for MSR analysis showing the R+A and A time gates of width T_G, separated by a fixed long delay T_{LD}.

certainty on the RTI moments. As mentioned previously, the Rossi-α distribution from TIA provides insight on the optimal choice of time gate widths. Figure 4.3 illustrates that given a trigger signal at $t = 0$, correlated counts appear at much shorter time difference where as the uncorrelated counts appear independent of the trigger signal. The time gate width for the MSR method should be chosen such that it is long enough to include the correlated counts but short enough such that the contribution from uncorrelated counts is minimized. Figure 4.7 shows the Rossi-α distribution from figure 4.3 with an overlay showing TIA-informed time gate width and the fixed long delay.

Once the number distribution of the detected signals in both the (R+A) and (A) gates have been extracted, the respective reduced factorial moments can then be calculated analogous to the RTI and STI method [16, 35, 66]. The neutron multiplicity count rates using the MSR method are then given by

$$S = S \cdot m_{n(0)} = \frac{m_{b(1)}}{T_G} = \frac{N_T}{T_M} m_{n(0)}, \tag{4.14}$$
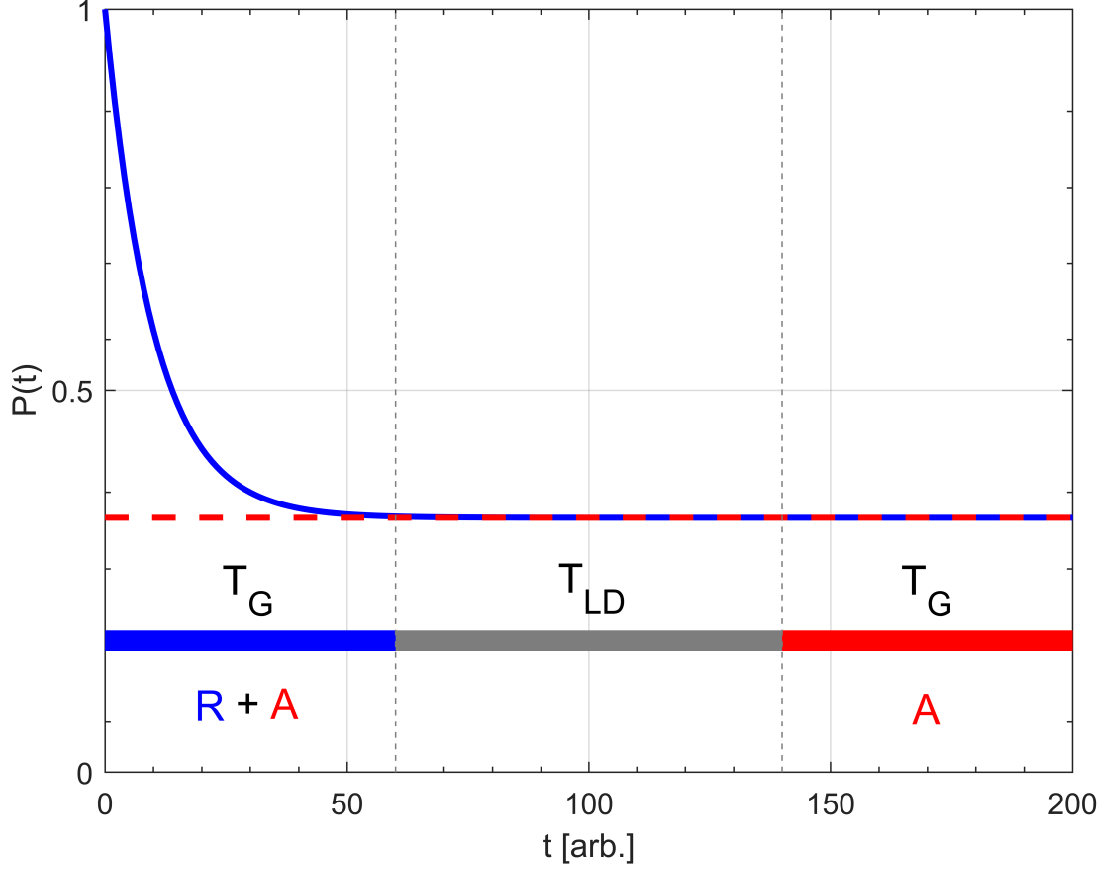
Figure 4.7: Time gate width, T_G and fixed long delay, T_{LD}, overlaid on the Rossi-α distribution showing how TIA can inform suitable lengths of T_G and T_{LD}.

$$D = \frac{S}{f}\left[m_{n(1)} - m_{b(1)}\right] = \frac{S}{f}\left[m_{n(1)} - S \cdot T_G\right], \tag{4.15}$$

and

$$
\begin{aligned}
T &= \frac{S}{f^2}\left[m_{n(2)} - m_{b(2)} - m_{b(1)}\left(m_{n(1)} - m_{b(1)}\right)\right] \\
&= \frac{S}{f^2}\left[m_{n(2)} - m_{b(2)} - (D \cdot T_G)\right],
\end{aligned}
\tag{4.16}
$$

where $m_{n(\mu)}$ and $m_{b(\mu)}$ are the μth-order reduced factorial moments from the (R+A) gates and the (A) gates, respectively. Figure 4.8 shows the measured Rossi-α distribution using an FNMC system for ^{252}Cf *sf* neutrons demonstrating the time scale for TCA in FNMC systems. The associated uncertainty in the measured neutron singles, doubles, and triples

rates using the MSR method can be found in Appendix A.
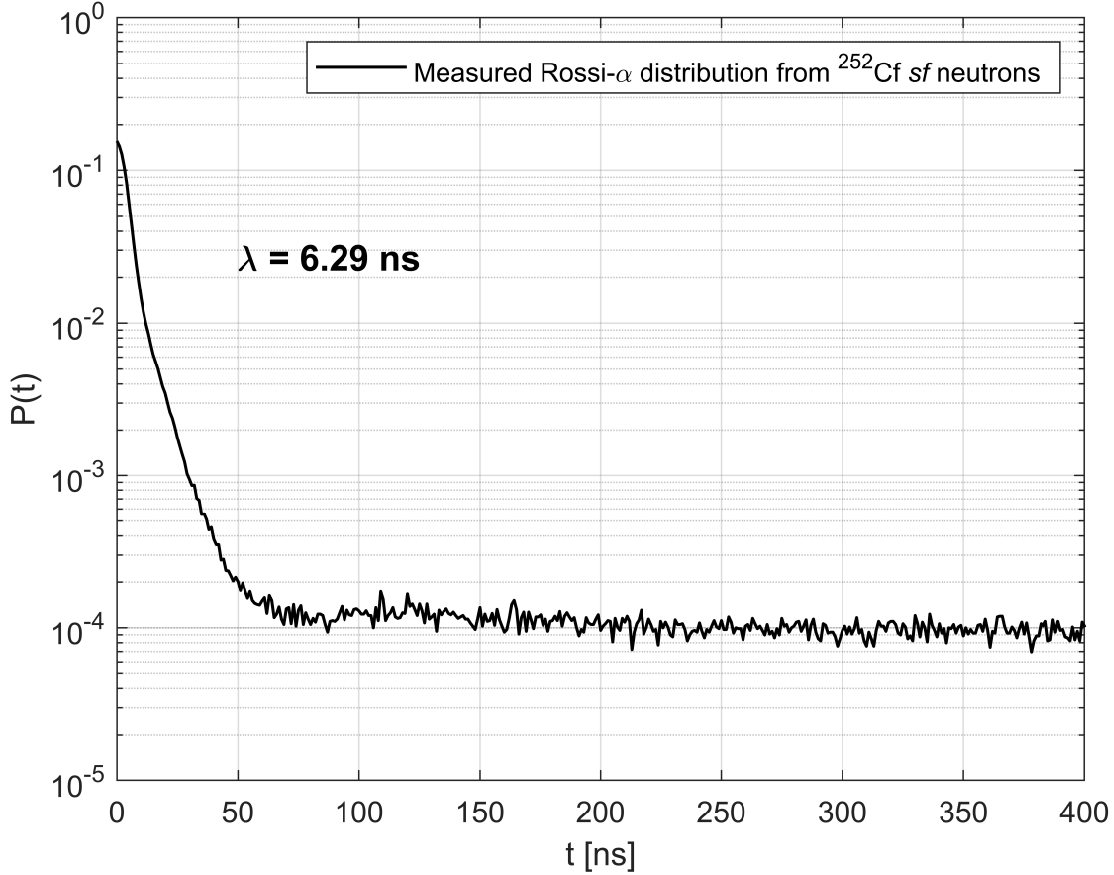
Figure 4.8: Measured Rossi-α distribution using an FNMC system for ^{252}Cf *sf* neutrons showing a system die-away time of 6.29 ns. The time gate widths used in FNMC systems are on the order of tens of nanoseconds.

4.2   Event-by-event Neutron-Neutron Correlations

Rather than analyzing the neutron pulse train through TIA and TCA, FNMC systems can also extract neutron-neutron correlations on an event-by-event basis. Since FNMC systems do not require any intervening moderating material, the timing information of emitted neutrons is not modulated prior to being detected in a detector. Leveraging the fact that the organic scintillators in FNMC systems have typical response times on the order of nanoseconds, the FNMC system is able to observe neutron-neutron correlations on the same

timescale as typical fission chains (order of nanoseconds) [42, 43, 68].

4.2.1 Neutron-Neutron Time-Difference Distributions

Consider a two-detector system of organic scintillators surrounding fissile material as shown in Figure 4.9. Figure 4.9 shows a fission event at $t = 0$ where three neutrons are
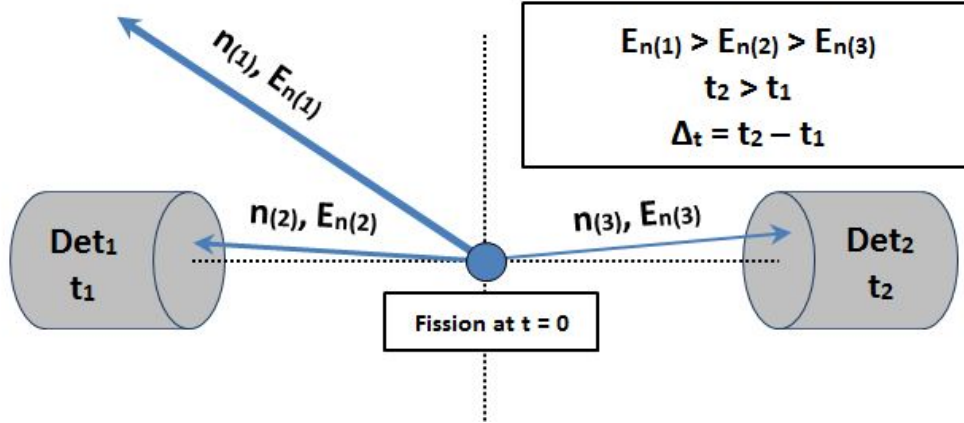
Figure 4.9: A schematic of a two-detector organic scintillator system with detectors Det_1 and Det_2, fissile material with a fission at $t = 0$ and an emitted neutron multiplicity of three. The three neutrons are emitted with energy $E_{n(\nu)}$, where $E_{n(1)} > E_{n(2)} > E_{n(3)}$. Two neutrons are detected by the system with a time of detection t_1 and t_2 in Det_1 and Det_2, respectively.

emitted, of which two of them are detected. Since $E_{n(2)}$ is greater than that of $E_{n(3)}$, $n_{(}2)$ will be detected in Det_1 at an earlier time relative to $n_{(}3)$ in Det_2. That is, the time of detection t_1 is less than t_2. Using the first time of detection (in either detector) as the trigger to open a time gate for all other detectors, the difference in detection times between the two detectors is calculated as $\Delta t = t_2 - t_1$, where the negative and positive sense is arbitrary and is dictated by which detector triggers the time gate. In other words, Δt would be positive in the case shown in Figure 4.9, and would be negative in the case that $E_{n(3)}$ was greater than $E_{n(2)}$. A histogram of all Δts between all pairs of detectors in an FNMC system yields the total neutron-neutron time-difference distribution. Consider an FNMC system with N detectors, where $H_{ij}(\Delta_t)$ represents the time-difference distribution between

detectors i and j. The total neutron-neutron time-difference distribution is given by

$$H_{tot}(\Delta_t) = \sum_{i=1}^{N-1} \sum_{j=i+1}^{N} H_{ij}(\Delta_t), \tag{4.17}$$

and the total detected neutron doubles rate, D, can be calculated with

$$D = \int_{-\infty}^{\infty} H_{tot}(\Delta_t). \tag{4.18}$$

Figure 4.10 shows the measured total neutron-neutron time-difference distribution from ^{252}Cf sf neutrons using an FNMC system with 24 detectors.
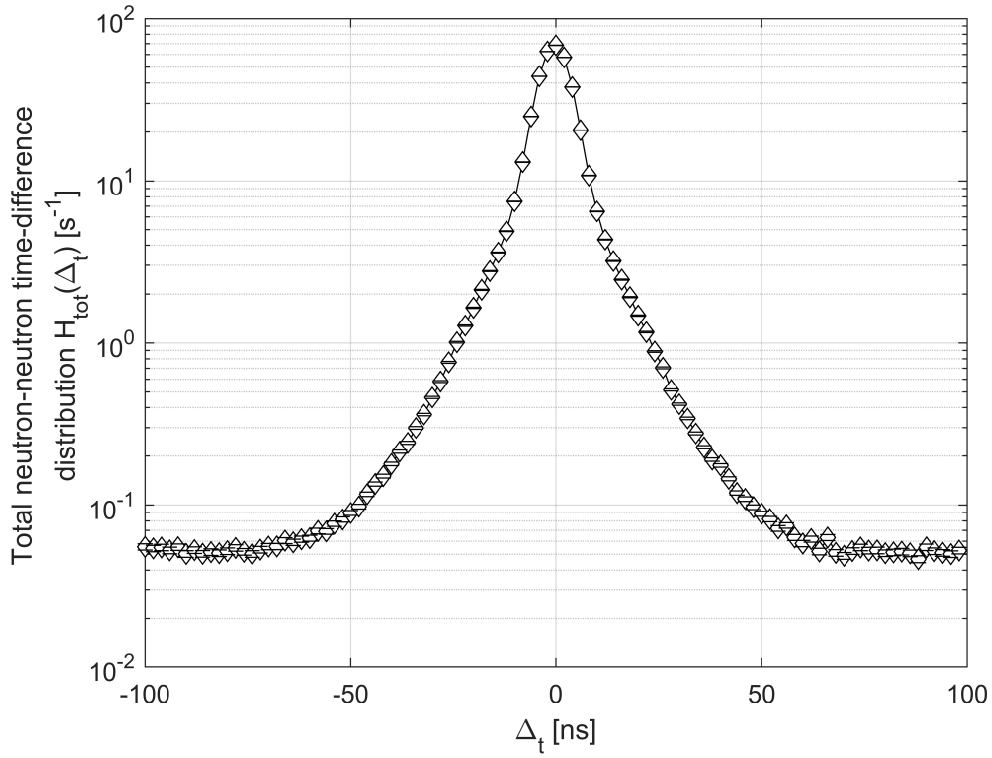
Figure 4.10: Measured total neutron-neutron time-difference distribution from ^{252}Cf sf neutrons using an FNMC system with 24 detectors with a detection threshold of 0.10 MeVee.

4.2.2 Neutron-Neutron Angular and Energy-Angle Correlations

An FNMC system arranged in a cylindrical array will have groups of detector pairs that exhibit the same detection angle. Figure 4.11 shows an FNMC system with eight detectors, with a fission event emitting three neutrons at $t = 0$.
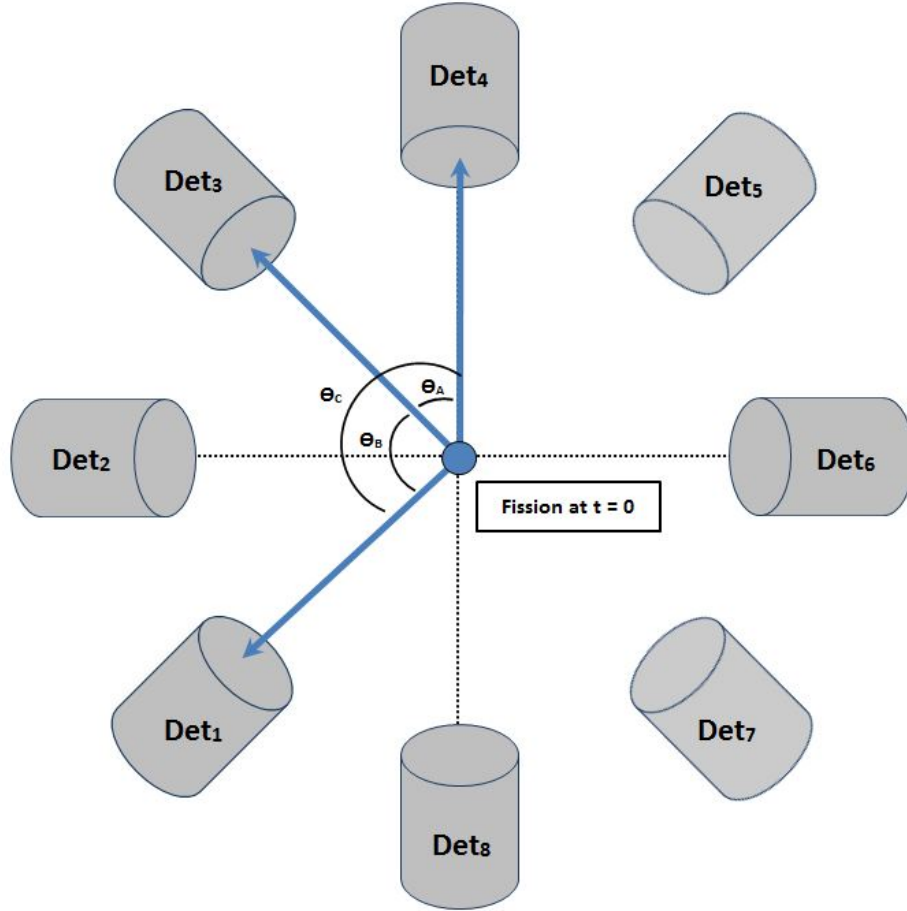
Figure 4.11: A schematic of an FNMC system surrounding fissile material with a fission event at $t = 0$. The total neutron-neutron time-difference distributions can be extracted by summing the distributions between all combinations of detection pairs (e.g., eight detectors gives 28 total unique pair combinations). Neutron-neutron time-difference distributions can also be extracted for detector pairs that exhibit similar detection angles.

The neutron-neutron detection angles for the three detected neutrons are shown as θ_A, θ_B, and θ_C. The time-difference distribution can be separated and categorized into unique angle groups, where the detected neutron doubles can be calculated as a function of the detection angle [21–27]. There are some cases where an FNMC system will have detector

69

pairs that exhibit the same angle, but appreciably different source-to-detector solid angle geometry. Therefore, the time-difference distribution for every detector pair is divided by the neutron singles counts to account for any detector nonuniformity in addition to difference in the source-to-detector solid angle. The singles-corrected time-difference distribution, H_{ij}^*, for a detector pair is given by

$$H_{ij}^*(\Delta_t) = \frac{H_{ij}(\Delta_t)}{S_i S_j}, \tag{4.19}$$

where S_i and S_j are the neutron singles counts in Det_i and Det_j. The singles-corrected neutron-neutron coincidences for a detector pair, D_{ij}^*, hereafter referred to as relative coincidences, can be calculated as

$$D_{ij}^* = \int_{-\infty}^{\infty} H_{ij}^*(\Delta_t). \tag{4.20}$$

Figure 4.12 shows the uncorrected and singles-corrected time-difference distribution for pairs of detectors with different source-to-detector distances but the same angle of separation (180°).
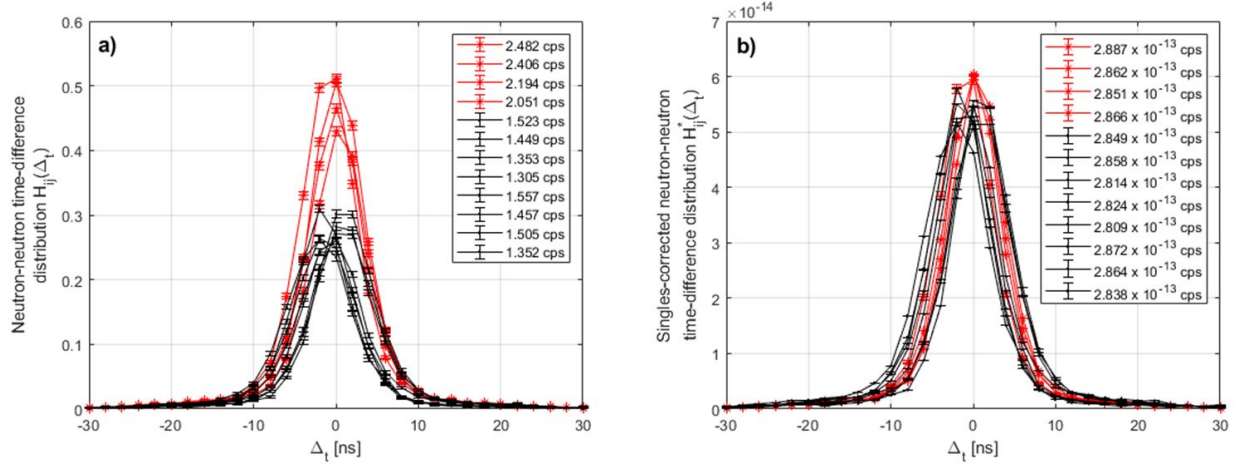
Figure 4.12: The uncorrected neutron-neutron time-difference distributions (a) and the singles-corrected neutron-neutron time-difference distributions (b) for detector pairs with different source-to-detector distances but same angle of separation (180°)

70

The relative coincidences for each pair are then sorted by their respective angle groups, where the average for each angle group, $W(\angle)$, is calculated using

$$W(\angle) = \frac{1}{K} \sum_{k=1}^{K} D_k^*, \tag{4.21}$$

where K is the total number of pairs in each angle group, and D_k^* is the kth pair of detectors in the angle group. Figure 4.13 shows an example of the measured neutron-neutron angular distribution for ^{252}Cf sf neutrons using an FNMC system.
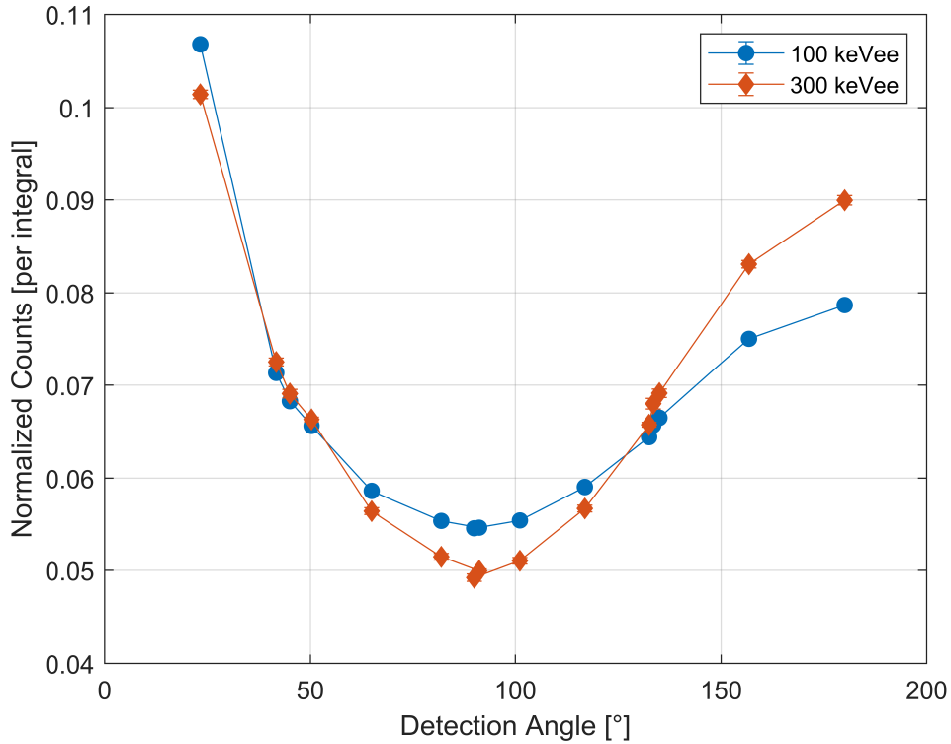
Figure 4.13: Full neutron-neutron angular distribution from ^{252}Cf sf neutrons for two different low-energy detection thresholds.

Figure 4.13 shows the well known anisotropic distribution of sf neutrons from single-fission events, demonstrated by the increase in neutron-neutron coincidences at the smaller and larger detection angles relative to those at (90°) [21–25]. The ratio of the relative coincidences at the largest angles (180°) to those observed perpendicular to one another

(90°) is calculated using

$$A = \frac{W(180°)}{W(90°)} \tag{4.22}$$

to provide a quantitative metric for the anisotropy, A, observed in the neutron-neutron coincidences [26]. A purely isotropically emitting source with no angular correlation would have an A value of unity, whereas a source with angular correlations would have an A value excess of unity.

The magnitude of the observed anisotropic distribution is also dependent on the low-energy detection threshold, which is a controllable processing parameter. That is, raising the detection threshold offers an observation of neutrons with higher energies (on average), and thus neutron-neutron energy-angle correlations can be characterized. Figure 4.14 shows the observed anisotropy as a function of the detection thresholds. Figure 4.14 shows that a positive correlation exists between the neutron-neutron anisotropy and the energy of the emitted neutrons when correlating *sf* neutrons from single fission events [26, 27]. This correlation is expected due to the kinematic boost in energy and momentum the emitted *sf* neutrons receive from the fission fragments, as described in Section 2.2.2.

4.3   Neutron Cross-Talk Effects in Time Series Analysis

Since organic scintillators are scatter-based detectors, a single neutron can scatter into and deposit energy above the detection threshold in multiple detectors causing spurious time-correlated counts in an FNMC system. Neutron cross-talk effects can be mitigated by raising the low-energy detection threshold; cross-talk neutrons will have lost a portion of their initial energy from the first detection [69]. The practical trade off is that the total system neutron detection efficiency will also decrease as the threshold is increased. Additionally, neutron cross-talk effects are also dependent on the relative solid angle between detectors; detectors that are in close proximity will have the most cross-talk events [69]. In summary, the fraction of spurious multiplicity counts from neutron cross-talk events relative to true
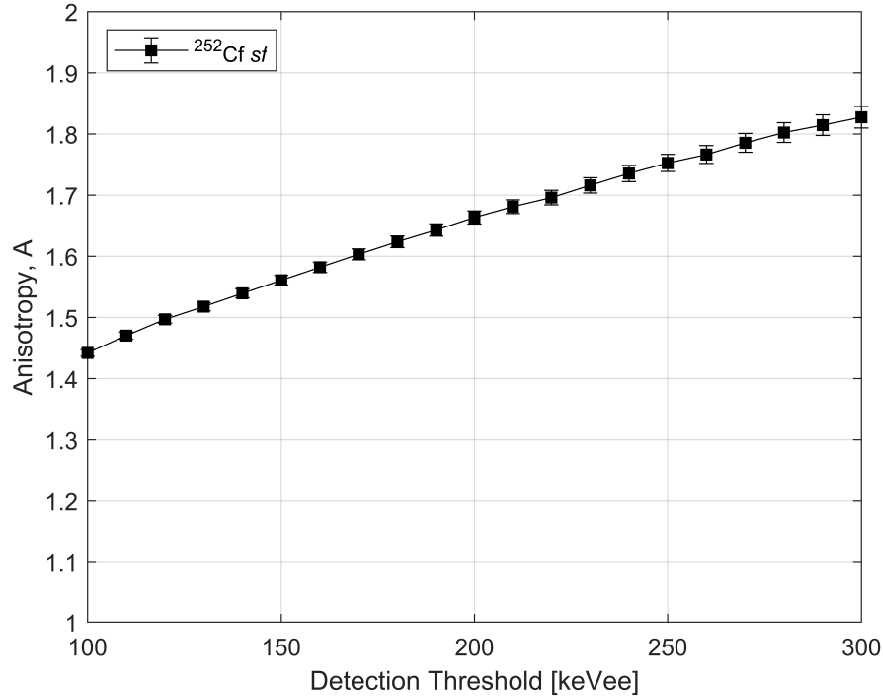
Figure 4.14: Neutron-neutron energy-angle correlation of ^{252}Cf *sf* neutrons.

multiplicity events is primarily dependent on the energy spectrum of the emitted neutrons, the low-energy detection threshold, and the geometric configuration of the detectors.

Neutron cross-talk events are possible for both correlated and uncorrelated neutrons. It is impractical to discriminate between cross-talk signals and true neutron multiplicity signals as they are indistinguishable from one another in time. Figure 4.15 shows a schematic of an FNMC system observing four detections for an emitted neutron multiplicity of three due to neutron cross-talk effects. The expected neutron pulse train considering cross-talk effects is shown in Figure 4.16; spurious cross-talk signals are labeled for clarity, but are indistinguishable from true neutron signals in practice. Figure 4.16 shows that the spurious cross-talk signal is detected close in time to the initial true signal, effectively appearing as a correlated count (correlated to the initial true signal). Although the presence of neutron cross-talk events are inevitable in FNMC systems, neutron cross-talk effects can be accounted for in the context of the PKE.
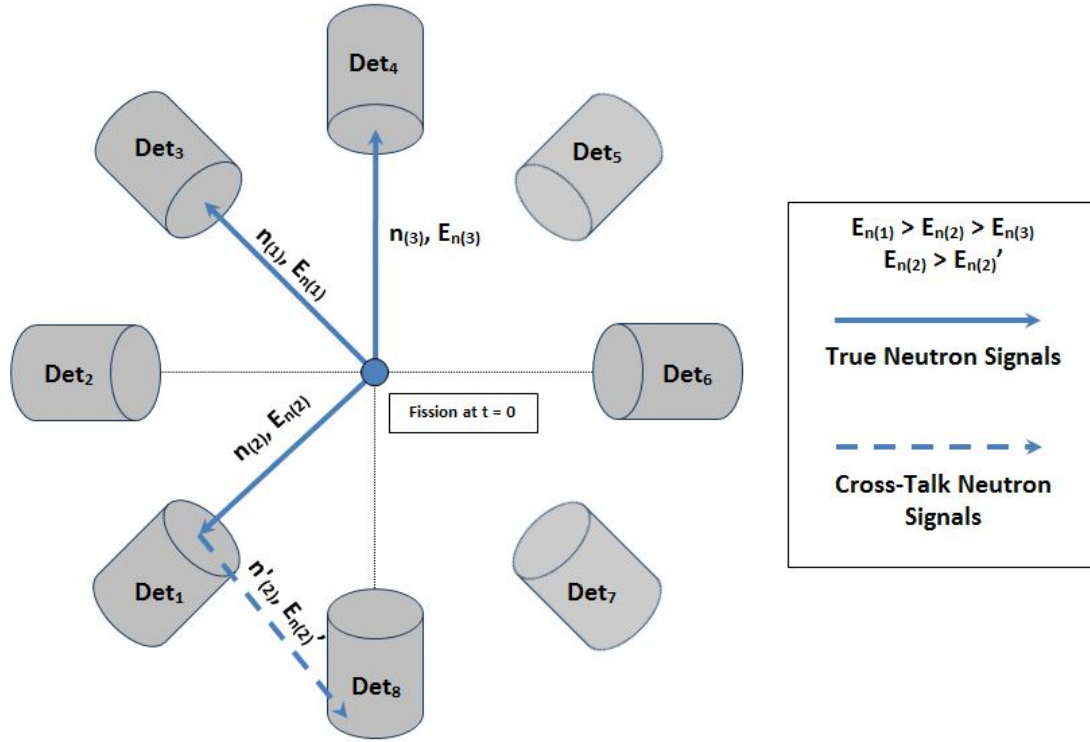
Figure 4.15: A schematic of an FNMC system surrounding fissile material with a fission event a $t = 0$. Three true neutron signals are detected with an additional fourth signal caused by a neutron cross-talk event.
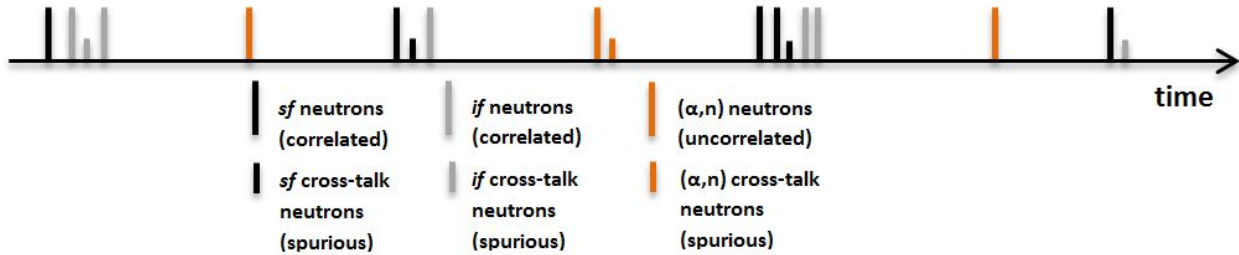
Figure 4.16: Visualization of the neutron pulse train from an FNMC system. The neutron pulse train includes the correlated signals from fission neutrons and uncorrelated signals from nonfission neutrons, as well as spurious neutron cross-talk signals.

4.4 Point Kinetics Equations with Neutron Cross-Talk Corrections

Extracting the detected neutron S, D, and T rates provides the three measurable quantities that can be used to analytically estimate the physical properties of SNM. The equations

that relate the measured S, D, and T rates to the three physical SNM properties (i.e., sf rate, F, the $\alpha-$ratio, α, and the leakage multiplication, M_L) are predicated on the point kinetics approximation and are referred to as the point kinetics equations (PKE) for NMC. Recalling the PKE physical assumptions outlined in Section 2.5, the emitted S, D, and T from Eqs. (2.33), (2.34), and (2.35) can be directly related to the measured S, D, and T given by Eqs. (4.14), (4.15), and (4.16) by considering the neutron detection efficiency and timing corrections. The PKE equations for a capture-based NMC system have been previously derived and are considered well established techniques validated by experimental data; however, these PKE equations are not directly applicable to FNMC systems primarily due to the effects of neutron cross-talk. New probability generating functions (PGF) are established to describe the number of detections a single neutron may cause in an FNMC system in order to account for the neutron cross-talk events.

4.4.1 Probability Generating Functions

PGFs are used as a mathematical tool to succinctly describe all possible realizations of a random discrete variable. In general, if the probability of the nth discrete random event is described by p_n, then the PGF, $G(z)$, is expressed as

$$G(z) = \sum_{n=0}^{\infty} p_n z^n, \tag{4.23}$$

with the normalizing condition

$$G(z = 1) = 1. \tag{4.24}$$

Once the PGF is established and properly normalized, the kth-order factorial moment is given by the kth derivative of $G(z)$ evaluated at $z = 1$. For this specific application, we establish the PGF to describe all possible detections a *single* neutron may cause in an FNMC system. For comparison, the PGF of a capture-based NMC system is described by

$$G(z) = z^0 \left[1 - \epsilon_0\right] + z^1 \left[\epsilon_0\right], \tag{4.25}$$

where ϵ_0 is the efficiency of detecting a neutron that has not been previously detected (i.e., probability of a first detection of a neutron emitted directly from the sample). The coefficient of the z^n terms represents the probability of detecting a neutron exactly n times, hereafter referred to as p_n. That is, Eq. (4.25) describes a system where a neutron will either not be detected with probability $p_0 = (1 - \epsilon_0)$, or will be detected with probability $p_1 = (\epsilon_0)$. Figure 4.17 shows the physical processes described by the PGF in Eq. (4.25) for capture-based NMC systems.
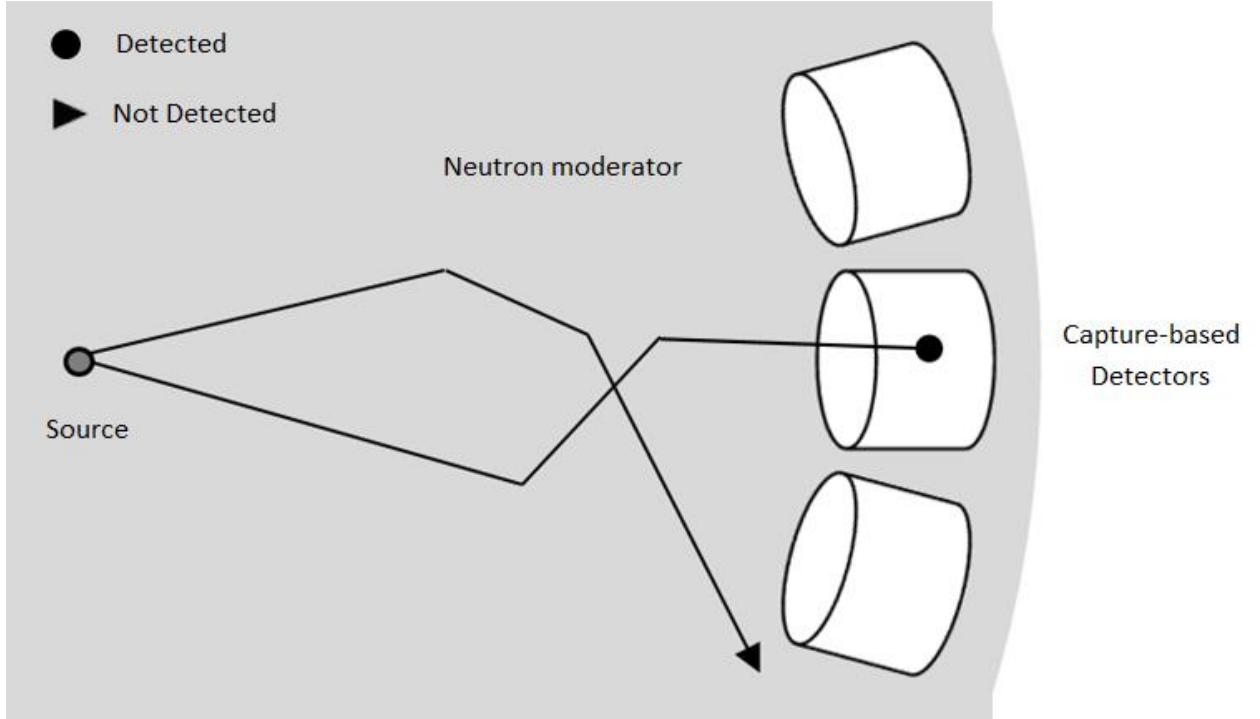
Figure 4.17: A schematic diagram of the physical processes for detection a neutron may undergo in a capture-based NMC system.

For FNMC systems, the presence of neutron cross-talk events must be accounted for and therefore the PGF should consider the case when a *single* neutron causes multiple detections. The PGF for an FNMC system is established (considering neutron cross-talk events up to order $N = 3$) and has the form

$$G(z) = z^0[(1 - \epsilon_0)] + z^1[(\epsilon_0)(1 - \epsilon_1)] + z^2[(\epsilon_0 \epsilon_1)(1 - \epsilon_2)] + z^3[(\epsilon_0 \epsilon_1 \epsilon_2)], \qquad (4.26)$$

where ϵ_j is the efficiency of detecting a neutron that has been previously been detected j times within the system. Figure 4.18 shows the physical processes for multiple counts caused by a single neutron in an FNMC system.
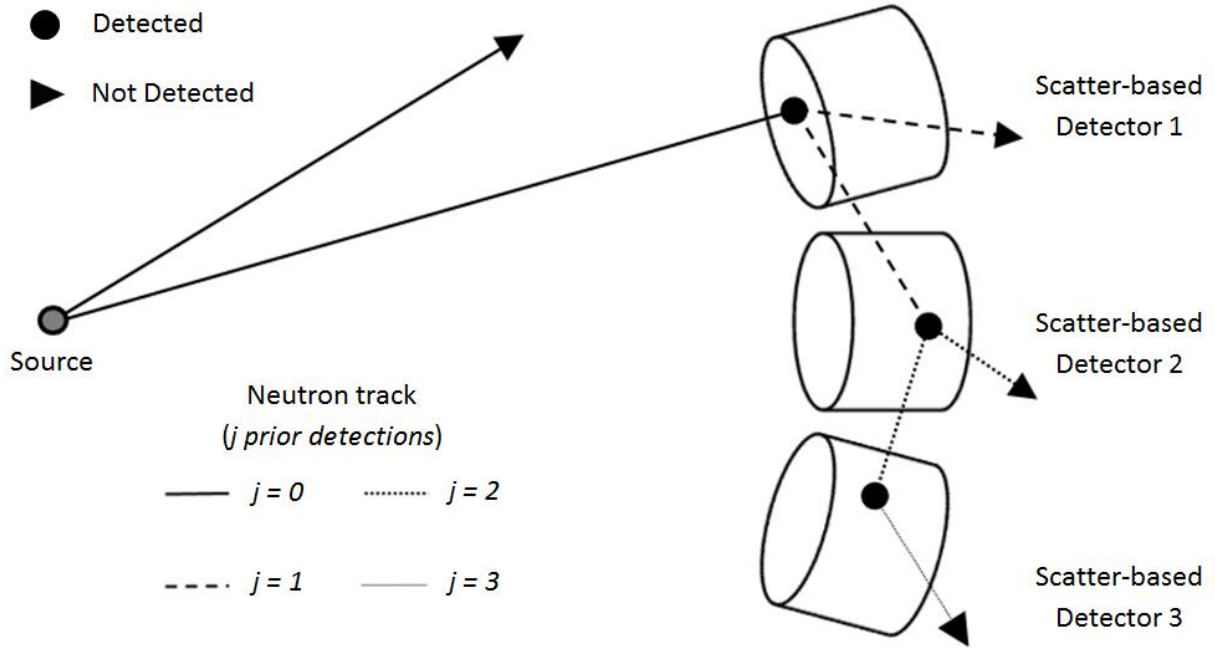
Figure 4.18: A schematic diagram of the physical processes for multiple detections (up to $N = 3$ detections) a neutron may undergo in a capture-based FNMC system.

The fully generalized form for the probability of detecting a neutron exactly n times is given by

$$p_n = (1 - \epsilon_n) \prod_{j=0}^{n-1} \epsilon_j, \quad 1 \leq n \leq N, \quad p_0 = (1 - \epsilon_0). \qquad (4.27)$$

Using Eq. (4.27), the generalized PGF for any given FNMC system that considers up to N maximum detections can be established using

$$G_N(z) = \sum_{n=0}^{N} p_n z^n, \quad \forall N \geq 1, \quad \prod_{j=0}^{N} \epsilon_j \approx 0. \tag{4.28}$$

As PGFs must describe *all* possible realizations of a random discrete variable, a physical assumption must be implemented in order to satisfy the normalizing condition in Eq. (4.24). The PGF shown in Eq. (4.26) holds the assumption that $(\epsilon_0 \epsilon_1 \epsilon_2 \epsilon_3) \approx 0$, which indicates that the probability of detecting a neutron that has already been detected three times prior is approximately 0. In practice, the reliability of the aforementioned physical assumption is application-specific depending on the sample, detector thresholds, and system geometry. Figure 4.19 summarizes all probabilities of detecting a neutron once, twice, up to $N = 3$ times.
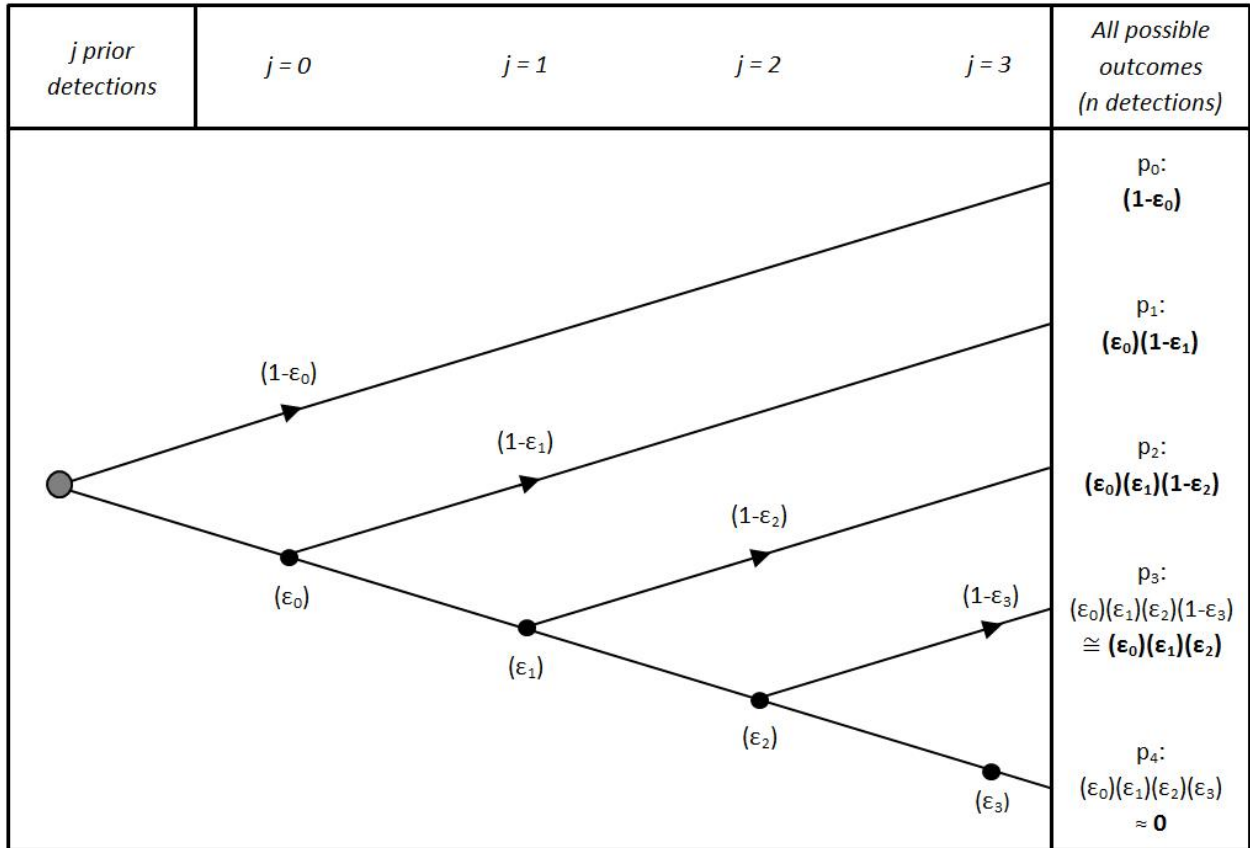
Figure 4.19: A tree diagram showing the probabilities associated with all possible outcomes. The possible outcomes represent the probability of detecting a neutron exactly n times.

Once the normalizing conditions have been met by taking the appropriate physical as-

sumption on N, we can then leverage the succinct derivation of the kth factorial moments, m_k, using the general relationship

$$\lim_{x \to 1} \frac{d^k G(x)}{dx^k} = G^{(k)}(1) = m_k, \quad \forall k \geq 1. \tag{4.29}$$

The kth derivative of $G(z)$ can be calculated by

$$\frac{d^k}{dz^k} G(z) = G^{(k)}(z) = \sum_{i=k}^{N} \left[\frac{i!}{(i-k)!} (1 - \epsilon_j) z^{i-k} \prod_{j-0}^{i-1} \epsilon_j \right], \quad \forall N \geq 1. \tag{4.30}$$

For simplicity, we define μ_k as the kth-order factorial moments of $G(z)$ as

$$\mu_k \equiv G^{(k)}(1) = \overline{n(n-1)(n-2)...(n-k+1)}. \tag{4.31}$$

The resulting factorial moments from the $N = 1$ and $N = 3$ are calculated to show the difference in the expected number single, double, and triple detections from a single neutron with and without neutron cross-talk corrections. The moments for $N = 1$ are calculated as

$$\mu_{1_{N=1}} = G^{(1)}_{N=1}(1) = \epsilon_0,$$
$$\mu_{2_{N=1}} = G^{(2)}_{N=1}(1) = 0, \tag{4.32}$$
$$\mu_{3_{N=1}} = G^{(3)}_{N=1}(1) = 0,$$

and the moments for $N = 3$ are calculated as

$$\mu_{1_{N=3}} = G^{(1)}_{N=3}(1) = \epsilon_0 + \epsilon_0 \epsilon_1 + \epsilon_0 \epsilon_1 \epsilon_2,$$
$$\mu_{2_{N=3}} = G^{(2)}_{N=3}(1) = 2\epsilon_0 \epsilon_1 (1 + 2\epsilon_2), \tag{4.33}$$
$$\mu_{3_{N=3}} = G^{(3)}_{N=3}(1) = 6\epsilon_0 \epsilon_1 \epsilon_2.$$

The first-order moment in Eq. (4.32) is calculated as ϵ_0, whereas the second- and third-order moments are calculated as 0, indicating that the PGF for $N = 1$ does not expect (and account for) any spurious double or triple count from a single neutron. However, when considering the possibility of neutron cross-talk, the expected value of total detections (first-order moment) increases to account for the increased spurious cross-talk counts. The second- and third-order moments also have nonzero expectations indicating that the PGF for $N = 3$ does indeed allow and accounts for spurious events. In principal, the established PGF should account for cross-talk events of order N such that

$$\mu_{1_N} \approx \mu_{1_{N \to \infty}}. \tag{4.34}$$

4.4.2 Derivation of the Detected Neutron Multiplicity Count Rates

The factorial moments of the total emitted neutron multiplicity distribution, Q_T, including sf, if, and (α,n) neutrons, are independent of the detection system, and are shown in Eqs. (2.29), (2.30), and (2.31). We introduce the definition of $H^{(k)}(1)$ as the kth derivative of the PGF that describes the factorial moments of Q_T as

$$
\begin{aligned}
\nu_{Q_T,1} &= H^{(1)}(1) \\
&= \frac{M_L}{(1 + \alpha \nu_{sf,1})} \nu_{sf,1}(1 + \alpha), \\
\nu_{Q_T,2} &= H^{(2)}(1) \\
&= \frac{M_L^2}{(1 + \alpha \nu_{sf,1})} \left[\nu_{sf,2} + \left(\frac{M_L - 1}{\nu_{if,1} - 1} \right) \nu_{sf,1}(1 + \alpha)\nu_{sf,2} \right], \\
\nu_{Q_T,3} &= H^{(3)}(1) \\
&= \frac{M_L^3}{(1 + \alpha \nu_{sf,1})} \left[\nu_{sf,3} + \left(\frac{M_L - 1}{\nu_{if,1} - 1} \right) [3\nu_{sf,2}\nu_{if,2} + \nu_{sf,1}(1 + \alpha)\nu_{if,3}] \right. \\
&\quad \left. + 3 \left(\frac{M_L - 1}{\nu_{if,1} - 1} \right)^2 \nu_{sf,1}(1 + \alpha)\nu_{if,2}^2 \right.
\end{aligned} \tag{4.35}
$$

Utilizing another useful property of PGFs allows us to relate the established PGF for the number of detections a single neutron may cause, $G(z)$, with the PGF of the total emitted neutron multiplicity distribution, $H(z)$, by using

$$R(z) = H(G(z)), \tag{4.36}$$

where $R(z)$ represents the number of detections that any emitted neutron may cause. Using Eqs. (4.30), (4.35), and (4.36), the factorial moments for the number of detections from any and all emitted neutrons are

$$
\begin{aligned}
\tilde{\nu}_1 &= R^{(1)}(1) \\
&= \nu_1 \mu_1, \\
\tilde{\nu}_1 &= R^{(2)}(1) \\
&= \left[\nu_2 \mu_1^2 + \nu_1 \mu_2 \right] f, \\
\tilde{\nu}_1 &= R^{(3)}(1) \\
&= \left[\nu_3 \mu_1^3 + 3\nu_2 \mu_1 \mu_2 + \nu_1 \mu_3 \right] f^2,
\end{aligned}
\tag{4.37}
$$

where f is the signal-triggered gate utilization factor described in Eq. (4.13). To relate these factorial moments to the detection rates described in Eqs. (4.14), (4.15), and (4.16), we note that these moments are proportional to the total rate of initiating events, Q_S, (the sum of sf and (α,n) reaction rates). Given that

$$Q_S = Q_{sf}(1 + \alpha \nu_{sf,1}), \tag{4.38}$$

the following equations are used to calculate the kth-order reduced factorial moments of the detected number of neutrons accounting for the neutron detection efficiency (i.e., S, D, and T):

81

$$C_k = Q_S \frac{\tilde{\nu}_k}{k!} = Q_{sf}(1 + \alpha\nu_{sf,1})\frac{\tilde{\nu}_k}{k!}, \tag{4.39}$$

where $C_1 \equiv S$, $C_2 \equiv D$, and $C_3 \equiv T$. The final expressions for the S, D, and T neutron count rates are

$$S = FM_L\mu_1\nu_{sf,1}(1 + \alpha), \tag{4.40}$$

$$D = \frac{FfM_L^2}{2}\left[(\mu_1)^2\left[\nu_{sf,2} + \left(\frac{M_L - 1}{\nu_{if,1} - 1}\right)\nu_{sf,1}(1 + \alpha)\nu_{if,2}\right]\right.$$
$$\left. + (\mu_2)\left[\frac{\nu_{sf,1}(1 + \alpha)}{M_L}\right]\right], \tag{4.41}$$

$$T = \frac{Ff^2M_L^2}{6}\left[(\mu_1^3)\left[\nu_{sf,3} + 3\left(\frac{M_L - 1}{\nu_{if,1} - 1}\right)\left[\left(\frac{M_L - 1}{\nu_{if,1} - 1}\right)\nu_{sf,1}\nu_{if,2}^2(1 + \alpha)\right.\right.\right.$$
$$\left.\left. + \frac{1}{3}\nu_{sf,1}\nu_{if,3}(1 + \alpha) + \nu_{sf,2}\nu_{if,2}\right]\right]$$
$$\left. + (\mu_1\mu_2)\left(\frac{3}{M_L}\right)\left[\nu_{sf,2} + \left(\frac{M_L - 1}{\nu_{if,1} - 1}\right)\nu_{sf,1}\nu_{if,2}(1 + \alpha)\right] + (\mu_3)\left[\frac{\nu_{sf,1}(1 + \alpha)}{M_L^2}\right]\right] \tag{4.42}$$

4.4.3 Solutions to the Point Kinetics Equations

The S, D, and T expressions in Eqs. (4.40), (4.41), (4.42) can then be directly related to the measured S, D, and T rates described in Eqs. (4.14), (4.15), and (4.16) to analytically solve for the three unknown SNM properties, F, α, and M_L.

Solving the system of equations formed by Eqs. (4.40), (4.41), (4.42) through variable substitution provides the solutions for F, α, and M_L. Eliminating F and α gives a cubic expression for the value of M_L in the form of

$$a + bM_L + cM_L^2 + M_L^3 = 0, \tag{4.43}$$

with coefficients

$$a = \frac{6\nu_{sf,2}\left(\nu_{if,1}-1\right)\left[S\left(\frac{\mu_1\mu_3}{6}-\frac{\mu_2^2}{2}\right)+D\left(\frac{\mu_1\mu_2}{f}\right)-T\left(\frac{\mu_1^2}{f^2}\right)\right]}{S\left(\nu_{sf,2}\nu_{if,3}-\nu sf,3\nu_{if,2}\right)\mu_1^4}, \tag{4.44}$$

$$b = \frac{2\left(S\left(\frac{\mu_2}{2}\right)-D\left(\frac{\mu_1}{f}\right)\right)\left(3\nu_{sf,2}\nu_{if,2}-\nu_{sf,3}\left(\nu_{if,1}-1\right)\right)}{S\left(\nu_{sf,2}\nu_{if,3}-\nu sf,3\nu_{if,2}\right)\mu_1^2}, \tag{4.45}$$

and

$$c = \frac{-6\nu_{sf,2}\nu_{if,2}\left(S\left(\frac{\mu_2}{2}\right)-D\left(\frac{\mu_1}{f}\right)\right)}{S\left(\nu_{sf,2}\nu_{if,3}-\nu_{sf,3}\nu_{if,2}\mu_1^2\right)}-1. \tag{4.46}$$

The solution for F is then written in terms of M_L, where M_L is obtained from solving the single positive and noncomplex solution to Eq. (4.43). F is solved using

$$F = \frac{\frac{2D}{\mu_1 f}S\left[\frac{M_L(M_L-1)\nu_{if,2}}{\nu_{if,1}-1}+\frac{\mu_2}{\mu_1^2}\right]}{\mu_1 M_L^2 \nu_{sf,2}}, \qquad \left[\frac{fiss}{s}\right]. \tag{4.47}$$

Lastly, the solution to α is given by

$$\alpha = \frac{S}{FM_L\nu_{sf,1}\mu_1}-1. \tag{4.48}$$

The ^{240}Pu$_{\text{eff}}$ mass can be estimated using

$$m_{240Pu_{eff}} = \frac{F}{A}, \quad A = 473\frac{fiss}{s\cdot g}. \tag{4.49}$$

CHAPTER V

Passive Non Destructive Assay of Pu-metal Plates for Fissile Mass Estimation

This chapter summarizes the results from an experimental campaign at the Zero Power Physics Reactor (ZPPR) at Idaho National Laboratory using an FNMC system consisting of eight 7.62 Ø cm x 7.62 EJ-309 liquid organic and eight 5.08 Ø cm x 5.08 cm *trans*-stilbene scintillators. Passive neutron multiplicity measurement were performed on two series of plutonium metal plate assemblies to measure the neutron multiplets and demonstrate the use of an FNMC for NDA of SNM. Portions of the results shown in this section are taken from my co-authored journal article titled "Fast neutron multiplicity counter for the assay of plutonium metal plates" published in *Nuclear Instruments and Methods in Physics Research Section A*[70].

5.1   Introduction and Motivation

MCA for nuclear safeguards applications often requires NDA of Pu-bearing SNM to verify the declared amount of fissile material [13, 17, 71]. NDA of Pu-bearing SNM can be implemented in a passive setting without the need of an external interrogation source; the passive *sf* neutron emission from the even isotopes of plutonium (primarily ^{240}Pu) is high enough such that the *sf* neutrons acts as a self-interrogation source to induce fissions on

^{239}Pu. The benefits of utilizing a FNMC system to perform NDA (compared to that of the traditional capture-based NMC systems) is the use of much shorter time gates (orders of ns), which leads to improved measurement precision for fixed acquisition times [43]. We developed an FNMC system that utilizes two different types of organic scintillators to measure the neutron multiplicity rates from Pu-metal assemblies. The measured neutron multiplicity count rates were used to perform NDA to estimate the ^{240}Pu$_{\text{eff}}$ mass with a one-, two-, and three-parameter assay technique.

5.2 Experimental Setup at Idaho National Laboratory

The FNMC system was used at the Zero Power Physics Reactor (ZPPR), Idaho National Laboratory (INL), to passively assay two sets of plutonium metal assemblies exhibiting the same total plutonium mass of approximately 100 g, but varying isotopic compositions thus exhibiting different multiplicative properties. The section describes the details of the FNMC system and the measured Pu-metal assemblies.

5.2.1 Description of Passive-Mode Fast-Neutron Multiplicity Counting System

The FNMC system consisted of 16 organic scintillators of two different types; eight 7.62 x 7.62 Ø cm EJ-309 liquid organic and eight 5.08 x 5.08 Ø cm *trans*-stilbene scintillators. The detectors were placed in a cylindrical array creating a sample cavity with a diameter of approximately 45 cm. The EJ-309 and *trans*-stilbene, hereafter referred to as EJ and SB, were arranged in an alternating "checkerboard" pattern where detectors of the same type were never adjacent to one another. Lead shielding (1.2 cm thickness) was placed in front of all detectors to mitigate the high photon flux, primarily from the decay photons of ^{241}Am. An aluminum sample holder was used to position the Pu-metal assemblies. Figure 5.1 is an image of the experimental setup [70].

Full waveforms from each detected signal from all detectors were digitized using a CAEN V1730 waveform digitizer (500 MHz sampling rate, 14-bit resolution, 2 V dynamic range, 16
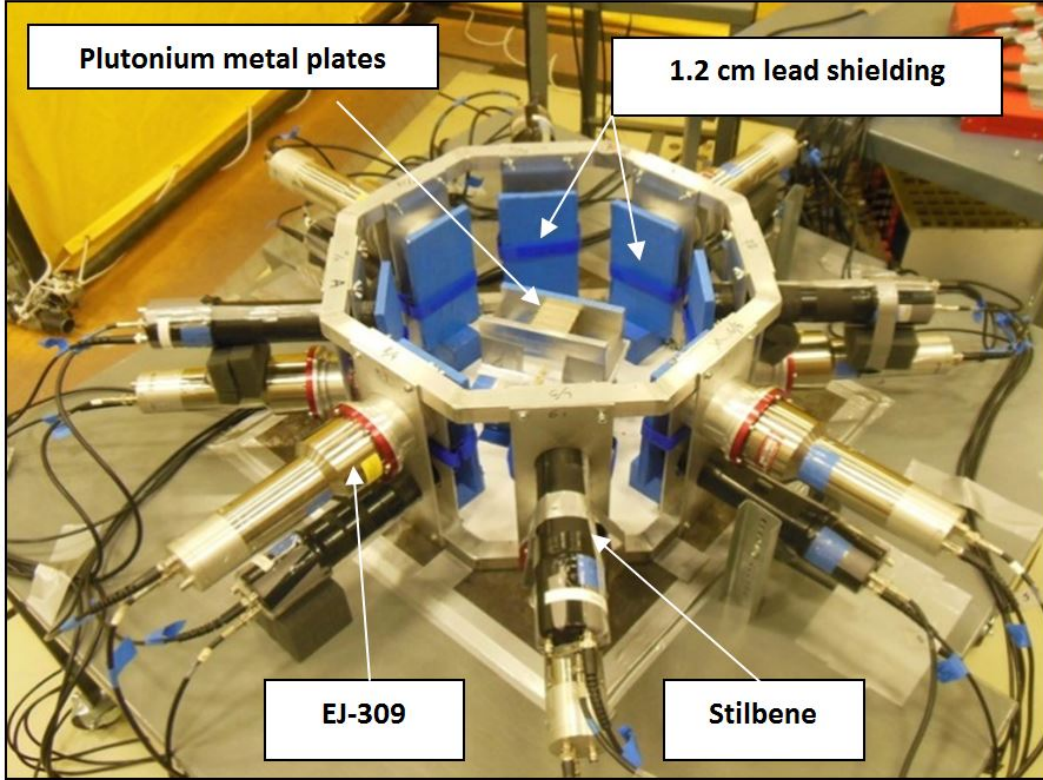
Figure 5.1: An image of the experimental setup showing the FNMC system with EJ and SB detectors surrounding an assembly of Pu-metal plates. Lead shielding (1.2 cm) was placed in front of all detectors to mitigate the high photon flux.

channels). The acquired digitized waveforms were transferred to a data acquisition system using an optical link achieving 60 MBps data rate corresponding to approximately 140,000 waveforms per second with negligible losses. Standard pulse-cleaning techniques were implemented in post-processing, where waveforms that exhibited pile-up events or that exceeded the dynamic range were removed from the analysis. Four quantities were extracted for all remaining waveforms that included the pulse height, pulse total-integral, pulse tail-integral, and the pulse timestamp. The pulse tail- and total-integrals are used to implement PSD to discriminate between neutron and photon events. The pulse height quantifies the proportional light produced from neutron and photon detections, and is used to infer the amount of energy deposited. Lastly, the pulse timestamp is used to implement TCA to extract the neutron multiplicity count rates. The integration windows for extracting the pulse tail- and total-integral were optimized based on PSD performance of the EJ and SB detectors. The

tail-integral start time was optimized to be 24 ns past the peak of all waveforms. Figure 5.2 shows a direct comparison of the PSD performance of the EJ and SB detectors demonstrating that the SB detectors offer better particle discrimination capability [70].
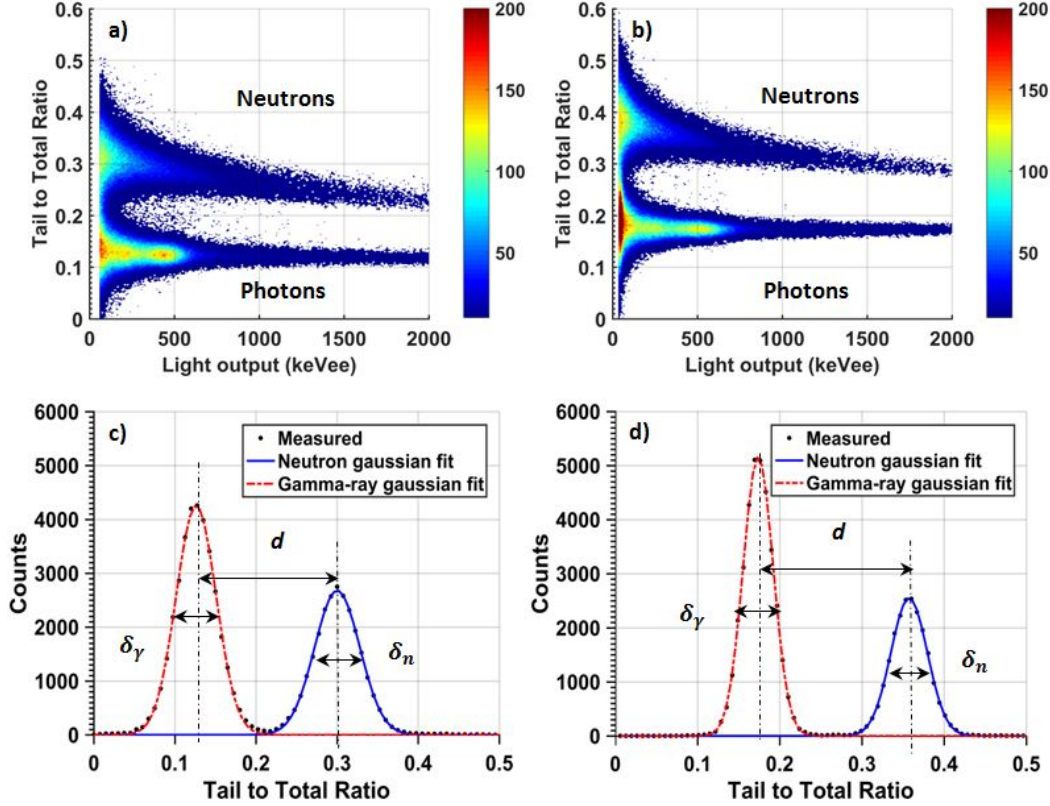
Figure 5.2: PSD analysis for an EJ-309 (a) and a stilbene detector (b). PSD plots correspond to detector irradiation with one of the plutonium metal samples. Count distribution as a function of the tail to total ratio for 0.1-0.2 MeVee light output, for EJ-309 (c) and stilbene (d).

The low-energy detection threshold were set based on the PSD capability of each detector type. Since the PSD performance degrades for signals with lower pulse heights, the threshold was set such that the gamma-ray misclassification rate (i.e., gamma rays classified as neutrons) was approximately on the order of 10^{-5} per incident particle. This resulted in a low-energy detection threshold of 0.050 and 0.035 MeVee for the EJ and SB detectors (in terms of the PHA light output function), respectively. This corresponds to an observable neutron-equivalent energy range of approximately 0.52-5.53 MeV for the EJ detectors and

0.36-6.50 MeV for the SB detectors considering the 2V dynamic range. All signals that were classified as neutron events were then combined into a single time-sorted series to produce the neutron pulse train.

5.2.2 Description of Pu-Metal Plates

Pu-metal plates of two different isotopic compositions were used to configure assemblies ranging from a 1-plate configuration to a 19-plate configuration, in increments of two. Originally designed as fuel plates for operating the ZPPR, both types of plates had similar geometries and encapsulations. The external dimensions of a single plate are 7.62 cm x 5.08 cm, with a thickness of 0.3175 cm. The plutonium metal core is encapsulated in a thin 304 L stainless steel cladding. Based on the fuel element geometry description outlined in [72], the core density was estimated to be 15.08 g/cm^3 and 15.09 g/cm^3 for the PAHN and PANN plates, respectively. The total neutron emission rates from a single PAHN and PANN plate are 1.17 x 10^4 and 2.20 x 10^3 per second, respectively [70]. Table 5.1 shows the isotopic composition (aged to the date of the experiment) for both types of Pu-metal plates, as well as the ^{240}Pu$_{\text{eff}}$ mass calculated using Eq. (2.4) [70].

Table 5.1: Isotopic composition of a single PAHN and PANN Pu-metal plate aged to August, 2015. Isotope mass uncertainty was calculated taking into account the known uncertainty in the half-life of each isotope and the aging time [70].

	PAHN mass [g]	PANN mass [g]
^{238}Pu	0.00020(7)	0.00023(6)
^{239}Pu	79.69(2)	98.89(2)
^{240}Pu	23.92(1)	4.70(1)
^{241}Pu	0.65(1)	0.04(1)
^{242}Pu	0.67(1)	<0.009
^{241}Am	1.87(1)	0.23(1)
Al	1.25	1.16
Total plutonium	106.79	103.87
^{240}Pu$_{\text{eff}}$ mass	24.97	4.71

Table 5.2 shows the ^{240}Pu$_{\text{eff}}$ mass for all measured configurations. The total ^{240}Pu$_{\text{eff}}$ mass for the full data set ranged from 4.72 to 474.56 g

Table 5.2: The total $^{240}\text{Pu}_{\text{eff}}$ mass for all measured PAHN and PANN plate configurations. The total $^{240}\text{Pu}_{\text{eff}}$ mass for the full data set ranged from 4.72 to 474.56 g

Number of Plates	PAHN Total $^{240}\text{Pu}_{\text{eff}}$ mass [g]	PANN Total $^{240}\text{Pu}_{\text{eff}}$ mass [g]
1	24.98	4.72
3	74.93	14.16
5	124.88	23.60
7	174.84	33.04
9	224.79	42.48
11	274.75	51.92
13	324.70	61.36
15	374.65	70.80
17	424.61	80.24
19	474.56	89.68

5.3 Data Analysis

The neutron S, D, and T count rates were extracted using TCA on the detected neutron pulse train according to the method described in Chapter IV with a time gate-width, T_G, of 100 ns. Using the extracted S, D, and T, three different methods of NDA were implemented to estimate the total $^{240}\text{Pu}_{\text{eff}}$ mass.

The first two methods involve a one- and two-parameter assay of the Pu-metal assemblies and are predicated on the standard approach of using mass-calibration curves. The mass-calibration curve approach involves measuring neutron multiplicity rates of several standardized calibration reference samples, where the $^{240}\text{Pu}_{\text{eff}}$ mass is known a priori, in order to create a curve that relates the observed multiplicity count rate to the $^{240}\text{Pu}_{\text{eff}}$ mass. A calibration function is then fit through the calibration data and extrapolated for the full $^{240}\text{Pu}_{\text{eff}}$ mass range of interest. Once the mass-calibration function is established, the multiplicity count rates of unknown samples are then measured using the same experimental setup, where the $^{240}\text{Pu}_{\text{eff}}$ mass can be estimated through the inversion of the mass-calibration function.

Most often, the neutron doubles rate, D, is used as the comparative metric for the mass-calibration curve. This is due to the fact that the S rate can be influenced by nonfission

neutron emissions (Pu-bearing items can have the same $^{240}\text{Pu}_\text{eff}$ mass but vastly different contributions from nonfission neutron emissions based on the elemental composition and form factor), where as the D rate is more directly related to the fissions (i.e., $^{240}\text{Pu}_\text{eff}$ mass) as fission reactions can emit more than one neutron per reaction. This approach (canonically referred to as neutron coincidence counting) is typically the most common form of passive NDA on Pu-bearing items as it offers a relatively fast procedure for verifying mass declarations; however, this approach has practical limitations. One limiting factor is that it requires prior calibration measurements, which necessitates the availability of well known reference samples. Secondly, this approach is vulnerable to biases from the geometry and form factor of the materials and thus any differences in the shape and composition between the reference samples and the unknown samples may lead to inaccuracies, primarily due to the difference in the multiplicative properties [13, 17, 71].

To demonstrate the FNMC system capability for perform NDA using the mass-calibration curve approach, a subset of the measured PAHN and PANN configurations were used as "calibration" reference samples. Specifically, the 3-plate, 9-plate, and 15-plate configurations for both types of Pu-metal plates were used to produce the mass-calibration curves, and the $^{240}\text{Pu}_\text{eff}$ mass was estimated for the remaining configurations.

It is possible to use the measured S, D, and T rates to analytically estimate the $^{240}\text{Pu}_\text{eff}$ mass if the SNM sample and FNMC system satisfies the set of PKE assumptions outlined in Section 2.4. The benefit of this technique is that there is no need for any prior calibration measurements assuming that the system efficiency (or efficiencies with neutron cross-talk corrections) is well known. The data from the 1-, 3-, 5- and 7-plate PANN configurations is used to provide proof of concept for analytically estimating the $^{240}\text{Pu}_\text{eff}$ mass with neutron cross-talk corrections.

5.3.1 One- and Two-parameter Mass-Calibration Curves

The one-parameter assay technique uses the measured D rate as the quantitative metric for the mass-calibration curve and is analogous to the traditional neutron coincidence counting technique. Recalling the PKE for the detected neutron multiplicity distributions outlined in Chapter IV, the detected D rate has a linear dependence (O^1) with the *sf* rate, Q_{sf}, and a nonlinear dependence (O^2) with the leakage multiplication, M_L. That is, the detected D rate scales as $D \propto Q_{sf}$ and $D \propto M_L^2$. Considering these dependencies, the mass-calibration function used to fit the mass-calibration curve using the measured D rate has the form

$$D = a \cdot {}^{240}Pu_{eff}^2 + b \cdot {}^{240}Pu_{eff}, \tag{5.1}$$

where a and b are fit parameters. A least-squares fitting algorithm was used to estimate the fit parameters, where their associated variances, σ_a and σ_b, are also estimated. The $^{240}\text{Pu}_{\text{eff}}$ mass of the remaining configurations (i.e., the unknown samples) can then be estimated by inverting Eq. (5.1) and has the form

$$^{240}Pu_{eff} = \frac{\left(\sqrt{4aD + b^2} - b\right)}{2a}. \tag{5.2}$$

The associated uncertainty of the estimated mass is also calculated by considering both the statistical uncertainty of the measured D rates and the uncertainty in the fit parameters of a and b. The total uncertainty, u, for the estimated $^{240}\text{Pu}_{\text{eff}}$ mass is calculated using

$$\begin{aligned}
u^2 &= \left(\frac{\partial^{240}Pu_{eff}}{\partial D}\right)^2 \sigma_D^2 + \left(\frac{\partial^{240}Pu_{eff}}{\partial a}\right)^2 \sigma_a^2 + \left(\frac{\partial^{240}Pu_{eff}}{\partial b}\right)^2 \sigma_b^2 \\
&\quad + 2\left(\frac{\partial^{240}Pu_{eff}}{\partial a}\right)\left(\frac{\partial^{240}Pu_{eff}}{\partial b}\right)\sigma_{ab},
\end{aligned} \tag{5.3}$$

where σ_{ab} is the covariance between the fit parameters, a and b.

The two-parameter assay technique utilizes both the measured S and D rates, and aims to reconcile the difference in the multiplicative properties of the PAHN and PANN plates

(due to the difference in the isotopic composition). Again, recalling the PKE for the detected S rate outlined in Chapter IV, we see that the S rate is linearly proportional to both Q_{sf} and M_L. Therefore, the ratio of the measured D to the S rates provides a quantitative metric that linearly proportional to M_L. Noting that the ratio of the measured D to the $^{240}\text{Pu}_{\text{eff}}$ mass is also linearly proportional to M_L, we use the mass-calibration function of the form

$$\frac{D}{S} = c \cdot \frac{D}{^{240}Pu_{eff}} + d, \tag{5.4}$$

where c and d are fit parameters. Equation (5.4) relates the measured S and D to the $^{240}\text{Pu}_{\text{eff}}$ mass that is linearly dependent on M_L. For a series of samples that exhibit equal contributions from nonfission neutron emissions (assumed to be negligible for the PAHN and PANN plates), a single calibration function of the form shown in Eq. (5.4) can be used for both PAHN and PANN configurations. Once the mass-calibration function was established, the $^{240}\text{Pu}_{\text{eff}}$ mass was calculated using

$$^{240}Pu_{eff} = \frac{c \cdot D}{\left(\frac{D}{S} - d\right)}. \tag{5.5}$$

The uncertainty in the estimated $^{240}\text{Pu}_{\text{eff}}$ mass, u, was propagated similarly to the one-parameter assay technique, and has the form

$$
\begin{aligned}
u^2 &= \left(\frac{\partial^{240}Pu_{eff}}{\partial D}\right)^2 \sigma_D^2 + \left(\frac{\partial^{240}Pu_{eff}}{\partial S}\right)^2 \sigma_S^2 \\
&+ \left(\frac{\partial^{240}Pu_{eff}}{\partial c}\right)^2 \sigma_c^2 + \left(\frac{\partial^{240}Pu_{eff}}{\partial d}\right)^2 \sigma_d^2 \\
&+ 2\left(\frac{\partial^{240}Pu_{eff}}{\partial c}\right)\left(\frac{\partial^{240}Pu_{eff}}{\partial d}\right) \sigma_{cd},
\end{aligned} \tag{5.6}
$$

where σ_c and σ_d are the uncertainty in the fit parameters c and d, and σ_{cd} is the covariance between c and d.

5.3.2 Analytic Fissile Mass Estimation with Three Parameters

The three-parameter assay utilizes all three measured S, D, and T rates to analytically estimate the sample fissile mass. A subset of the PANN data set (the 1-plate and 3-plate configurations) are used to demonstrate the reliability of using the FNMC PKE with neutron cross-talk corrections outlined in Section 4.4. The neutron detection efficiencies, ϵ_j, where j denotes the number of times the neutron was detected in the system previously, were estimated using MCNPX-PoliMi simulations of a singly-emitting neutron source with the ^{240}Pu sf Watt energy spectrum. Figure 5.3 shows the MCNPX-PoliMi simulation model of the FNMC system. The simulated efficiencies were 4.27 % for ϵ_0 and 0.53 % for ϵ_1. Considering
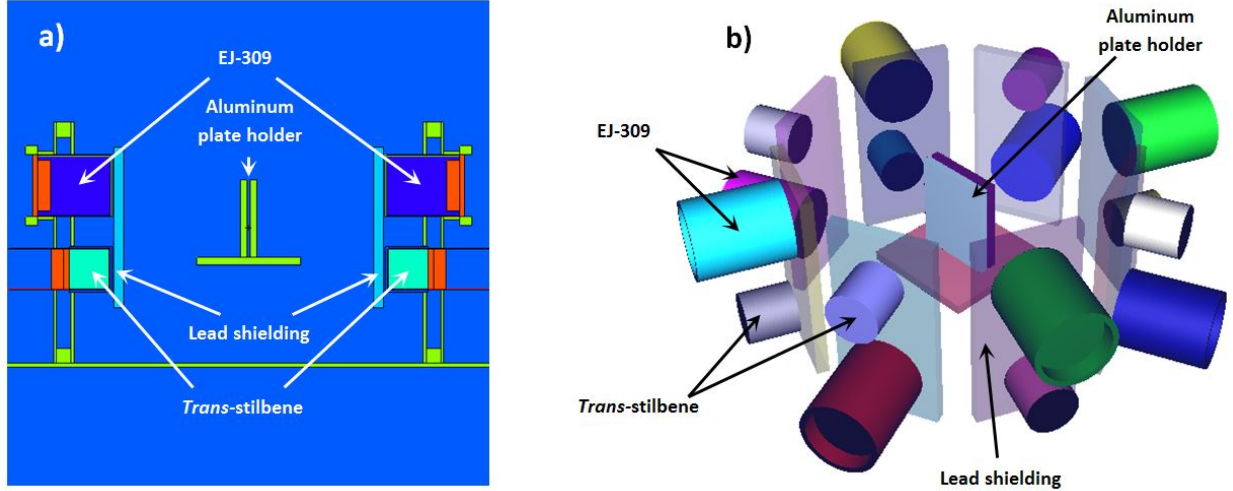
Figure 5.3: MCNPX-PoliMi simulation model of the FNMC system from a side view (a) and a 3D view (b). A singly-emitting neutron source with ^{240}Pu Watt energy spectrum is placed in the center of the system to calculate the neutron detection efficiencies.

the detection thresholds applied in this experiment, the FNMC PKE for neutron cross-talk events up to order $N = 2$ was adequate to yield accurate results where the assumption in Eq. (4.34) holds. Using Eq. (4.47), the solution for Q_{sf} with $(N = 2)$ and without $(N = 1)$ neutron cross-talk corrections has the form

$$Q_{sf_{N=1}} = \frac{\frac{2D}{\epsilon_0 f} - S \left[\frac{M_L(M_L-1)\nu_{if,2}}{\nu_{if,1}-1} \right]}{\epsilon_0 M_L^2 \nu_{sf,2}}, \tag{5.7}$$

and

$$Q_{sf_{N=2}} = \frac{\frac{2D}{(\epsilon_0 + \epsilon_0 \epsilon_1)f} - S\left[\frac{M_L(M_L-1)\nu_{if,2}}{\nu_{if,1}-1} + \frac{2\epsilon_0 \epsilon_1}{(\epsilon_0 + \epsilon_0 \epsilon_1)^2}\right]}{(\epsilon_0 + \epsilon_0 \epsilon_1) M_L^2 \nu_{sf,2}}, \tag{5.8}$$

respectively. Once the Q_{sf} is estimated using Eqs. (5.7) and (5.8), Eq. (4.49) is used to estimated the ^{240}Pu$_{\text{eff}}$ mass. Table 5.3 shows the measured S, D, and T for the 1-plate and 3-plate PANN configurations.

Table 5.3: Measured S, D, and T rates for the 1-plate and 3-plate PANN configurations used to analytically estimate the ^{240}Pu$_{\text{eff}}$ mass, 30-min acquisition time

Number of plates	Pu mass [g]	S [cps]	D [cps]	T [cps]
1	4.72	428.5 ± 0.5	11.63 ± 0.08	0.373 ± 0.014
3	14.16	1349.3 ± 1.2	46.60 ± 0.16	2.057 ± 0.034
5	23.60	2745.2 ± 1.9	136.26 ± 0.42	9.178 ± 0.109
7	33.04	3861.2 ± 2.2	212.29 ± 0.52	17.018 ± 0.148

5.4 Results

5.4.1 Fissile Mass Estimation with Mass-Calibration Curves

Figure 5.4 and 5.5 shows the one-parameter mass-calibration curve (from the reference assemblies) and the validation of the mass-calibration curve using the remaining unknown assemblies for PAHN and PANN, respectively.

Figures 5.4 and 5.5 demonstrate that the mass-calibration function used for the one-parameter assay is in good agreement to the measured D as shown by the comparison of the actual versus estimated ^{240}Pu$_{\text{eff}}$ masses. Table 5.4 and 5.5 summarize the results for the estimated ^{240}Pu$_{\text{eff}}$ mass using a one-parameter assay approach for the PAHN and PANN assemblies.

The relative difference between the actual and estimated ^{240}Pu$_{\text{eff}}$ mass for both PAHN and PANN assemblies were within ± 4 % considering the uncertainties. It is important to recognize that the one-parameter mass-calibration function used for the PANN assemblies is
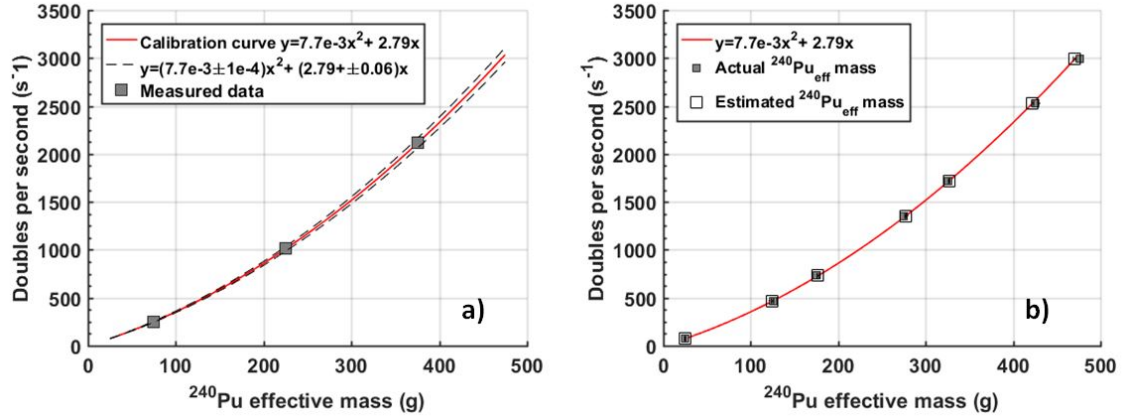
Figure 5.4: One-parameter assay mass-calibration curve (a) from the reference assemblies (3-, 9-, and 15-plate configurations) and the validation of the calibration using the remaining unknown assemblies (b). Both figures are the for PAHN assemblies.
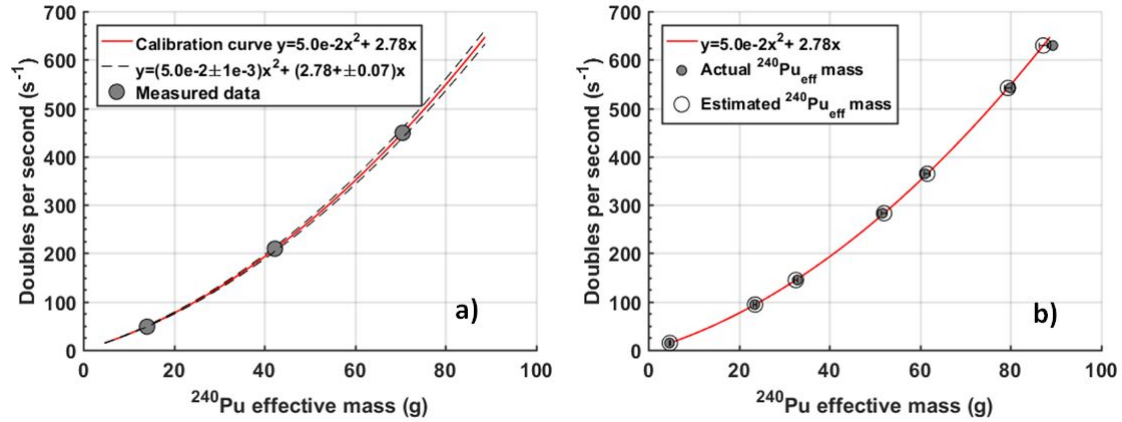
Figure 5.5: One-parameter assay mass-calibration curve (a) from the reference assemblies (3-, 9-, and 15-plate configurations) and the validation of the calibration using the remaining unknown assemblies (b). Both figures are the for PANN assemblies.

not directly applicable to any of the PAHN assemblies, and vice versa. In other words, two separate mass-calibration functions had to be used to estimate the $^{240}Pu_{eff}$ mass of the two different types of plate configurations.

To reconcile the differences in the isotopic composition of the PAHN and PANN assemblies, we use the two-parameter mass-calibration function shown in Eq. (5.4). For the two-parameter assay approach, only the PANN reference assemblies were used to fit the mass-calibration curve, and all remaining PANN and all PAHN assemblies were then assayed. Figure 5.6 shows the two-parameter mass-calibration curve (from the PANN refer-

Table 5.4: Summary of the estimated ^{240}Pu$_{eff}$ mass for the PAHN assemblies for the one-parameter assay approach

Number of Plates	Actual ^{240}Pu$_{eff}$ mass [g]	Estimated ^{240}Pu$_{eff}$ mass [g]	Relative Difference [%]
1	24.98	24.92 ± 0.49	**0.23 ± 1.97**
5	124.88	124.98 ± 1.13	**-0.08 ± 0.91**
7	174.84	177.10 ± 1.08	**-1.29 ± 0.62**
11	274.75	276.99 ± 0.74	**-0.82 ± 0.27**
13	324.70	326.75 ± 0.66	**-0.63 ± 0.20**
17	424.61	422.30 ± 1.09	**0.54 ± 0.26**
19	474.56	470.53 ± 1.49	**0.85 ± 0.31**

Table 5.5: Summary of the estimated ^{240}Pu$_{eff}$ mass for the PANN assemblies using a one-parameter assay

Number of Plates	Actual ^{240}Pu$_{eff}$ mass [g]	Estimated ^{240}Pu$_{eff}$ mass [g]	Relative Difference [%]
1	4.72	4.78 ± 0.10	**-1.27 ± 2.12**
5	23.60	23.43 ± 0.24	**0.72 ± 1.02**
7	33.04	32.45 ± 0.22	**1.78 ± 0.67**
11	51.92	51.48 ± 0.16	**0.84 ± 0.31**
13	61.36	61.46 ± 0.15	**-0.17 ± 0.25**
17	80.24	80.25 ± 0.21	**-0.02 ± 0.26**
19	89.68	88.79 ± 0.26	**0.99 ± 0.29**

ence assemblies) and the validation of the mass-calibration curve using the remaining PANN assemblies and all PAHN assemblies.
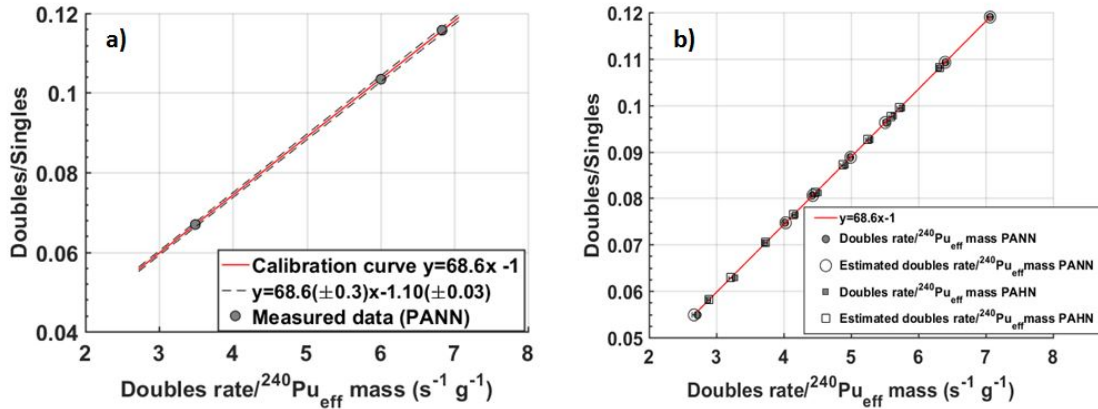
Figure 5.6: Two-parameter assay mass-calibration curve (a) from the PANN reference assemblies (3-, 13-, and 17-plate configurations), and the validation of the calibration using the remaining PANN and all PAHN assemblies (b).

Figure 5.6 demonstrates that the two-parameter mass-calibration curve is linear as a function of the D per ^{240}Pu$_{\text{eff}}$ mass, which verifies the semi-empirical mass-calibration function described in Eq. (5.4). Ultimately, this two-parameter mass-calibration function can be used to assay both PAHN and PANN assemblies, rendering it unnecessary to have mass-calibration functions specific to the isotopic composition (given similar nonfission neutron contributions, assumed to be negligible in these assemblies). Table 5.6 summarize the results for the estimated ^{240}Pu$_{\text{eff}}$ mass using a two-parameter assay approach for the remaining PANN and all PAHN assemblies.

Table 5.6: Summary of the estimated ^{240}Pu$_{\text{eff}}$ mass for the PANN assemblies for the two-parameter assay approach

PAHN Assemblies			
Number of Plates	Actual ^{240}Pu$_{\text{eff}}$ mass [g]	Estimated ^{240}Pu$_{\text{eff}}$ mass [g]	**Relative Difference [%]**
1	24.98	24.65 ± 0.35	**1.30 ± 1.40**
3	74.93	75.89 ± 0.21	**-1.28 ± 0.28**
5	124.88	123.71 ± 0.19	**0.94 ± 0.15**
7	174.84	174.58 ± 0.17	**0.15 ± 0.10**
9	224.79	225.47 ± 0.16	**-0.30 ± 0.07**
11	274.75	274.88 ± 0.14	**-0.05 ± 0.05**
13	324.70	324.37 ± 0.13	**0.10 ± 0.04**
15	374.65	374.71 ± 0.04	**-0.01 ± 0.01**
17	424.61	424.69 ± 0.04	**-0.02 ± 0.01**
19	474.56	469.98 ± 0.04	**0.96 ± 0.01**
PANN Assemblies			
Number of Plates	Actual ^{240}Pu$_{\text{eff}}$ mass [g]	Estimated ^{240}Pu$_{\text{eff}}$ mass [g]	**Relative Difference [%]**
1	4.72	4.72 ± 0.24	**<0.001 ± 1.23**
5	23.60	23.60 ± 0.21	**<0.001 ± 0.89**
7	33.04	33.04 ± 0.19	**<0.001 ± 0.58**
9	42.31	42.31 ± 0.17	**<0.001 ± 0.24**
11	51.92	51.92 ± 0.16	**<0.001 ± 0.31**
15	70.51	70.51 ± 0.14	**<0.001 ± 0.20**
19	89.68	89.68 ± 0.13	**<0.001 ± 0.15**

Overall, the two-parameter assay approach yields more accurate and precise estimates of the ^{240}Pu$_{\text{eff}}$ mass, in addition to the fact that a single mass-calibration function was used for

both PAHN and PANN assemblies. Figure 5.7 shows the relative difference of the estimated ^{240}Pu$_{\text{eff}}$ mass for both the one-parameter and two-parameter assay approach.
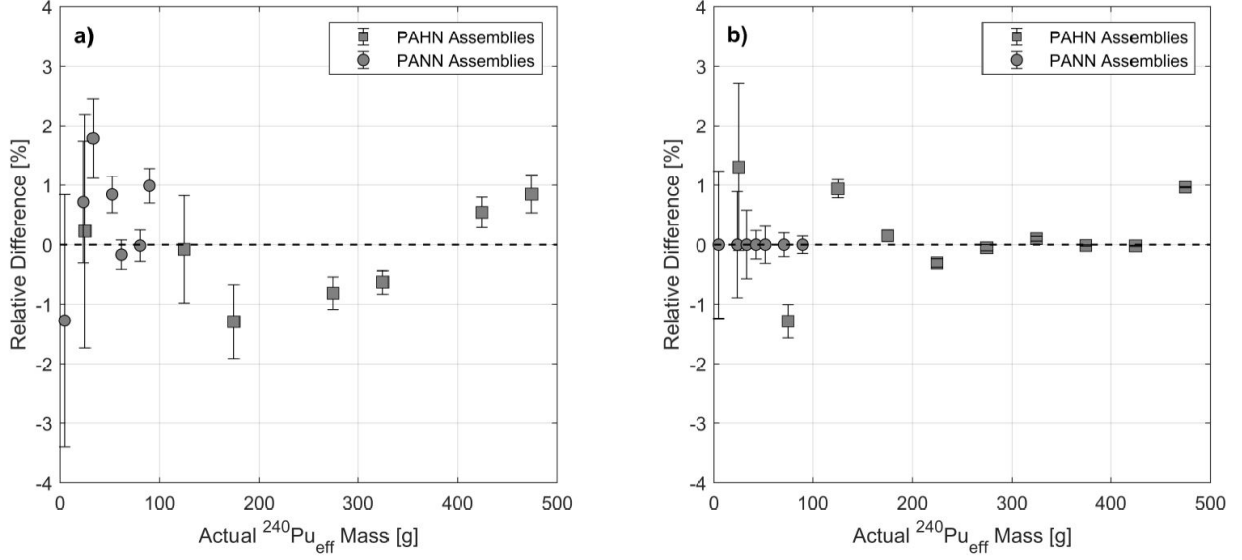
Figure 5.7: Relative difference in the estimated ^{240}Pu$_{\text{eff}}$ mass for the one-parameter assay approach (a), which requires two separate mass-calibration functions for the PAHN and PANN assemblies, and for the two-parameter assay approach (b), which only uses a single mass-calibration function.

The uncertainty in the relative difference is smaller for the two-parameter assay compared to the one-parameter assay results. This demonstrates that the linear relationship in the two-parameter mass-calibration function is less susceptible to errors in the fitted parameters. In other words, the assumption of a linear two-parameter mass-calibration function introduced in Eq. (5.4) is justified for the ^{240}Pu$_{\text{eff}}$ mass range. Furthermore, the linear two-parameter mass-calibration function is also advantageous for extrapolating to the relatively low and high ^{240}Pu$_{\text{eff}}$ mass ranges.

5.4.2 Analytic Fissile Mass Estimation with Three-Parameter Assay

The *sf* rate, Q_{sf} is estimated using the solution to the FNMC PKE without neutron cross-talk corrections, (Eq. (5.7)), and with neutron cross-talk corrections of order $N = 2$, (Eq. (5.8)). Table 5.7 summarizes the results for the anayltic estimation of the ^{240}Pu$_{\text{eff}}$ mass with and without neutron cross-talk corrections.

Table 5.7: Summary of the estimated $^{240}Pu_{eff}$ mass for a subset of the PANN assemblies using a three-parameter assay approach

No cross-talk correction, N = 1			
Number of plates	$^{240}Pu_{eff}$ mass [g]	Estimated $^{240}Pu_{eff}$ mass [g]	**Relative difference [%]**
1	4.72	5.35 ± 0.18	**13.34 ± 3.81**
3	14.16	16.97 ± 0.32	**19.84 ± 2.26**
5	23.60	33.52 ± 0.62	**42.04 ± 2.63**
7	33.04	45.42 ± 0.71	**37.47 ± 2.15**
Cross-talk correction, N = 2			
Number of plates	$^{240}Pu_{eff}$ mass [g]	Estimated $^{240}Pu_{eff}$ mass [g]	**Relative difference [%]**
1	4.72	4.51 ± 0.21	**-3.81 $\pm$ 4.45**
3	14.16	14.55 ± 0.36	**2.75 ± 2.54**
5	23.60	29.09 ± 0.67	**23.26 ± 2.84**
7	33.04	39.42 ± 0.75	**19.30 ± 2.27**

Table 5.7 shows that neutron cross-talk corrections of order $N = 2$ drastically improves the estimated $^{240}Pu_{eff}$ mass for the 1-plate and 3-plate configurations. The relative difference without neutron cross-talk corrections overestimated the mass by 13.35 and 19.84 % for the 1-plate and 3-plate PANN assemblies, however, when neutron cross-talk events of order $N = 2$ is accounted for in the PKE, we see that the estimate of the $^{240}Pu_{eff}$ mass agrees to within $\pm$ 4 % of the actual mass. Applying neutron cross-talk corrections in the case of the 5-plate and 7-plate configurations yields more accurate mass estimations relative to that without any corrections, but is overestimated regardless. The overestimation is attributed to the fact that these configurations begin to have an appreciable geometry, deviating from the assumed point-like behavior.

5.5 Conclusions

The results in this work demonstrated that an FNMC systems can perform passive NDA for estimating the fissile mass in Pu-bearing SNM materials. The results for NDA using a one-parameter mass-calibration curve showed that the FNMC system is able to used the measured

neutron doubles rate as a comparative metric for estimating the mass of unknown SNM materials given that a set of well known calibration samples are available that are similar in geometry and isotopic composition. A unique one-parameter mass-calibration curve was established for the PAHN and PANN series, and the estimated mass from the NDA resulted in an average percent deviation of $\pm$ 3 % of the actual mass. Using a two-parameter mass-calibration curve allowed for a single mass-calibration function to be used for both the PAHN and PANN series, thus not relying as heavily on the availability of well known calibration samples. The ratio of measured neutron doubles and singles rates was used as a comparative metric to produce a mass-calibration function that is linearly dependent on the multiplication (assuming constant contributions from nonfission neutrons). The two-parameter NDA results yielded mass estimates that were within $\pm$ 2 % of the actual mass. Lastly, a proof of concept for using a three-parameter assay to analytically estimate the fissile mass was also demonstrated using the FNMC PKE with consideration of neutron cross-talk effects. The clear advantage in the three-parameter assay is that it requires no calibration samples to be measured a priori to the assay (assuming the system efficiencies are well known). A subset of the PANN configurations was used to analytically estimate the fissile mass using the PKE with and without cross-talk corrections. Overall, we see that the implementing neutron cross-talk corrections improves to overall accuracy of the estimated mass. However, the three-parameter NDA results begin to overestimate due to the deviation from the PKE assumptions, highlighting the limitations of the three-parameter assay technique. Firstly, the system detection efficiencies may become geometrically dependent on the sample size and thus the nonuniform system response to neutrons emitted at different locations within the sample become non-negligible. The geometrically dependent system response could be mitigated by increasing the cavity diameter. Secondly, the organic scintillators within the FNMC system can become neutronically coupled to the sample of SNM, where neutrons can thermalize within the scintillators and reenter the sample causing thermal-neutron induced fission chains. The coupling between the scintillators and the sample can be suppressed by

placing cadmium sheets between the sample and the detectors.

CHAPTER VI

Active Non Destructive Assay of Uranium Oxide Assemblies for Mass Diversion Scenarios

This chapter summarizes the results from an experimental campaign at the Zero Power Physics Reactor (ZPPR) at Idaho National Laboratory using an FNMC system consisting of eight 7.62 Ø cm x 7.62 EJ-309 liquid organic, eight 5.08 Ø cm x 5.08 cm *trans*-stilbene scintillators, and two AmLi interrogation sources. Active neutron multiplicity measurement were performed on fuel-bundle like uranium-oxide fuel pin assemblies, where the goal was to characterize the sensitivity of an FNMC system for detecting mass-diversion scenarios. MCNPX-PoliMi simulations were also performed to directly compare the mass-diversion sensitivity of an FNMC system with the currently-deployed capture-based Uranium Neutron Collar (UNCL) for active NDA of 17 x 17 pressurized water reactor (PWR) fresh fuel assemblies.

6.1 Introduction and Motivation

Unlike plutonium, the even isotopes of uranium (mainly ^{238}U) have an extremely low activity for *sf* neutron emissions and do not provide the continuous internal source of neutrons to induce subsequent fission on ^{233}U and ^{235}U [13, 73]. Therefore, NDA for uranium bearing SNM typically requires an external interrogative source to drive *if* reactions on ^{233}U and ^{235}U

and falls in the category of active NDA techniques. Figure 6.1 shows the neutron-induced fission cross sections for ^{233}U and ^{235}U [48].
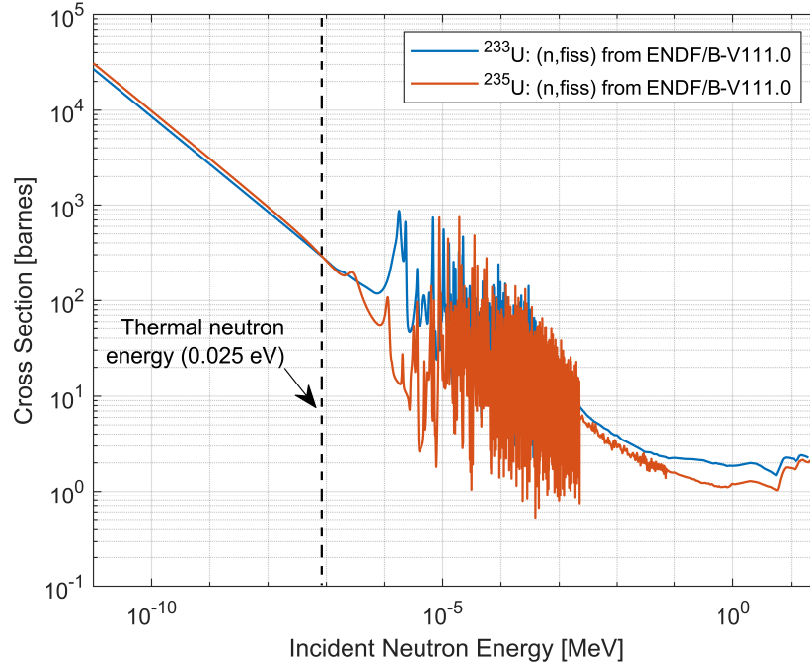
Figure 6.1: Neutron-induced fission cross sections for ^{233}U and ^{235}U.

Interrogative sources in nuclear safeguards applications are typically (α,n) neutron emitters (e.g., AmLi, PuBe, AmBe). The neutrons emitted by interrogative sources are moderated to thermal energies to capitalize on the much higher fission cross sections in the thermal region in Figure 6.1. The thermalized interrogative neutrons will enter the uranium sample and drive *if* reactions, subsequently emitting multiplets of *if* neutrons. The primary aim for active NDA is to measure the neutron doubles emitted from the *if* reactions, where similar approaches to the passive NDA techniques can then be implemented [13, 73]. The ability to perform active NDA to estimate the fissile mass in uranium-bearing SNM was demonstrated in previous works by Di Fulivio et al, using a one- and two-parameter mass-calibration curve approach [74].

An important aspect for MCA is the sensitivity of detecting diverted SNM, where the aim is to conclude whether fissile material had been diverted for misuse. Material-diversion

scenarios are of particular interest for monitoring and accounting for fresh reactor fuel bundles, where the operational burden is quite high [8]. Implementing the PKE in active NDA is much more complex compared to its passive counterpart primarily due to the complications that arise from the interrogative source, and is impractical considering the long required assay times to achieve statistically confident measured neutron triples rate [73]. Rather, active NDA typically focuses on coincidence counting methods and leverage the use of mass-calibration curves to infer the amount of fissile material.

6.2 Experiment at Idaho National Laboratory

An FNMC system consisting of 16 organic scintillators and two AmLi interrogation sources was used to perform active NDA in the context of material-diversion scenarios at the ZPPR facility at INL. The goal of this experiment was to characterize the FNMC system sensitivity for detecting a diversion scenario with fuel-bundle type geometries, and to provide confidence intervals on the diversion declaration. The study is extended with MCNPX-PoliMi simulations of a hypothetical FNMC system to investigate the sensitivity to real-world fuel assemblies. The simulated results of the FNMC system are directly compared to benchmark simulations of the currently-deployed ^{3}He capture-based system to investigate potential improvements.

6.2.1 Description of UO$_2$ Pins and Assembly

The measured uranium assemblies had different arrangements of UO$_2$ pins, each with a ^{235}U enrichment of 16.37 % and a total uranium mass of 79.52 g; Table 6.1 shows the details of single UO$_2$ pin composition and geometry.

The full assembly consisted of 32 individual UO$_2$ pins with a total uranium mass of 2544.64 g. The neutron doubles rate measured from the full assembly is then compared to the neutron doubles measured from incrementally diverted assemblies to assess when the FNMC would be able to see a statistically significant difference. An image of the measured

Table 6.1: Description of an individual UO_2 pin used for the measured uranium assemblies.

Total mass [g] (clad + fuel)	Clad mass [g]	Fuel mass [g] (U + O)	Uranium mass [g] (16.37% enriched)	Length x Diameter [mm]
102.75	12.46	90.29 (79.52 g U) (10.72 g O)	79.52 (13.02 g 235U) (65.50 g 238U)	152.4 x 9.5

assemblies is shown in Figure 6.2. Table 6.2 details the total uranium mass and the associated mass defect percentages for the assemblies shown in Figure 6.2.
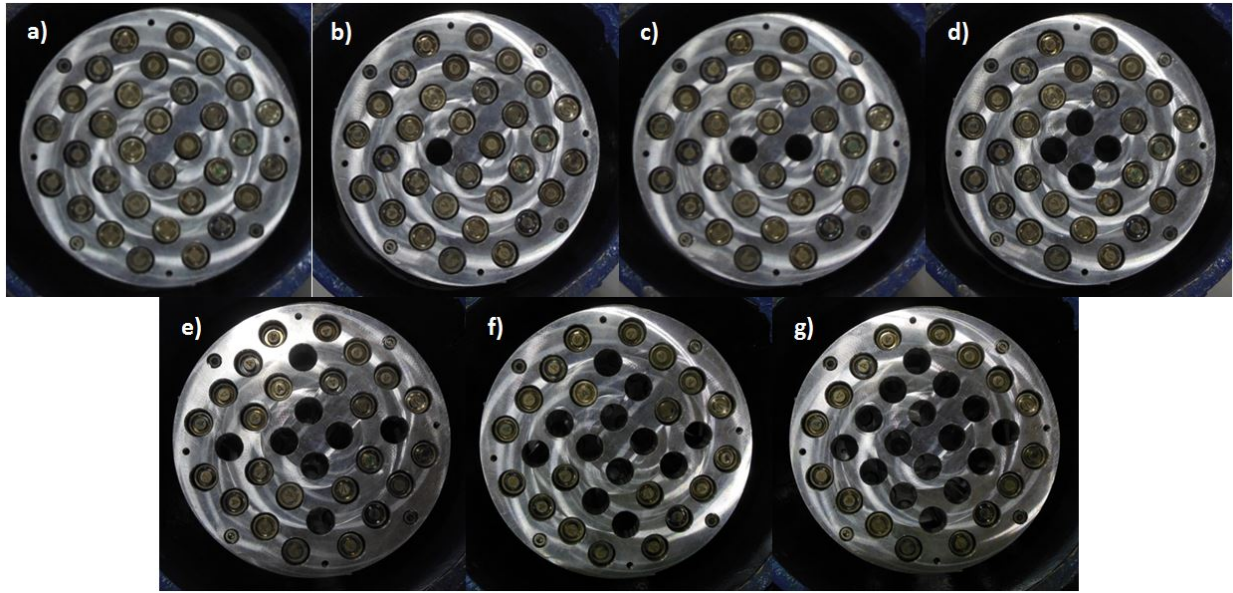
Figure 6.2: An image of the measured uranium assemblies configured in its full arrangement (a), and its diverted arrangements (b-g). The mass defect percentage for the diverted arrangements ranged from 3 % to 50 %.

Table 6.2: Description of the measured full and partially diverted uranium assemblies.

Number of UO_2 pins removed	Total uranium mass [g]	**Mass defect [%]**
0	2544.64	**0.00**
1	2465.12	**3.13**
2	2385.60	**6.25**
4	2226.56	**12.50**
8	1908.48	**25.00**
12	1590.40	**37.50**
16	1272.32	**50.00**

6.2.2 Experimental Methods and Detector Setup

The FNMC system consisted of eight 7.62 Ø cm x 7.62 cm EJ-309 liquid and eight 5.08 Ø cm x 5.08 cm *trans*-stilbene organic scintillators arranged in a cylindrical array with a sample cavity diameter of approximately 22 cm. The two different types of scintillators were placed in an alternating pattern. Figure 6.3 shows an image of the experimental setup.
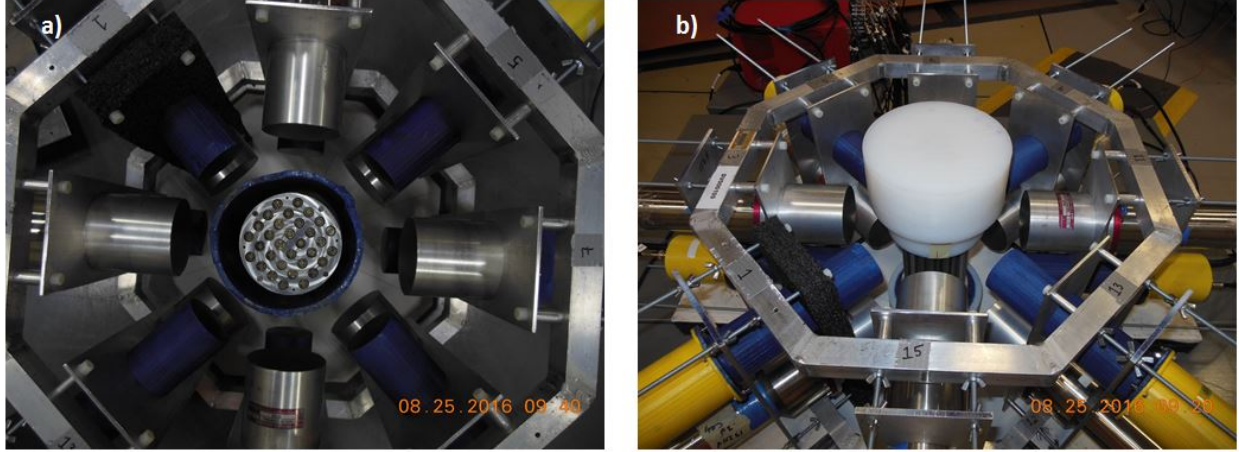
Figure 6.3: The experimental setup of the FNMC system from a top-down view (a), and during the actual assay measurement (b).

Two AmLi interrogation neutron sources (Gammatron AN-HP, ≈ 50,000 n/s) were used to drive *if* reactions in the measured uranium assemblies. The interrogation sources were embedded in a ultra-high-molecular-weight polyethylene (UHMWPE) to provide the moderation of the emitted AmLi neutrons; the interrogation sources were placed above and below the uranium assembly. Lead shielding (thickness of 6 mm) was placed around the measured assemblies to mitigate pulse pile-up effects primarily due to the relatively low-energy radioactive decay photons. Figure 6.4 shows a detailed schematic of the FNMC system geometry.

Full waveforms from all 16 detectors were digitized with a CAEN V1730 waveform digitizer (500 MHz sampling rate, 14-bit resolution, 2V dynamic range). The data was transferred to a data acquisition system using an optical data link with a transfer rate of up to 60 MBps without losses. Raw waveforms were post-processed to remove any instances of
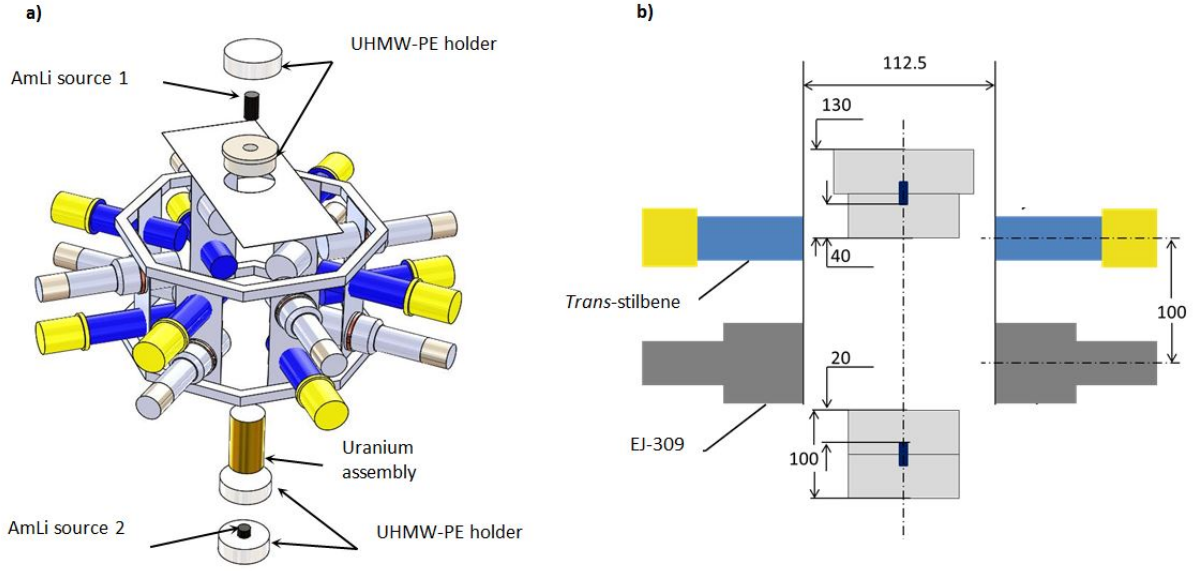
Figure 6.4: The experimental setup of the FNMC system from a top-down view (a), and during the actual assay measurement (b).

pile-up and saturated events. From the remaining well-separated waveforms, the pulse time stamp, tail-integrals, and total-integrals were extracted to perform PSD and TCA to obtain the neutron doubles rates. Figures 6.5 and 6.6 show measured tail-to-total ratios versus the light output for a representative EJ-309 and *trans*-stilbene detector, respectively.

^{137}Cs calibration measurements were performed prior to the active NDA measurements to ensure detector uniformity and provide the signal-to-light output conversions. The low-energy detection threshold were set to 0.035 MeVee (approx. 0.44 MeV neutron-equivalent) and 0.05 MeVee (approx. 0.51 MeV neutron-equivalent) for the *trans*-stilbene and EJ-309 detectors, respectively.

6.2.3 Data Analysis

The neutron doubles rate was obtained using Eq. (4.15) with a time gate width of 100 ns and a long delay of 1000 ns for three different acquisition times of 60, 180, and 300 seconds. The associated statistical uncertainty in the neutron doubles rate was calculated to provide insight on how the measurement time affects the confidence level of declaring a diverted
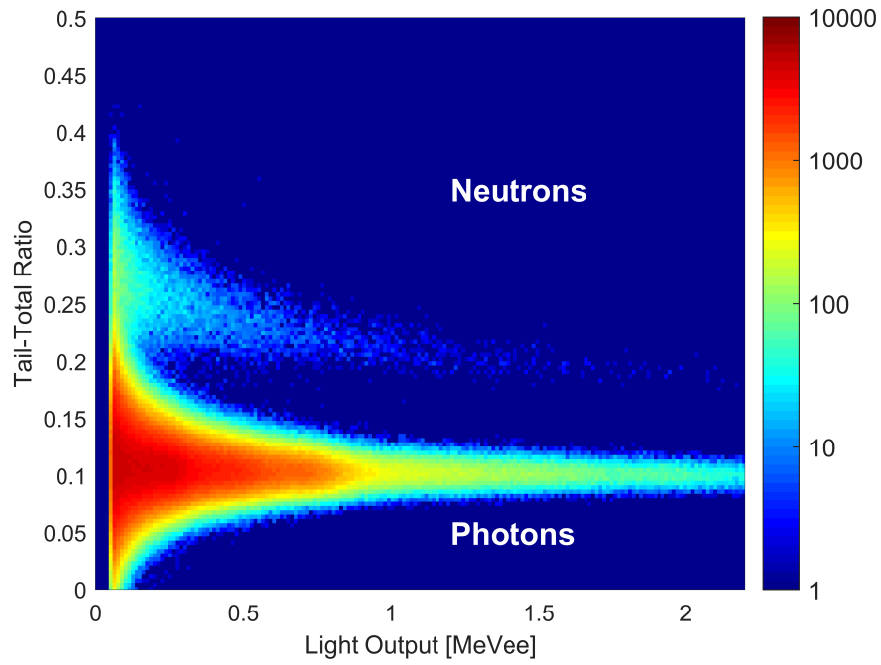
Figure 6.5: Measured tail-to-total ratio versus light output for a representative EJ-309 detector from the full assembly assay.
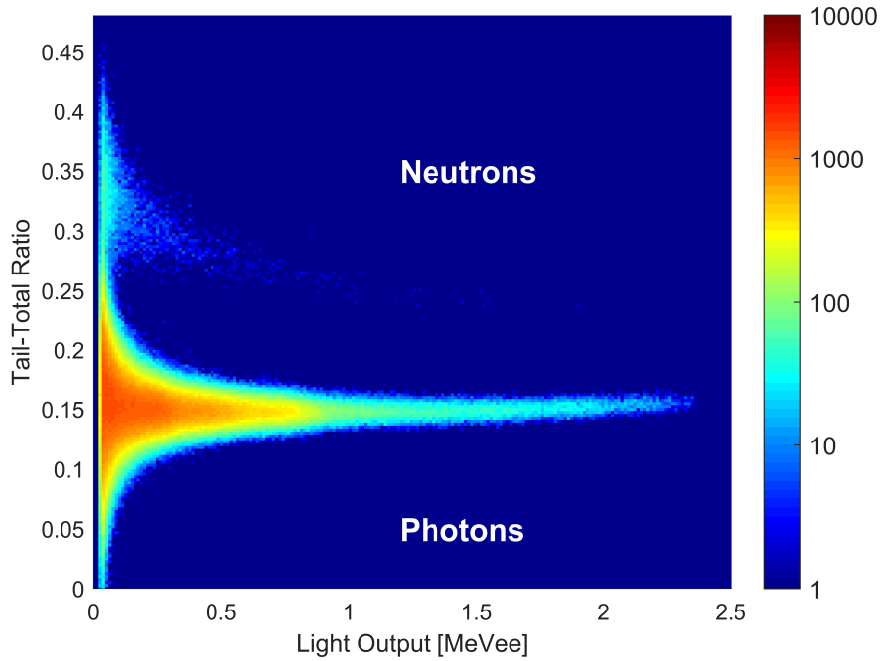
Figure 6.6: Measured tail-to-total ratio versus light output for a representative *trans*-stilbene detector from the full assembly assay.

scenario. The sensitivity of detecting a diversion scenario was characterized by comparing the neutron doubles rate from the full assembly, D_F, to the diverted assemblies, D_i, where i is the number of UO$_2$ pins removed. The relative deviation in the neutron doubles rate from the full assembly for an assembly with i pins removed, RD_i, is calculated using

$$RD_i = \frac{D_F - D_i}{D_F}, \tag{6.1}$$

and the standard deviation of RD_i assuming D_F is independent of D_i, σ_{RD_i} has the form

$$\sigma_{RD_i} = \sqrt{\left(\frac{\partial RD_i}{\partial D_F}\right)^2 \sigma_{D_F}^2 + \left(\frac{\partial RD_i}{\partial D_i}\right)^2 \sigma_{D_i}^2}, \tag{6.2}$$

where σ_{D_F} and σ_{D_i} are the uncertainty in D_F and D_i. The calculated σ_{RD_i} can then be used to provide confidence intervals. The significance of the observed relative deviation is calculated using

$$\#\sigma_i = \frac{RD_i}{\sigma_{RD_i}}. \tag{6.3}$$

Using the two-sided hypothesis testing, the confidence intervals (CI) are attributed as

$$
\begin{aligned}
\#\sigma_i &\geq 1, & CI &> 68\% \\
\#\sigma_i &\geq 2, & CI &> 95\% \\
\#\sigma_i &\geq 3, & CI &> 99\%.
\end{aligned}
\tag{6.4}
$$

6.3   Experimental Results: Fissile Mass Diversion Sensitivity

Figures 6.7, 6.8, and 6.9 shows the relative deviation in the neutron doubles rate from the full assembly for all measured diversion scenarios for assay times of 60, 180, and 300 seconds, respectively. A summary of the results is shown in Tables 6.3.

The results from this study demonstrate that longer assay times yield a higher sensitivity and confidence in declaring that fissile mass has been removed from the full assembly. This

109
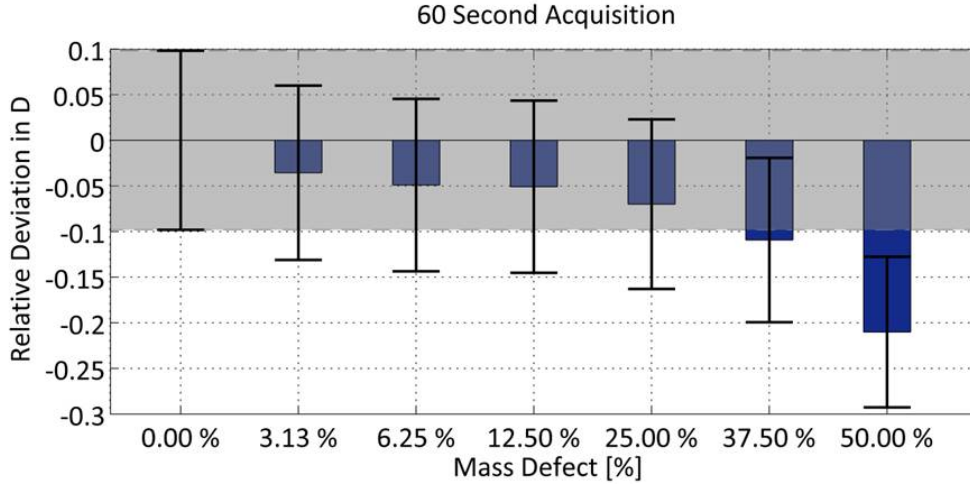
Figure 6.7: Relative deviation in the neutron doubles rate from the full assembly for a 60 second assay time showing that the FNMC system is only sensitive to a 50.00 % mass defect with > 95 % confidence
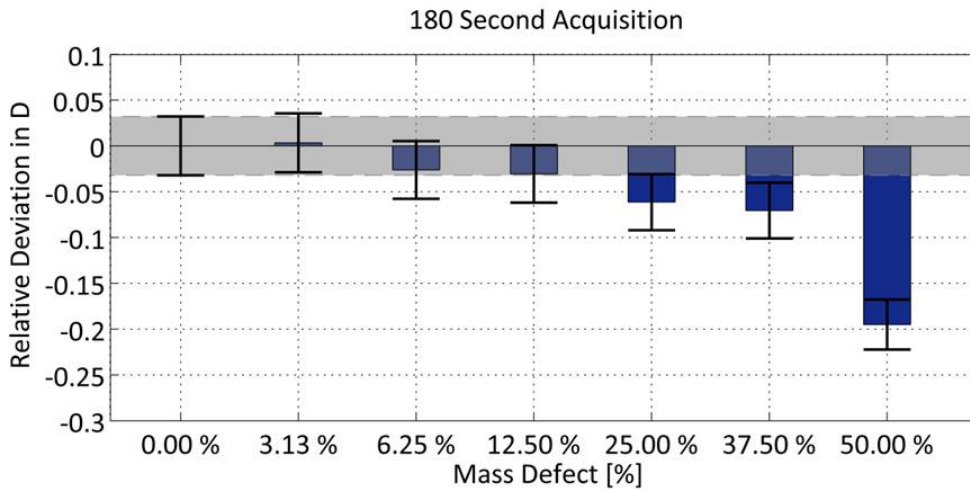
Figure 6.8: Relative deviation in the neutron doubles rate from the full assembly for a 180 second assay time showing that the FNMC system is sensitive up to a 25.00 % mass defect with > 95 % confidence

improvement in the sensitivity is attributed to the increased precision in the measured neutron doubles rates, which provides a higher significance in the observed relative deviation. However, the rate of improvement in the measurement precision of the doubles rate begins to drop for longer assay times. Figure 6.10 is the uncertainty in the measured neutron doubles of the full assembly as a function of assay time showing diminishing improvements in the precision.
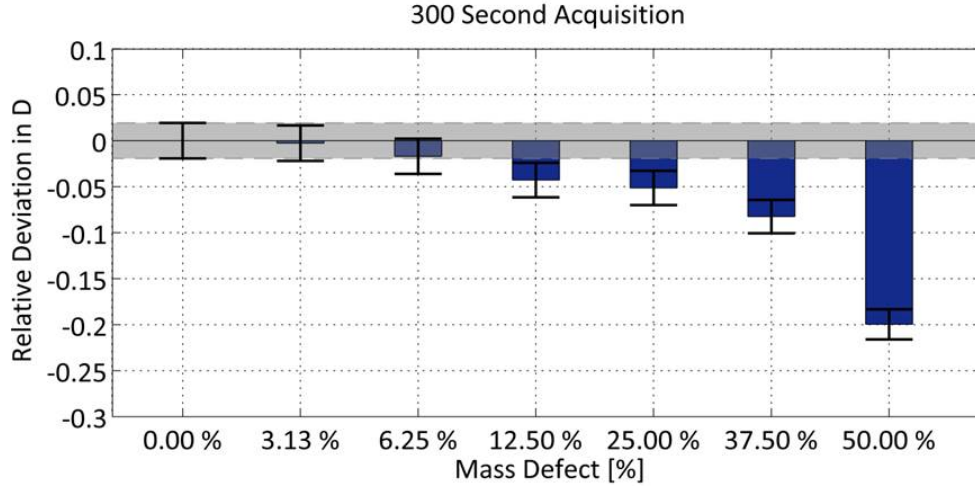
Figure 6.9: Relative deviation in the neutron doubles rate from the full assembly for a 300 second assay time showing that the FNMC system is sensitive up to a 12.5 0% mass defect with > 95 % confidence
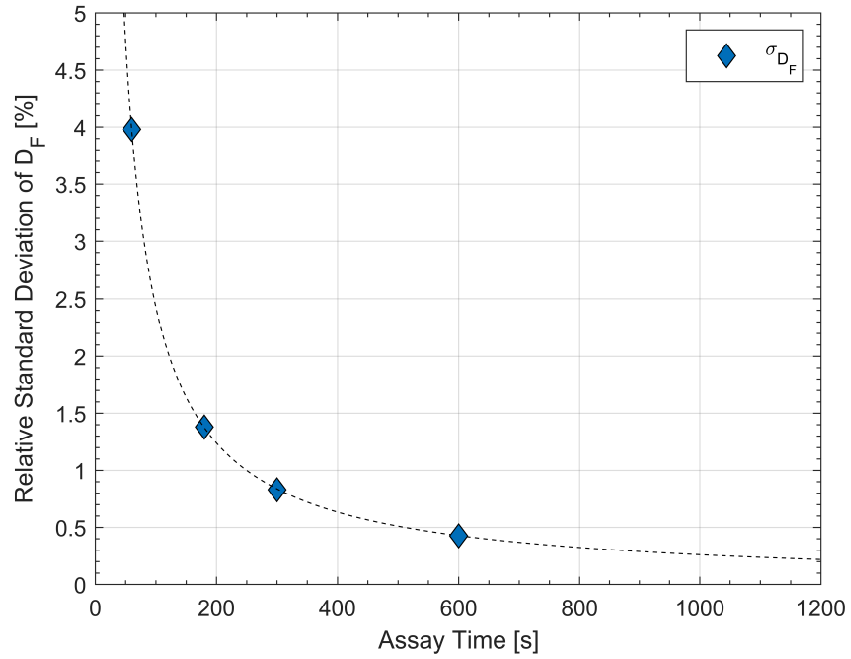
Figure 6.10: Statistical uncertainty in the measured neutron doubles of the full assembly versus the assay time.

Table 6.3: Summary of the FNMC system sensitivity to mass-diversion scenarios.

Number of UO$_2$ pins removed	Mass defect [%]	D	σ_D	RD	σ_{RD}	#σ	Diversion detected >95 % CI
60 second assay time							
Full assembly	0.00	17.32	0.69	0	0.098	0	N/A
1	3.13	16.70	0.68	-0.036	0.096	0.373	No
2	6.25	16.47	0.68	-0.049	0.095	0.520	No
4	12.50	16.44	0.69	-0.051	0.094	0.540	No
8	25.00	16.11	0.67	-0.070	0.093	0.754	No
12	37.50	15.43	0.66	-0.109	0.090	1.215	No
16	**50.00**	**13.68**	**0.62**	**-0.210**	**0.083**	**2.548**	**Yes**
180 second assay time							
Full assembly	0.00	16.67	0.23	0	0.032	0	N/A
1	3.13	16.73	0.23	0.003	0.032	0.103	No
2	6.25	16.23	0.22	-0.026	0.031	0.837	No
4	12.50	16.16	0.22	-0.031	0.031	0.976	No
8	**25.00**	**15.65**	**0.22**	**-0.061**	**0.031**	**2.011**	**Yes**
12	**37.50**	**15.50**	**0.22**	**-0.071**	**0.030**	**2.325**	**Yes**
16	**50.00**	**13.42**	**0.20**	**-0.195**	**0.027**	**7.318**	**Yes**
300 second assay time							
Full assembly	0.00	16.84	0.14	0	0.019	0	N/A
1	3.13	16.79	0.14	-0.003	0.019	0.142	No
2	6.25	16.55	0.14	-0.017	0.019	0.888	No
4	**12.50**	**16.12**	**0.13**	**-0.043**	**0.019**	**2.289**	**Yes**
8	**25.00**	**15.97**	**0.13**	**-0.051**	**0.019**	**2.765**	**Yes**
12	**37.50**	**15.45**	**0.13**	**-0.083**	**0.018**	**4.549**	**Yes**
16	**50.00**	**13.48**	**0.12**	**-0.200**	**0.016**	**12.16**	**Yes**

6.4 Simulation Studies of Mass Diversion Scenarios in Fresh Fuel Assemblies

MCNPX-PoliMi simulations were performed to compare the performance of an FNMC system relative to the currently-deployed ^{3}He-based system. The Uranium Neutron Collar UNCL is a ^{3}He-based system specifically designed to assay fuel assemblies for international safeguards applications; the UNCL system has been used in the field for decades. The UNCL consists of an array of 18 ^{3}He gas proportional counters embedded in polyethylene

(1 cm diamter, 4 atm). The ^{3}He tubes are arranged in three detection slabs surrounding a rectangular cavity designed to contain the fuel assembly of interest. The fourth slab contains the AmLi interrogation source, which is also embedded in polyethylene. The system also include removable cadmium sheets of 0.5 mm thickness in front of all four slabs, and are designed to mitigate any excess thermal neutron-induced fissions from neutrons scattering and reentering the assembly from the polyethylene. Figure 6.11 shows an image of the UNCL system along with a detailed MCNP model used for the benchmark simulations.
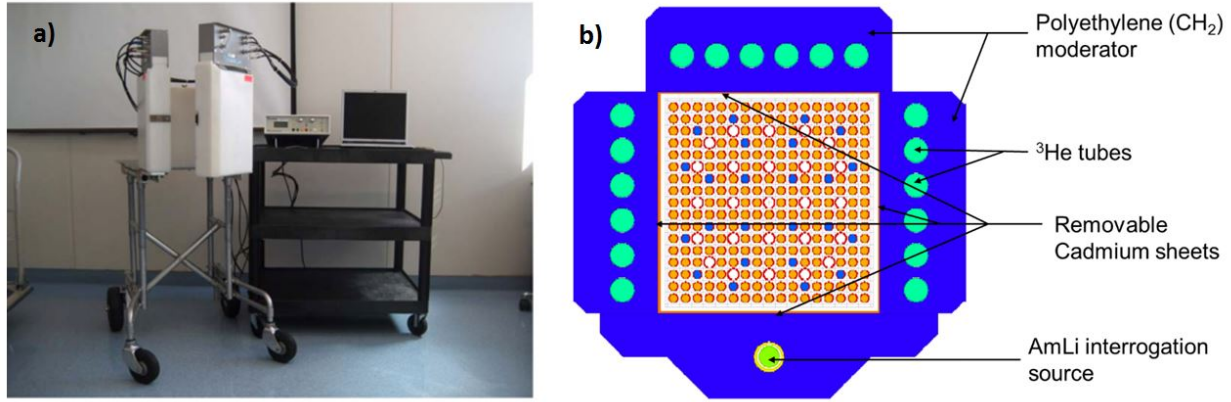
Figure 6.11: An image of the UNCL system (a), and the benchmarked MCNP simulation model (b).

Benchmark simulations of the UNCL system have been validated in many previous works for a wide range of different types of fuel assembly. As part of the Defense Nuclear Non-proliferation Neutron Rodeo Project [44, 75], the benchmark simulated data of the UNCL system for assaying 17x17 fresh fuel assemblies for pressurized water reactors (PWR) were provided as a baseline to compare alternative detector technologies. A comprehensive study on the potential improvements and limitations of using organic scintillators can be found in [75]; the results in this section focuses specifically on the mass defect sensitivity study.

The simulated AmLi spectrum was referenced from the experimentally-measured sources [76], where (α,n) reactions on the oxygen atoms are considered. Figure 6.12 shows the input spectrum of the AmLi interrogation source used in all simulation studies in this work, along with the thermalized spectrum (through 2.54 cm polyethylene) entering the fuel assembly.
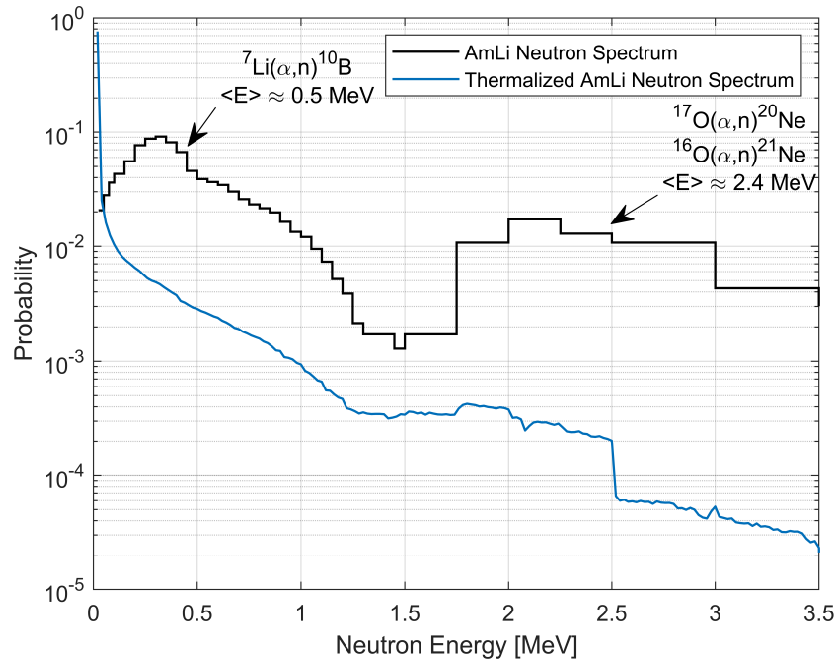
Figure 6.12: Simulated input energy spectrum for the AmLi interrogation source, and the outgoing thermalized spectrum through 2.54 cm of polyethylene moderating material.

6.4.1 Simulated Fresh Fuel Assemblies

The full assembly with no diverted mass was a 17x17 fresh fuel assembly with 264 low-enriched uranium (LEU) fuel pins (4 % enriched) and 25 non-fuel pins yielding a ^{235}U linear density of 51.9 g/cm. The simulated mass diversion scenarios were performed by replacing the LEU fuel pins with depleted uranium (DU) fuel pins, which reflected a mass defect percentage of approximately 3 % to 15 % relative to the ^{235}U linear density of the full assembly. Figure 6.13 shows the simulated fuel assemblies for the full and diverted cases. Table 6.4 summarizes all simulated fuel assemblies.

6.4.2 Simulated Active-mode Fast-Neutron Multiplicity Counter based on *trans*-stilbene Detectors

The simulated FNMC system for assaying the PWR fresh fuel assemblies was designed based on the form factor of the UNCL system, and included three detector panels along with

114
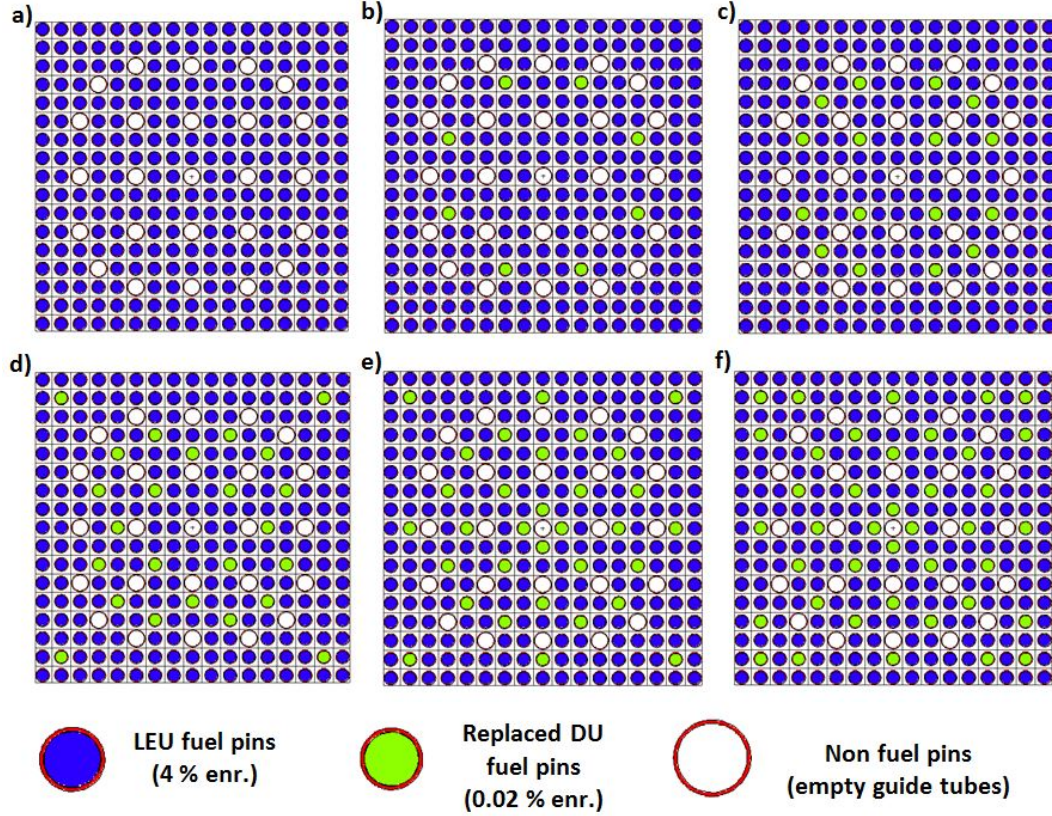
Figure 6.13: Simulated 17x17 PWR fresh fuel assembly showing the full assembly (a), and the diverted assemblies (b-f) where the LEU fuel pins are replaced with DU fuel pins.

a fourth panel containing the AmLi interrogation source. Each detector panel contained 10 5.08 Ø cm x 5.08 cm *trans*-stilbene detectors for a total of 30 detectors. Figure 6.14 shows the MCNP simulation model of the FNMC system.

All simulations were run with time dependent source definitions to match the assumed activity of the AmLi interrogation source (50,000 n/s); the *if* on ^{233}U and ^{235}U from ^{238}U *sf* neutrons were assumed to be constant for all assemblies and negligible relative to the induced fission rate of the thermal AmLi neutrons. The mass diversion sensitivity analysis was performed similarly to the method used for the experimental data in the previous section, where the relative deviation in the measured neutron doubles rate from the full assembly was used according to Eqs. (6.1) and (6.2). The simulated neutron doubles rate was extracted with MSR gate-generation method using Eq. (4.15) with a time gate width of 100 ns and a
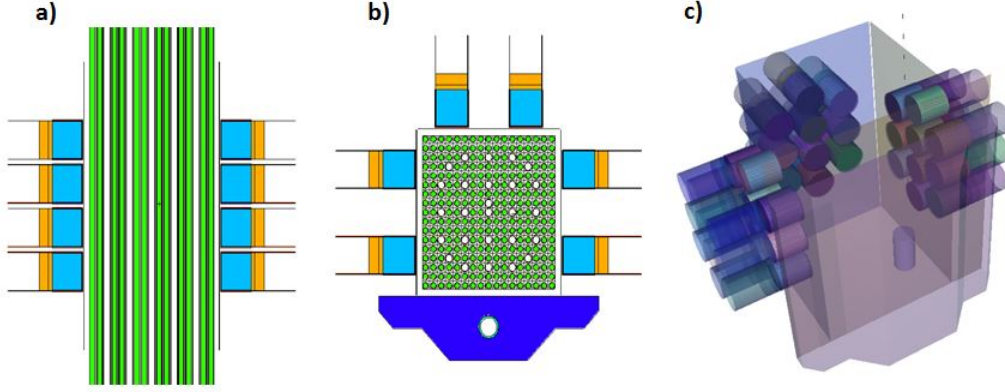
Figure 6.14: MCNP simulation model of the FNMC system consisting of 30 5.08 Ø cm x 5.08 cm *trans*-stilbene detectors and an AmLi interrogation neutron source embedded in polyethylene. Cadmium sheets of 0.5 mm thickness are placed in front of all detector and AmLi source panels.

long delay of 1000 ns. The significance of the observed relative deviation was again calculated using Eq. (6.3). An assumed systematic uncertainty of 2 % was implemented for both the UNCL and the FNMC system and was summed in quadrature with the statistical counting uncertainty. The analysis was performed for an assay time of both 600 and 1800 seconds.

6.5   Simulation Results: Comparison of the UNCL and the FNMC system

Figures 6.15 and 6.16 show a direct comparison of the sensitivity results for an assay time of 600 and 1800 seconds, respectively. Table 6.4 and 6.5 show a detailed summary of the sensitivity results shown in Figures 6.15 and 6.16.

The UNCL system is able to detect a mass diversion of 32 fuel pins with > 95 % confidence, while the FNMC system can detect a mass diversion of 16 fuel pins > 95 % confidence for an assay time of 600 seconds. The relative deviations observed in the neutron doubles rate for the diverted scenarios are quite similar for both the UNCL and FNMC system, however the lower uncertainty given by the FNMC system yields higher confidence for declaring a diversion. When the assay time is increased to 1800 seconds, we see that the UNCL is

116
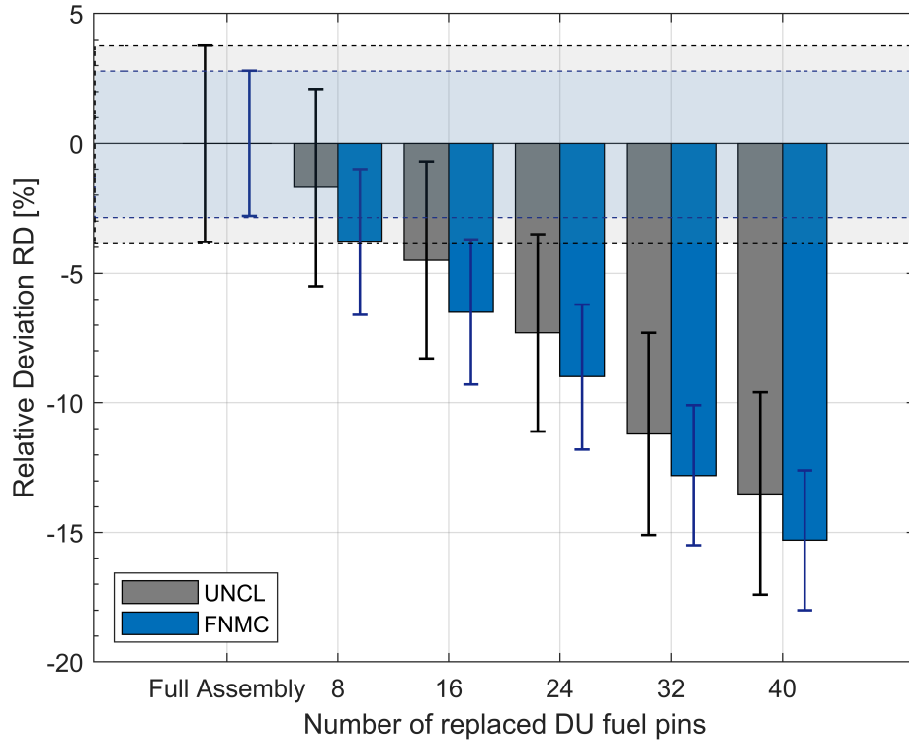
Figure 6.15: Sensitivity analysis of the simulated mass diversion scenarios for the UNCL system and the FNMC system with an assay time of 600 seconds.

now able to detect a mass diversion of 24 fuel pins with > 95 % confidence, mainly due to the increased counting statistics reflecting a lower uncertainty on the relative deviation. The results for the FNMC system using an assay time of 1800 seconds are very similar to the 600 second assay; a slight increase in the diversion significance values are observed due to the increased counting statistics.

The incremental improvement seen in the sensitivity of the FNMC system when comparing the results from 600 and 1800 second assay times demonstrates that the system does not benefit from longer assay times; this result is supported by the diminishing improvement on the precision of the neutron doubles rate shown in Figure 6.10. Furthermore, the assumed 2 % systematic uncertainty begins to dominate the uncertainty in the relative deviation as the assay time increases. On the other hand, the UNCL system benefits significantly from the longer assay time demonstrating that the UNCL system (i.e., any capture-based system)
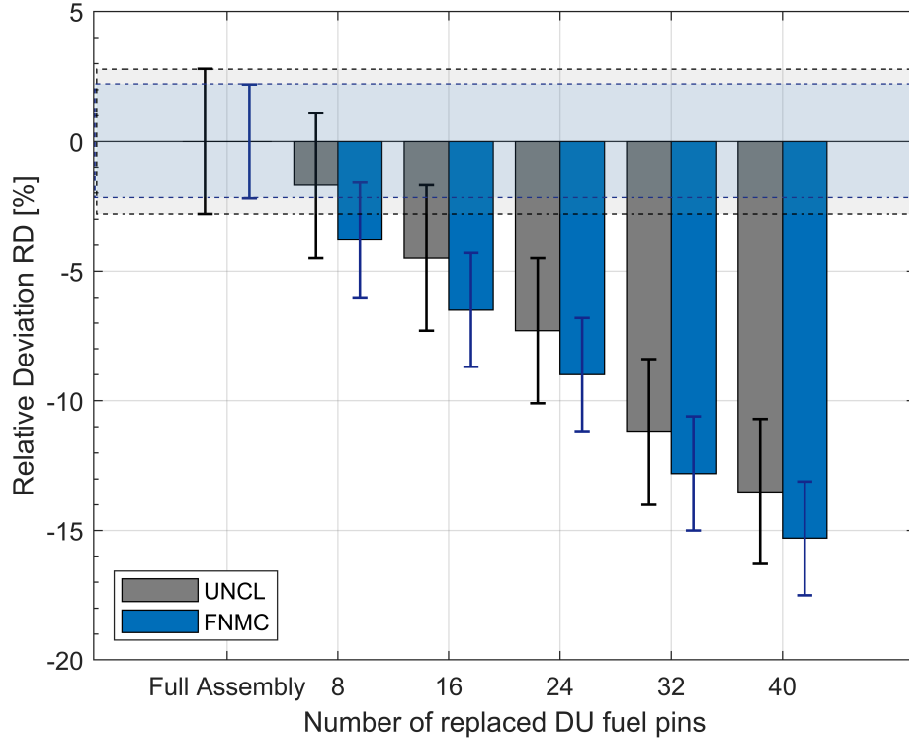
Figure 6.16: Sensitivity analysis of the simulated mass diversion scenarios for the UNCL system and the FNMC system with an assay time of 1800 seconds.

requires much longer assay times to reach the same level of precision as an FNMC system.

6.6 Conclusions

This work characterizes the FNMC system to implement active NDA for detecting mass-diversion scenarios. The FNMC system utilized two AmLi interrogation neutron sources to induce fissions in UO_2 pins, arranged in a fuel bundle type geometry. The experimental results shows that the FNMC system is able to detect (with > 95 % CI) a 50.00 % mass removal for a 60-second assay, and down to 12.50 % mass removal for a 300-second assay. The sensitivity study for mass-diversion scenarios was extended using MCNPX-PoliMi simulations, where simulated results of an FNMC system was directly compared to benchmarked simulations of the currently-deployed UNCL capture-based system. The simulated results show that the FNMC system is more sensitive to mass-diversion scenarios compared to the

Table 6.4: Summary of the sensitivity analysis for mass diversion scenarios with an assay time of 600 seconds

Number of replaced DU pins	^{235}U LD [g/cm]	RD [%]	σ_{RD} [%]	#σ	Diversion detected with >95 % CI
UNCL					
Full assembly	51.9	0	3.8	0	N/A
8	50.4	-1.7	3.8	0.5	No
16	48.9	-4.5	3.8	1.2	No
24	47.4	-7.3	3.8	1.9	No
32	**45.9**	**-11.2**	**3.9**	**2.9**	**Yes**
40	**44.4**	**-13.5**	**3.9**	**3.5**	**Yes**
FNMC					
Full assembly	51.9	0	2.8	0	N/A
8	50.4	-3.8	2.8	1.7	No
16	**48.9**	**-6.5**	**2.8**	**2.9**	**Yes**
24	**47.4**	**-9.0**	**2.8**	**4.1**	**Yes**
32	**45.9**	**-12.8**	**2.8**	**5.8**	**Yes**
40	**44.4**	**-15.3**	**2.8**	**6.9**	**Yes**

Table 6.5: Summary of the sensitivity analysis for mass diversion scenarios with an assay time of 1800 seconds

Number of replaced DU pins	^{235}U LD [g/cm]	RD [%]	σ_{RD} [%]	#σ	Diversion detected with >95 % CI
UNCL					
Full assembly	51.9	0	2.8	0	N/A
8	50.4	-1.7	2.8	0.6	No
16	48.9	-4.5	2.8	1.6	No
24	**47.4**	**-7.3**	**2.8**	**2.6**	**Yes**
32	**45.9**	**-11.2**	**2.8**	**4.0**	**Yes**
40	**44.4**	**-13.5**	**2.8**	**4.8**	**Yes**
FNMC					
Full assembly	51.9	0	2.2	0	N/A
8	50.4	-3.8	2.2	1.8	No
16	**48.9**	**-6.5**	**2.2**	**3.0**	**Yes**
24	**47.4**	**-9.0**	**2.2**	**4.2**	**Yes**
32	**45.9**	**-12.8**	**2.2**	**5.9**	**Yes**
40	**44.4**	**-15.3**	**2.2**	**7.1**	**Yes**

UNCL system given a fixed acquisition time.

CHAPTER VII

Neutron-Neutron Energy-Angle Correlations versus Leakage Multiplication

This chapter summarizes the techniques and results for extracting energy-angle correlations as a function of the SNM assembly leakage multiplication. I analyze the PANN data from the passive neutron multiplicity measurement in Chapter V specifically to observe neutron-neutron angular and energy-angle correlations by looking at the frequency of neutron-neutron coincidences for detector pairs exhibiting different angles. This work is taken from my journal article titled "Prompt fission neutron anisotropy in low-multiplying subcritical plutonium metal assemblies" published in *Nuclear Instruments and Methods in Physics Research Section A* [77].

7.1   Introduction and Motivation

Robust characterization of the neutron multiplication of unknown assemblies of SNM is an important aspect of nuclear safeguards and nonproliferation applications. The neutron multiplication, defined as the expected total additional neutrons generated by a single initiating neutron [28], is an important physical property for fuel and weapons use. An assembly of SNM will undergo self-propagating fission chain reactions initiated by a source of incident neutrons, and will exhibit a multiplication of greater than one. In contrast,

neutron sources that do not have self-sustained fission chain reactions (e.g. ^{252}Cf, AmBe, PuBe, etc.) will have a multiplication that is equal to one. Thus, an accurate estimate of the multiplication can be used to identify typical SNM such as weapons-grade plutonium or highly enriched uranium. There are several well-established techniques for measuring the multiplication of an unknown SNM assembly, such as neutron multiplicity counting [16, 17] and Feynman-Y analysis [30]. These techniques typically rely on an array of ^{3}He thermal neutron detectors embedded in moderating material (e.g. polyethylene). Previous work has shown that using organic scintillators to directly detect the unmoderated fast neutrons can improve the measurement precision in the context of these well-established techniques [43, 78]; however, organic scintillators enable additional capabilities unavailable to ^{3}He based systems. An array of organic scintillators is sensitive to the initial energy and direction of the emitted neutrons due to the absence of moderation material between the source and detectors. Neutron-neutron angular distributions [21–27, 79] can be measured by quantifying the frequency of neutron-neutron coincidences observed from detector pairs placed at different angles with respect to the source. This technique has been used extensively to study the well-known anisotropic emission of prompt fission neutrons for single spontaneous fission events from ^{252}Cf [21–25] and ^{240}Pu [26, 27]; results from these studies show that neutrons from the same fission event are correlated in angle. The study of how this anisotropy changes in the propagated fission chains of highly multiplying subcritical assemblies was demonstrated by J.M. Mueller et al. [79]. However, no measured data exist that characterize the neutron anisotropy for subcritical assemblies as a function of the multiplication. The experiment and analysis performed in this work aimed to measure the neutron-neutron angular distribution and characterize the neutron anisotropy from low-multiplying plutonium metal assemblies. The measured neutron-neutron angular distribution was also analyzed at varying low-energy detection thresholds to characterize the change in the neutron anisotropy as a function of the minimum observable neutron energy.

7.2 Description of Plutonium Metal Assemblies

Neutron coincidence counting measurements of plutonium metal assemblies were performed at the Zero Power Physics Reactor (ZPPR) at Idaho National Laboratory (INL) [70]. Each plutonium metal plate, hereafter referred to as PANN, had a total plutonium mass of 103.9 g with 95% ^{239}Pu content by mass; Table 7.1 shows the isotopic composition for a single plate aged to the date of the experiment, August 2015. A single PANN plate emits approximately 5.13 x 103 neutrons per second; neutrons from (α,n) reactions were negligible.

Table 7.1: The isotopic composition of a single PANN plate. Isotope mass is corrected for decay, and the mass uncertainty was calculated using the known uncertainty in the half-life of each isotope

Isotope	Mass [g]
^{238}Pu	0.00023(6)
^{239}Pu	98.89(2)
^{240}Pu	4.70(1)
^{241}Pu	0.04(1)
^{242}Pu	<0.009
^{241}Am	0.23(1)
Al	1.16
Total Pu	103.87

The dimensions of a single plate are 7.62 cm by 5.08 cm, with a 0.3175 cm thickness. The active plutonium metal core is contained in a thin layer of 304 L stainless steel cladding. The density of each plate was estimated to be 15.09 g/cm3, based on the PANN element geometry [80]. For subcritical assemblies, the main loss mechanism for neutrons is the leakage out of the assembly. Thus, the multiplicative property for these types of assemblies is typically described by the leakage multiplication, defined as the expected total additional neutrons that are created and leak (escape) the assembly from a single initiation neutron [28]. The leakage multiplication was estimated using MCNPX-PoliMi simulations [58]. The neutron source term for these simulations was assumed to be purely from spontaneous fission of ^{240}Pu. The leakage multiplication, M_L (assuming the probability for non-fission captures is

low) for each assembly was calculated using

$$M_L = M_T p_L, \tag{7.1}$$

where p_L is the leakage probability out of the assembly, and M_T is the total multiplication. Ten different configurations were measured, ranging from a single-plate configuration to a 19-plate configuration yielding a mass range of 104 g to approximately 2 kg and a leakage multiplication range from 1.0722(3) to 1.6006(4). The leakage multiplication were estimated using MCNPX-PoliMi simulations of the measured configurations. Table 7.2 summarizes the total mass and leakage multiplication of the ten measured assemblies.

Table 7.2: The total plutonium mass and simulated leakage multiplication of the measured plutonium metal assemblies.

Assembly ID	Number of Plates	Total Pu Mass [g]	Total Multiplication	Leakage Multiplication
PANN1	1	103.87	1.1068(3)	1.0722(3)
PANN3	3	311.61	1.2482(4)	1.1674(3)
PANN5	5	519.35	1.3660(4)	1.2466(4)
PANN7	7	727.09	1.4694(4)	1.3161(4)
PANN9	9	934.83	1.5604(4)	1.3772(4)
PANN11	11	1142.6	1.6421(4)	1.4320(4)
PANN13	13	1350.3	1.7158(5)	1.4814(4)
PANN15	15	1558.1	1.7804(5)	1.5247(4)
PANN17	17	1765.8	1.8402(5)	1.5649(4)
PANN19	19	1973.5	1.8936(5)	1.6006(4)

Figure 7.1 shows the fraction of leaked neutrons (out of the assembly that are then available for detection) that originate from spontaneous and induced fissions as a function of the number of plates in the configuration.

7.3 Experimental Methods and Detector Setup

The detection system consisted of 16 organic scintillator detectors of two different types; eight 7.62 Ø cm by 7.62 cm EJ-309 liquid organic scintillators and eight 5.08 Ø cm by 5.08
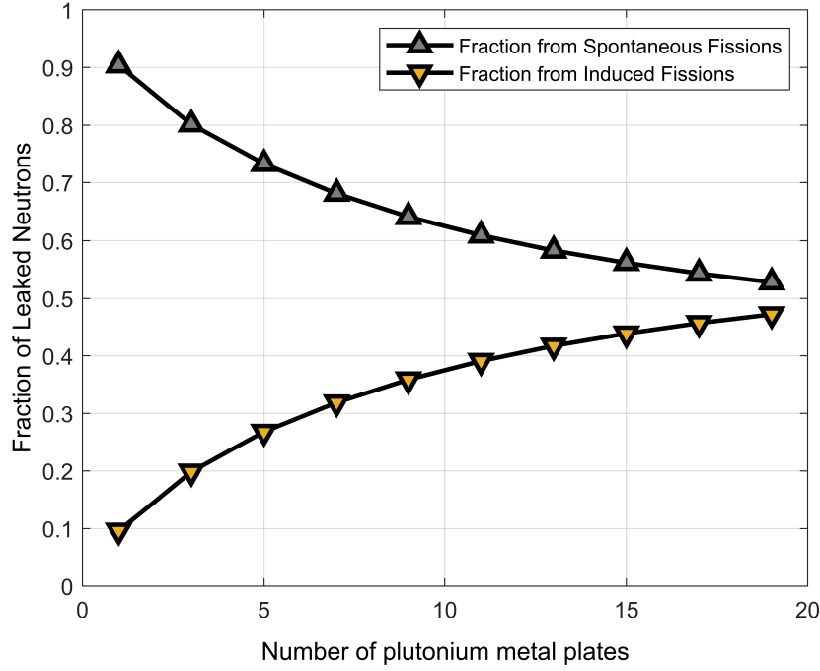
Figure 7.1: MCNP simulation of the fraction of leaked neutrons that originate from spontaneous and induced fissions. Error bars are smaller than the symbol.

cm stilbene crystals, hereafter referred to as EJ and SB, respectively. The detectors were configured in a cylindrical array surrounding the PANN assemblies; the experimental setup is shown in Figure 7.2. All detectors were placed 22.4 cm from the center of the array and were arranged such that no detectors of the same type were adjacent to one another. Lead shielding (1.2 cm) was placed in front of all detectors to attenuate the strong gamma-ray emissions, primarily from the ^{241}Am content in the PANN plates. Full waveforms (within a 416 ns window) from each detector were acquired using a CAEN 16-channel V1730 digitizer, which has a 14-bit resolution, 500 Msps sampling rate, and a 0-2 V dynamic range. The data was transferred through a fiber optic cable that can transfer up to 60 MBs/s with no losses from dead time. Raw waveforms were processed offline, and all waveforms with pulses that either exceeded the dynamic range (i.e. clipped pulses) or had multiple pulses within the same window (i.e. piled-up pulses) were removed. The remainders of the well-separated waveforms were then processed to extract three quantities; a short-gate integral (i.e. tail integral), a long-gate integral (i.e. total integral), and the trigger timestamp.

^{137}Cs calibration measurements were performed to ensure detector response uniformity. The voltage bias on each detector was set such that the ^{137}Cs Compton edge (0.478 MeV) was located at 0.4 V, which corresponds to a maximum light output of 2.4 MeVee for a 2 V dynamic range.
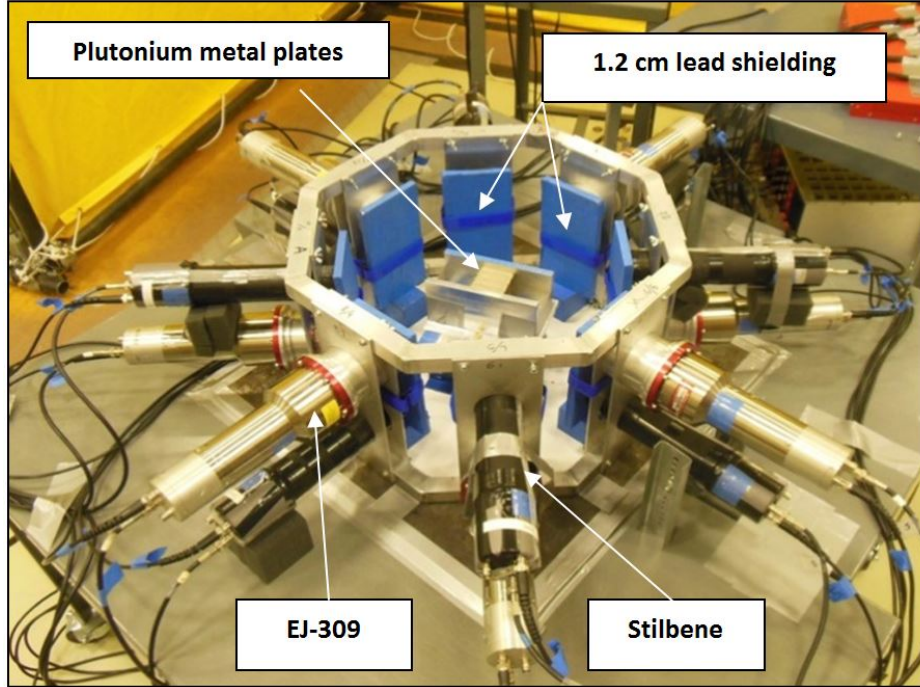
Figure 7.2: Experimental setup for measuring neutron-neutron coincidences from plutonium metal assemblies. The assemblies were placed in the center of the detection system array inside an aluminum holder. 1.2 cm of lead shielding was placed in front of all detectors.

7.3.1 Pulse-Shape Discrimination

The organic scintillator detectors used in this experiment are sensitive to both fast neutrons and gamma rays. A pulse-shape discrimination (PSD) technique based on charge integration was performed to distinguish the neutron from the gamma-ray events, where the charge collected in the tail region of the pulse is compared to the total collected charge [56]. The start of the tail integral was optimized for each detector type; starting a tail integral window 24 ns past the pulse peak achieved the best PSD performance for both EJ and SB detectors [70]. The discrimination line that separates neutron and gamma-ray events was

optimized using an iterative algorithm outlined in [57]. Figure 7.3 and 7.4 shows a representative PSD scatter plot for an EJ and SB detector, respectively, showing two distinct regions for neutron and gamma-ray induced pulses.
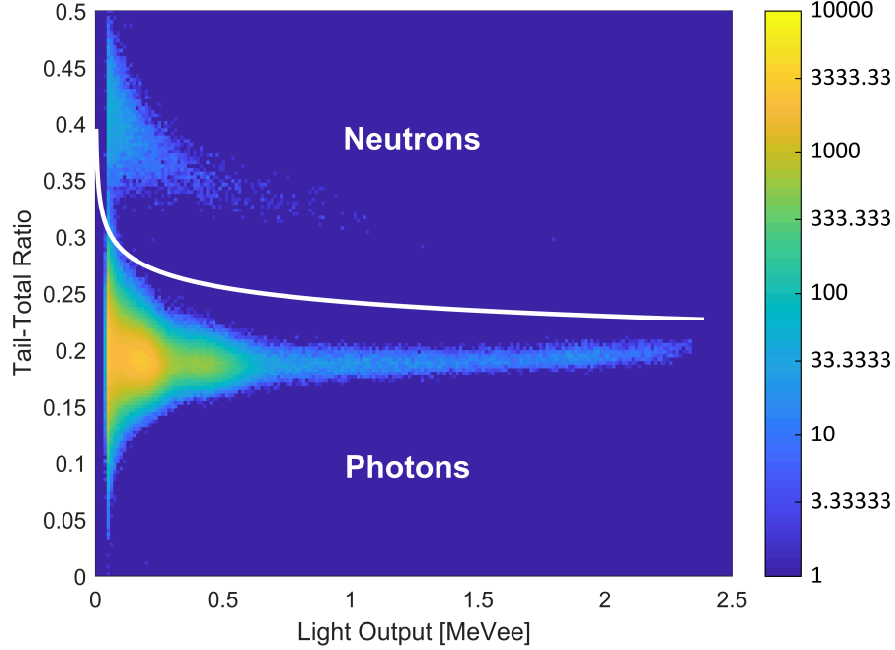
Figure 7.3: Measured pulse tail to the total integral distribution from a single PANN plate measured with an EJ-309 detector as a function of the light output. The white discrimination line separates neutron events (top cluster) and gamma-ray events (bottom cluster).

7.3.2   Light-Output Functions for Low-Energy Detection Thresholds

A variety of low-energy detection thresholds were applied to observe neutron coincidences of higher energy. Because two different types of organic scintillator detectors were used in this experiment, the detection thresholds were expressed in terms of neutron energy (MeV) due to the different amount of light produced by an EJ and SB; the light output depends on the detector composition and volume, the particle type, and the amount of deposited energy [40, 41]. Gamma rays primarily interact in the organic scintillators through Compton scattering on electrons, and the light produced has a linear 1:1 relationship for the observable energy range (0.478 MeV gamma-ray energy deposition = 0.478 MeVee). The signal produced
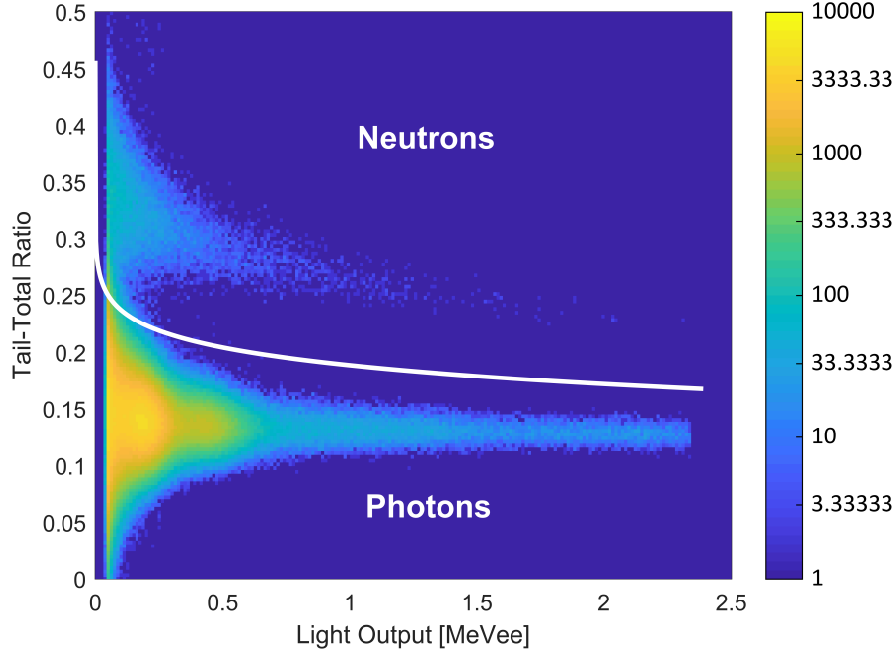
Figure 7.4: Measured pulse tail to the total integral distribution from a single PANN plate measured with a stilbene detector as a function of the light output. The white discrimination line separates neutron events (top cluster) and gamma-ray events (bottom cluster).

by neutrons is primarily attributed to elastic scattering on hydrogen nuclei (i.e. protons), which results in a non-linear relationship where much less light is produced for a given energy deposition [40, 41, 54]. A semi-empirical neutron response function based on Birks function was used to convert the neutron-equivalent energy (assuming all the deposited energy was transferred in a single elastic scatter on a recoil proton) to light units for both EJ and SB detectors, and has the form

$$L(E) = \int \frac{a}{1 + b\left(\frac{dE}{dx}\right) dE},$$ (7.2)

with

$$a = \begin{cases} 1.630 & \text{for SB} \\ 1.903 & \text{for EJ} \end{cases}, \quad b = \begin{cases} 27.83 & \text{for SB} \\ 26.03 & \text{for EJ} \end{cases}$$ (7.3)

where $L(E)$ is the light output in MeVee, $\frac{dE}{dx}$ is the recoil particle stopping power of the detector material, and a and b are fitted parameters [54, 81]. In Eq. (7.2)- (7.3), the parameter

a relates to the scintillation efficiency, while the parameter *b* is related to the ionization density and quenching effects and is a function of the material [40, 41]. Figure 8.4 shows the relationship between the deposited neutron energy and the light output for EJ and SB detectors using the semi-empirical detector response model above.
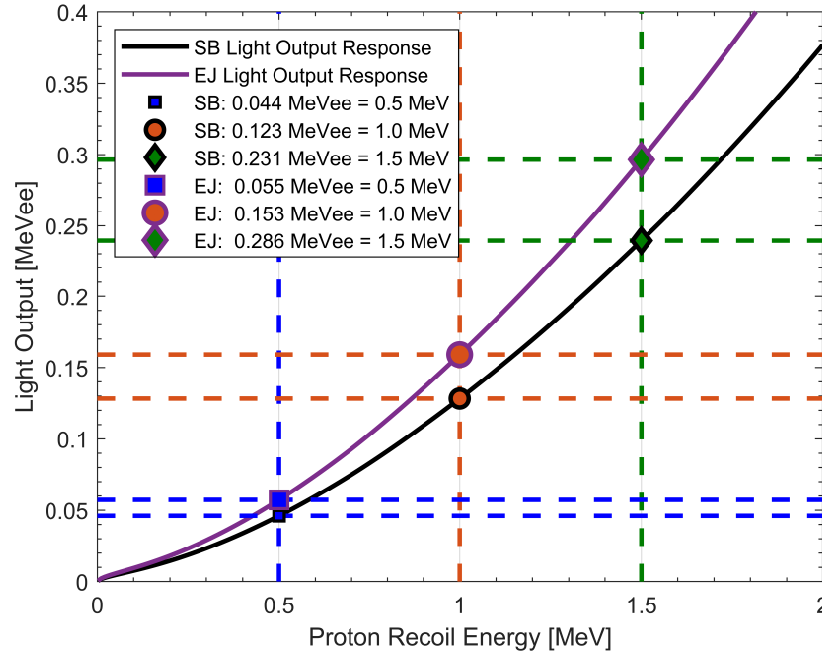
Figure 7.5: Light output response functions for the EJ and SB detectors used to calculate the low-energy detection thresholds in neutron-equivalent energy.

7.3.3 Pulse Timing

The timestamp is required to process time-correlated pulses within a prescribed coincidence window, and is calculated using a DCFD technique, with a CFD fraction of 0.5 relative to the pulse height. Neutron and gamma-ray events were separated for each detector, and a list-mode dataset of all time-tagged neutron events from all detectors was created. The measured timing resolution between detector pairs was less than two nanoseconds at the full-width half-maximum.

7.4 Data Analysis

There are a total of 120 unique detector pairs in this experimental setup, where each pair can consist of two EJs, two SBs, or one EJ and one SB detectors. These 120 detector pairs can be categorized into nine groups that exhibit similar angles (within $\pm$ 1°). The angles and their respective geometric uncertainties were calculated by taking the average of the maximum and minimum angles that could be formed considering the diameter of the detectors within the pair. Table 7.3 summarizes the nine angle groups and the number of detector pairs in each group.

Table 7.3: Summary of the angle groups, the number of pairs in each group, and the combination of detector types.

Angle [°]	Unc. in Angle [$\pm$°]	Number of Pairs N	Combination
25.96	15.18	8	EJ-SB
45.65	15.57	16	EJ-SB
51.67	15.14	16	EJ-EJ + SB-SB
85.63	9.30	16	EJ-EJ + SB-SB
92.81	14.69	16	EJ-SB
127.64	13.59	16	EJ-SB
136.09	14.97	16	EJ-EJ + SB-SB
152.91	12.74	8	EJ-EJ + SB-SB
170.45	9.55	8	EJ-SB

Neutron-neutron coincidences within a 100 ns time window were extracted for each pair; figure 7.6 shows the relative time differences of neutron-neutron coincidences from all 120 detector pairs for the single-plate case.

The distributions shown in Figure 5 were separated by their respective angle groups, and the integral of the separated distributions yielded the neutron-neutron coincidence rate observed at a given angle. However, the relative source-to-detector solid angle for a detector pair is dependent on what combination of detectors it is made up of (i.e. EJ-EJ, EJ-SB or SB-EJ, and SB-SB pairs) as the EJ and SB detectors had different diameters. The neutron-neutron coincidence rates for each pair were corrected by the singles count rates of the two detectors in the pair to eliminate inconsistencies in source-to-detector solid angle as well
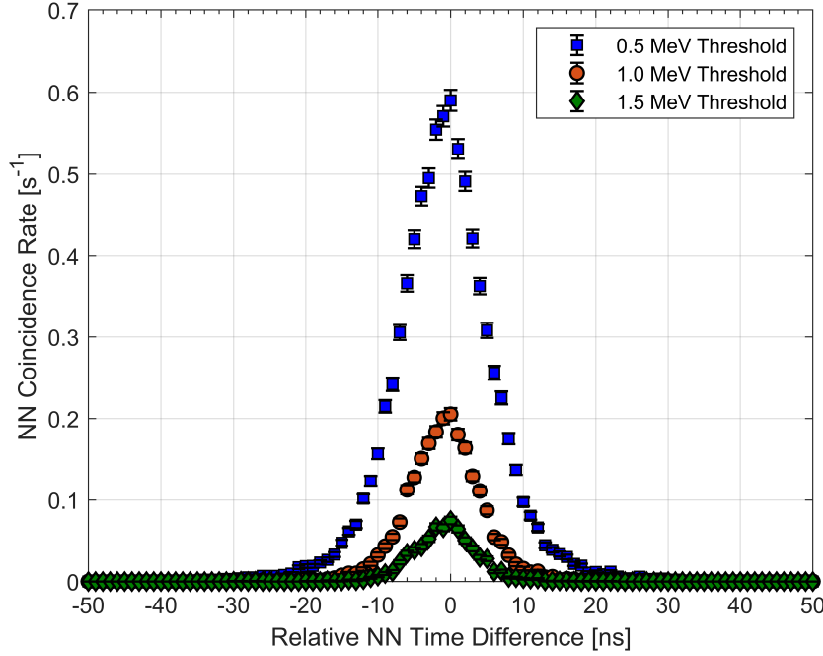
Figure 7.6: Relative time difference between neutron-neutron coincidences from all pairs of detectors for three different low-energy detection thresholds for the single-plate case.

as detector efficiency uniformity as suggested in [79]. This allows for a corrected quantity for the detected coincidences independent of which detectors the pairs are made up of, and is particularly important when quantifying the coincidences from detectors of two different dimensions. The singles-corrected neutron-neutron coincidences (i.e., relative coincidences) observed by a pair are calculated using Eq. (4.20). The relative coincidences for each pair are then sorted by their respective angle group, and the average for each angle group is calculated using Eq. (4.21). Figure 7.7 shows the full integral-normalized neutron-neutron angular distribution for the single-plate PANN1 case (i.e. the most anisotropic case) at three different low-energy thresholds.

Figure 7.7 shows more neutron coincidences at the low- and high-angles ($\approx 0°$ and $\approx 180°$) relative to those at $90°$. A significant fraction of the coincidences observed at lower angles ($< 45°$) are attributed to neutron cross-talk effects [12], thus we use the coincidences at approx. $90°$ and approx. $180°$ to quantify a comparative metric for the observed anisotropy. The neutron anisotropy is quantified by taking the ratio of relative coincidences at $180°$ and
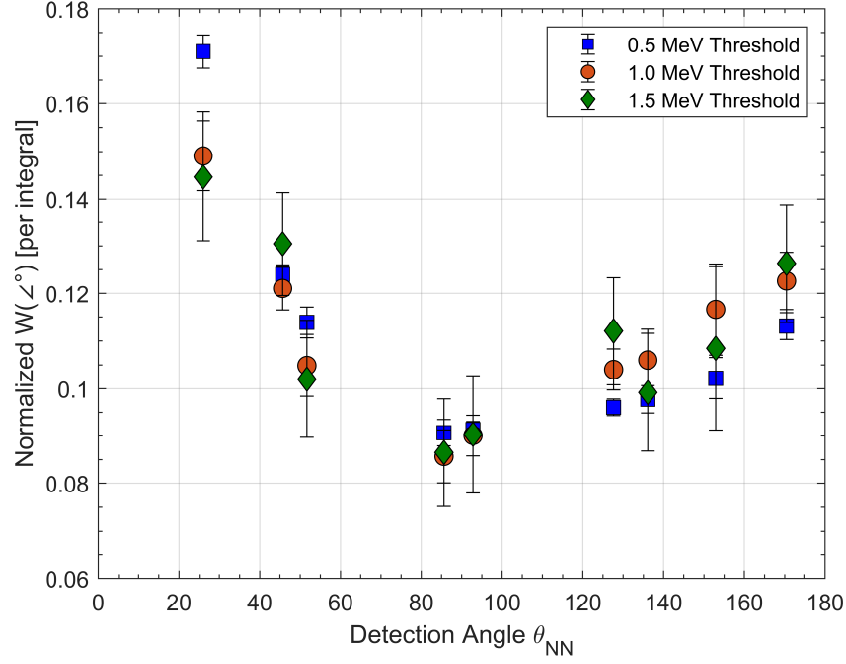
Figure 7.7: Full neutron-neutron angular distribution for the PANN1 configuration at three different low-energy detection thresholds. 2-std. statistical error bars shown.

90° using Eq. (4.22).

7.5 Results and Discussion

The measured neutron anisotropy as a function of the assembly leakage multiplication is shown in Figure 7.8 for the three low-energy detection thresholds. The results in Figure 7.8 demonstrate that the neutron-neutron coincidences appear more isotropic as the multiplication of the assembly increases, due to the weakening of the angular correlation as the fission chain lengths become longer. Although there is insufficient data in this work to conclude the behavior at higher multiplication, simulations performed in [79] suggest that this behavior asymptotically approaches unity.

Figure 7.9 shows the measured neutron anisotropy as a function of the low-energy detection threshold for all ten configurations. The measured neutron anisotropy increases as the detection threshold increases, demonstrating that neutron energy and anisotropy are posi-
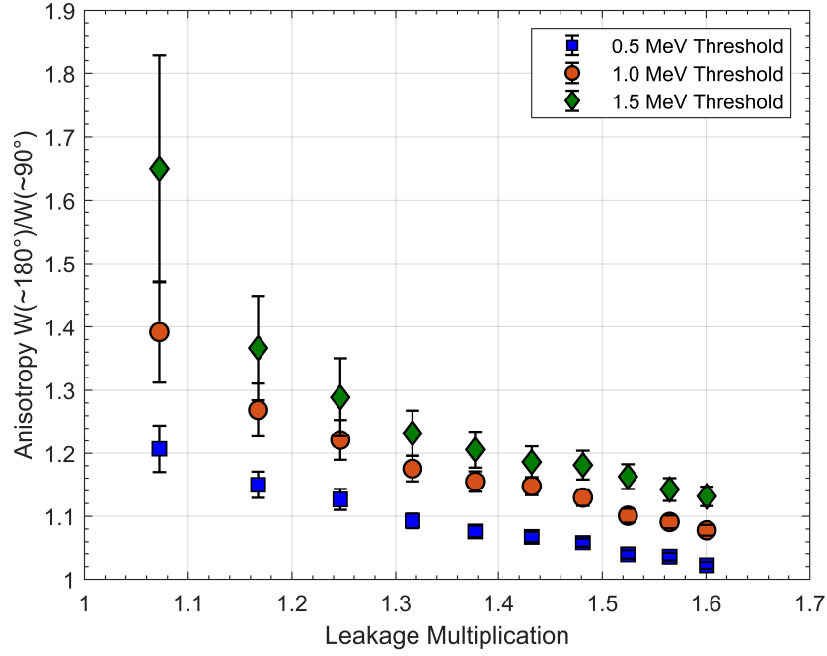
Figure 7.8: Measured neutron anisotropy as a function of the assembly leakage multiplication showing a monotonically decreasing trend. 2-std. statistical error bars shown.

tively correlated as shown in many previous studies for non-multiplying point fission sources [21–27].

7.6 Sources of Error

Organic scintillators will inevitably misclassify some particles: neutrons will be classified as gamma rays and vice versa. Therefore, these neutron-tagged gamma rays were included in the analysis for extracting the neutron coincidences and thus may lead to some spurious additional counts. However, we expect the contribution from misclassified gamma rays in the full angular distribution to be independent of the detection angle [82]. Thus, the effect on the neutron-neutron coincidences due to particle misclassification are expected to be relatively constant at 180° and 90°. The rate of misclassified neutrons (i.e. neutrons classified as gamma-rays) was calculated to be 8.64 x 10^{-4} and 8.42 x 10^{-4} per detection for the EJ and SB detectors, respectively.
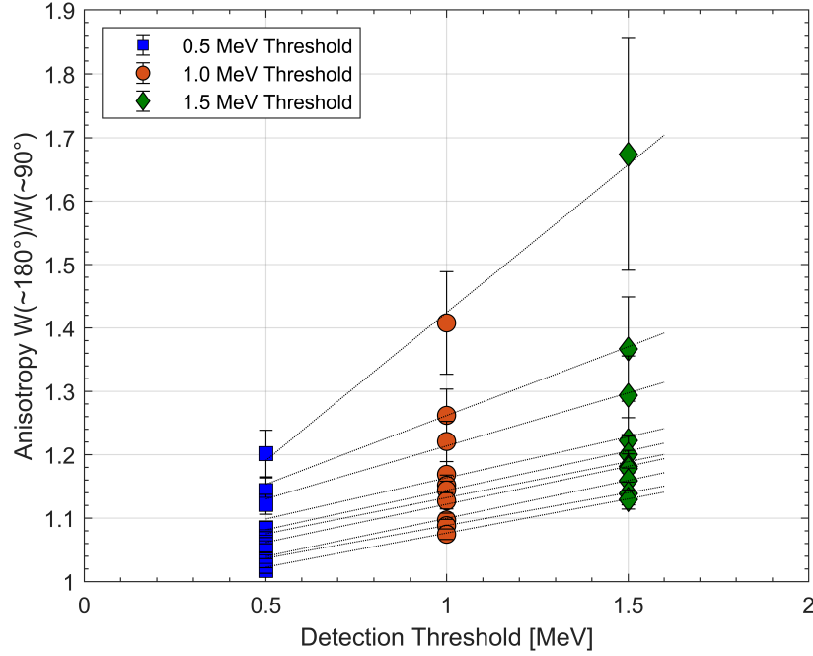
Figure 7.9: Measured neutron anisotropy as a function of low-energy detection threshold showing a positive correlation between anisotropy and neutron energy. 2-std. statistical error bars shown.

Another system effect that may result in spurious additional counts is neutron cross-talk, where a single neutron can scatter into and induce counts in multiple detectors. Previous work has shown that neutron cross-talk effects in organic scintillators are strongly dependent on the relative solid angle between detector pairs as well as the detection threshold [26, 69]. From these works, we expect to see 1) higher neutron cross-talk effects for low-angle detector pairs relative to those at higher angles and 2) less neutron cross-talk effects overall as the detection threshold increases. Neutron cross-talk counts were quantified in simulations by M.J. Marcath et al. [12] for a similar array of organic scintillators and detection thresholds and shows that the cross-talk counts are comparable at 180° and 90° (slightly more counts at 90°). The systematic error introduced by neutron cross-talk effects would cause, in principle, the observed angular distribution appears more isotropic; however, we expect this error to have a lesser effect at higher detection thresholds.

7.7 Summary and Conclusions

This work experimentally characterized the neutron anisotropy for low-multiplying sub-critical plutonium metal assemblies. The neutron anisotropy was quantified using the ratio of relative neutron-neutron coincidences at approx. 180° to those observed at 90° for assemblies that exhibited a leakage multiplication between 1.0722 and 1.6006. The dependence of the observed anisotropy on the detection threshold was also characterized and suggests that the positive correlation between neutron anisotropy and energy is propagated through fission chain reactions, but is less prominent as the fission chain lengths increase. Overall, the results are consistent with the postulated outcomes from previous works.

The results presented in this work could have potential use in nuclear safeguards applications, where the goal is to deliver a robust characterization of unknown special nuclear material. The prompt fission neutron anisotropy provides a characteristic signature that is closely related to the fission chain dynamics in assemblies of special nuclear material. Therefore, the use of the prompt fission neutron anisotropy to characterize assemblies of special nuclear material can provide an independent evaluation of the multiplicative properties complementary to the currently-implemented techniques including neutron multiplicity counting and Feynman-Y analysis.

Further investigation on the prompt fission neutron anisotropy is necessary for assemblies that have non-fissile surrounding material (e.g. shielding, reflectors, etc.). The presence of these types of material could modulate the expected neutron anisotropy through scatters, or reflect neutrons back into the assembly inducing more fission chains. This would result in an inaccurate representation of the multiplication.

CHAPTER VIII

Neutron-Neutron Energy-Angle Correlations versus α-ratio

This chapter summarizes the results from an experimental campaign at Los Alamos National Laboratory using an FNMC system consisting of 24 5.08 Ø cm x 5.08 cm *trans-stilbene* scintillators. The experiment was designed to measure neutron-neutron angular and energy-angle correlations for small plutonium samples with similar ^{240}Pu$_{\text{eff}}$ masses and leakage multiplication, but varying α-ratios due to the different low-z impurity contained in each sample. This work is taken from my journal article submission titled "Neutron-neutron angular and energy-angle correlations of plutonium samples with varying α-ratio" submitted to *Nuclear Instruments and Methods in Physics Research Section A*[83].

8.1 Introduction and Motivation

The primary objective of nuclear safeguards is to deter the nonpeaceful uses of nuclear materials and technology through early detection of misused SNM or associated technology. International safeguards are typically implemented by international inspectorates (e.g., the IAEA), and are performed through a declaration-verification protocol between the inspectorate and the state under the safeguards agreement. MCA is a subset of nuclear safeguards, which focuses on accounting for all SNM in a declared facility. The ability to characterize

physical properties pertinent to SNM is significant to accurately quantify the amount of fissile material. Relevant physical properties include the fissile mass, leakage multiplication, and the α-ratio, defined as the ratio of neutrons from non-fission events (typically (α,n) reactions) to those from spontaneous fission events. Current techniques typically use capture-based neutron detectors (e.g., ^3He proportional counters) to observe the emitted neutron multiplicity distribution to infer the three physical properties; these techniques are commonly referred to as neutron multiplicity counting techniques [16, 17].

Recent research efforts have used scatter-based organic scintillators to directly observe the fast, unmoderated fission neutrons emitted from the SNM to improve measurement precision in the context of neutron multiplicity counting [43, 78]. In addition to the benefits of not having any intervening moderating material, these organic scintillator-based systems have the added capability of retaining additional information unavailable to thermal-energy capture-based systems. Mainly, organic scintillator-based systems are sensitive to a portion of the emitted neutron multiplicity, angular, and energy distributions, and have been used extensively to investigate correlated signatures such as neutron-neutron (n-n) angular distributions in single-fission events [21–27] and induced-fission chains [77, 79], as well as (n-n) energy-angle correlations [23–27].

A previous technique proposed by J.M. Verbeke et al. utilizes organic scintillators to determine the α-ratio by exploiting the difference in the fast neutron energy spectrum of fission neutrons and (α,n) neutrons, demonstrating how the energy sensitivity of organic scintillators can be used for spectral analysis [84]. The technique proposed by L. Holewa et al. describes how organic scintillators can be used to measure (n-n) angular distributions to estimate the α-ratio given high-fidelity a priori Monte Carlo simulations [85]. These techniques show how organic scintillators can use additional information other than the neutron multiplicity to characterize SNM, however; these techniques use the information (energy and angular) independently rather than in unison of one another.

This work presents experimental results of (n-n) angular distributions of plutonium sam-

ples with similar fissile mass and leakage multiplication, but with α-ratio that ranges from 1.6 to 11.5. The results show that observed (n-n) correlations transition away from a true (n-n) fission coincidences to cross talk-induced coincidences associated with a single (α,n) neutron with increasing -ratio.

There has been extensive previous experimental work that aimed to measure the (n-n) angular distribution [21–27, 77, 79]. From these results, one can conclude that:

1. (n-n) coincidences are anisotropic when observing correlated neutrons from single-fission events. [21–27]. This observed anisotropy is due to the kinematic boost received by the neutrons from the fission fragments travelling in opposing directions. Therefore, the (n-n) angular distribution shows a minimum at 90°, with more coincidences appearing at lower ($\rightarrow$0°) and higher ($\rightarrow$180°) angles.

2. (n-n) coincidences appear more anisotropic when observing higher-energy correlated neutrons from single-fission events. [23–27].

3. The anisotropy is characteristic to the spontaneously fissioning element. That is, the anisotropy observed in single-fission events from ^{252}Cf is different than the anisotropy observed in single-fission events from ^{240}Pu [23, 26, 27].

4. (n-n) coincidences appear more isotropic as the average fission-chain length (and in turn, the leakage multiplication) within the SNM increases [77, 79]. The diminishing anisotropy is attributed to the weakening of the angular correlation between the initiating neutron and all subsequent induced-fission neutrons.

5. Neutron cross-talk effects, where a single neutron deposits energy (above the detection threshold) in multiple detectors causing spurious coincidences, is an inherent systematic effect in an array of organic scintillators and will modulate the true emitted (n-n) angular correlation. The magnitude of neutron cross-talk effects is dependent on the detection threshold and the relative solid angle between pairs of detectors.

In the ideal case with no systematic effects (i.e., at emission), the singly emitted (α,n) neutron is uncorrelated in time with the multiple-emitted fission neutrons and therefore the observed (n-n) angular correlations are expected to diminish as the contribution of (α,n) neutrons increase. Considering the neutron cross-talk effect, we must address the fact that spurious (n-n) correlations may be observed that are purely an artifact of the detection system used. That is, (n-n) correlations can be observed from an (α,n) neutron that has been correlated with itself, in particular when the detector pairs are in close proximity to one another. Of course, fission neutrons may also undergo neutron cross-talk events and will similarly cause an increase in the observed (n-n) correlations compared to what was truly emitted. In summary, the (n-n) correlations that are observed in this work can arise from

1. True (n-n) correlations from two fission neutrons

2. Cross-talk (n-n) correlations from a single fission neutron

3. Cross-talk (n-n) correlations from a single (α,n) neutron

This work investigates the dependence of the observed (n-n) angular and energy-angle correlations for Pu-bearing samples with varying α-ratio. Specifically, this experiment aims to isolate the contribution to the observed (n-n) correlations from the fission neutrons, while varying the contribution from (α,n) neutrons. We expect that that the observed (n-n) angle and energy-angle correlations transition away from contributions from fission neutrons (cross-talk and true) to contributions from (α,n) neutron (cross-talk only).

8.2 Experiment at Los Alamos National Laboratory

8.2.1 Description of Measured Special Nuclear Material

The plutonium samples (94% ^{239}Pu by weight) used for this experiment had similar total mass and leakage multiplication, but varying α-ratio due to the different types of impurities. Table 8.1 summarizes the four plutonium samples that were measured, and includes the

estimated $^{240}Pu_{eff}$ mass, leakage multiplication, and α-ratio given by an independent neutron multiplicity measurement using an Epithermal Neutron Multiplicity Counter (ENMC) [86]. A ^{252}Cf spontaneous fission source was also measured to optimize parameters used in post-processing.

Table 8.1: A summary of the measured plutonium samples with estimated physical properties from an independent neutron multiplicity measurement using an ENMC.

Samples	Declared $^{240}Pu_{eff}$ Mass [g]	Estimated $^{240}Pu_{eff}$ Mass from ENMC [g]	Estimated Leakage Multiplication from ENMC	Estimated α-ratio from ENMC
^{252}Cf	—	—	—	—
PuO_2	9.964	9.929 ± 0.068	1.010 ± 0.001	**1.583 ± 0.017**
Pu + Si	10.068	9.847 ± 0.086	1.007 ± 0.001	**2.632 ± 0.030**
Pu + Al	9.968	10.052 ± 0.176	1.007 ± 0.001	**6.448 ± 0.125**
Pu + Mg	9.968	10.451 ± 0.310	1.008 ± 0.001	**11.498± 0.361**

Each plutonium sample was encapsulated in a small disk-like containment that was approximately 5.72 cm diameter X 5.08 cm. Given the similar total mass and leakage multiplication, any observable differences among the samples are attributed to the varying contribution of neutrons from (α,n) reactions. Table 8.2 summarizes the average relative neutron yield for the (α,n) reaction on each type of impurity contained in the samples [13].

Table 8.2: Neutron yield and average neutron energy for (α,n) reactions on various impurities.

Impurity (natural isotopic composition)	Neutron yield per 10^6 5.2 MeV a-particles (Pu average)	Average neutron energy for 5.2 MeV a-particles [MeV]
O	0.059 ± 0.002	1.9
Si	0.076 ± 0.003	1.2
Al	0.41 ± 0.01	1.0
Mg	0.89 ± 0.02	2.7

8.2.2 Description of *Trans*-stilbene Fast-Neutron Multiplicity Counting System

The detection system consisted of a cylindrical array of 24 - 5.08 cm Ø x 5.08 cm trans-stilbene scintillators (hereafter referred to as stilbene) arranged in three rows of eight detectors creating a cavity with a diameter of 27.54 cm. A cylindrical lead shield of approximately 1 cm thickness was used to surround each sample to mitigate the relatively high emission of low-energy photons. Each sample was placed on an aluminum source holder, and was centered both radially and vertically. Figure 8.1 shows an image of the experimental setup. The full-waveforms (within a 288 ns window) from each of the 24 detectors were digitized
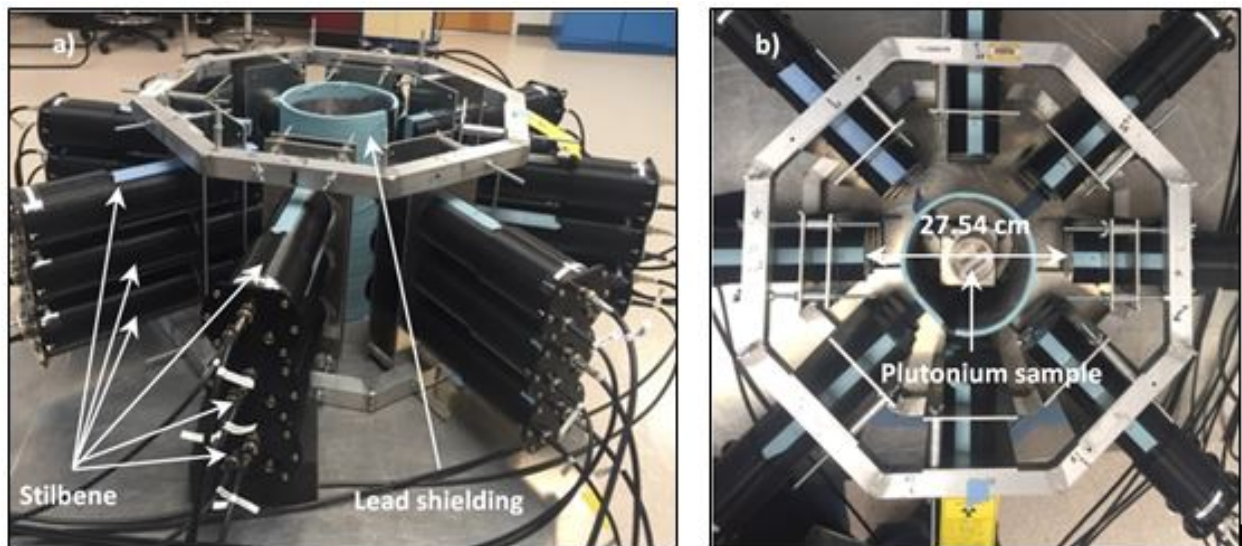
Figure 8.1: Experimental setup using 24 5.08 Ø cm x 5.08 cm stilbene detectors arranged in a cylindrical array surrounding the plutonium sample. Lead shielding was used to attenuate low-energy gamma rays. The detector array had a 27.54 cm diameter cavity, with each detector placed 13.77 cm from the center.

using two CAEN V1730 waveform digitizers (16 channels, 500 MHz sampling rate, 14-bit resolution, 2-V dynamic range). The data was transferred using two optical links with a combined maximum data transfer rate of 110 Mb/s with negligible loss. The time of detected events was determined with the CAEN built-in digital constant fraction discrimination algorithm (attenuation factor of 75% and a delay of 6 ns) [50]. Raw waveforms were post-processed offline, where waveforms that exceeded the dynamic range or that exhibited a

pile-up event were removed. Subsequently, two additional quantities were extracted from the remaining well-separated waveforms to perform pulse-shape discrimination (PSD) for particle identification: the tail and total integral. All detectors were calibrated with a ^{137}Cs source to ensure uniform detector response, and the maximum observable light output was 2.50 MeVee (approximately 5.73 MeV neutron-equivalent energy). Figure 8.2 shows the
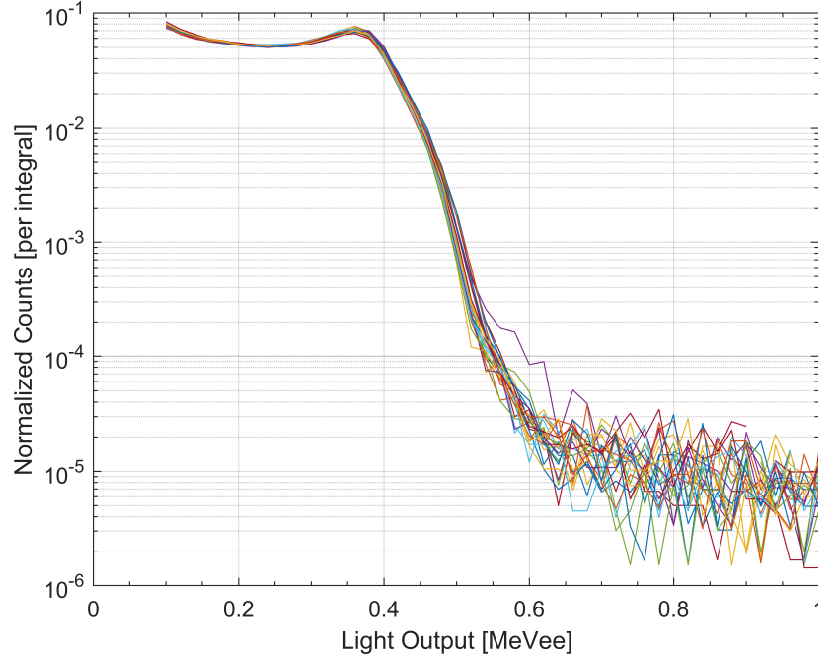
Figure 8.2: Measured light output distributions (normalized per integral) from a ^{137}Cs calibration measurement showing uniform detector response for all 24 stilbene detectors.

light output distributions for all 24 detectors from ^{137}Cs calibration measurement showing detector response uniformity. The stilbene detectors are sensitive to both fast neutrons and gamma rays. PSD based on charge integration was performed for each detector to separate neutron and gamma-ray induced pulses [41, 55, 87]. The integral ranges for the tail integral were optimized for the best PSD performance based on the canonical figure of merit [55]; starting the tail integral window 26 ns past the pulse peak resulted in the highest figure of merit. Figure 8.3 shows the measured pulse tail-to-total integral ratio distribution as a function of the pulse light output for a representative stilbene detector, and shows two regions of data indicative of neutron (upper cluster) and gamma-ray (lower cluster) induced
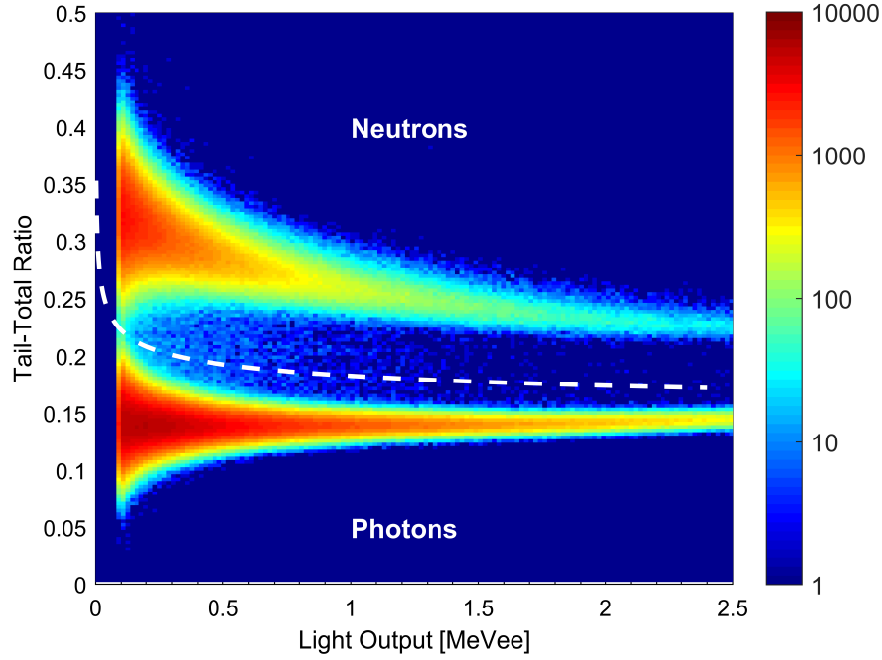
Figure 8.3: Measured pulse tail to total integral ratio distribution as a function of light output for a representative stilbene detector from a ^{252}Cf measurement showing neutron-induced (above the discrimination line) and gamma ray-induced (below the discrimination line) pulses.

pulses for the ^{252}Cf measurement. The discrimination line was optimally determined through an iterative algorithm based on the methods outlined in [57]. The PSD discrimination line was optimized for the ^{252}Cf measurement, which was then used for all measured plutonium samples. Figure 8.4 shows the figure of merit as a function of the light output for a representative stilbene detector. Low-energy detection thresholds were implemented to observe neutrons of different energy groups. The detection thresholds were set in light-output units: thresholds of 0.10, 0.15, and 0.20 MeVee were used for this work. The neutron-equivalent energy (assuming a single scatter full-energy deposition on a recoil proton) was calculated to be 0.73, 0.96, 1.16 MeV for 0.10, 0.15, and 0.20 MeVee, respectively.

Timing offsets due to inherent signal delays in the cables and waveform digitizers were corrected for using the photon-photon coincidences from the ^{252}Cf measurement. The full-width at half maximum of the photon-photon coincidence distribution was approximately
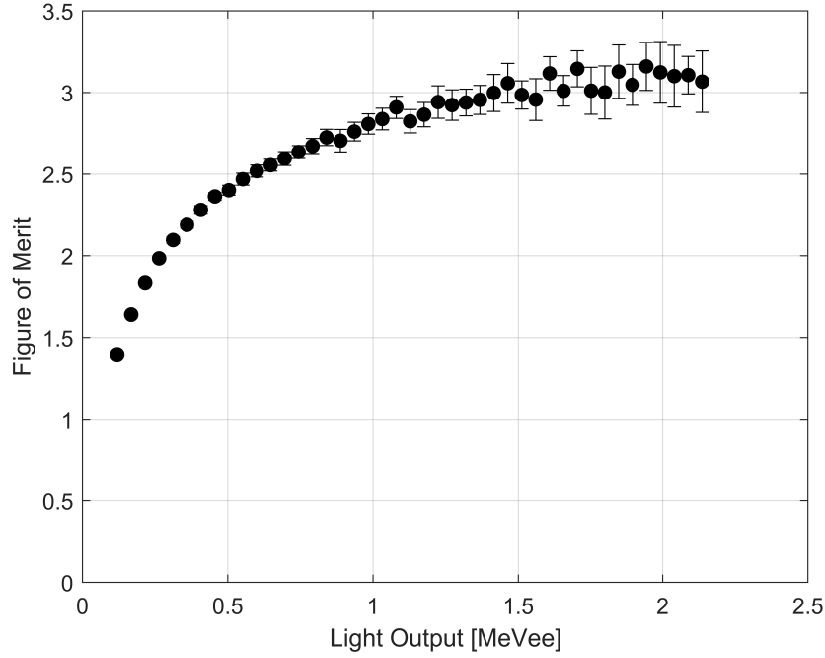
Figure 8.4: The figure of merit for describing the PSD capability of the representative stilbene detector as a function of light output. Error bars represent 2-std. dev. statistical uncertainty; some error bars may be smaller than the marker.

1.6 ns for ^{252}Cf fission photons.

8.3 Data Analysis

The 24 detectors used in this experimental setup yields 276 total possible detection pairs, which can then be categorized into 13 different groups with detection pairs that exhibit similar angles (within 1°). The detection angles were calculated from the center of the detection system to the center position of each detector face, and the full geometric angular range were calculated by considering the maximum and minimum angles that can be formed considering the diameter of each detector. Table 8.3 summarizes the 13 angle groups and its associated geometric angular range, as well as the total number of pairs N within each group.

The (n-n) coincidences within a 200 ns time window for each detector pair was extracted by integrating the (n-n) coincidence time distribution. Figure 8.5 shows the (n-n) coincidence

Table 8.3: A summary of all detection angle groups including the geometric uncertainty and the number of pairs contained in each group.

Detection Angle [°]	Geometric Angular Range [± °]	Number of Pairs N
21.40	± 19.50	16
42.51	± 18.81	24
45.00	± 20.90	8
49.58	± 19.10	32
62.29	± 19.91	16
83.29	± 18.63	16
90.53	± 19.14	40
99.43	± 19.49	16
119.56	± 14.95	16
135.03	± 18.52	48
145.23	± 23.32	16
158.60	± 19.50	16
180.00	± 10.45	12

time distribution for all 276 detector pairs for the ^{252}Cf measurement.
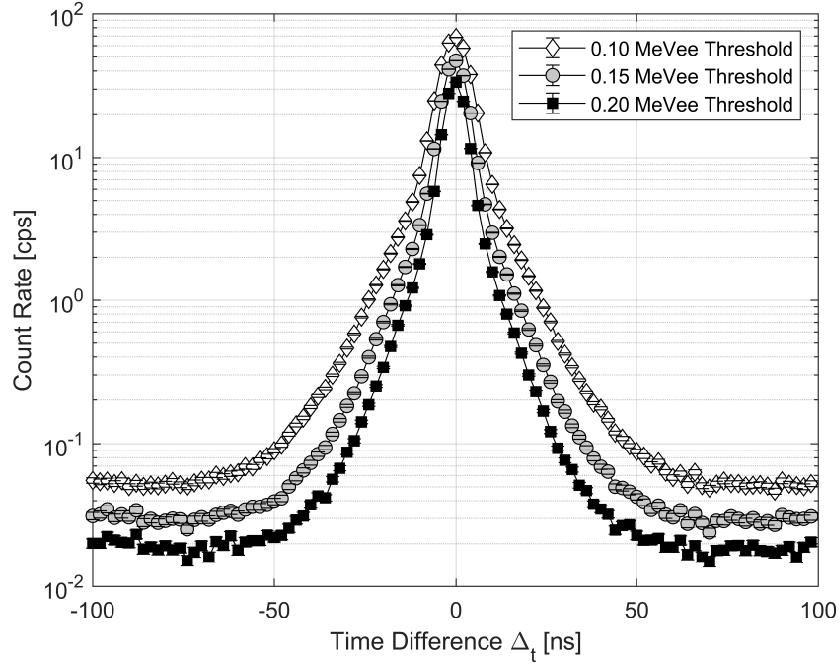
Figure 8.5: (n-n) coincidence time distribution for all 276 detector pairs for the ^{252}Cf measurement for the three different detection thresholds. Error bars represent 2-std. dev. statistical uncertainty; some error bars may be smaller than the marker.

The total (n-n) coincidence time distribution shown in Figure 8.5 can be separated by

each angle group, where the integral of the distribution gives the (n-n) coincident count rate. However, there exist detector pairs that exhibit the same detection angle but different sample-to-detector solid angle. Figure 8.6 shows an example of such scenarios, specifically for the 180° detection angle group.
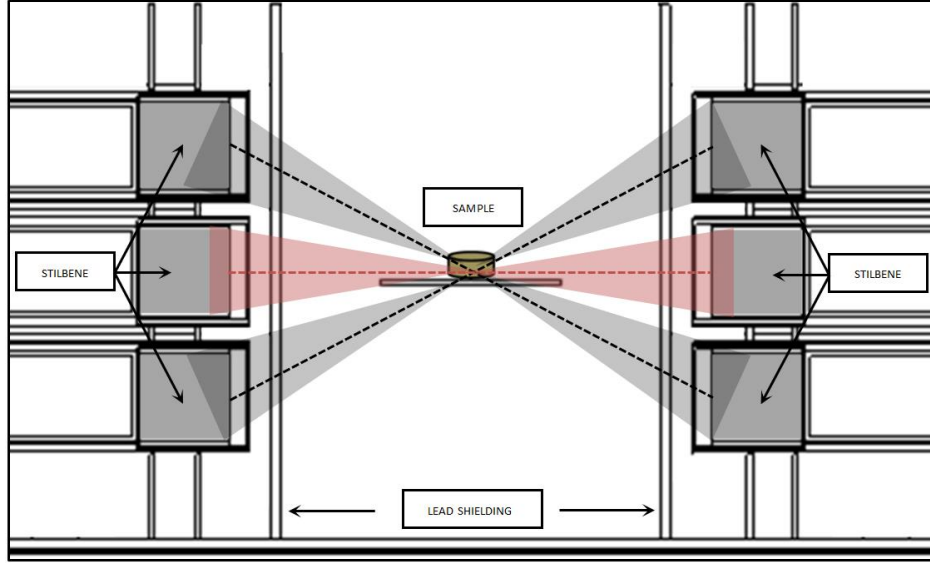
Figure 8.6: A schematic diagram of the experimental setup showing pairs of detectors that exhibit similar angles but different source-to-detector solid angle. The pairs shown in red observe more counts overall relative to the pairs shown in black.

The total coincident count rate for each detector pair can be corrected by dividing the product of the neutron singles counts from the detectors within the pair as described in Eq. (4.20). Figure 8.7 shows the uncorrected (n-n) coincidence time distribution for detector pairs in the 180° group calculated using Eq. (4.17), where there exist two groupings that correspond to pairs that were closer (shown in red) and farther away (shown in black) from the sample. Figure 8.8 shows the singles-corrected (n-n) time-difference distribution calculated using Eq. (4.19) showing good agreement for all pairs in the 180° angle group.

The singles-corrected coincidence counts (i.e., relative coincidences) for each angle group are then calculated by taking the average for all pairs within the group. The relative coincidences for each angle group are calculated using Eq. (4.21). Figure 8.9 shows the full (n-n) angular distribution for the ^{252}Cf measurement.
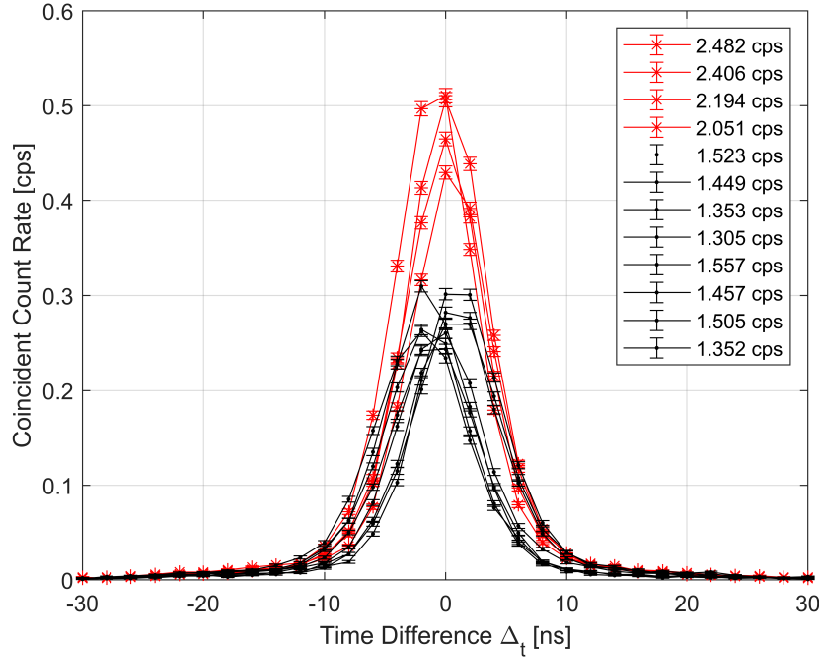
Figure 8.7: The uncorrected (n-n) coincidence time distribution showing the difference between detector pairs that are closer (red) and farther (black) from the sample. The detector pairs that are closer to the sample observe a higher rate of coincident counts. Error bars represent 2-std. dev. statistical uncertainty; some error bars may be smaller than the marker.

From figure 8.9, it is clear that there exists a minimum number of (n-n) coincidences at approximately 90°, and an increase in coincidences at the lower (→0°) and higher (→180°) detection angles. This behavior shows the well-known anisotropic distribution of neutrons from single fission events without any contribution from non-fission neutron emissions. A significant portion of the coincidences observed at the lower angles are attributed to neutron cross-talk effects [26, 69], where a single neutron can scatter and deposit energy above threshold into multiple detectors causing spurious coincident counts. Neutron cross-talk counts between detector pairs are primarily dependent on the relative solid angle between the detectors, as well as the applied detection threshold [69]. That is, we expect the cross-talk counts to diminish as both the relative solid angle and detection threshold increases. This reduction in cross-talk counts is supported by the fact that the coincidences at the lowest-angle, where the detector pairs are adjacent and share a large relative solid angle

147
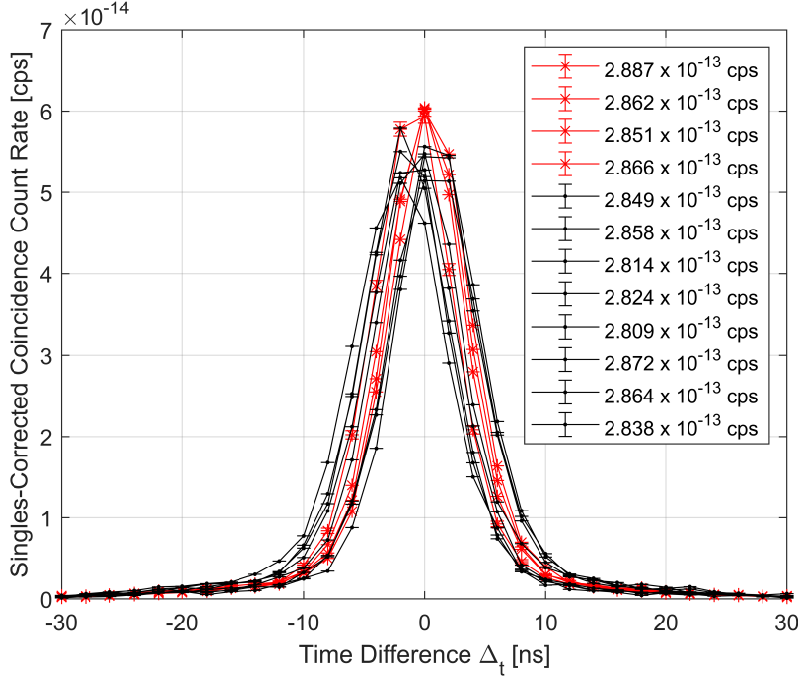
Figure 8.8: The singles-corrected (n-n) coincidence time distribution showing good agreement for all detector pairs regardless of the sample-to-detector solid angle. Error bars represent 2-std. dev. statistical uncertainty; some error bars may be smaller than the marker.

to one another, decreases as the detection threshold is increased The opposite trend exists for the coincidences at the highest angle (180°), which shows that the coincidences become more anisotropic for more energetic neutrons due to the kinematic boost received from the fully-accelerated fission fragments [21–27]. Considering these effects, we quantify the neutron anisotropy by taking the ratio of relative coincidences at 180° to those at approximately 90° using Eq. (4.22), where a value of one represents the case of a purely isotropically emitting source.

8.4 Results and Discussion

Figures 8.10- 8.12 show the full (n-n) angular distributions for each of the plutonium bearing samples using a low energy detection threshold of 0.10, 0.15, and 0.20 MeVee, respectively.

In the ideal case (at the point of emission) where a pure singly-emitting neutron source
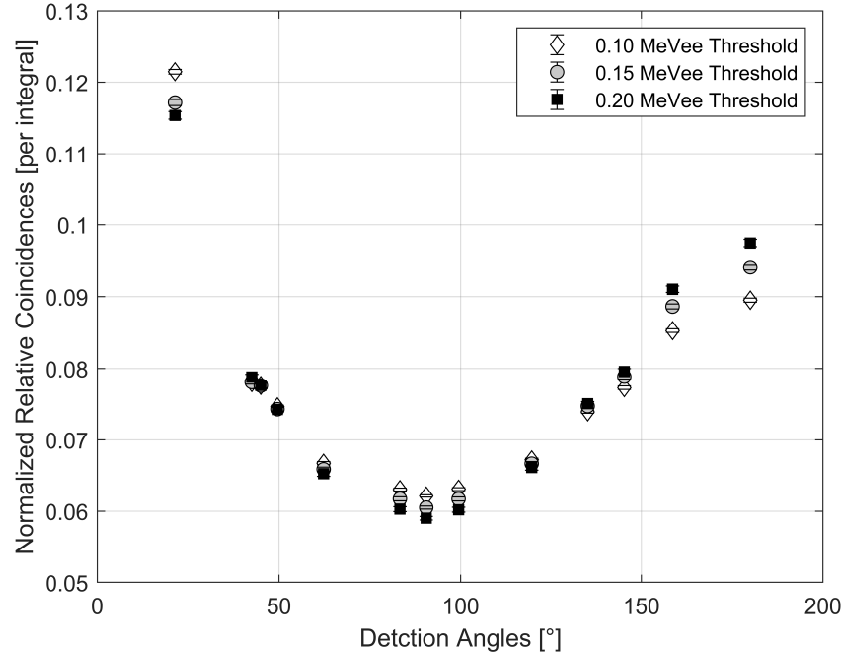
Figure 8.9: Full (n-n) angular distribution (normalized per integral) from the ^{252}Cf measurement for three different detection thresholds. Error bars represent 2-std. dev. statistical uncertainty; some error bars may be smaller than the marker.

is placed in the detection system, one would assume that the angular distribution shown in Figures 10-12 should appear uniform throughout all detection angles; however, we see that there exists some (n-n) correlations due to the cross-talk events from single (α,n) neutrons. Given that the plutonium content is very similar among all the measured sample, the distributions in Figures 8.10 - 8.12 show how the observed n-n angular correlation begins to transition from the true (n-n) correlations from fission neutrons (primarily from ^{240}Pu spontaneous fission) to the cross-talk (n-n) correlations from single (α,n) neutrons. In other words, these results demonstrate how the cross-talk (n-n) correlations associated with (α,n) neutrons reduce the observed n-n angular correlation with increasing α-ratio. Figures 8.10-8.12 also show that the Pu + Mg sample is the most affected by neutron cross-talk events, as evident by the highest relative coincidences at the lowest angle compared to the others. This is as expected since the average energy of the (α,n) neutron from Mg is approximately 2.7 MeV, which is higher than all other samples. Neutrons emitted at higher energies will
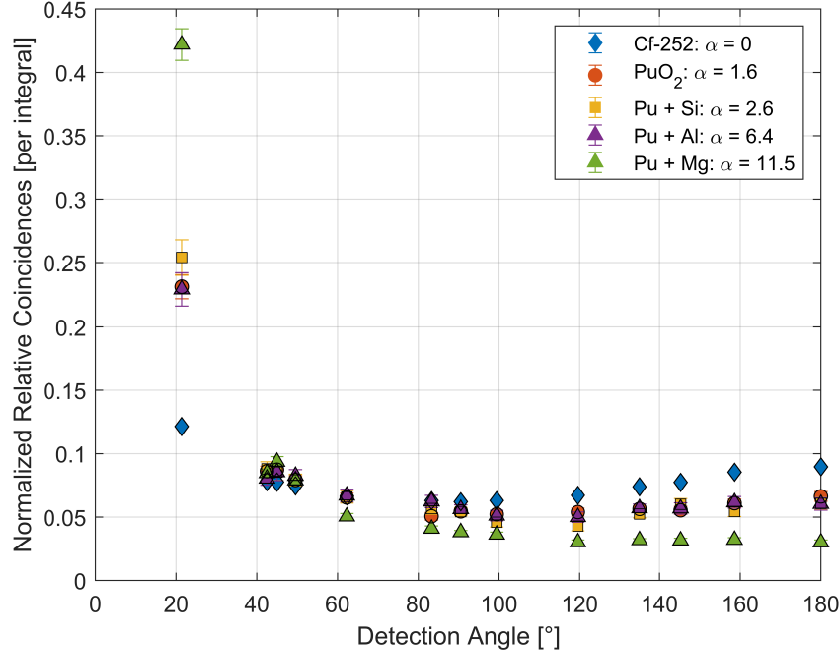
Figure 8.10: Full (n-n) angular distribution (normalized per integral) from all measured samples for a 0.10 MeVee detection threshold. Error bars represent 2-std. dev. statistical uncertainty; some error bars may be smaller than the marker.

exhibit greater neutron cross-talk effects as it has a higher probability of retaining enough energy, after the first detection, to cause a second detection above the detection threshold. Using Eq. (4.22), the observed neutron anisotropy as a function of the detection threshold can be extracted to characterize any existing (n-n) energy-angle correlations. Figure 8.13 shows the neutron anisotropy as a function of the low detection thresholds for ^{252}Cf and the plutonium bearing samples

Overall, a positive correlation between the apparent neutron anisotropy seen by our detection system and the detection threshold can be seen. It is apparent that the positive correlation is relatively unaffected by the contribution from (α,n) neutrons. The Pu + Mg (n-n) coincidences exhibits an anisotropy value of less than one for the 0.10 and 0.15 MeVee case, showing that the neutron cross-talk events are dominating the observed (n-n) coincidences. The anisotropy is resolved for the Pu + Mg (n-n) coincidences at a detection threshold of 0.20 MeVee, where the value is now greater than one. Figure 8.14 shows the neutron anisotropy
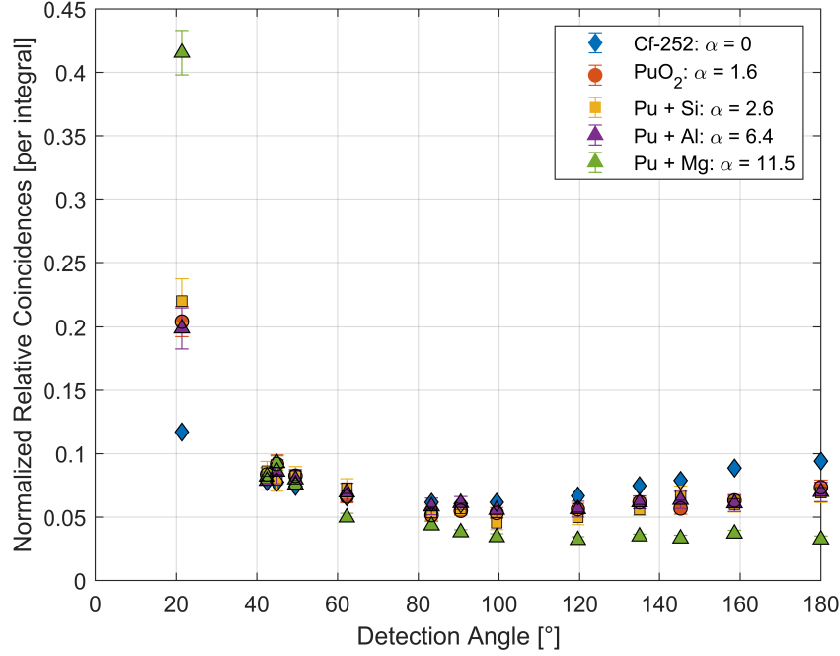
Figure 8.11: Full (n-n) angular distribution (normalized per integral) from all measured samples for a 0.15 MeVee detection threshold. Error bars represent 2-std. dev. statistical uncertainty; some error bars may be smaller than the marker.

as a function of the known α-ratio for the three different detection thresholds.

From Figure 8.14, the (n-n) coincidences appear more isotropic as the α-ratio increases, which confirms that the observed anisotropy is diminished due to the isotropic emission probability of the singly-emitted (α,n) neutrons. It is also evident that the sensitivity of the observed anisotropy is dependent on the detection threshold. A higher detection threshold observes neutrons of higher energy increasing the magnitude of the anisotropy, due to the kinematic boost received by the fission fragments (evident by the ^{252}Cf results), but also reduces the contribution from neutron cross-talk effects. Ultimately, a higher detection threshold enhances the observed anisotropy from the fission neutrons and simultaneously suppresses the adverse effects of neutron cross-talk events
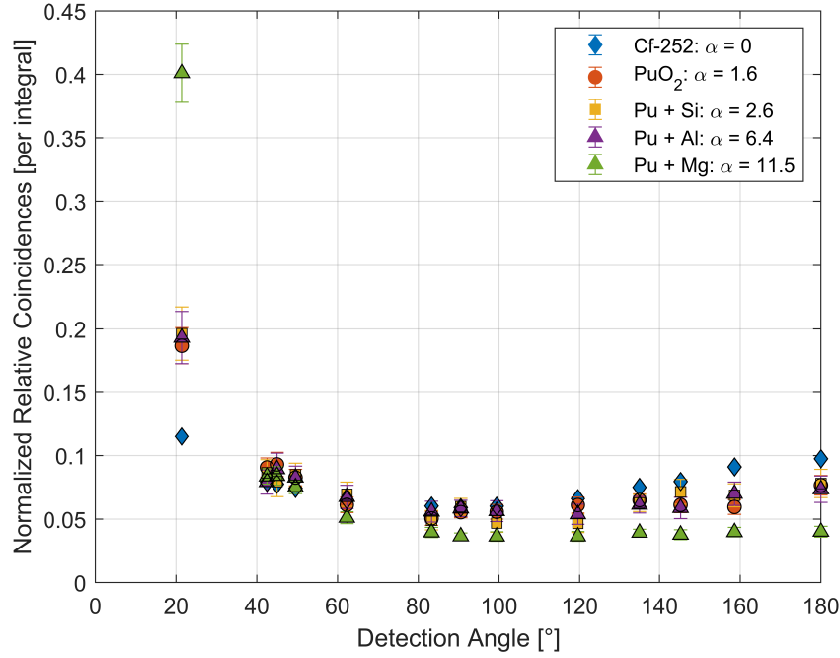
Figure 8.12: Full (n-n) angular distribution (normalized per integral) from all measured samples for a 0.20 MeVee detection threshold. Error bars represent 2-std. dev. statistical uncertainty; some error bars may be smaller than the marker.

8.5 Sources of Error

The systematic error from neutron cross-talk effects would contribute to the calculation of the neutron anisotropy. The anisotropy may have been calculated to be slightly less than the actual emitted anisotropy due to non-zero probability at all detection angles of cross-talk events occurring. Furthermore, scatters within the encapsulation of the samples could also modulate the initial direction of the outgoing neutrons, which again could result in an observed anisotropy that is slightly less than the actual emitted anisotropy. It is assumed that this scattering effect is consistent for all measured plutonium samples since the encapsulation for each sample were nearly identical. A source of error specific to organic scintillators is the fidelity of particle identification. Misclassification of neutrons as gamma rays does not affect the results because these neutrons, classified as gamma rays, are not used in the analysis. On the contrary to neutron misclassification, gamma rays that are misclassified as neutrons will affect the overall results as they are included in the analysis. However, the
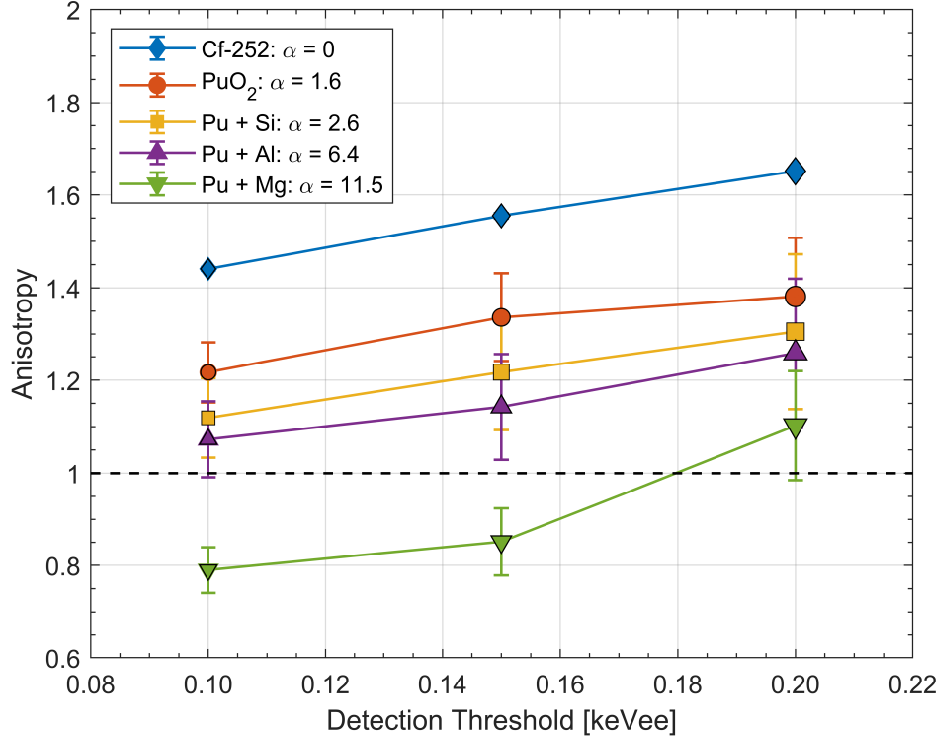
Figure 8.13: Neutron anisotropy as a function of low energy detection threshold showing a positive energy-angle correlation. Error bars represent 2-std. dev. statistical uncertainty; some error bars may be smaller than the marker.

effect on the (n-n) coincidences from the neutron-classified gamma rays are expected to be independent of detection angle since the fission gamma-ray angular distribution is known to be relatively isotropic [82]. Therefore, the calculated neutron anisotropy is relatively unaffected by sporadic neutron-classified gamma rays. The gamma-ray misclassification rate (per incident particle) was estimated to be 3.812×10^{-5}, 3.067×10^{-6}, and 5.017×10^{-6} for a detection threshold of 0.10, 0.15, and 0.20 MeVee, respectively.

8.6   Summary and Conclusions

In this work, I have performed dedicated experiments to characterize the observed (n-n) angular distribution and (n-n) energy-angle correlations for plutonium samples of similar mass and multiplication, but varying α-ratios. The experimental results show that the
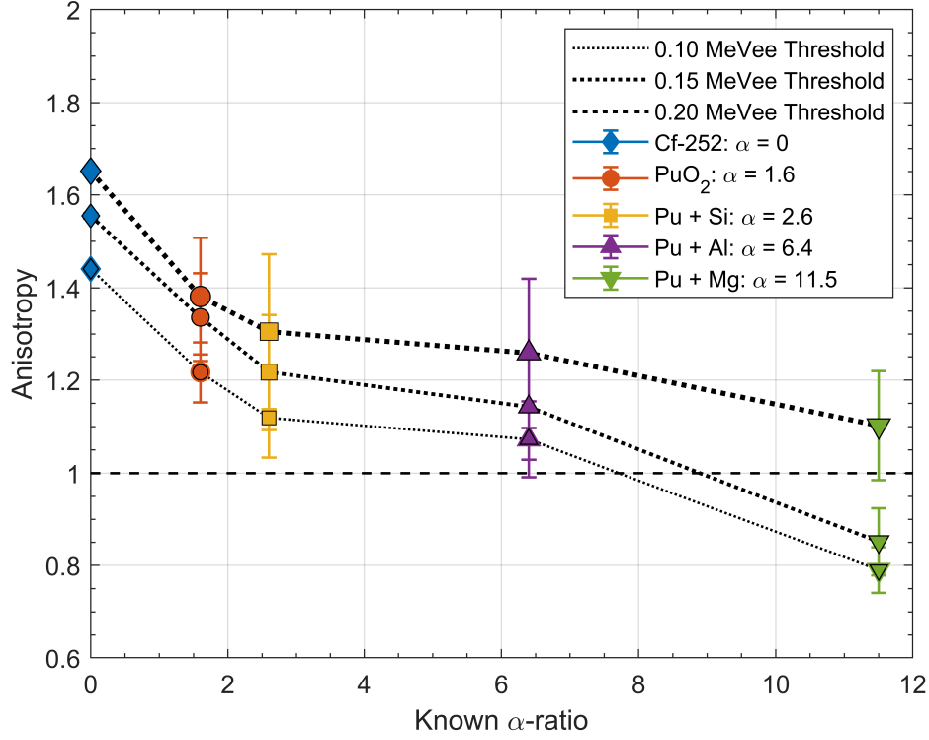
Figure 8.14: Neutron anisotropy as a function of the α-ratio showing the (n-n) coincidences appear more isotropic as the contribution from (α,n) neutrons increase. Error bars represent 2-std. dev. statistical uncertainty; some error bars may be smaller than the marker.

neutron-neutron angular correlations seen by the detection system shifts from observing the true n-n correlations from fission neutrons to observing cross-talk (n-n) correlations associated with a single (α,n) neutron being detected in two detectors. In addition, neutron-neutron energy-angle correlations were extracted by implementing varying low-detection thresholds to observe neutrons of higher energies. The results demonstrate a positive correlation between the neutron anisotropy and energy that is relatively independent of the α-ratio. Furthermore, we demonstrate that the sensitivity of the observed neutron anisotropy on the α-ratio is directly related to the applied detection threshold; raising the threshold enhances the anisotropy signatures from the fission neutrons, while simultaneously suppressing adverse neutron cross-talk effects. The characteristic signatures observed in the neutron energy and angular distribution can provide the means for new techniques that simultaneously utilize both types of information.

CHAPTER IX

Conclusions and Future Work

9.1 Summary of Results

I began in Chapter I with the historical, political, technical motivations for my thesis work in the context of nuclear safeguards application. I also discuss the current limitations of international safeguards inspections, where the speed, accuracy, and sensitivity to detect the diversion of fissile mass are paramount for practical applications. I provide the overview of the chapters, and highlight the specific contributions of my work.

In Chapter II, I describe the timescale of the nuclear fission process, and the characteristic energy, angular, and multiplicity distribution of prompt fission neutrons as well as nonfission neutrons. I provide an explanation of the possible pathways a neutron may undergo in a typical sample of SNM, and relate these pathways to the fissile material physical properties including the ^{240}Pu$_{\text{eff}}$ mass, the leakage multiplication, and the α-ratio. I describe the previous theoretical formulation for the factorial moments of the emitted neutron multiplicity distribution from the superfission process.

In Chapter III, I discuss the detection mechanisms of organic scintillators and provide a detailed characterization of the *trans*-stilbene detectors I used for this work. I also discuss digital pulse processing techniques to implement PSD and TCA on the detected signals. I use a detailed MCNP detector model and experiment-informed detector response algorithm to produce high fidelity simulations of the *trans*-stilbene detector response. I present experi-

mental results characterizing the expected behavior of neutron cross-talk effects considering the system geometry and detection thresholds. From these results, I conclude that cross-talk effects are more prevalent for lower detection thresholds and for detector pairs in close proximity.

In Chapter IV, I present both the theoretical and practically techniques specific for FNMC systems. I discuss the various methods of extracting neutron multiplicity count rates, and also present techniques to extract event-by-event neutron-neutron correlations. I present my PKE with neutron cross-talk corrections, which is derived from the PKE described in Chapter II, and provide the analytic solutions for the three fissile material physical properties of interest.

In Chapter V, I analyzed experimental data to demonstrate the FNMC system capability for implementing passive NDA on Pu-metal plates using a one-parameter, two-parameter, and three-parameter assay approach. I show that as more parameters are used for the NDA, less demand on the availability of well known calibration samples is required (e.g., three-parameter assay requires no calibration samples assuming a well known system efficiency). Using a one-parameter assay, the average deviation from the true mass of all assayed assemblies was $\pm$ 3 %. Using a two-parameter assay, the average deviation from the true mass of all assayed assemblies was $\pm$ 2 %. I provide, for the first time, experimental verification of the FNMC PKE with neutron cross-talk corrections, where I show that the corrections improve the analytic mass estimates for the 1-plate and 3-plate configuration substantially. I also discuss the limitations of the three-parameter assay approach using the 5-plate and 7-plate configurations, where the PKE assumptions become unreliable.

In Chapter VI, I summarize the experimental results from my experiment at Idaho National Laboratory for characterizing the FNMC system sensitivity for detecting the diversion of UO_2 fuel pins. From the experimental results, I demonstrate that the FNMC system is able to to detect (with > 95 % CI) a 50.00 % mass removal for a 60-second assay, and down to 12.50 % mass removal for a 300-second assay. I extend the study in simulations, where

I use benchmarked simulations of the currently deployed capture-based UNCL system and directly compare to simulations of an FNMC system where I show that the FNMC system is more sensitive to smaller mass-diversions than the UNCL system for fixed assay times of 600 and 1800 seconds.

In Chapter VII, I analyzed the experimental data from the passive FNMC measurements for the PANN Pu-metal assemblies specifically to extract the angular and energy-angle correlations as a function of the assembly leakage multiplication. I show, for the first time, that the observed angular and energy-angle correlations diminish as the leakage multiplication increases, attributed to the weakening of the angular correlations as fission chain lengths become longer. The observed angular correlation (quantified by the anisotropy) with a 0.5 MeV neutron-equivalent threshold ranges from ≈ 1.2 to ≈ 1 showing that the angular correlation asymptotically approaches unity as the leakage multiplication increases. The observed angular correlation for the assembly with the lowest leakage multiplication of 1.072 ranges from ≈ 1.2 to ≈ 1.7 for detection thresholds of 0.5 to 1.5 MeV neutron-equivalent energies. From these results, I conclude that the energy-angle correlations exhibit a positive trend as the detection threshold increases, and that the magnitude of the correlation diminishes as the leakage multiplication increases.

In Chapter VIII, I analyzed the experimental data from my experiment at Los Alamos National Laboratory, where I extract the angular and energy-angle correlations as a function of the α-ratio. I measured a series of plutonium samples with similar mass and leakage multiplication, but varying contributions from (α, n) neutrons due to the different types of low-z impurities contained in each sample. I demonstrate that the observed angular correlations transitions from true fission neutron correlations to cross-talk induced correlations from the singly emitted (α, n) neutron, specifically shown by the correlation observed in the coincidences from the Pu + Mg where the anisotropy is less than one. I show that raising the detection threshold can be used to enhance the true fission neutron correlations and simultaneously suppress the cross-talk induced correlations. I present experimental results,

for the first time, showing the observed angular correlations and energy-angle correlation as a function of the α-ratio.

9.2 Conclusions

The theoretical, practical, and experimental results I present in this dissertation demonstrates that the FNMC is a unique and viable alternative method for NDA of SNM in nuclear safeguards applications. FNMC offers improvements in the measurement precision for fixed acquisition times, which in turn improves the current limitations of NDA such as the speed, sensitivity, and accuracy of detecting diverted mass. Furthermore, FNMC provides access to unique correlated signatures in the emitted neutron multiplicity, energy, and angular distribution, unlike traditional capture-based NMC that is only sensitive to the emitted neutron multiplicity. The correlated signatures observed from FNMC could provide independent characterization of the physical fissile material properties complimentary to other characterization techniques (i.e., FNMC PKE). There exists several limitations that are inherent to FNMC techniques and systems. One limitation involves the geometrically dependent system response for large volume SNM, where the FNMC PKE become unreliable. I provide possible pathways to mitigate the break down of the point model approximation in Chapter V, such as increasing the distance as well as adding cadmium sheets between the detectors and the SNM. Another challenge that may arise in more practical settings is the gamma-ray sensitivity of FNMC systems, where a high photon flux can degrade the fidelity of particle identification using PSD.

9.3 Future Work

Future work should consider the transition from laboratory settings to in-field deployment, where the robustness, reliability, and longevity should be well characterized. Although I have shown that the FNMC system and associated techniques are viable for nuclear safe-

guards applications, many of the experiments were performed in controlled laboratory environment. Factors such as the environmental effects (e.g., temperature, other sources of radiation, etc.) must be well characterized prior to deployment. The form factor of the FNMC system should also be considered for in-field deployment, where the size, portability, and ease-of-use are prioritized to ensure that the users of these systems are able to systematically perform NDA in a consistent manner [8].

APPENDICES

APPENDIX A

Uncertainty of Neutron Multiplicity Count Rates using Various Gate Generation Techniques

This appendix shows the expressions for the error in the measured neutron singles, doubles, and triples count rates using the MSR gate generation method outlined in Section 4.1; the MSR gate generation technique was used throughout this work. The expressions shown here are taken from the work of M. K. Prasad et. al. [67]. The error in the measured neutron singles rate, σ_S, is calculated as

$$\sigma_S = \left[\frac{S + 2Dx_2}{T_M} \right]^{\frac{1}{2}}, \tag{A.1}$$

where

$$x_k = \frac{w_k}{f^{k-1}} \tag{A.2}$$

is the ratio of the RTI and STI gate utilization factor defined in (4.9) and (4.13). The error in the measured neutron doubles rate, σ_D, is calculated as

$$\sigma_D = \left[\frac{D + 2S^2 T_G + 2T + 4DST_G x_2 + 2\frac{D^3 x_2}{S^2}}{T_M} \right]^{\frac{1}{2}}. \tag{A.3}$$

161

The error in the measured neutron triples rate, σ_T, is calculated as

$$\sigma_T = \left[\frac{T + D^2T_G + DST_G + 2STT_G + S^3T_G^2 + 2\frac{DT^2x_2}{S^2} + 10D^2T_Gx_2}{T_M} \right.$$
$$+ \frac{2\frac{D^3T_Gx_2}{S} + 2DST_Gx_2 + 4DTT_Gx_2 + 4DS^2T_G^2x_2 + 4D^2ST_G^2x_2^2}{T_M}$$
$$\left. + \frac{12DTT_Gx_3 + 12STT_Gx_3 + 6Z_4 + 12ST_Gx_4Z_4 + 6Z_5}{T_M} \right]^{\frac{1}{2}} \tag{A.4}$$

with

$$Z_k = R_k f^k \tag{A.5}$$

where R_k are the uncorrected k^{th}-order moments from the $m_{n(\mu)}$ and $m_{b(\mu)}$. Relating the Z_k to the measured neutron singles, doubles, and triples rates gives the following relationships:

$$\begin{aligned} Z_1 &= S = R_1 \quad , \\ Z_2 &= D = R_2 f \quad , \\ Z_3 &= T = R_3 f^2 \quad , \\ Z_4 &= R_4 f^3 \quad , \quad \text{and} \\ Z_5 &= R_5 f^4. \end{aligned} \tag{A.6}$$

Figure A.1 shows the relative standard deviation in the measured neutron doubles rate using RTI, STI, and MSR gate generation methods as a function of the time gate width for a fixed acquisition time. Expressions for the counting errors using the RTI and STI gate generation methods can be found in [67].
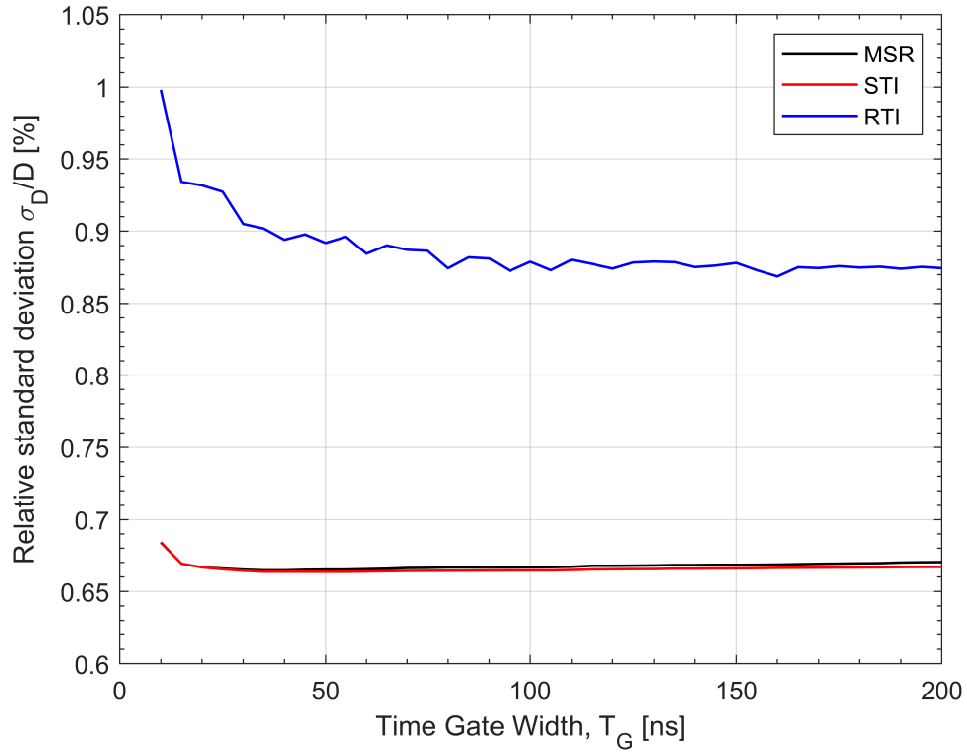
Figure A.1: Calculated relative standard deviation of the measured neutron doubles rate using the various gate generation methods. The MSR method was used throughout this work.

APPENDIX B

Source Code for PSD Optimization Algorithm

This appendix shows the slice PSD optimization algorithm adopted from the work of J. K. Polack et. al. [57] written in MATLAB. This algorithm utilizes the tail-to-total ratio versus measured light output as the two discriminating parameters for PSD, rather than using tail integral versus the total integral shown in [57]. This is the main source code Slice_Script_PID.m, which requires the functions Discrimination.m, Slice_script_prefit.m, and GaussFit.m

```
% Main Slice PSD algorithm code, requires Slice_prefit_PID.m, Discrimination.m,
% and GaussFit.m
% Slice PSD algorithm optimizes the PSD discrimination
% line on an energy-dependent basis
% T.H. Shin
% March 2015



%%%%%%%%%%%%%%%%%%%%%%%%%%%%%%%%%%%%%%%%%%%%%%%%%%%%%%%%%%%%%%%%%%%%%%%%%%%%%%
% User inputs
%%%%%%%%%%%%%%%%%%%%%%%%%%%%%%%%%%%%%%%%%%%%%%%%%%%%%%%%%%%%%%%%%%%%%%%%%%%%
vars = struct();
```

```matlab
ask = 'Maximum Integral? ';

vars.Vmax = input(ask);

ask = 'Cs-edge [V*ns]? ';

vars.Cs_edge = input(ask);

ask = 'Minimum number of pulses per slice? ';

vars.min_pulses_slice = input(ask);

ask = 'Number of slices? ';

vars.slices = input(ask);

ask = 'Data file name? ';

vars.fname = input(ask,'s');
%%%%%%%%%%%%%%%%%%%%%%%%%%%%%%%%%%%%%%%%%%%%%%%%%%%%%%%%%%%%%%%%%%%%%%%%%%%%%%%%%
data_in = dlmread(vars.fname);

% Run Pre Fit


Slice_prefit_PID

clearvars -except vars data_in



data_out = struct();


s0 = vars.good_slices(end);

single_mean_mode = 0;

start_slice = round(0.1*s0);

S0 = s0-start_slice;

data_out.slice_numbers = linspace(1,s0-start_slice,S0)';

for i = vars.good_slices(1):S0

    clearvars -except vars slicefit_prior R2_prior s0 single_mean_mode ...

    i data_out S0

    sn = S0-i+vars.good_slices(1);

    disp(['Evaluating slice ' num2str(sn)])

    % Grab PH and D for single slice

    if sn == 1

        holder_PH(:,1) = vars.PH(vars.PH<=vars.s_bins(sn));
```

```matlab
        holder_D(:,1) = vars.D(vars.PH<=vars.s_bins(sn));
    else
        holder_PH(:,1) = vars.PH(vars.PH<=vars.s_bins(sn));

        holder_D(:,1) = vars.D(vars.PH<=vars.s_bins(sn));

        holder_D = holder_D(holder_PH > vars.s_bins(sn-1));

        holder_PH = holder_PH(holder_PH > vars.s_bins(sn-1));
    end


    histD = histc(holder_D,vars.D_bins_tf);


    if single_mean_mode == 0
        if sn == S0
            data_out.npulses(sn,1) = length(holder_PH);
            [gauss_fit,gof] = GaussFit(2,sn,vars,data_out,1,1,histD);
            R2 = gof.rsquare;
            if R2 < 0.95
                R2_old = R2;
                gauss_fit_old = gauss_fit;
                [gauss_fit,gof] = GaussFit(99,sn,vars,data_out,1,1,histD);
                R2 = gof.rsquare;
                if R2 < R2_old
                    gauss_fit = gauss_fit_old;
                    R2 = R2_old;
                end
            end
        else
            data_out.npulses(sn,1) = length(holder_PH);
            norm_ratio = data_out.npulses(sn)/data_out.npulses(sn+1);
            if R2_prior >= 0.95
                [gauss_fit,gof] = GaussFit(3,sn,vars,data_out,norm_ratio, ...
                slicefit_prior,histD);
                R2 = gof.rsquare;
            else
```

```matlab
            [gauss_fit,gof] = GaussFit(2,sn,vars,data_out,1,1,histD);

            R2 = gof.rsquare;

        end

        if R2 < 0.95

            R2_old = R2;

            gauss_fit_old = gauss_fit;

            [gauss_fit,gof] = GaussFit(4,sn,vars,data_out,norm_ratio, ...

            slicefit_prior,histD);

            R2 = gof.rsquare;

            if R2 < R2_old

                gauss_fit = gauss_fit_old;

                R2 = R2_old;

            end

        end

    end

    data_out.slice_Tfits(sn,:) = [gauss_fit.a1 gauss_fit.b1 gauss_fit.c1 ...

            gauss_fit.a2 gauss_fit.b2 gauss_fit.c2];

    data_out.slice_Gfits(sn,:) = [gauss_fit.a1 gauss_fit.b1 gauss_fit.c1];

    data_out.slice_Nfits(sn,:) = [gauss_fit.a2 gauss_fit.b2 gauss_fit.c2];

    CI = confint(gauss_fit,0.95);

    data_out.slice_Tfits_CI(sn,:) = abs(data_out.slice_Tfits(sn,:)-CI(1,:));

    data_out.slice_Gfits_CI(sn,:) = data_out.slice_Tfits_CI(sn,1:3);

    data_out.slice_Nfits_CI(sn,:) = data_out.slice_Tfits_CI(sn,4:6);

else

    disp('Single Mean Mode =(')

    data_out.npulses(sn,1) = length(holder_PH);

    norm_ratio = data_out.npulses(sn)/data_out.npulses(sn+1);

    [gauss_fit,gof] = GaussFit(1,sn,vars,data_out,norm_ratio, ...

    slicefit_prior,histD);

    R2 = gof.rsquare;

    data_out.slice_Tfits(sn,:) = [gauss_fit.a1 gauss_fit.b1 ...

    gauss_fit.c1 gauss_fit.a2 gauss_fit.b2 gauss_fit.c2];

    data_out.slice_Gfits(sn,:) = [gauss_fit.a1 gauss_fit.b1 gauss_fit.c1];
```

167

```matlab
        data_out.slice_Nfits(sn,:) = [gauss_fit.a2 gauss_fit.b2 gauss_fit.c2];

        Conf_Int = confint(gauss_fit,0.95);

        data_out.slice_Tfits_CI(sn,:) = Conf_Int(1,:);

        data_out.slice_Gfits_CI(sn,:) = data_out.slice_Tfits_CI(sn,1:3);

        data_out.slice_Nfits_CI(sn,:) = data_out.slice_Tfits_CI(sn,4:6);

end



% single mean mode qualifications
if sn == 1

    single_mean_mode = 0;

else

    Gfit_intercept_NfitHM = data_out.slice_Gfits(sn,2) + ...
        data_out.slice_Gfits(sn,3)*sqrt(-(log(data_out.slice_Nfits(sn,1) ...
        /2/data_out.slice_Gfits(sn,1))));

    if Gfit_intercept_NfitHM < data_out.slice_Nfits(sn,2)

        single_mean_mode = 0;

    else

        single_mean_mode = 1;

    end

end


data_out.slice_hist(sn,:) = histD;

data_out.weight(sn,1) = abs(vars.G_pfit(sn)-vars.N_pfit(sn));

R2_prior = R2;

slicefit_prior = data_out.slice_Tfits(sn,:);


% Discriminate particles
kg = 1;

kn = 1;

[discr_opt,data_out] = Discrimination(sn,data_out,kg,kn,vars);

data_out.discr(sn,1) = discr_opt;
```

168

```matlab
end


clearvars -except data_out vars


data_out.discr_fit = fit(vars.s_plotx(1:length(data_out.discr)), ...
data_out.discr,'power2');
x = (linspace(0,0.478/vars.Cs_edge*vars.Vmax,1001)');




figure(2)
hold on
tdloghist(0.478/vars.Cs_edge.*vars.PH,vars.D,linspace(0, ...
max(0.478/vars.Cs_edge.*vars.PH),200),linspace(min(vars.D),max(vars.D),200))
scatter(vars.s_plotx(1:length(vars.G_pfit)),vars.G_pfit,'ro')
scatter(vars.s_plotx(1:length(vars.N_pfit)),vars.N_pfit,'go')
plot(x,vars.N_mean_pfit.a.*x.^vars.N_mean_pfit.b,'g--')
plot(x,vars.G_mean_pfit.a.*x.^vars.G_mean_pfit.b,'r--')
scatter(vars.s_plotx(1:length(data_out.discr)),data_out.discr,'kx')
plot(x,data_out.discr_fit.a.*x.^data_out.discr_fit.b+ ...
data_out.discr_fit.c,'k--')
ylim([vars.bin_low vars.bin_high])
xlabel('Light Output [MeVee]')
ylabel('Ratio')




figure(3)
errorbar(vars.s_plotx(1:length(data_out.slice_FOM)), ...
data_out.slice_FOM,data_out.slice_FOM_sigma(:,2),'kx')
title('FOM')
xlabel('Light Output [MeVee]')
ylabel('FOM')
```

169

```matlab
g = 1;
ask = 'Would you like to see a specific slice? [yes/no]: ';
see_slice = input(ask,'s');
toss_index = 0;
while strcmp(see_slice,'yes') == 1
    ask = ['Which slice would you like to see? Available  ...
    slices are ' num2str(data_out.slice_numbers(1)) ' to ...
    ' num2str(data_out.slice_numbers(end)) ': '];
    see_slice_n = input(ask);
    figure(5)
    hold on
    plot(vars.D_bins_tf,data_out.slice_hist(see_slice_n,:)./vars.D_dx,'k')
    plot(vars.D_bins_tf,data_out.slice_Gfits(see_slice_n,1) ...
    .*exp(-((vars.D_bins_tf-data_out.slice_Gfits(see_slice_n,2)) ...
    /data_out.slice_Gfits(see_slice_n,3)).^2)./vars.D_dx,'r')
    plot(vars.D_bins_tf,data_out.slice_Nfits(see_slice_n,1) ...
    .*exp(-((vars.D_bins_tf-data_out.slice_Nfits(see_slice_n,2)) ...
    /data_out.slice_Nfits(see_slice_n,3)).^2)./vars.D_dx,'b')
    ask = ['Keep slice ' num2str(see_slice_n) '? [yes/no]: '];
    keep_slice = input(ask,'s');
    close 5
    if strcmp(keep_slice,'yes') == 0
        toss_index(g) = see_slice_n;
        g = g+1;
    end
    ask = 'Would you like to see another slice? [yes/no]: ';
    see_slice = input(ask,'s');
end

if toss_index ~= 0
    vars.s_plotx_removed = vars.s_plotx(data_out.slice_numbers);
    vars.s_plotx_removed(toss_index) = [];
    data_out.discr_removed = data_out.discr;
```

```matlab
data_out.discr_removed(toss_index) = [];
data_out.discr_removed_fit =  fit(vars.s_plotx_removed, ...
data_out.discr_removed,'power2');
data_out.mc_N_removed = data_out.mc_N;
data_out.mc_N_removed(toss_index) = [];
data_out.slice_FOM_removed = data_out.slice_FOM;
data_out.slice_FOM_removed(toss_index) = [];
data_out.slice_FOM_removed_sigma = data_out.slice_FOM_sigma;
data_out.slice_FOM_removed_sigma(toss_index,:) = [];


close 2 3
figure(2)
hold on
tdloghist(0.478/vars.Cs_edge.*vars.PH,vars.D,linspace(0, ...
max(0.478/vars.Cs_edge.*vars.PH),200),linspace(min(vars.D) ...
,max(vars.D),200))
scatter(vars.s_plotx(1:length(vars.G_pfit)),vars.G_pfit,'ro')
scatter(vars.s_plotx(1:length(vars.N_pfit)),vars.N_pfit,'go')
plot(x,vars.N_mean_pfit.a.*x.^vars.N_mean_pfit.b,'g--')
plot(x,vars.G_mean_pfit.a.*x.^vars.G_mean_pfit.b,'r--')
scatter(vars.s_plotx_removed,data_out.discr_removed,'kx')
plot(x,data_out.discr_removed_fit.a.*x.^data_out.discr_removed_fit.b ...
+data_out.discr_removed_fit.c,'k--')
ylim([vars.bin_low vars.bin_high])
xlabel('Light Output [MeVee]')
ylabel('Tail-Total Ratio')
box on


figure(3)
errorbar(vars.s_plotx_removed,data_out.slice_FOM_removed, ...
data_out.slice_FOM_removed_sigma(:,2),'kx')
xlabel('Light Output [MeVee]')
ylabel('FOM')
```

```
    box on
    data_out.discr_removed_fit
else
    data_out.discr_fit
end


clearvars -except data_out vars psd0_FOM
```

The Slice_script_prefit.m function provides initial conditions for the slice-by-slice analysis using the full dataset


```
% Pre-fitting of the total neutron and photon data used to inform
% slice-by-slice Gaussian fitting
% T.H. Shin
% March 2015
vars.D = data_in(:,3);
vars.PH = data_in(:,2);
vars.nbins = 500;
vars.bin_low = min(vars.D);
vars.bin_high = max(vars.D);
vars.peak_comp = 5;
vars.s_bins = (linspace(0+vars.Vmax/vars.slices,vars.Vmax,vars.slices))';
vars.ds = vars.s_bins(2)-vars.s_bins(1);
vars.s_plotx = 0.478/vars.Cs_edge.*(vars.s_bins - vars.ds/2);



G_mean = zeros(vars.slices,1);
N_mean = zeros(vars.slices,1);



clear peaks_tf
vars.D_bins_tf = (linspace(vars.bin_low,vars.bin_high,vars.nbins))';
```

```matlab
vars.D_pulses_tf = histc(vars.D(:,1),vars.D_bins_tf)';

[peaks_tf(:,1), peaks_tf(:,2)] = findpeaks(vars.D_pulses_tf);

sortpeaks_tf = sort(peaks_tf(:,1));

G_peak_loc_tf = peaks_tf(peaks_tf(:,1) == sortpeaks_tf(end),2);


for j = 1:length(sortpeaks_tf)-1

    N_peak_loc_tf = peaks_tf(peaks_tf(:,1) == sortpeaks_tf(end-j),2);

    if length(N_peak_loc_tf) > 1

        N_peak_loc_tf = N_peak_loc_tf(end);

    end

    if length(G_peak_loc_tf) > 1

        G_peak_loc_tf = ceil(mean(G_peak_loc_tf));

    end

    if (sortpeaks_tf(end)/sortpeaks_tf(end-j) > vars.peak_comp) && ...

    (vars.D_bins_tf(N_peak_loc_tf) > vars.D_bins_tf(G_peak_loc_tf))

        break

    else

    end

end

x = vars.D_bins_tf;

dx = abs(x(end)-x(end-1));

[Val_tf, Val_loc_tf] = min(vars.D_pulses_tf(G_peak_loc_tf:N_peak_loc_tf));

Val_loc_tf = Val_loc_tf+G_peak_loc_tf-1;

GD_pulses_tf = zeros(length(vars.D_bins_tf),1);

ND_pulses_tf = zeros(length(vars.D_bins_tf),1);

GD_pulses_tf(1:Val_loc_tf) = vars.D_pulses_tf(1:Val_loc_tf);

GD_pulses_tf(Val_loc_tf:end) = 0;

ND_pulses_tf(1:Val_loc_tf) = 0;

ND_pulses_tf(Val_loc_tf:end) = vars.D_pulses_tf(Val_loc_tf:end);


vars.D_dx = vars.D_bins_tf(end)-vars.D_bins_tf(end-1);

for i2 = 1:vars.slices

    i = vars.slices-i2+1;
```

173

```matlab
    clear holder_D holder_PH D_bins D_pulses GD_pulses ...
        ND_pulses G_peaks N_peaks G_sorted_peaks N_sorted_peaks ...
        G_peak_loc G_peak N_peak_loc N_peak
    % Grab PH and D for single slice
    if i == 1
        holder_PH(:,1) = vars.PH(vars.PH<=vars.s_bins(i));
        holder_D(:,1) = vars.D(vars.PH<=vars.s_bins(i));
    else
        holder_PH(:,1) = vars.PH(vars.PH<=vars.s_bins(i));
        holder_D(:,1) = vars.D(vars.PH<=vars.s_bins(i));
        holder_D = holder_D(holder_PH > vars.s_bins(i-1));
        holder_PH = holder_PH(holder_PH > vars.s_bins(i-1));
    end
    % Check to see if slice contains min number of pulses
    if isempty(holder_D) == 1 || length(holder_D) <= vars.min_pulses_slice
        disp(['Not enough pulses for slice ' num2str(i)])
    else
        vars.good_slices(i,1) = i;
%         D_bins = (linspace(vars.bin_low,vars.bin_high,vars.nbins))';
        D_pulses = histc(holder_D(:,1),vars.D_bins_tf)./vars.D_dx;
        GD_pulses = D_pulses;
        GD_pulses(Val_loc_tf:end) = 0;
        ND_pulses = D_pulses;
        ND_pulses(1:Val_loc_tf) = 0;
        [G_peaks(:,1), G_peaks(:,2)] = findpeaks(GD_pulses);
        G_sorted_peaks = sort(G_peaks(:,1));
        G_peak_loc = G_peaks(G_peaks(:,1) == G_sorted_peaks(end),2);
        G_peak = G_sorted_peaks(end);
        [N_peaks(:,1), N_peaks(:,2)] = findpeaks(ND_pulses);
        N_sorted_peaks = sort(N_peaks(:,1));
        if isempty(N_sorted_peaks) == 1
%             disp('No Neutron Peak')
        else
```

174

```
        N_peak_loc = N_peaks(N_peaks(:,1) == N_sorted_peaks(end),2);
        N_peak = N_sorted_peaks(end);
            if length(N_peak_loc) > 1
                N_peak_loc = N_peak_loc(1);
            end
            if length(G_peak_loc) > 1
                G_peak_loc = G_peak_loc(1);
            end
            G_mean(i,1) = vars.D_bins_tf(G_peak_loc);
            N_mean(i,1) = vars.D_bins_tf(N_peak_loc);
        end
    end
end
vars.good_slices(vars.good_slices == 0) = [];


G_mean(G_mean(:,1) == 0,:) = [];
N_mean(N_mean(:,1) == 0,:) = [];


vars.G_mean_pfit = fit(vars.s_plotx(1:length(G_mean)),G_mean(:,1),'power1');
vars.N_mean_pfit = fit(vars.s_plotx(1:length(N_mean)),N_mean(:,1),'power1');
vars.G_pfit = vars.G_mean_pfit.a.*vars.s_plotx.^vars.G_mean_pfit.b;
vars.N_pfit = vars.N_mean_pfit.a.*vars.s_plotx.^vars.N_mean_pfit.b;
x = (linspace(0,0.478/vars.Cs_edge*vars.Vmax,1001)');
```

The GaussFit.m function is an iterative Gaussian fitting function that is informed by the initial conditions from the Slice_script_prefit.m function.

```
function [ gauss_fit, gof ] = GaussFit( gauss_params, sn, ...
vars, data_out, norm_ratio, slicefit_prior, histD )
% Iterative Gaussian fitting routine
% for fitting the neutron and photon distributions
% T.H. Shin
```

```matlab
% March, 2015
clear LB UB SP
if size(histD,2)>size(histD,1)
    histD = histD';
end
if gauss_params == 1
    LB = [0,0,0,0,0.5*slicefit_prior(5),0];
    UB = [data_out.npulses(sn),1.25*vars.G_pfit(sn), ...
    0.5,data_out.npulses(sn), ...
        1.25*vars.N_pfit(sn),0.5];
    SP = [norm_ratio*slicefit_prior(1),vars.G_pfit(sn),slicefit_prior(3), ...
        norm_ratio*slicefit_prior(4),vars.N_pfit(sn),slicefit_prior(6)];
    [gauss_fit, gof] = fit(vars.D_bins_tf,histD,'gauss2','Lower',LB, ...
    'Upper',UB,'Startpoint',SP);
elseif gauss_params == 2
    LB = [0,0.75*vars.G_pfit(sn),0,0,0.75*vars.N_pfit(sn),0];
    UB = [data_out.npulses(sn),1.25*vars.G_pfit(sn), ...
    0.5,data_out.npulses(sn), ...
        1.25*vars.N_pfit(sn),0.5];
    [gauss_fit, gof] = fit(vars.D_bins_tf,histD,'gauss2','Lower',LB, ...
    'Upper',UB);
elseif gauss_params == 3
    LB = [0,0.75*vars.G_pfit(sn),0,0,0.75*vars.N_pfit(sn),0];
    UB = [data_out.npulses(sn),1.25*vars.G_pfit(sn), ...
    0.5,data_out.npulses(sn), ...
        1.25*vars.N_pfit(sn),0.5];
    SP = [norm_ratio*slicefit_prior(1),vars.G_pfit(sn),slicefit_prior(3), ...
        norm_ratio*slicefit_prior(4),vars.N_pfit(sn),slicefit_prior(6)];
    [gauss_fit, gof] = fit(vars.D_bins_tf,histD,'gauss2','Lower',LB, ...
    'Upper',UB,'Startpoint',SP);
elseif gauss_params == 4
    LB = [0,0.75*slicefit_prior(2),0,0,0.75*slicefit_prior(5),0];
    UB = [data_out.npulses(sn),1.25*slicefit_prior(2), ...
```

```
        0.5,data_out.npulses(sn), ...
            1.25*slicefit_prior(5),0.5];
        SP = [norm_ratio*slicefit_prior(1),slicefit_prior(2),slicefit_prior(3), ...
            norm_ratio*slicefit_prior(4),slicefit_prior(5),slicefit_prior(6)];
        [gauss_fit, gof] = fit(vars.D_bins_tf,histD,'gauss2','Lower',LB, ...
        'Upper',UB,'Startpoint',SP);
    else
        LB = [0,0,0,0,0,0];
        [gauss_fit, gof] = fit(vars.D_bins_tf,histD,'gauss2','Lower',LB);
    end



    end
```

The Discrimination.m function calculates the optimal discrimination value for each slice of data, and returns the optimized value for all slices. It also calculates the figure of merit and the particle misclassification rate for each slice.

```
function [ discr_opt,data_out] = Discrimination( sn,data_out,kg,kn,vars )
% Optimization of the discrimination value for each slice of data
% T.H. Shin
% March, 2015
x = vars.D_bins_tf;
dx = vars.D_dx;

Gfit_func = @(x) (data_out.slice_Gfits(sn,1).*exp(-((x- ...
data_out.slice_Gfits(sn,2))/data_out.slice_Gfits(sn,3)).^2))./dx;
Nfit_func = @(x) (data_out.slice_Nfits(sn,1).*exp(-((x- ...
data_out.slice_Nfits(sn,2))/data_out.slice_Nfits(sn,3)).^2))./dx;
data_out.GTotal(sn) = integral(Gfit_func,0,1);
data_out.NTotal(sn) = integral(Nfit_func,0,1);
```

177

```matlab
MC_options = zeros(length(x),1);


for j = 1:length(x)

    MC_options(j) = kg/data_out.GTotal(sn)*(integral(Gfit_func,x(j),1)) ...

        + kn/data_out.NTotal(sn)*(integral(Nfit_func,0,x(j)));

end
[~,discr_opt] = min(MC_options);

discr_opt = x(discr_opt);

data_out.det_G(sn,1) = integral(Gfit_func,0,discr_opt);

data_out.mc_G(sn,1) = integral(Gfit_func,discr_opt,1);

data_out.det_N(sn,1) = integral(Nfit_func,discr_opt,1);

data_out.mc_N(sn,1) = integral(Nfit_func,0,discr_opt);


d = abs(data_out.slice_Gfits(sn,2)-data_out.slice_Nfits(sn,2));

FWHM_gamma = 2*abs((data_out.slice_Gfits(sn,2) - ...

data_out.slice_Gfits(sn,3) ...

    *sqrt(log(data_out.slice_Gfits(sn,1)/ ...

    (data_out.slice_Gfits(sn,1)/2))))-data_out.slice_Gfits(sn,2));

FWHM_neutron = 2*abs((data_out.slice_Nfits(sn,2) - ...

data_out.slice_Nfits(sn,3) ...

    *sqrt(log(data_out.slice_Nfits(sn,1)/ ...

    (data_out.slice_Nfits(sn,1)/2))))-data_out.slice_Nfits(sn,2));

data_out.slice_FOM(sn,1) = d/(FWHM_gamma+FWHM_neutron);


sigma_FWHM_gamma = 2*sqrt(log(2))*data_out.slice_Gfits_CI(sn,3);

sigma_FWHM_neutron = 2*sqrt(log(2))*data_out.slice_Nfits_CI(sn,3);


sigma_d = data_out.slice_Nfits_CI(sn,2)^2+data_out.slice_Gfits_CI(sn,2)^2;

data_out.slice_d(sn,1) = sigma_FWHM_gamma;

data_out.slice_d(sn,2) = sigma_FWHM_neutron;

data_out.slice_d(sn,3) = sigma_d;
```

```matlab
data_out.slice_FOM_sigma(sn,1) = sigma_d/(FWHM_gamma+FWHM_neutron)^2 ...
+(d^2*sigma_FWHM_neutron^2+d^2*sigma_FWHM_gamma^2) ...
/(FWHM_neutron+FWHM_gamma)^4;
data_out.slice_FOM_sigma(sn,2) = data_out.slice_FOM(sn)*sqrt((sigma_d/d)^2 ...
+(sigma_FWHM_gamma/FWHM_gamma)^2+(sigma_FWHM_neutron/FWHM_neutron)^2);
data_out.slice_FOM_sigma(sn,3) = sqrt((1/(FWHM_gamma+FWHM_neutron))^2 ...
*sigma_d^2);
clear MC_options


end
```

BIBLIOGRAPHY

BIBLIOGRAPHY

[1] O. Hahn and F. Strassmann, "Uber den Nachweis und das Verhalten der bei der Bestrahlung des Urans mittels Neutronen entstehenden Erdalkalimetalle," *Naturwissenschaften*, vol. 27, no. 1, pp. 11–15, 1939.

[2] L. Meitner and O. R. Frisch, "Products of the fission of the uranium nucleus," *Nature*, vol. 143, no. 3620, pp. 471–472, 1939.

[3] R. Rhodes, *Making of the Atomic Bomb*. New York: Simon and Schuster, 1986.

[4] A. Einstein and L. Szilard, "Letter to President Roosevelt." [Online]. Available: http//hypertextbook.com/e-world/einstein.shtml

[5] "Atoms for Peace Address." [Online]. Available: https://www.iaea.org/about/history/atoms-for-peace-speech

[6] J. E. Doyle, *Nuclear Safeguards, Security, and Nonproliferation*. Oxford: Butterworth-Heinemann, 2008.

[7] "Treaty on the Non-Proflieration of Nuclear Weapons." [Online]. Available: http://disarmament.un.org/treaties/t/npt

[8] "Safeguards techniques and equipment: 2011 edition," International Atomic Energy Agency, Vienna, Austria, Tech. Rep., 2011.

[9] "Special Nuclear Material." [Online]. Available: https://www.nrc.gov/materials/sp-nucmaterials.html

[10] T. H. Shin, J. D. Hutchinson, R. Bahran, and S. A. Pozzi, "A note on the nomenclature in neutron multiplicity mathematics," *Nuclear Science and Engineering*, 2019.

[11] C. Wagemans, *The Nuclear Fission Process*. : CRC Press, 1991.

[12] R. P. Feynman, D. F., and R. Serber, "Ststical fluctuations in the water boiler and the dispersion of neutrons emitted per fission (LA-101)," Los Alamos National Laboratory, Tech. Rep., 1944.

[13] D. Reilly, N. Ensslin, and H. Smith, "Passive nondestructive assay of nuclear materials, 2007 addendum, chapter 11 (la-ur-90-732)," Los Alamos National Laboratory, Los Alamos, NM U.S.A, Tech. Rep., 1981.

[14] B. C. Diven, H. C. Martin, R. F. Taschek, and J. Terrell, "Multiplicities of fission neutrons," *Physical Review*, vol. 101, p. 1012, 1956.

[15] D. M. Cifarelli and W. Hage, "On the factorial moments of the neutron multiplicity expressions in nuclear safeguards," *Nuclear Instruments and Methods in Physics Research Section A*, vol. 236, pp. 165–177, 1985.

[16] D. Cifarelli and W. Hage, "Models for a three-parameter analysis of neutron signal correlation measurements for fissile material assay," *Nuclear Instruments and Methods in Physics Research Section A*, vol. 251, pp. 550–563, 1986.

[17] Ensslin, N. and Geist, W. H. and Krick, M. S. and Pickrell, M. M, "Application Guide to Neutron Multiplicity Counting (LA-13422-M)," Los Alamos National Laboratory, Los Alamos, NM U.S.A, Tech. Rep., 1998.

[18] D. B. Pelowitz, "MCNPX User's Manual version 2.7.0 (LA-CP-11-00438)," Los Alamos National Laboratory, Tech. Rep., 2011.

[19] R. C. Haight, H. Y. Lee, T. N. Taddeucci, J. M. O'Donnell, B. A. Perdue, N. Fotiades, M. Devlin, J. L. Ullmann, A. Laptev, T. Bredeweg, M. Jandel, R. O. Nelson, S. A. Wender, M. C. White, C. Y. Wu, E. Kwan, A. Chyzh, R. Henderson, and J. Gostic, "The Prompt fission neutron spectrum measurement program at LANSCE," *Nuclear Data Sheets*, vol. 119, pp. 205–208, 2012.

[20] P. Talou, K. T., and I. Stetcu, "Monte Carlo Hauser-Feshback calculations of prompt fission neutrons and gamma rays: Application to thermal neutron-induced fission reactions on U-235 and Pu-239 (LA-UR-12-25059)," Los Alamos National Laboratory, Los Alamos, NM, U.S.A., Tech. Rep., 2012.

[21] H. R. Bowman, S. G. Thompson, J. C. Milton, and W. J. Swiatecki, "Velocity and angular distributions of prompt neutrons from spontaneous fission of Cf252," *Physical Review*, vol. 126, no. 6, pp. 2120–2136, 1962.

[22] J. S. Pringle and F. D. Brooks, "Angular correlation of neutrons from spontaneous fission of Cf252," *Physical Review Letters*, vol. 35, no. 23, pp. 1563–1566, 1975.

[23] C. Budtz-Jørgensen and H. H. Knitter, "Simultaneous investigation of fission fragments and neutrons in ^{252}Cf (SF)," *Nuclear Physics, Section A*, vol. 490, no. 2, pp. 307–328, 1988.

[24] A. M. Gagarski, I. S. Guseva, V. E. Sokolov, G. V. Val'ski, G. A. Petrov, D. O. Krinitsin, D. V. Nikolaev, T. A. Zavarukhina, and V. I. Petrova, "Neutron-neutron angular correlations in spontaneous fission of 252Cf," *Bulletin of the Russian Academy of Sciences: Physics*, vol. 72, no. 6, pp. 773–777, 2008.

[25] S. A. Pozzi, B. Wieger, A. Enqvist, S. D. Clarke, M. Flaska, M. Marcath, E. Larsen, R. C. Haight, and E. Padovani, "Correlated neutron emissions from 252cf," *Nuclear Science and Engineering*, vol. 178, no. 2, pp. 250–260, 2014.

[26] M. J. Marcath, T. H. Shin, S. D. Clarke, P. Peerani, and S. A. Pozzi, "Neutron angular distribution in plutonium-240 spontaneous fission," *Nuclear Instruments and Methods in Physics Research Section A*, vol. 830, pp. 163–169, 2016.

[27] J. M. Verbeke, L. F. Nakae, and R. Vogt, "Neutron-neutron angular correlations in spontaneous fission of Cf 252 and Pu 240," *Phys. Rev. C*, vol. 97, no. 4, 2018.

[28] R. Serber, "The definition of 'neutron multiplication' (LA-355)," Los Alamos National Laboratory, Tech. Rep., 1945.

[29] K. Bohnel, "The effect of multiplication on the quantitative determination of spontaneously fissioning isotopes by neutron correlation analysis," *Nuclear Science and Engineering*, vol. 90, pp. 75–82, 1985.

[30] R. P. Feynman, D. F., and R. Serber, "Intensity fluctuations of a neutron chain reactor (LADC-256)," Los Alamos National Laboratory, Tech. Rep., 1956.

[31] R. P. Feynman, F. De Hoffmann, and R. Serber, "Dispersion of the neutron emission in U-235 fission," *Journals of Nuclear Energy*, vol. 3, pp. 64–69, 1956.

[32] J. D. Orndoff, "Prompt neutron periods of metal critical assemblies," *Nuclear Science and Engineering*, vol. 2, pp. 450–460, 1957.

[33] G. R. Keepin, *Physics of Nuclear Kinetics.* : Addision-Wesley Publication Co., 1965.

[34] I. Pazsit and L. Pal, *Neutron Fluctuations.* : Elsevier Ltd., 2008.

[35] S. Croft, H. D., and H. D. K., "Extraction of correlated count rates using various gate generation techniques: Part I theory," *Nuclear Instruments and Methods in Physics Research Section A*, vol. 691, pp. 152–158, 2012.

[36] R. E. Uhrig, *Random Noise Techniques in Nuclear Reactor Systems, Chapter 3.* : Ronald Press, 1970.

[37] R. Sanchez, J. Bounds, T. Bredeweg, J. Goda, T. Grove, D. Hayes, K. Jackman, G. Mckenzie, and W. Myers, "Reaction rate, fission product yield, and Rossi-α measurements using a HEU metal, coper, reflected critical assembly," *Journals of Nuclear Science and Technology*, vol. 52, pp. 1018–1025, 2015.

[38] G. E. Hansen, "The Rossi Alpha method (LA-UR-85-4176)," Los Alamos National Laboratory, Tech. Rep., 1985.

[39] I. Pazsit, A. Enqvist, and L. Pal, "A note on the multiplicity expressions in nuclear safeguards," *Nuclear Instruments and Methods in Physics Research Section A*, vol. 603, pp. 541–544, 2009.

[40] G. F. Knoll, *Radiation Detection and Measurements*, 4th ed. United States of America: John Wiley & Sons, 2011.

[41] J. B. Birks, *The Theory and Practice of Scintillation Counting.* Oxford, United Kingdom: Pergamon Press, 1964.

[42] K. Frame, W. Clay, T. Elmont, E. Esch, P. Karpius, M. D., M. E., P. Santi, M. Smith, J. Thron, and R. Williams, "Development of a liquid scintillator neutron multiplicity counter (LSMC)," *Nuclear Instruments and Methods in Physics Research Section A*, vol. 579, pp. 192–195, 2007.

[43] D. L. Chichester, S. A. Pozzi, J. L. Dolan, M. T. Kinlaw, A. C. Kaplan, M. Flaska, J. T. Johnson, and S. Watson, "MPACT Fast Neutron Multiplicity System Design Concepts," Idaho National Lab, University of Michigan, Tech. Rep., 2012.

[44] D. A., T. H. Shin, S. D. Clarke, P. S.A., J. Sanders, D. L. Chichester, D. Lee, P. Feng, M. Root, W. Geist, H. O. Menlove, M. Prasad, and J. Verbeke, "Neutron Rodeo Phase II Final Report," University of Michigan, Tech. Rep., 2019.

[45] T. H. Shin, P. L. Feng, J. S. Carlson, S. D. Clarke, and S. A. Pozzi, "Measured neutron light-output response for trans-stilbene and small-molecule organic glass scintillators - under review," *Nuclear Instruments and Methods in Physics Research Section A*, 2019.

[46] N. Zaitseva, A. Glenn, I. Carman, P. H., R. Hatarik, H. Klapper, and S. Payne, "Scintillation properties of solution-grown trans-stilbene single crystals," *Nuclear Instruments and Methods in Physics Research Section A*, vol. 789, pp. 8–15, 2015.

[47] A. Di Fulvio, K. Beyer, T. H. Shin, N. Giha, S. D. Clarke, and S. A. Pozzi, "SiPM readout of stilbene crystals for safeguards applications," ser. IEEE Nuclear Science Symposium and Medical Imaging Conference, 2017.

[48] D. Brown, M. Chadwick, R. Capote, A. Kahler, A. Trkov, M. Herman, A. Sonzogni, Y. Danon, A. Carlson, M. Dunn, D. Smith, G. Hale, G. Arbanas, R. Arcilla, C. Bates, B. Beck, B. Becker, F. Brown, R. Casperson, J. Conlin, D. Cullen, M.-A. Descalle, R. Firestone, T. Gaines, K. Guber, A. Hawari, J. Holmes, T. Johnson, T. Kawano, B. Kiedrowski, A. Koning, S. Kopecky, L. Leal, J. Lestone, C. Lubitz, J. M. Damin, C. Mattoon, E. McCutchan, S. Mughabghab, P. Navratil, D. Neudecker, G. Nobre, G. Noguere, M. Paris, M. Pigni, A. Plompen, B. Pritychenko, V. Pronyaev, D. Roubtsov, D. Rochman, P. Romano, P. Schillebeeckx, S. Simakov, M. Sin, I. Sirakov, B. Sleaford, V. Sobes, E. Soukhovitskii, I. Stetcu, P. Talou, I. Thompson, S. van der Marck, L. Welser-Sherrill, D. Wiarda, M. White, J. Wormald, R. Wright, M. Zerkle, G. erovnik, and Y. Zhu, "Endf/b-viii.0: The 8th major release of the nuclear reaction data library with cielo-project cross sections, new standards and thermal scattering data," *Nuclear Data Sheets*, vol. 148, pp. 1 – 142, 2018, special Issue on Nuclear Reaction Data. [Online]. Available: http://www.sciencedirect.com/science/article/pii/S0090375218300206

[49] M. Berger, J. Hubbell, S. Seltzer, J. Chang, J. Coursey, R. Sukumar, D. Zucker, and K. Olsen, "XCOM: Photon cross sections database," *[Online]. Available : https://physics.nist.gov/cgi-bin/Xcom/xcom2*, 2018.

[50] "DPP-PSD Digital Pulse Processing for Pulse Shape Discrimination, User Manual UM2580 Rev. 9," Tech. Rep., 2018.

[51] J. A. Brown, B. L. Goldblum, T. A. Laplace, K. P. Harrig, L. A. Bernstein, D. L. Bluel, W. Younew, D. Reyna, B. E., and P. Marleau, "Proton light yield in organic scintillators using a double time-of-flight technique," *Journal of Applied Physics*, vol. 124, p. 045101, 2018.

[52] D. A., T. H. Shin, M. C. Hamel, and S. A. Pozzi, "Digital pulse processing for NaI(Tl) detectors," *Nuclear Instruments and Methods in Physics Research Section A*, vol. 806, pp. 169–174, 2015.

[53] N. V. Kornilov, I. Fabry, S. Oberstedt, and F. J. Hambsch, "Total charecterization of neutron detectors with a ^{252}Cf source and a new light output determination," *Nuclear Instruments and Methods in Physics Research Section A*, vol. 599, pp. 226–233, 2009.

[54] M. A. Norsworthy, P.-R. A., M. L. Ruch, S. D. Clarke, and S. A. Pozzi, "Evaluation of neutron light output response functions in ej-309 organic scintillators," *Nuclear Instruments and Methods in Physics Research Section A*, vol. 842, pp. 20–27, 2017.

[55] F. Brooks, "A Scintillation Counter with Neutron and Gamma-Ray Discriminators," *Nuclear Instruments and Methods*, vol. 4, pp. 151–163, 1959.

[56] F. D. Brooks, R. W. Pringle, and B. L. Funt, "Pulse shape discrimination in a plastic scintillator," *IRE Transactions on Nuclear Science*, vol. 7, no. 2-3, pp. 35–38, 1960.

[57] J. K. Polack, M. Flaska, A. Enqvist, C. S. Sosa, C. C. Lawrence, and S. A. Pozzi, "An algorithm for charge-integration, pulse-shape discrimination and estimation of neutron/photon misclassification in organic scintillators," *Nuclear Instruments and Methods in Physics Research Section A*, vol. 795, pp. 253–267, 2015.

[58] S. A. Pozzi, S. D. Clarke, W. J. Walsh, E. C. Miller, J. L. Dolan, M. Flaska, B. M. Wieger, A. Enqvist, and E. Padovani, "Mcnpx-polimi for nuclear nonproliferation applications," *Nuclear Instruments and Methods in Physics Research Section A*, vol. 694, pp. 119–125, 2012.

[59] E. C. Miller, S. D. Clarke, M. Flaska, S. A. Pozzi, and E. Padovani, "MCNPX-PoliMi post-processing algorithm for detector response simulations," *Journals of Nuclear Materials Management*, vol. 40, pp. 34–41, 2012.

[60] G. Dietze and H. Klein, "Gamma-calibration of NE 213 scintillation counters," *Nuclear Instruments and Methods in Physics Research*, vol. 193, pp. 549–556, 1982.

[61] P. Desesquelles, A. J. Cole, A. Dauchy, A. Giomi, D. Heuer, A. Lleres, C. Morand, J. Saint-Martin, P. Stassi, J. B. Viano, B. Chambon, B. Cheynis, D. Drain, and C. Pator, "Cross talk and diaphony in neutron detectors," *Nuclear Instruments and Methods in Physics Research Section A*, vol. 307, pp. 366–373, 1990.

[62] M. Cronqvist, B. Jonson, T. Nilsson, G. Nyman, K. Riisager, H. A. Roth, O. Skeppstedt, O. Tengblad, and K. Wilhelmsen, "Experimental determination of cross-talk between neutron detectors," *Nuclear Instruments and Methods in Physics Research Section A*, vol. 317, pp. 273–280, 1992.

[63] T. H. Shin, M. Y. Hua, M. J. Marcath, D. L. Chichester, I. Pazsit, A. Di Fulvio, S. D. Clarke, and S. A. Pozzi, "Neutron multiplicity counting moments for fissile mass estimation in scatter-based neutron detection systems," *Nuclear Science and Engineering*, vol. 188, pp. 246–269, 2017.

[64] S. Croft and L. C. Bourva, "The measurement of passive neutron multiplicity counter gate utilization factors and comparisons with theory," *Nuclear Instruments and Methods in Physics Research Section A*, vol. 453, pp. 553–568, 2000.

[65] D. Henzlova, S. Croft, H. O. Menlove, and M. T. Swinhoe, "Extraction of correlated count rates using various gate generation techniques: Part II experiment," *Nuclear Instruments and Methods in Physics Research Section A*, vol. 691, pp. 159–167, 2012.

[66] R. Dierckx and W. Hage, "Neutron signal multiplet analysis for the mass determination of spontaneous fission isotopes," *Nuclear Science and Engineering*, vol. 85, pp. 325–338, 1983.

[67] M. K. Prasad, N. J. Snyderman, and J. M. Verbeke, "Analytical error bars and RSD for neutron multiplicity counting," *Nuclear Instruments and Methods in Physics Research Section A*, vol. 903, pp. 25–31, 2018.

[68] M. M. Monterial, P. Marleau, M. Paff, S. D. Clarke, and S. A. Pozzi, "Multiplication and presence of shielding material from time-correlated pulse-height measurements of subcritical plutonium assemblies," *Nuclear Instruments and Methods in Physics Research Section A*, vol. 851, pp. 50–56, 2017.

[69] T. H. Shin, M. J. Marcath, A. Di Fulvio, S. D. Clarke, and S. A. Pozzi, "Neutron cross-talk characterization of liquid organic scintillators," ser. IEEE Nuclear Science Symposium and Medical Imaging Conference, 2015.

[70] A. Di Fulvio, T. H. Shin, T. Jordan, C. S. Sosa, M. L. Ruch, S. D. Clarke, D. L. Chichester, and S. A. Pozzi, "Passive assay of plutonium metal plates using a fast-neutron multiplicity counter," *Nuclear Instruments and Methods in Physics Research Section A*, vol. 855, pp. 92–101, 2017.

[71] H. Menlove, S. J., S. Qiao, T. Wenz, and P. Verrecchia, "Neutron collar calibration and evaluation for assay of LWR fuel assemblies containing burnable neutron absorbers," *Los Alamos National Laboratory Report*, pp. LA–11 965–MS, 1990.

[72] C. W. Solbrig, J. Andrus, and C. Pope, "ZPPR fuel element thermal stress-strain analysis," *World Journal of Nuclear Science and Technology*, vol. 4, pp. 123–128, 2014.

[73] N. Ensslin, W. H. Geist, M. S. Krick, and M. M. Pickrell, "Active neutron multiplicity counting (LA-UR-07-1403)," Los Alamos National Laboratory, Tech. Rep., 1998.

[74] A. Di Fulvio, T. H. Shin, A. Basley, A. Swenson, C. Sosa, S. D. Clarke, J. Sanders, S. Watson, D. L. Chichester, and S. A. Pozzi, "Fast-neutron multiplicity counter for active measurements of uranium oxide certified material," *Nuclear Instruments and Methods in Physics Research Section A*, vol. 907, pp. 248–257, 2018.

[75] A. Belian, A. Dougan, A. Iyengar, D. Chichester, S. Clarke, S. Croft, D. Decman, W. Geist, H. P., H. Jianwei, M. R., M. H., J. Newby, S. Pozzi, M. Prasad, J. Sanders, T. Shin, S. Thompson, and J. Verbeke, "Advanced neutron detection technology rodeo," ser. ESARDA Symposium, 39th Annual Meeting, 2017.

[76] H. Tagziria and D. J. Roberts, "Measurement of the 241Am-Li radionuclide neutron source spectrum," *Nuclear Instruments and Methods in Physics Research Section A*, vol. 510, pp. 346–356, 2003.

[77] T. H. Shin, A. Di Fulvio, S. D. Clarke, D. L. Chichester, and S. A. Pozzi, "Prompt fission neutron anisotropy in low-multiplying subcritical plutonium metal assemblies," *Nuclear Instruments and Methods in Physics Research, Section A: Accelerators, Spectrometers, Detectors and Associated Equipment*, vol. 915, pp. 110–115, 2019.

[78] D. L. Chichester, S. J. Thompson, M. T. Kinlaw, J. T. Johnson, J. L. Dolan, M. Flaska, and S. A. Pozzi, "Statistical estimation of the performance of a fast-neutron multiplicity system for nuclear material accountancy," *Nuclear Instruments and Methods in Physics Research Section A*, vol. 784, pp. 448–454, 2015.

[79] J. M. Mueller and J. Mattingly, "Using anisotropies in prompt fission neutron coincidences to assess the neutron multiplication of highly multiplying subcritical plutonium assemblies," *Nuclear Instruments and Methods in Physics Research Section A*, vol. 825, pp. 87–92, 2016.

[80] D. L. Chichester, "Properties of nuclear fuel used in tests with the llnl gamma-ray mirror," vol. MIS-14-33068, 2014.

[81] M. M. Monterial, P. Marleau, and S. A. Pozzi, "Characterizing subcritical assemblies with time of flight fixed by energy estimation distributions," *Nuclear Instruments and Methods in Physics Research Section A*, vol. 888, pp. 240–249, 2018.

[82] A. S. Vorobyev, O. A. Shcherbakov, Y. S. Pleva, A. M. Gagarski, G. V. Val'ski, G. A. Petrov, V. I. Petrova, and T. A. Zavarukhina, "Measurements of angular and energy distributions of prompt neutrons from thermal neutron-induced fission," *Nuclear Instruments and Methods in Physics Research Section A*, vol. 598, no. 3, pp. 795–801, 2009.

[83] T. H. Shin, C. A. Bravo, W. H. Geist, J. Marlow, S. D. Clarke, and S. A. Pozzi, "Neutron-neutron angular and energy-angle correlations in plutonium samples with varying α-ratio - under review," *Nuclear Instruments and Methods in Physics Research Section A*, 2019.

[84] J. M. Verbeke, G. F. Chapline, L. F. Nakae, and S. A. Sheets, "Distinguishing pu metal from pu oxide and determining α-ratio using fast neutron counting," *Nuclear Instruments and Methods in Physics Research Section A*, vol. 782, pp. 126–132, 2015.

[85] L. Holewa, W. Charlton, E. Miller, and S. Pozzi, "Using neutron angular anisotropy information to dynamically determine the ratio of the (α,n) rate to spontaneous fission rate for coincidence counting applications," *Nuclear Instruments and Methods in Physics Research Section A*, vol. 701, pp. 249–253, 2013.

[86] W. H. Geist, "Pu button - multiplicity measurements in the enmc," Tech. Rep., 2006.

[87] L. F. Miller, J. Preston, S. A. Pozzi, M. Flaska, and J. Neal, "Digital pulse shape discrimination," *Radiation Protection Dosimetry*, vol. 126, pp. 1–4, 2007.